Technische
Universität
Wien

Vienna
University of
Technology

Dissertation

Investigations of mobile ion transport processes in thin layers upon bias-temperature stress

ausgeführt zum Zwecke der Erlangung des akademischen Grades eines
Doktors der technischen Wissenschaften

unter der Leitung von

Ao. Univ. Prof. Dipl.-Ing. Dr. techn. Herbert Hutter

am Institut für Chemische Technologien und Analytik (E164)

eingereicht an der Technischen Universität Wien
Fakultät für Technische Chemie

von

Dipl.-Ing. Stefan Krivec
Matrikelnummer 0101136
Birkenweg 23
A-9241 Wernberg

Wien, am 16. Mai 2011

This work was jointly funded by the Federal Ministry of Economics and Labor of the Republic of Austria (contract 98.362/0112-C1/10/2005) and the Carinthian Economic Promotion Fund (KWF) (contract 18911 | 13628 | 19100).

This work was accomplished in the framework of project M1 - RoMI (Robust Metallization and Interconnects) at KAI - Kompetenzzentrum Automobil- und Industrieelektronik GmbH (Europastrasse 8, 9524 Villach/St.Magdalen, Austria) in collaboration with the Institute of Chemical Technologies and Analytics at the University of Technology in Vienna and Infineon Technologies Austria AG in Villach.

Acknowledgements

I want to give sincere thanks to all people who contributed to this work by means of ideas, discussions, practical guidance and specimen preparation.

Prof. Herbert Grünbacher, Dipl.-Ing. Josef Fugger and Dr. Thomas Detzel for giving me the opportunity to work three years in a professional environment of a well organized collaboration. Especially, I gratefully acknowledge Dr. Detzel, who conducted the M1 RoMI project in a perfect manner, giving me an insight how to successfully manage such a project.

Special thanks to Prof. Herbert Hutter from the Institute of Chemical Technologies and Analytics at the University of Technology in Vienna, who enabled this thesis and supervised me throughout three years of practical and theoretical work. He teached me a lot about physical analytics and physics in general, broadening my spectrum of education.

People from Infineon Technologies Austria AG always had an open ear for my issues. In particular I want to thank Dipl.-Ing. Michael Buchmayr for accompanying me throughout 3 years with discussions and helpful hints, Dr. Michael Nelhiebel for ideas and discussions and Reinhold Grilz for providing me with wafers for experiments.

All colleagues from KAI and the TU Vienna are gratefully acknowledged for giving me a perfect working environment. Special thanks to Dipl.-Chem. Till Frömling, Dr. Stefan Puchner and Dipl.-Ing. Markus "Mol" Holzweber for accompanying me three years with fruitful discussions during and after work.

My sincere thanks to Dr. Magdalena Forster and Dipl.-Ing. Gerald Holzlechner for proof-reading the manuscript.

Last but not least, I want to thank my family for the support during the last three years. My parents Felix and Sieglinde always encouraged me in my decisions in terms of my education and supported my way. Thank you very much.

I want to separately mention my own founded family: My love Martina who supported my way of education I have chosen and my little son Matthias, who is all the happiness in the world for me. I am pleased to shaping my future together with the both of you.

Investigations of mobile ion transport processes in thin layers upon bias-temperature stress

Abstract

Mobile ions are well known to cause severe problems in the semiconductor industry. Incorporated by numerous sources during and after chip production these ions can alter the properties of a MOSFET device e.g. by contamination of the gate oxide. Mobile sodium ions (Na^+) are thereby a particular danger, since encountered in comparable large amounts. In order to investigate mobile ion incorporation from an external source, deliberately and defined contaminated with mobile ions, into an underlying thin insulating or conductive material film and the subsequent transport therein, a developed methodology is presented. This approach comprises the preparation of a sample including the attachment of an appropriate host matrix for mobile ions onto the specimen with the material layer of interest being the topmost layer, a subsequent stressing procedure by applying a bias voltage while keeping the sample at a constant temperature (B-T stress) and a final physical analysis by time of flight - secondary ion mass spectrometry (ToF-SIMS). But the determination of mobile ion distributions in insulating samples by means of ToF-SIMS depth profiling has always been a challenge. This is in particular true for thin insulating films on conducting substrates when ${O_2}^+$ is used as sputter species. Such depth profiles exhibit severe artifacts in the mobile ion depth distribution, due to the appearance of an electric field within the insulator, arising by means of sample charging during the sputter process. This problem is addressed by investigation of the temperature dependence of Na migration. The here obtained results enables data processing in order to gain artifact free and thus reliable ToF-SIMS depth profiles, e.g. of Gaussian shaped Na implantation profiles. By the acquisition of depth profiles at different sample temperatures it is also possible to analyze mobile ion distributions in samples after B-T stress application in a reliable manner. With this feature, the presented methodology enables the assessment of thin material films on mobile ion incorporation and their permeability against mobile ion transport under different B-T stress conditions. Insulating and conductive films of high importance for the semiconductor devices are investigated: silicon dioxide (SiO_2), silicon oxynitride (SiO_xN_y), silicon nitride (Si_3N_4), boron-phosphosilicat glass (BPSG) and an aluminum-silicon-copper alloy (AlSiCu), a common material for metalization layers. In particular SiO_2 is examined in detail, both qualitatively and quantitatively: For the example of Na^+, a comparison is given between the calculated provided amount in the host matrix with potentiostatic data from B-T-stress and spectrometric data from quantification of ToF-SIMS depth profiles. Appropriate physico-chemical models are adapted on the present samples and thus parameters describing mobile ion transport in SiO_2 are condensed out of potentiostatic data (activation energy, incorporation rate and diffusion constant).

Untersuchungen von Transportvorgängen mobiler Ionen in dünnen Schichten aufgrund Bias-Spannung und Temperatur

Kurzfassung

In der Halbleiterindustrie können mobile Ionen schwerwiegende Folgen bezüglich der Zuverlässigkeit der erzeugten Produkte verursachen. Es gibt unzählige Möglichkeiten Mikrochips und andere Bauteile mit mobile Ionen zu kontaminieren. Ursachen dafür findet man während und auch nach der Produkterzeugung, die alle potentiell dazu führen können die Eigenschaften von Bauteilen zu verändern. Metall Oxid Halbleiter (MOS) Transistoren sind dabei überaus empfindlich auf Kontamination mit mobilen Ionen im Gate Oxid. Eine besondere Gefahr in diesem Bezug sind mobile Natriumionen (Na^+), welche in verschiedensten Verbindungen und in vergleichsweise großer Häufigkeit auftreten. Die Untersuchung von Transportvorgängen mobiler Ionen in dünnen Schichten leitender und nichtleitender Materialien liefert daher wichtige Informationen für die Halbleiterindustrie. Um die Inkorporation von mobilen Ionen aus einer definiert kontaminierten Quelle in diese Schichten und den darauffolgenden Transport darin zu analysieren, wird eine dafür entwickelte Methodik vorgestellt. Diese beinhaltet die Herstellung einer Probe, bei welcher eine mit mobilen Ionen kontaminierte Polymermatrix auf den zu untersuchenden Probenkörper aufgebracht ist. Transportvorgänge mobiler Ionen werden dann über eine extern angelegte Spannung (Bias-Spannung) ermöglicht, während die Probe auf konstanter Temperatur ist. Die Verteilungen der mobilen Ionen nach dieser Belastung werden mittels Flugzeit - Sekundärionenmassenspekrometrie (ToF-SIMS) Tiefenprofilerung untersucht. Dies ist bis heute problematisch, da insbesondere der Sputterprozess mit ${O_2}^+$ während der Messung Artefakte in Tiefenverteilungen mobiler Ionen verursacht. Ziel einer detailierten experimentellen Studie ist der Einfluss der Probentemperatur auf Artefakte während der Aufnahme eines ToF-SIMS Tiefenprofiles. Es wird gezeigt, dass diese Maßnahme Tiefenprofile von Proben nach Belastung mit Bias-Spannung und Temperatur zuverlässig auf auftretende Artefakte überprüft. Desweitern kann man dadurch aber auch artefaktfreie ToF-SIMS Tiefenprofile von Proben mit bekannter Verteilung, wie z.B. einer gaussformigen Na Implantation, durch geeignete Methoden der Datenverarbeitung ermitteln. Resultate von Untersuchungen von Transportvorgängen mobiler Ionen in den folgenden Materialien werden präsentiert: Siliziumdioxid (SiO_2), Siliziumoxinitrid (SiO_xN_y), Siliziumnitrid (Si_3N_4), Borphosphorsilikatglas und einer Aluminium-Silizium-Kupfer Legierung. SiO_2 dient dabei als Material für detailierte qulitative und quantitative Untersuchungen von Na^+ Transportvorgängen und für die Anwendung physikalisch-chemischer Modelle, um Parameter zur Beschreibung von Transportvorgängen mobiler Ionen in SiO_2 zu berechnen (Aktivierungsenergie, Inkorporationsrate und Diffusionskonstante).

Contents

Chapter 1

Introduction

Mobile ions display a permanent and present danger for the reliability of semiconductor products. A well known problem is the instability of metal oxide semiconductor field effect transistors (MOSFET) due to contamination of the gate oxide by mobile ions. In order to avoid such harmful effects, crucial device regions are protected by barrier layers, hindering the transport of harmful species. A detailed knowledge on ion transport phenomena in materials, commonly appearing in device structures, is of utmost significance. But also the exchange of contaminants between material layers in terms of incorporation processes are important issues in this context. All these effects are governed by driving forces of thermodynamic nature, as reflected by diffusion and drift processes as two prominent candidates. Since nowadays impurity levels in materials used for device fabrications are extremely low, the potentially biggest danger arises from mobile ion contaminations on interfaces or surfaces. Conditions in actual use of a device, thus electric fields or temperature, may trigger transport processes. Device batches get deliberately contaminated and tested under extreme stress conditions, in order to ensure the quality of a product prior to shipping to the customer.

The initial point of this thesis was to study and discuss the effects mobile ions have on MOS transistors, thus the basic structures of this technology dominated the concept of presented investigations. In general, the following fundamental considerations have to be mentioned:

- Silicon (Si) was taken as the semiconductor substrate material. Si therefore typically represents the semiconductor within the term "metal oxide semiconductor" (MOS).
- Due to its outstanding importance in terms of potentially harmful effects for MOS transistors, the role of sodium (Na) and thus its ionic form Na^+ in transport processes was the main focus of research. Comparison to other mobile ions are given in the respective passages of the thesis.

Chapter 2 contains an overview of the effects mobile ions have on the reliability of MOS transistors, but also common electrical approaches for their detection and quantification are discussed. However, such approaches suffer from some disadvantages as for instance the lack of direct physical evidence of the presence of mobile ions within device structures or the basic restriction to conductor(semiconductor)/insulator/conductor(semiconductor) sandwich systems.

On this point the core issue of this thesis comes into play: Thin layers of materials were deliberately contaminated with mobile ions on the surfaces, and probed under extreme stress conditions. The term thin film ($\equiv$ thin layer), in general, describes hereby thicknesses of up to 1 μm. The insulating and conducting materials were chosen due to the significance in MOSFET devices for various application purposes as e.g. gate oxide, barrier layers, metalization. A polymer host matrix for mobile ions was elaborated, containing a defined and adjustable dose of the respective contaminant. Attached on the material layer to be investigated in the form of a thin film and covered by an electrode, the application of bias-temperature (B-T) stress enabled mobile ion transport processes within both the polymer and the material layer below. Thin gold (Au) layers were deposited on the host matrix, representing the metal in the MOS structure. Subsequent to the stressing procedure, physical analysis by means of time of flight secondary ion mass spectrometry (ToF-SIMS) provided unambiguous detection of mobile ions in terms of their spatial distribution within the investigated material layer.

In Chapter 3, the methodology for B-T stress is presented systematically. Due to its outstanding relevance for experiments a detailed overview on ToF-SIMS and its fundamental technique will be given. A substantial part of Chapter 3 is devoted to ToF-SIMS depth profiling. Appearing measurement artifacts for insulating samples are shown and discussed, with mobile ion migration processes as the most dominating one.

Reasons for mobile ion migration and possibilities to counteract this effect during ToF-SIMS depth profiling are discussed in chapter 4, with the emphasize on Na migration. Results of experimental investigation on the influence of the sample temperature during ToF-SIMS depth profiling are presented and discussed.

Chapters 5 and 6 describe the experimental results on transport processes of mobile ions within thin films of insulating and conductive materials. Again, special attention was laid on Na^+ incorporation from the polymer host matrix into the investigated material. In Chapter 5 a physico-chemical model for the quantitative assessment of Na^+ incorporation into SiO_2 and transport therein is presented.

Chapter 2

Mobile ions in MOS transistors

2.1. Industrial relevance of reliability

One of the most crucial features of semiconductor high tech products is their reliability, for its major relevance in terms of quality, confidence, reputation and of course success of the manufactured item. Under specified conditions a manufacturer has to guarantee reliability, i.e. maximum product lifetimes with a, from a statistical point of view, negligible failure probability. Unrestricted operation must be ensured within this specified time period and any kind of malfunctions must be excluded. An application field where this can be illustrated in a proper way is the automotive industry. A modern car contains a huge number of semiconductor devices e.g. for the use in airbag systems , for power supply integrated circuits or as a sensor. One can easily imagine that instabilities, malfunctions or failures of these components can have severe consequences. Since the beginning of modern semiconductor technology reliability issues have been the reason for huge effort and investigations in terms of research on device second order effects and failure mechanism. In industry, numerous monitoring tools and reliability tests are employed in order to inspect the products on possible sources of errors. These measures are carried out at extreme stress conditions (such as high temperatures, increased bias, high humidity,. . .) for an accelerated failure rate with appropriate models to be applied for a subsequent extrapolation to actual operation conditions. Only device batches that pass the broad spectrum of tests can be shipped to the customer. Fig. 2.1 depicts a prominent graphic for a hazard function, the so called bathtube curve [1], which displays the failure rate of a semiconductor product in terms of its status. In the initial state, the production of the chip, the thorough screening for faulty devices and systematic malfunctions is of utmost significant in order to enable full functionality of the product during the specified lifetime. Usually, a comparable high infant mortality is the consequence, in order to restrict the failure rate in the useful device lifetime on a ultra low level of statistically occurring random failures. Towards the end, due to factors as material fatigue, the failure rate commonly increases again in the wearout.

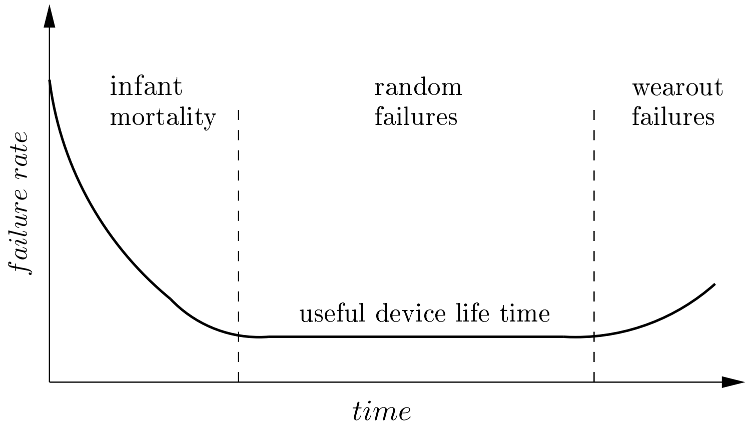

Figure 2.1.: For reliability illustration the bathtube curve is widely used as a hazard function representing the stages of device lifetime

The reasons for possible device failure and degradation are versatile and it is not the aim of this introduction to go into detail with this topic. However, it is important to distinguish between different categories: (i) Induced during device fabrication, intrinsic failures occur during operation within the specified use conditions by means of internal causes [2]. Examples are point defects in crystal lattices, void formation in the metalization, unwanted chemical reactions, inter-diffusion between material layers and many more. Getting detected by device tests after fabrication, such failures explain comparatively high failure rate in the infant mortality period of 2.1. (ii) On the other hand during their useful life period, devices in actual use, although passing all device tests, may also suffer from extrinsic failures by various external influences as contaminations but also from misapplications, as for instance electrical overstress [2]. In literature there are numerous references, which covers all these topics (e.g. [3, 4]).

One issue with significant relevance is the influence of contaminations on the reliability of semiconductor products, potentially leading to both internal and external failures. The term contamination concerns foreign atoms, molecules and particles, different from the chemical state of the actual material, which gets impacted. Every possible physical aggregate state is thereby included with the ability to end up as a surface contaminant or as an impurity within a matrix. Intrinsic contaminations are potentially possible at each stage of device fabrication from early stages as silicon crystal grow processes until assembly steps by process-induced factors, operators, environmental influences or equipment. Clean rooms are therefore a stringent requirement for device fabrication. Despite this measures extrinsic influences during operation may also exhibit sources of potential contamination. Extensive care in form of barrier layers or protections are ensuring contaminant free and hence secure operation during the warranted device life time.

The spectrum of possible contaminations is broad and it is not possible to go into detail on this point. Though, some examples are worthy to mention here, in order to communicate consequences due to their impact on semiconductor devices: A first problem concerns tungsten (W) introduced by chemical vapor deposition (CVD) as is in use for interconnecting plugs, metalizations or in WSi_x as gate metal. Since tungsten hexafluoride (WF_6) is used as a precursor for this process, contamination with fluorine (F) is a frequently encountered problem. Owing to its high reactivity with other elements as titanate (Ti) and aluminum (Al), this could give rise to increased resistivity between W plugs and adjacent conductive layers [5]. Furthermore F^- is well known for its ability as a fast diffusor at elevated temperatures as used during some process steps may lead to gate oxide degradation [6]. A second example subjects organic substances, contaminating the surface of Si wafers. For instance wafer transfer using transport boxes can be a reason for contamination, since such boxes may tend to release organic additives which attach on the wafer surface [7]. Typical substances found are butyl hydroxy toluen (BHT), an antioxidant for polypropylene, or dibutyl phtalate (DBP) and dioctyl phtalate (DOP), plasticizer for polymer production. Moreover, some outgassing organic volatiles may arise from operation in clean room facilities, originating e.g. from sealants, panels or electric cables. Amongst other problems, these compounds could be disadvantageous to the integrity and thus the quality of thermally grown gate oxides in metal oxide semiconductor (MOS) structures [8, 9, 10] or lead to deviations in the thickness of CVD films [11]. But also weakening of gold (Au) wire bond adhesion has been reported due to contamination of the respective Al pads with organic compounds arising from epoxy resins [12], as in use for die attachment on lead frames.

2.2. The impact of mobile ions on MOS transistors

A further contamination type, that has particular significance are metal contaminations. There are numerous elements all across the periodic table of elements which are potentially harmful to device operations as e.g. iron (Fe), copper (Cu), nickel (Ni) and many more. Alkali metals display an outstanding position in this context. Appearing in compounds and thus in its respective ionic forms, these elements have, compared to other metal ions, small ionic radii (Tab. 2.1). In the semiconductor technology community these elements are commonly referred to as mobile ions and hence having the ability of being fast diffusors in a broad variety of materials.

Table 2.1.: Ionic radii of relevant alkali and earth alkali elements

Ion	Ionic radius [Å]
Lithium (Li^+)	0.76
Sodium (Na^+)	1.02
Potassium (K^+)	1.38
Magnesium (Mg^2+)	0.72
Calcium (Ca^2+)	1.00

Additionally, one can add hydrogen ions (H^+) to the group of mobile ions, with significantly influencing device stabilities [13]. Since amongst alkali metals sodium (Na) in its ionic form Na^+ has an outstanding position, for its small ionic radius and comparable high abundance as a contaminant, the discussion of mobile ions in terms of reliability emphasizes on this species. In particular, metal oxide semiconductor field effect transistor (MOSFET) devices are extremely vulnerable to mobile ion contamination [14]. For didactic purposes it is helpful to show the assembly of a MOS structure in a graphical way (Fig. 2.2(a)), whereas the focus lying on nMOS transistors due to its outstanding position in terms of Na^+ contamination.

The device is hereby in *on* state, hence a positive gate source voltage V_{GS} is applied in order to build-up an electric conductive path, the n-channel, in the p-doped Si substrate on the interface towards the gate oxide. A detailed description on the basics and functionality of MOS transistors can be found in respective literature (e.g. [15]). In Fig. 2.2(b) a typical nMOSFET transfer characteristic with the drain current I_D as a function of V_{GS}, is displayed. An crucial parameter for MOSFET design is the threshold voltage V_{th}, the V_{GS} value where the MOS structure goes into strong inversion and a n-channel arises below the gate oxide, determining whether the transistor is in *off* state ($V_{GS} < V_{th}$) or turned on ($V_{GS} > V_{th}$). Frequently, transfer characteristics are plotted in the form $\sqrt{I_{DS}}$ vs. V_{GS}, in order to emphasize the subthreshold region. Once Na^+ has intruded into the gate oxide, transport processes within the gate oxide may occur in actual use under the influence of the applied V_{GS}, finally leading to Na^+ accumulating at the interface of gate oxide and Si substrate (Fig. 2.2(c)). This is of special importance for nMOS transistors, since a positive V_{GS} is applied to turn the device on. In this case, the transfer characteristics of the transistor exhibit V_{th} instabilities, consequently altering the functionality of the transistor. In order to analyze this effect, it is necessary to mention the mathematical expression for V_{th} [15]:

$$V_{th} = V_{FB} + 2\phi_F + \gamma\sqrt{2\phi_F + V_{SB}} \tag{2.1}$$

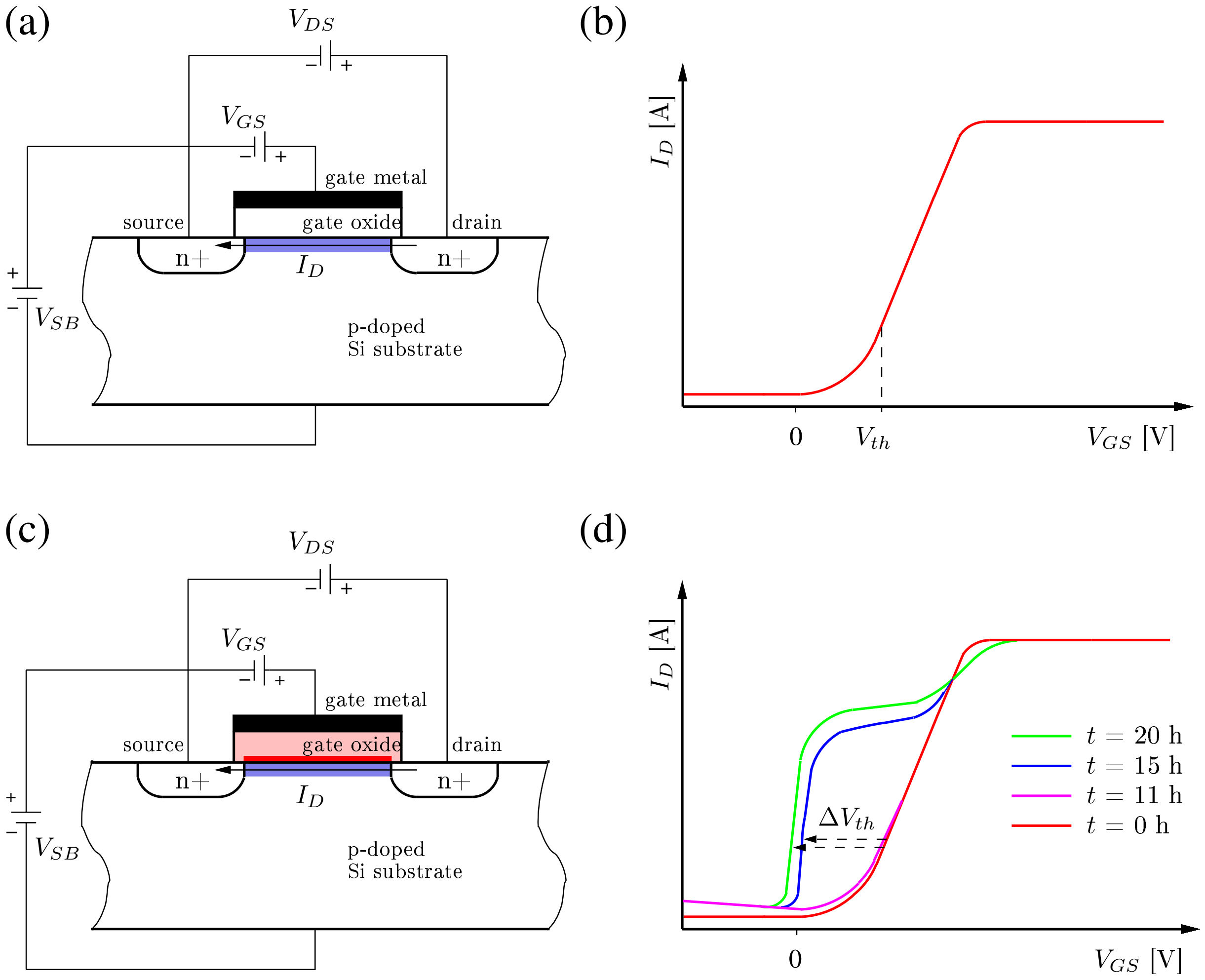

Figure 2.2.: (a) nMOS structure in strong inversion with $V_{GS} > V_{th}$ and the n-channel displayed by a blue region on the Si-faced side of the gate oxide / Si interface. The illustration has been taken over and adapted from [15]. (b) Scheme of nMOSFET transfer characteristics with expected behavior. V_{th} is displayed as an arbitrary value. (c) nMOS structure in strong inversion with Na^+ present in the gate oxide and accumulated at the gate oxide / Si interface, respectively, as marked by a red shading in the gate oxide. (d) Typical ΔV_{th} due to Na^+ present in the gate oxide and exposure to extreme stress conditions. The scheme represents the detection of faulty devices on wafer scale. (a) and (d) are reconstructed from data out of reliability tests (Courtesy of Infineon Technologies Austria AG) and presented without scale due to industrial restrictions.

Therein V_{FB} is the flatband voltage of the transistor and ϕ_F the potential difference between the intrinsic Fermi level and the actual Fermi level as determined by Si doping. Thus, in the case of p-doping, ϕ_F illustrates the hole density in the Si-substrate. V_{SB} is the voltage arising from connecting source with bulk and applied back biasing thereof. As observable in 2.2(a) and (b), $V_{GB} = V_{GS} + V_{SB}$ is effectively biasing the MOS structure. The grade of influence of V_{SB} on V_{th} is governed by γ, the so called body factor. For reasons of simplification in this introduction, however, the effect of V_{SB} is considered as negligible, hence assuming $V_{GB} = V_{GS}$. On this point it is necessary to take a closer look on V_{FB} by considering its definition

$$\phi_{Ox} + \phi_S = 0 \tag{2.2}$$

with $\phi_{Ox}, \phi_S > 0$ for a nMOS transistor in accumulation. Thus V_{FB} is determined by the applied V_{GS} where ϕ_{Ox}, the voltage drop across the gate oxide, and ϕ_S, the voltage drop due to majority carrier accumulation on the Si faced side of the gate oxide / Si interface, are compensated and no distortion of valenece and conduction band are present reference (Fig. 2.3(a) as adapted from [15]).

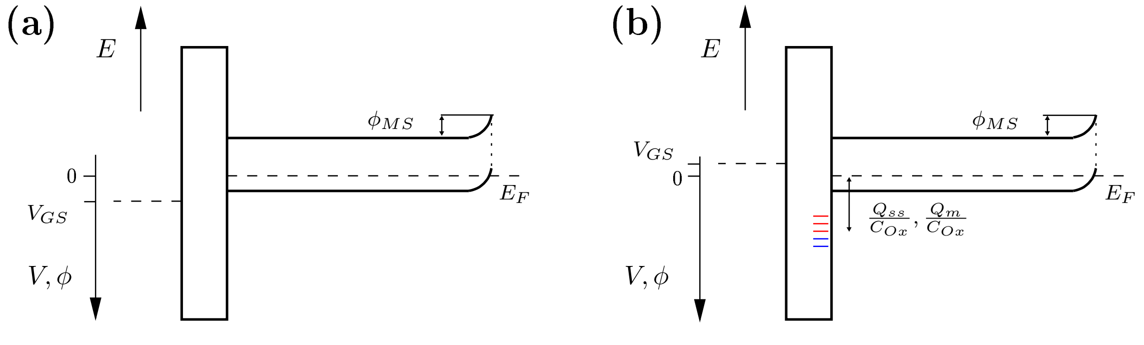

Figure 2.3.: (a) Energy band scheme of a nMOS transistor with $V_{GS} = V_{FB}$. (b) Energy band scheme of a nMOS transistor including impurity levels within the gate oxide (arbitrary chosen). Fixed charges and interface traps are marked by blue color. Mobile ions are marked by red color. $V_{GS} = V_{FB}$ is applied , thus V_{FB} is shifted towards lower absolute values by the presence of mobile ions.

In other words, by applying $V_{GS} = V_{FB}$ the transistor get into depletion, and by $V_{GS} \geq V_{th}$ into inversion (as given by eq. (2.1)). If the gate oxide / Si interface exhibits intrinsic interface traps or fixed charges in the quantity Q_{SS} or mobile ions (e.g. Na$^+$ in the quantity Q_m are present the gate oxide), the effective V_{GS} affecting the generation of an inversion layer in the MOS structure becomes increased by [16]

$$\phi_{Ox} + \phi_S = V_{GS} - \phi_{MS} + \frac{Q_{SS}}{C_{Ox}} + \frac{1}{x_{Ox} \cdot C_{Ox}} \int_0^x x\rho(x)\mathrm{d}x \tag{2.3}$$

with ϕ_{MS} representing the work function difference between metal and semiconductor (assuming direct contact as shown in Fig. 2.2(a) and $\rho(x)$ the mobile ion distribution within the gate oxide. C_{Ox} is the capacitance of the gate oxide and x_{Ox} its thickness. In order to fulfill equation (2.2) and hence achieve V_{FB}, the corresponding V_{GS} is lowered by the 3^{th} (interface traps) and 4^{th} (mobile ions) term on the right hand side of eq.(2.3). Fig. 2.3(b) illustrated this effect by means of energy band schemes. Interface traps and fixed oxide charges may arise by various influences (e.g. [17, 18]) and cause an initial offset of V_{FB} and thus V_{th} towards lower values. The same effect is triggered by mobile ions as Na^+ located within the gate oxide, mobilized by temperature impact and bias application (V_{GS}), and transported towards the gate oxide / Si interface. The effective influence on V_{th} is thus due to induced charges located in the vicinity of this interface (as marked by the dark red box in Fig. 2.2(c)). The magnitude of the effect is of course a function of Q_m (in this context $\equiv Q_{Na^+}$) and hence the Na^+ ion dose quantities ϕ_{Na^+} at the interface (As potentially given by $\rho(x)$). Already $\phi_{Na^+} = 1{\cdot}10^{10}$ cm^{-2},[1] i.e. the magnitude of 10 ppm per atom of a monolayer per cm^2, lead to a detectable shift of the threshold voltage ΔV_{th} [2]. For V_{GS} in actual use I_D would be increased, in particular for low V_{GS} values in the subthreshold region as observable by a gradual decreased sloping in Fig. 2.2(d). For practical purposes, the transistor turns on at a lower V_{GS}, which is an unacceptable malfunction. A device failure has thus occurred. Fig. 2.2(d) represents ΔV_{th} due to extreme stress conditions read at different times up to 20 h. As sufficient negative V_{GS} values would result in Na^+ transfer towards the adjacent metal / gate oxide interface, I_D drops instantaneously for these conditions. Due to this effect ΔV_{th} is manifested by the typical shoulder in the transfer characteristics. Na^+ reliability tests are commonly made on wafer scale containing a large number of devices. Hence, faulty devices and dies can be detected and mapped as illustrated in Fig. 2.4. Additionally, the height of the shoulder in Fig. 2.2(d) indicates the number of faulty devices on the wafer.

Additionally to V_{th} instabilities, effects as enhanced resonant tunneling through silicon dioxide ($\mathrm{SiO_2}$) [20] have been reported as a consequence of Na^+ contamination of gate oxides. However, for newer MOSFET technologies Na^+ may influence the device performance even in an enhancing manner as for instance increased electron mobility in the n-channel inversion layer for SiC substrates [21].

Considering the mentioned physical model for nMOS transistors, pMOS transistors commonly do not suffer from device degradation due to mobile ion contamination. This is obvious, since the negative V_{GS}, as applied in actual use, causes ion transport towards the metal / gate oxide interface. Thus the transfer characteristics are not affected by contaminants as Na^+. For such devices only interface traps and fixed charges in the vicinity of the gate oxide / Si interface harm the device by a V_{th} shift towards higher

---

[1] The unit [cm^{-3}] represents [at/cm^3] and [ions/cm^3]

[2] Experiment values of ϕ_{Na^+} were delivered from Infineon Technologies Austria AG.

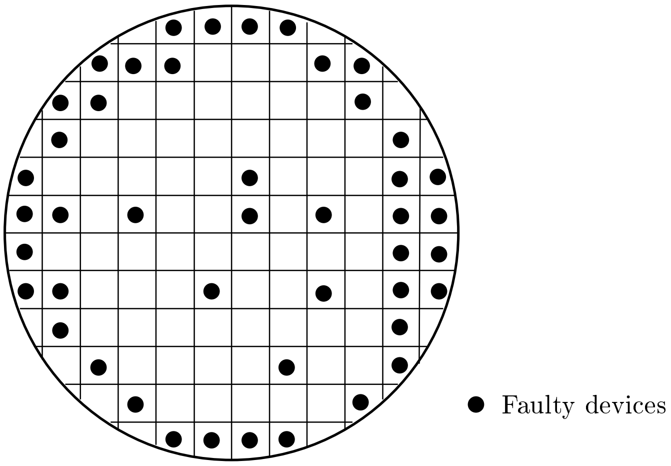

Figure 2.4.: Wafer map on the detection of faulty devices. The scheme has been adapted from [19]

values. However, under certain circumstances unwanted V_{th} instabilities have been reported even for Na^+ contaminations [22], due to immobilization at the gate oxide / Si interface.

Possibilities to introduce mobile ions during device fabrication are always present, even in clean rooms of highest classes [19], with front end of line process steps: The generation of the MOS structure particularly vulnerable with respect to intrinsic Na^+ contamination. Components of production facilities may contain considerable amounts of Na compounds in its gaseous form, due to its remarkable volatility at high temperature operation. Furthermore, Na from the environment should be taken into account as a possible source as well. Since in this context the volatility at low temperatures is negligible, gaseous airborne Na is only a minor contributor. However, Na compounds potentially are present in particle (aerosol) form emanating from humans for instance by breath or body fluids as well as from necessary disposables as gloves, masks or overalls [23]. In particular, NaCl is a commonly appearing candidate. All these facts account for the absolute necessity to exclude potential Na sources as well as to maintain all facilities as proposed by industrial standards (e.g. as defined by clean room norms ISO 14644-1 and ISO 14644-2). The trend of a steadily decreasing allowed Na contamination budget has nowadays reached the magnitude of $\phi_{Na^+} = 1 \cdot 10^9$ cm^{-2}. However, also back end of line processes themselves in front end fabrication may induce considerable amounts of Na compounds (e.g. by photoresists [24]), as does back end fabrication. Eventually, the actual use of the device has additionally to be taken into account, because potentially leading to extrinsic device failures. Therefore, measures for avoiding Na transport towards crucial device regions as the gate oxide of a MOS transistor have to be taken. Protection by the use of barrier and getter layers enables reliable operation of semiconductor devices during the warranted life time. Common materials in use for that purpose are e.g. silicon nitride (Si_3N_4) [25, 26] or boron-phosphosilica glass (BPSG) [27].

2.3. Approaches to detect mobile ions in MOS transistors

The common approaches for mobile ion detection and quantification in the gate oxide of MOS transistors and the investigation of the corresponding mechanism rely basically on electrical measurements. Properties of the MOS structure are utilized for assessing e.g. the quality of the gate oxide in terms of stability of the transfer characteristics. Commonly, electrical measurements are carried out as analysis approach for changes derived from the MOS structure by physical, chemical or electric phenomena as triggered by device stress tests. However, such approaches provides solely information on electrical states. Although various types of mobile ions may get separated by time resolved response signals, direct evidence on physical presence of certain ions and elements, respectively, cannot be given. Furthermore, their spatial distribution within a material layer is not accessible by electrical measurements.

Among various ways a device can be investigated under extreme stress conditions bias-temperature (B-T) stress has to be mentioned explicitly on this point. It combines the application of a significant V_{GS} in combination with elevated device temperatures. Mobile ions react on B-T stress by transport processes and, as discussed in the previous section, alter the transfer characteristics of MOS transistors. In this context, measuring the transfer characteristics after different times of B-T stress (Fig. 2.2(a)) application exhibits a popular possibility to assess the quantity of mobile ion contamination due to ΔV_{th}. However, there are much more approaches available for analyzing effects due to device stress by bias and/or temperature with the most prominent ones briefly discussed in this section:

Capacitance - voltage plots

The use of capacitance - voltage (C-V) plots in combination with B-T stress have been of utmost significance in the development of modern semiconductor devices. The work of Grove, Deal, Snow and co-workers (e.g. [16, 28, 29]) in the mid 60's is a main contribution for MOS transistor mass productions as known nowadays. In this time period nMOS transistors reacted very unstable on positive gate stress concerning influences identified as Na^+ contaminations in the gate oxide. Based on these investigations, awareness for the resulting harmful effects of mobile ions and the necessity for keeping the gate oxide free of them arose. In general, C-V plots base on eq. (2.3). Here, the term of interest does not correspond to V_{GS}, but to the MOS capacitance while biasing the device with V_{GS}. The capacitance C of a MOS structure in C-V plots is screened by a DC ramp, superimposed by an AC signal of defined frequency, from a start value for V_{GS} towards an end value of opposite polarity. Fig. 2.5 shows typical results (the figure is out of Ref. [30]). Assuming no interface traps or fixed charges at the gate oxide / Si interface and no contamination of the gate oxide with mobile ions, the theoretical characteristic of $C(V_{GS})$ by varying V_{GS} in a C-V plot obeys [28]

$$C(V_{GS}) = -\frac{\mathrm{d}Q_s}{\mathrm{d}V_{GS}} = C_{Ox}/(1+\frac{\epsilon_{r,ox}\cdot x_{DL}}{\epsilon_{r,DL}\cdot x_{Ox}}) \tag{2.4}$$

with Q_s being the total charge generated in the semiconductor and C_{Ox} the maximum capacity achievable as described by this equation[1]. $\epsilon_{r,ox}$ and $\epsilon_{r,DL}$ are dielectric constants of the gate oxide and the depletion region of the MOS structure, respectively (For details on MOS device physics see [15]). In C-V plots the detected $C(V_{GS})$ equals C_{Ox} if $x_{DL} = 0$, i.e. when the MOS structure is in accumulation ($V_{GS} < V_{FB}$), thus the gate oxide with thickness x_{Ox} determines the measured capacitance $C(V_{GS})$. However, if a depletion layer is generated at $V_{GS} > V_{FB}$, C decreases gradually until the maximum width of the depletion layer x_{DL} is reached (deep depletion), where the ratio $C(V_{GS})/C_{Ox}$ reaches its minimum. Fig. 2.5 shows typical results on C-V plots of nMOS transistors. For pMOS transistors the theoretical curve exhibit vertically mirrored characteristics. C-V plots may distinguish from the theoretical behavior, enabling the detection of interface traps, fixed charges or mobile ions. In the previous section the shift in V_{FB} has been mentioned. With respect to the theoretical C-V plot, initial measurements, i.e. prior to any stress tests, are able to quantify Q_{SS}. B-T stress triggers mobile ion transport. Thus, subsequent C-V plots indicate the quantity of mobile ions by a horizontal displacement as given in Fig. 2.5 (Here Q_{Na^+} quantifies Na^+ present in the SiO_2 gate oxide). In general, these shifts are reversible by switching between a positive and negative V_{GS}. In measurements, C-V plots often exhibit a different characteristic than shown here, since e.g. the mobile distribution could be spatially inhomogeneous throughout the gate oxide [30]. Despite the great relevance in terms of MOS technology, the C-V method has some disadvantages: The detectable shifts in V_{FB} can be too small for thin gate oxides (< 100 nm), which can be correlated to a possibly insufficient detection limit ($1\cdot 10^{10}$ cm^{-2}) [31]. Additionally, it is not possible to clearly distinguish between different types of mobile ions.

Triangular voltage sweep

Triangular voltage sweep (TVS) overcome some of the limitations of the C-V method [31]. This technique records the displacement current $I(V_{GS})$ flowing through the gate oxide as a ohmic response on V_{GS} [32] during a a constant DC ramp. Kept on a constant temperature typically above 250 - 300 °C [31, 33],

---

[1] Note that eq. (2.4) is only valid for high frequency capacitance analysis. With these conditions minority carrier transport cannot follow the signal variation. Thus inversion of the MOS structure cannot be reached and Q_s, the total charge induced in the semiconductor due to application of V_{GS}, is governed by the width of the depletion region x_{DL} (see [28]).

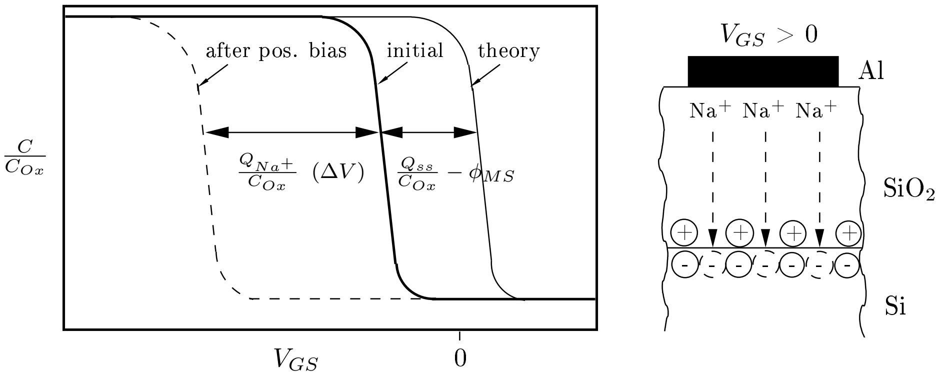

Figure 2.5.: C-V plots of a nMOS structure using high frequency analysis at a temperature of 300 °C. The horizontal displacements between the theoretical curve and the curve initially recorded enables quantification of interface traps and fixed charges in the near interface region. The dashed curve illustrates the displacement due to influences of mobile ions (Na^+). As given by the value for ΔV, representing the V_{FB} shift, the quantity of Na^+ can be calculated.

the MOS structure gets stressed by V_{GS} for a short period of time. By a constant rate α the V_{GS} is subsequently swept towards 0 and further to the previous V_{GS} value, however of opposite polarity. Thus, $I(V_{GS})$ is given by

$$I(V_{GS}) = \alpha \cdot C_{V_{GS}} \tag{2.5}$$

At room temperature and without any mobile ions in the gate oxide, $I(V_{GS})$ characteristics under quasi-static conditions resemble those obtained from low frequency C-V analysis [28]. Due to the rapid increase of intrinsic charge carriers in a semiconductor material at elevated temperatures (typically $> 300\,°C$) one can approximate for the whole voltage sweep with a constant $I(V_{GS})$ by

$$C(V_{GS}) \cong C_{Ox} \tag{2.6}$$

If the gate oxide contains mobile charge carriers, though, the displacement current varies consequently. Emphasized by means of elevated temperatures, mobile ions, transported to the respective interface during the initial bias stress, may redistribute by the oppositely signed bias [32]. Such processes commonly appear near $V_{GS} = 0$ and result in an increased displacement current which superimposes with the above mentioned low frequency C-V characteristics (which acts as a base line). Adapted from [32], Fig. 2.6 shows typical TVS displacement current characteristics. Note that the ordinate could be assigned to a capacitance scale as well (e.g. [33]). The area of the TVS peak with respect to the base line determines the quantity of mobile ions (here Na^+) in the gate oxide by [32, 31]

$$Q_{Na^+} = \frac{1}{\alpha} \int_{-V_{GS}}^{+V_{GS}} [I(V_{GS}) - \alpha \cdot C_{Ox}] \mathrm{d}V \tag{2.7}$$

From this equation the advantage of TVS is obvious: By the superimposition of two components, the result is unaffected by influences as interface traps or fixed charge. Their quantity Q_{ss} is included in the base line characteristics and the peaks appearing during TVS can be assigned solely to mobile ions. Hence the detection limit decreases in contrast to the B-T stress C-V method down to $1{\cdot}10^9$ cm^{-2}, and there is the possibility to separate between different types of mobile ions, since appearing at different values for V_{GS} during sweeping [34]. In principle, TVS can be applied not only to MOS structures but to all dielectrics, sandwiched between two conductive layers [35]. High accuracy can be obtained when a measurement setup is used, that simultaneously acquires the quasi-static and low frequency C-V data [36].[1]

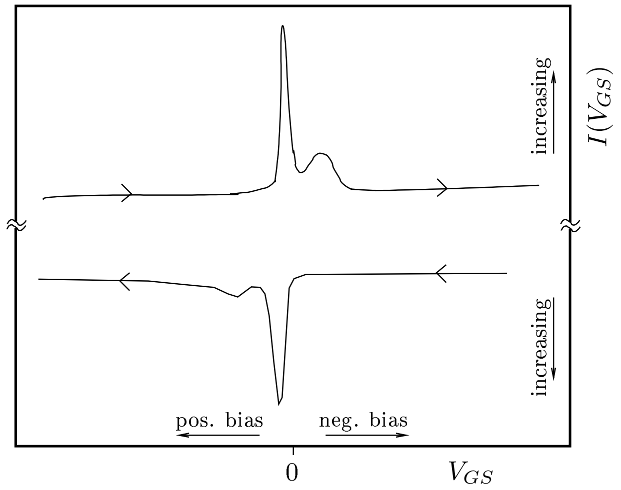

Figure 2.6.: TVS scheme for quantification of Na$^+$ at a sample temperature of 350 °C. The upper curve displays TVS measurements on an nMOS structure with V_{GS} sweeping from positive to negative values. Thus Na$^+$ transport from silicon towards gate metal is recorded. The lower curve displays the contrary sweep conditions with Na$^+$ transport from gate metal towards silicon. The detected $I(V_{GS})$ is typically in the magnitude of 10^9 A. Differences in the peak areas indicate different Na$^+$ release condition from the respective interface. Variation of the temperature may change the peak area and thus clarify such questions.

Thermally stimulated ionic current

A further method for the detection of mobile ions in MOS transistors is the thermally stimulated ionic current (TSIC) method, which measures the transit time of mobile ions through an insulating film as the gate oxide upon temperature sweep while keeping the sample at a constant V_{GS} [37]. This technique allows

---

[1] Attention: In literature, the chosen frequency is often assigned to the high frequency region

the investigation of kinetic properties as the mobility of mobile ions [38, 39, 40]. In the TSIC method the displacement current $I(T)$ is plotted as a function of gradual temperature increase at constant V_{GS} as illustrated in Fig. 2.7 (Adapted from [37]). Typical temperatures range from 0 °C up to 500 °C. Based on these analysis several features concerning mobile ions are accessible. The quantity of mobile ions can be calculated by integration of the occurring TSIC peak, assignable to a certain mobile ion species. Additionally, the peak position reveals information on the activation energy E_a for mobile ion transport. Assuming that all mobile ions are initially located on an interface of gate oxide with an adjacent layer of the MOS structure, the measured current can be assigned, for a certain temperature, to a mobile ion current $I(T)$ described by [37]

$$I(T) = -q \cdot \frac{\mathrm{d}n_t}{\mathrm{d}t} = n_t \cdot q \cdot s \cdot \exp(-\frac{E}{k_B \cdot T}) \tag{2.8}$$

From another point of view, $I(T)$ correlates to the time dependent decrease of n_t, the number of mobile ions still present on the interface at time t. q is the mobile ion charge (commonly just single charged ions are involved, thus $q = e$), k_B denotes Boltzmann's constant and s a preexponential factor representing the frequency of mobile ions attempting to leave the interface trap [38]. Eq. (2.8) is valid only for detrapping controlled transport through the gate oxide, i.e. when the mobile ion release from an interface (either to the metal or the semiconductor) is the rate determining step. In literature, a continuous distribution of detrapping energies from the interface has been proposed [38]. If on the other hand the bulk transport through the gate oxide governs the transfer rate, other models have to be applied [37]. Similar to TVS, TSIC can potentially be applied to all insulating materials sandwiched between two conductive layers as well. Different mobile ion species can be separated since they result in distinguishable peaks during the measurement. The peaks in Fig. 2.7 can be assigned to different types of mobile ions, but also to different transport or detrapping mechanism.

2.4. Transport processes for mobile ions

Harmful effects of mobile ions on the stability of crucial device parameters and thus on reliability issues are inherently connected with transport processes of mobile ions in materials, used for fabrication of MOS transistors. In general, these phenomena are manifested in a flux governed by a generalized driving force X and can be written by means of a linear flux-force relationship [41]

$$J = \beta \cdot X \tag{2.9}$$

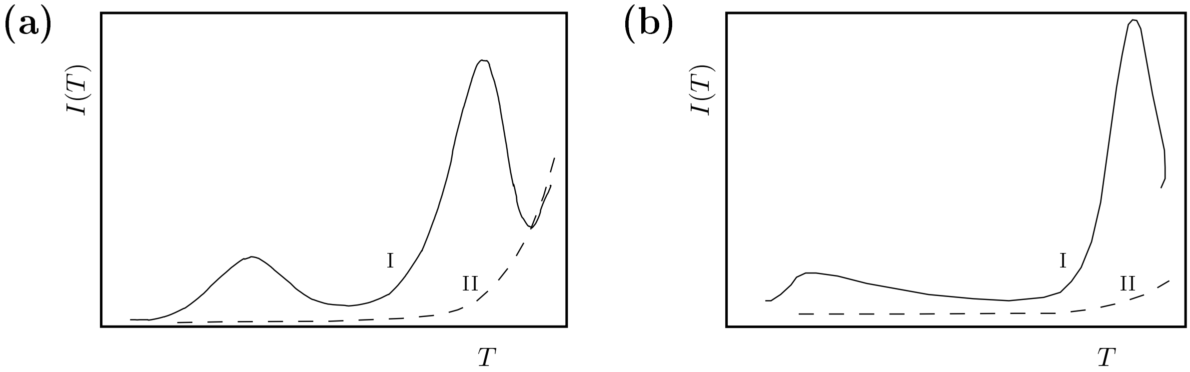

Figure 2.7.: Scheme of TSIC measurements with mobile ions initially located on the metal / gate oxide interface. (a) TSIC during positive V_{GS} bias showing mobile ion release from the metal / gate oxide interface and transport towards the gate oxide / Si interface. (b) TSIC during subsequent negative sample biasing. The curved marked with I are assigned to $I(T)$ caused by mobile ions. II denotes TSIC due to electric background (leakage) current.

with β as a constant of proportionality. Particle transport in any media occurs because of a spatial gradient, which is the derivative of involved driving force with respect to its spatial distribution. Typical quantities for driving forces are differences in concentration or electric potential, both of them potentially causing mobile ion transport. The term "transport processes" includes therefore diffusion processes and drift processes. A brief description of these processes is given with the restriction to one dimensional systems with $J = J_x$:

Thermal diffusion

Diffusion in solid materials are the content of numerous sources in literature (e.g. [42, 43, 44]). For semiconductor devices diffusion has crucial importance with respect to doping processes for the generation of e.g. conductive regions or n-p junctions [19]. Prominent doping techniques are thermal in-diffusion of an externally supplied dopant source and ion implantation. However, diffusion is also an important aspect for the unwanted transport of impurities and contaminations within materials used for device fabrication[1]. Nowadays knowledge on diffusion, a fundamental physico-chemical phenomenon, enables the prediction and simulation of particle transport of any aggregate state by the knowledge from certain boundary conditions. Basically, diffusion is a kinetic process: Thermal motion of particles, which get spatially transported within a system in a random manner. Differences in the chemical potential μ and respective occurring gradients in the system act hereby as the driving force pushing the system towards thermodynamic equilibrium ($\nabla\mu = 0$). The concentration dependence[2] is expressed by [45]

---

[1] Compare to section 5.2.3.

[2] For higher concentrations c must be replaced by the activity a. For impurities this is not necessary.

$$\mu = \mu_0 + k_B \cdot T \cdot \ln c \tag{2.10}$$

$$\nabla\mu \propto \nabla c \tag{2.11}$$

with μ_0 as the chemical potential at standard conditions. In the case of complete ionization of e.g. alkali metals, c can be replaced by the charge carrier density n for diffusion of charged particles as e.g. mobile ions. Possible mechanism to be considered are basically interstitial and vacancy type diffusion. An inhomogeneous distribution of the impurity concentration within a solid material has the ambition to achieve equilibrium conditions by means of homogenization [42]. This is driven by ∇c, the driving force for particle transport, resulting in a particle flux as given by Fick's first law of diffusion:

$$J = -D \cdot \nabla c = -D \cdot (\frac{\partial c}{\partial x}) \tag{2.12}$$

In the case of complete homogenization $\nabla c = 0$, and no particle flux is possible. Further factors are correlation (memory) effects evolving from particle transport in a non-random fashion. This is due to interactions between e.g. tracer atoms and vacancies in the lattice [44].

The relation to eq. (2.9) gets immediately obvious with the concentration gradient as the driving force of particle flux and D, the diffusion coefficient or diffusivity, as a constant of proportionality containing kinetic aspects. Note that eq. (2.12) may describe various types of thermal diffusion processes, the diffusivity potentially having different phenomenological meanings[1]: (i) Tracer diffusion describes either self-diffusion of labeled matrix constituents within the matrix itself or the diffusion of impurities in the matrix. Tracer diffusion may be governed by correlation effects evolving from particle transport in a non-random fashion [44]. By correlation factors f, the random diffusivity D can be compared to a correlated diffusion mechanism as described by means of the tracer diffusivity D^*

$$f = \frac{D^*}{D} \tag{2.13}$$

For interstitial type diffusion, as considered for mobile ions, f is considered to equal unity (and $D \equiv D^*$), i.e. no memory effect due to interactions with neighboring sites is taken into account. However, correlation effects may occur when charged particles are present in high concentrations (thus $f < 1$). (ii) If there is the situation of a binary diffusion couple, e.g. two metals in direct contact, interdiffusion occurs. Kinetically this is described by the chemical diffusion coefficient $\widetilde{D}$ [44]. Using thermodynamic approaches, it is possible to convert $\widetilde{D}$ into D (and thus D^*) [46].

Considering mass continuity

---

[1] A more detailed discussion on this topic can be found in the reference cited in this section.

$$-\frac{\partial J}{\partial x} = \frac{\partial c}{\partial t} \tag{2.14}$$

and substitution of eq. (2.11) Fick's second law of diffusion, is obtained [42], which describings by a second order differential equation how thermal diffusion changes the concentration gradient with time:

$$\frac{\partial^2 c}{\partial x^2} = \frac{1}{D} \cdot \frac{\partial c}{\partial t} \tag{2.15}$$

Dependent on given boundary conditions, numerous solutions for eq. (2.15) are available (analytically and numerically) [43]. In case of diffusion of a finite source deposited with concentration c_0 onto an isotropic medium (i.e. at position $x = 0$) and spreading into one half-space, as for instance representing thermal in-diffusion of contamination located on the surface of a material layer, a comparably simple solution of Fick's second law of diffusion can be obtained [44]:

$$c(x,t) = \frac{M}{\sqrt{\pi \cdot D \cdot t}} \cdot \exp(-\frac{x^2}{4 \cdot D \cdot t}) \tag{2.16}$$

M is therein the number of diffusion particles (thus the dose) per unit area[1]. This solution enables the illustration of the concentration profile in x direction within a system (in this context a solid material) the as a function of diffusion time. For the case of an one dimensional solution, the term $2 \cdot \sqrt{D \cdot t}$ yields the diffusion length, indicating how far the diffusing species propagated into the target material in a defined time. Graphical examples for this will be given in section 5.2.3. The crucial parameter for thermal diffusion is the diffusion coefficient D, which quantitatively describes the diffusivity of particles as e.g. impurities in the target material. In solid materials the temperature dependence of D can be expressed by an exponential relation [47]:

$$D = D_0 \cdot \exp(\frac{-E_a}{k_B \cdot T}) \tag{2.17}$$

with k_B denoting Boltzmann's constant and E_a representing the required activation energy for a transition of a particle from one lattice site to another. D_0 is a frequency factor and gives the hypothetical diffusivity at infinite high temperature. The higher the temperature the faster a diffusion process. Tab. 2.2 lists an overview for values of D_0 and E_a of different mobile ions in Si [48] (Calculation via *ab initio* molecular dynamics).

---

[1] The notation of eq. (2.16) is according to the given literature reference. In this thesis the dose of transported species is commonly notated by the symbol ϕ (Not to be confused with the electric potential).

Table 2.2.: Parameter for diffusion of mobile ions in Si at different temperatures. For reasons of estimation, the respective value for D at the given temperature was included. The diffusion length was calculated when keeping the substrate at this temperature for t = 1h.

Mobile ion	T [K]	D_0 [cm^2/s]	E_a [eV]	D [cm^2/s]	$2 \cdot \sqrt{D \cdot t}$ [μm]
Li^+	1000	$3.72 \cdot 10^{-3}$	0.58	$4.46 \cdot 10^{-6}$	5198.42
Na^+	500	$2.08 \cdot 10^{-3}$	0.95	$5.52 \cdot 10^{-13}$	43.68
	1000	$1.92 \cdot 10^{-3}$	0.95	$3.13 \cdot 10^{-8}$	719.31
	1500	$1.79 \cdot 10^{-3}$	0.95	$1.15 \cdot 10^{-6}$	2440.13
K^+	1000	$0.59 \cdot 10^{-3}$	0.89	$1.93 \cdot 10^{-8}$	503.65

Drift and field-assisted diffusion

For insulating materials thermal diffusion potentially can be replaced or accompanied by drift phenomena. This is true when a e.g. a bias voltage is applied on the insulator and thus an electric filed is acting on charged particles [44]. For semiconductor devices this scenario is encountered frequently as for instance in the gate oxide of a MOS transistor during operation. Different to pure thermal diffusion in eq. (2.9), the driving force here is additionally governed by the electric field [41]. From a thermodynamic point of view the electrochemical potential $\widetilde{\mu}$ is responsible for particle transport

$$\widetilde{\mu} = \mu + z \cdot e \cdot \phi \tag{2.18}$$

with z being the charge number of the particle and e the elemental charge. Assuming large bias voltages applied at thin insulating films (resulting in electric fields E of the magnitude 10^5-10^6 MV/cm), the electric potential difference $\nabla\phi$ can be treated as the dominating contribution to the driving force. The bias voltage thus governs the particle flux (by means of E):

$$\nabla\widetilde{\mu} = z \cdot e \cdot \nabla\phi \tag{2.19}$$

Considering eq. (2.19) in eq. (2.9) and σ as the mobile ion conductivity in an insulator, one obtains the electric current density j out of the particle flux J by

$$\sigma = z^2 \cdot e^2 \cdot \beta \tag{2.20}$$

$$j = z \cdot e \cdot J = \sigma \cdot \nabla\phi \tag{2.21}$$

$$I = \frac{V}{R} \tag{2.22}$$

which is known as of Ohm's law [41] and can also be written in the more familiar version in eq. (2.22) with I being the electric current and R the resistivity of the thin insulating layer. Again the relation to eq. (2.9) becomes immediately obvious. Since drift dominated the particle transport, the flux of mobile ions can be treated as Ohmic conduction. However, mobile ion drift in an insulator with an initial homogeneous mobile ion distribution ($\nabla c = 0$) would induce a redistribution by ion movement as given by $\nabla \widetilde{\mu}$. It is thus obvious that drift and diffusion are coupled phenomena, simultaneously causing mobile ion transport towards the electrochemical equilibrium, when e.g. both phenomena cancel out each other. Considering this condition, its obvious to equate the particle flux of eq. (2.12) with those of eq. (2.21) leading to

$$D_\alpha = \frac{k_B \cdot T \cdot \sigma}{c \cdot z^2 \cdot e^2} \tag{2.23}$$

which is the Nernst - Einstein equation, that relates the field-assisted diffusion coefficient of a mobile ion (representing an interstitial) with its conductivity in a solid. In eq. (2.23) σ describes a directed charge carrier transport potentially including different types of species, dependent on the present mechanism (e.g. interstitial type, vacancy type). Basically, D_α barely changes the quantity of σ into a diffusion coefficient and cannot directly be equated with D in eq. (2.12) (thus nor with D^*). Correlation of thermal diffusivity with field-assisted diffusivity can be done by Haven ratios [44, 49, 50] or, if possible, more simply again by respective correlation factors f_α [42]. Tab. 2.3 shows examples for D of Na^+ in soda lime glass by conductivity measurements:

Table 2.3.: Na^+ diffusivity in soda lime glass for various temperatures out of Ref. [42], obtained by conductivity measurements. The Na^+ content in the insulating matrix material in this example was > 10 at%, thus a correlation effect was taken into account. For more dilute contents interstitial diffsion would be expected in a random manner with f_{exp} approaching unity.

T [°C]	D [cm^2/s]	σ [$\Omega\cdot$ cm]$^{-1}$	f_{exp}
200	$4.2\cdot10^{-13}$	$5.05\cdot10^{-8}$	0.23
250	$4.0\cdot10^{-12}$	$3.25\cdot10^{-7}$	0.29
300	$2.6\cdot10^{-11}$	$1.51\cdot10^{-6}$	0.38

Chapter 3

Methodology and analytical approach

An approach has been developed in order to investigate thin layers of materials, frequently applied for semiconductor device fabrication. In contrast to electrical measurements, as discussed in section 2.3, the methodology is based on bias-temperature (B-T) stress in combination with physical analysis. The idea was to provide an unambiguous detection of mobile ions subsequent to B-T stress in terms of their lateral and depth distribution in a thin material layer. Information should be gained on the reaction of a material of interest to certain stress conditions. One issue of special interest in this context concerned mobile ion incorporation into various materials under these conditions. The term "incorporation" refers to the transition of mobile ions from an external source into the material of investigation, simulating situations as for instance contaminations on a material surface. Transport processes of mobile ions within the investigated material, as discussed in section 2.4, followed the incorporation. The focus of research laid on the element sodium (Na) and its ionic form Na^+. A comparison to other mobile ions will be given in the according sections. In the following, each single step of the methodology will be discussed in detail. Fig. 3.1 gives a general survey on the sample process flow from sample preparation to the B-T stress procedure and finally to physical analysis by time of flight secondary ion mass spectrometry (ToF-SIMS).

Before presenting each process step, some basic facts in terms of sample production have to be mentioned:

- All samples and the deposited material layers, which have been investigated were produced using industrial facilities at Infineon Technologies Austria AG in Villach at wafer scale. Due to the contaminant free conditions in the respective class I clean rooms, an intrinsic Na^+ concentration, below the ToF-SIMS detection limit was assured (Due to their lower abundance in comparison to Na^+, further mobile ion cannot be detected either).

- As a substrate for the deposition of insulating and conductive layers (up to 1 μm thickness) a highly n-doped silicon (Si) substrate was used (dopant: antimony (Sb)). A backside metalization ensured the possibility of a proper electric contact. The Si wafer thickness was 380 μm.
- All wafers were cut into 1 × 1 cm^2 samples again using facilities at Infineon Technologies Austria AG in Villach.
- The wafers were carefully stored, in order to avoid subsequent contact to any contamination source. No wafer cleaning procedure was carried out prior to deposition of the host matrix.

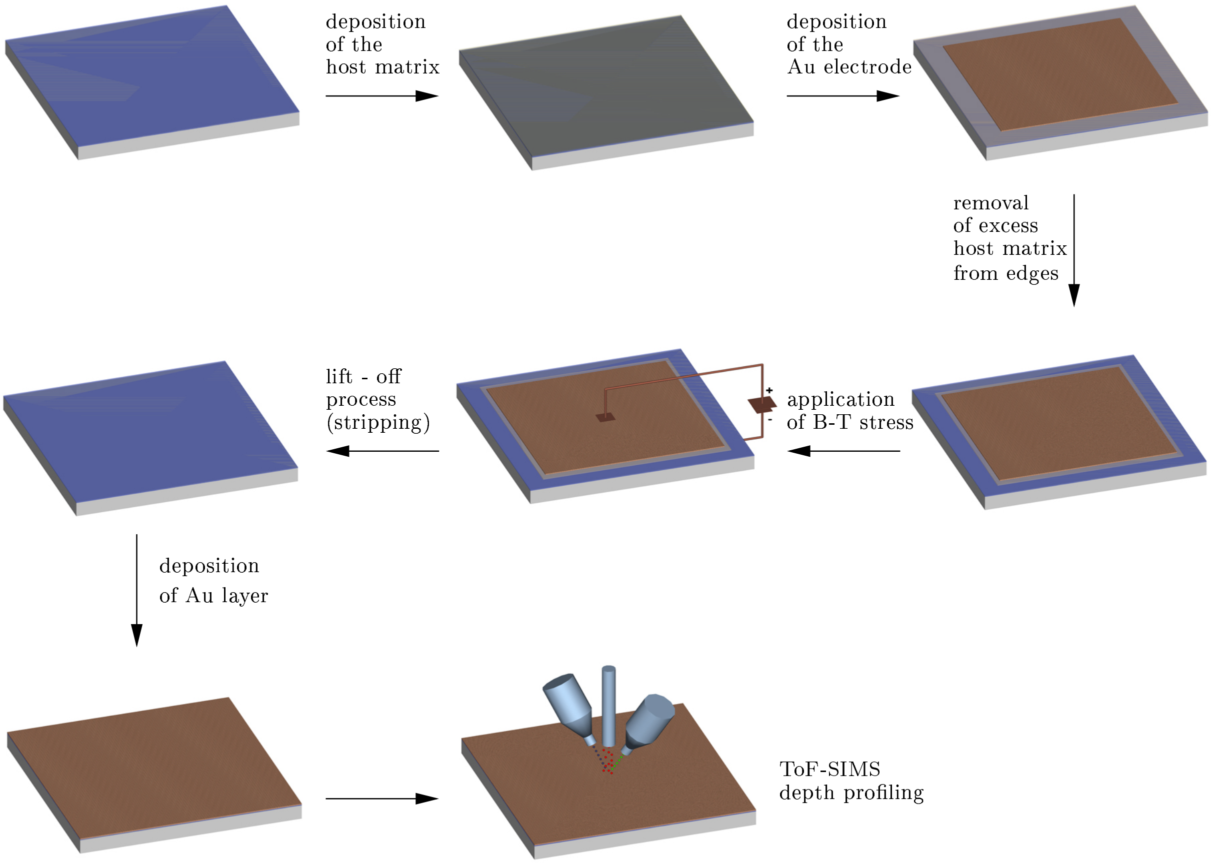

Figure 3.1.: Sample process flow for studying mobile ion incorporation and transport in various materials. The steps "removal of excess host matrix from edges" and "deposition of Au layer" were abandoned when the investigated layer had conductive character. Details on electrode contacting for B-T stress in terms of insulating and conductive layers are given in section 3.2.

The investigated materials were selected according to their relevance for application in semiconductor devices: Gate oxide, barrier layer, metalization. Tab. 3.1 gives a survey of the relevant parameters for each material used for investigations. Due to industrial constrains specifications on stoichiometry and density of silicon oxynitride (SiO_xN_y) and Boron-phoshosilicate glass (BPSG) cannot be given. The exact amounts of Si and Cu in the Aluminum-silicon-copper alloy (AlSiCu) are not given either (the stoichiometric fraction is in the low one-digit % region, though, and thus negligible).

Table 3.1.: Investigated materials and relevant parameters thereof.

Material	Layer thickness d [nm]	Deposition process	Density $\rho(M)$ [g/cm^3]	Comment
SiO_2	100, 200	thermal	2.27	dry oxide
	400	thermal	2.18	wet oxide
Si_3N_4	400	CVD	3.44	
SiO_xN_y	400	CVD	N/A	
BPSG	910	CVD	N/A	
AlSiCu	1000	PVD	N/A	

3.1. Host matrix for mobile ions

3.1.1. Polymer materials and mobile ion agent

Polymers were considered to be a suitable solution for application as host matrix, due to their wide variety of available categories and being a routine substance group in semiconductor device manufacturing processes (lithography). Chemical and physical properties of the host matrix had to fulfill several restrictions: The choice of the solvent had crucial importance for sample processing. Both the host matrix material and the hosted mobile ion agent had to be sufficiently soluble for the planned investigations. Additionally, melting and boiling point were important parameters, in order to define the temperature range of the experiments. Basically, two substance categories were chosen for experiments containing samples with insulating and conductive top layers, respectively: PMMA and positive photoresist. The properties of these substances will be discussed in the following:

Poly(methyl methacrylate) (PMMA)

Generally synthesized by radical polymerization of methyl methacrylate, PMMA (Fig. 3.2) is a rigid, colorless, and thus transparent polymer with a broad field of applications (Glass substitute, medical technology, light technology, . . .). This makes PMMA one of the major polymers in terms of annually produced volume. A common field of application to be mentioned separately is semiconductor technology, where PMMA is used as a resist for structuring processes using electron beams. The properties of the chosen PMMA made it a candidate for the use as host matrix (Tab. 3.2. PMMA is soluble in common solvents, preferably of polar, aprotic character. According to literature [51], thermal degradation of PMMA begins at 160 °C. Up to 230 °C decomposition is caused by impurities, purified PMMA does not show this behavior. Finally , above 230 °C PMMA decomposes due to random scission. Thermal analysis (by means of STA[1]) of the used PMMA indicated glass transition at temperatures between 121.6 °C - 127.7 °C and an onset of thermal decomposition at 244 °C. The maximum temperature for applications was restricted accordingly.

For experimental application two solvents were considered: Acetonitrile and anisole. (i) For reasonable use at room temperature (RT), PMMA was dissolved in acetonitrile (Sigma-Aldrich, Chromasolv® for HPLC super gradient grade) to a concentration of 4% per weight (≡ wt%). At higher concentrations the viscosity of the solution increased drastically, prohibiting the application as a host matrix for practical reasons (see 3.1.2). In general, 2 wt% PMMA in acetonitrile was used as the standard solution for experiments. (ii) for solutions with a higher PMMA content than 4 wt%, anisole (Sigma-Aldrich, ReagentPlus® 99%) was used as solvent.

Table 3.2.: Physical and chemical properties of atactic PMMA used in this work (purchased from Sigma-Aldrich). The data has been taken from Sigma-Aldrich's safety data sheet of product no. 182265 and from [52]

Molecular mass	average ~996,000 g/mol
Density	1.2 g/cm^3
Glass transition temperature	105 °C
Flash point	> 250 °C
Ignition point	304 °C
Soluble in e.g.	acetone, ethyl acetate , anisole, chloro benzene, acetonitrile

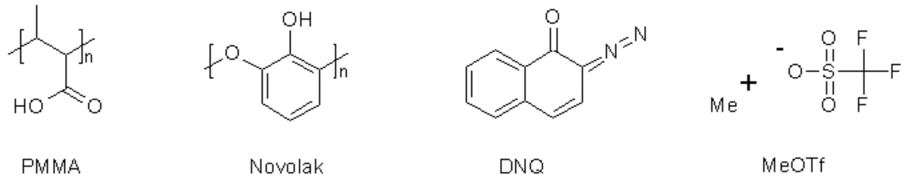

Figure 3.2.: Chemical structures of host matrix resins (PMMA, Novolak), the photoresist sensitizer (DQN) and the mobile ion agent (MeOTf).

---

[1] Simulataneous thermal analysis: Combined approach for acquiring data by thermogravimetric analysis (TGA) and differential scanning calorimetry (DSC); instrument: Netzsch STM 449 F1 Jupiter®

Novolak based, positive photoresist

Photoresists are a key substance class in semiconductor technology for lithography steps in the course of e.g. masking processes, material structuring and patterning [19]. In general, positive photoresists are provided with the resin (usually novolak based) in dissolved state, and get cured by a bake-out step causing vaporisation of the solvent. Sensitizer molecules, with diazo naphtaquinone (DNQ) derivates as a common compound class, inhibit the dissolution of the resin component in the solvent. However by exposure to light, commonly of ultraviolet wavelength, the sensitizer decomposes and the illuminated resin is rendered soluble. Thus a pattern can be generated in the positive photoresist by the UV light exposure, with the soluble resin subsequently washed out using a developer [53]. A final hard-bake process finalizes the deposition process of the positive photoresist.

Tab. 3.3 summarizes the important physical and chemical parameters of the positive photoresist (Fujifilm OIR 305-22) used as host matrix for experiments. The structures of novolak and DNQ are shown in Fig. 3.2. The temperature range of the resin for applications was lower than that of PMMA.

Table 3.3.: Physical and chemical properties of the positive photoresist used in this work. The data has been taken out from the safety data sheet of the product: Fujifilm OIR 305-22

Resin	novolak based
Sensitizer	DNQ derivate
Solvents	ethyl-3-ethoxy proprionate methyl-3-methoxy proprionate
Density	0.96 - 1.04 g/cm^3
Boiling point	$>$ 145 °C

Mobile ion agent

This component had to fulfill two crucial tasks: First, full solubility in the host matrix solution, i.e. the solvent had to be the same as for the polymer or it had to be completely miscible in the solvent of the polymer. Second, in dissolved state, the mobile ion agent should be fully dissociated, in order to quantitatively provide mobile ions. Alkali trifluoro methane sulfonate (Alkali triflate; MeOTf) was considered to be an appropriate candidate, due to its solubility in acetonitrile and the mesomerism of the triflate anion, which minimizes attracting effects with respect to the alkali cation. In Fig. 3.2 the chemical structure of MeOTf compounds is depicted and Tab. 3.4 lists the respective compounds used for experiments.

Table 3.4.: Alkali triflate compounds used as mobile ion agents including their respective molar masses M_{MeOTf}

Compound	Abbreviation	$M_{MeOTf}[g/mol]$	Supplier
lithium trifluoro methane sulfonate	LiOTf	156.01	Sigma-Aldrich
sodium trifluoro methane sulfonate	NaOTf	172.09	Sigma-Aldrich
potassium trifluoro methane sulfonate	KOTf	188.17	Sigma-Aldrich

Each of the MeOTf compounds was dissolved in acetonitrile in a concentration of $c_{MeOTf} = 1$ wt% for the use as stock solutions. Considering $n_{MeOTf} = n_{Me^+}$ for the amount of substance of an alkali ion with the charge number $z = 1$, one can calculate $c_{Me^+,stock}$, the concentration of alkali ions in the stock solution for a given c_{MeOTf} by

$$c_{Me^+,stock} = \frac{n_{Me^+}}{V_{solvent}} = \frac{c_{MeOTf} \cdot \rho_{solvent}}{M_{MeOTf} \cdot (100 - c_{MeOTf})} \tag{3.1}$$

with $V_{solvent}$ and $\rho_{solvent}$ as the volume and the density of the solvent. Note the difference between c_{MeOTf} and $c_{Me^+,stock}$ with respect to their units: While, for practical reasons, c_{MeOTf} is given in wt%, $c_{Me^+,stock}$ has the unit [mol/cm^3]. Considering x and y for c_{MeOTf} of the stock solution (1 wt%) and the host matrix solution (0 wt%), respectively, one could prepare a host matrix formulation spiked with c_{MeOTf} of z wt% using the calculatin according to Pearson's square:

$$\begin{tikzcd}
x \arrow[dr] & & z-y \\
& z \arrow[ur] \arrow[dr] & \\
y \arrow[ur] & & x-z
\end{tikzcd}$$

The necessary parts of stock solution and host matrix solution are given by $z - y$ and $x - z$, respectively. Referred to a total initial weight of the host matrix formulation of 3 g, this results in:

$$\begin{aligned}
m_{stock} &= \frac{3 \cdot (z - y)}{x - y} \\
m_{host} &= \frac{3 \cdot (x - z)}{x - y}
\end{aligned} \tag{3.2}$$

m_{stock} and m_{host} denote the necessary initial weights in [g] of stock solution and host matrix solution, respectively. m_{resin}, the amount of resin in m_{host} is thus given by the concentration of resin in the host matrix solution (e.g. 2 wt% PMMA). For the positive photoresist the exact novolak content was not available and thus m_{resin} could not be given. Assuming the solvents contain a negligible amount of alkali ions, it is obvious that after solvent vaporization solely PMMA and MeOTf remain as a solid. $c_{Me^+,calc}$

denotes the concentration of the respective alkali ion in the remaining PMMA when applied as a host matrix:

$$c_{Me^+,calc} = \frac{m_{stock} \cdot c_{Me^+,stock} \cdot \rho_{resin} \cdot N_A}{\rho_{solvent} \cdot m_{resin}} \tag{3.3}$$

Tab. 3.5 lists the formulations used for experiments. For NaOTf formulations, an intrinsic $c_{Na^+,calc}$[1] of $9.48 \cdot 10^{18}$ cm^{-3} is taken into account for PMMA[2].

Table 3.5.: Host matrix formulations. The initial weights are referred to 3 g total weight. The scale (Sanatorius analytical balance) had an accuracy of ± 0.0001 g. $c_{Me^+,calc}$ is given in [cm^{-3}]. c_{MeOTf} for the host matrix formulations is given in ppm per weight ($\equiv 10^{-4}$ wt%).

Host matrix solution	c_{MeOTf} [ppm]	m_{stock} [g]	m_{host} [g]	m_{resin} [g]	$c_{Me^+,calc}$ [cm^{-3}]
2 wt% PMMA in acetonitrile	300 ppm LiOTf	0.0910	2.9190	0.0601	$5.87 \cdot 10^{19}$
	300 ppm NaOTf	0.0946	2.9164	0.0601	$7.62 \cdot 10^{19}$
	600 ppm NaOTf	0.1825	2.8205	0.0601	$1.43 \cdot 10^{20}$
	900 ppm NaOTf	0.2736	2.7314	0.0601	$2.15 \cdot 10^{20}$
	300 ppm KOTf	0.0910	2.9090	0.0601	$7.62 \cdot 10^{19}$
9 wt% PMMA in anisole	900 ppm NaOTf	0.2730	2.7330	0.0601	$7.62 \cdot 10^{19}$
Positive photoresist	900 ppm NaOTf	0.2815	2.8460	N/A	N/A

3.1.2. Deposition of the host matrix

Prior to this process step, a thorough removal of possibly occurring dust particles or splinters from the Si wafer substrate on the specimen (1 × 1 cm^2) surface by means of purging with N_2 was necessary. Deposition of the host matrix was done in two different ways:

(i) Putting one drop of the host matrix formulation centrally onto the specimen. Applied formulation: 900 ppm NaOTf in 9 wt% PMMA / anisole. The sample was subsequently pre-baked for 3 min at 60 °C (in order to remove anisole), heated up to 190 °C within 1 min and subsequently kept at this temperature for a 30 min bake-out. In a final step, an 80 nm gold (Au) layer (0.3 × 0.3 mm) was deposited onto the host matrix (description see below). Due to the convex apearance of the resulting PMMA host matrix, a resonable determination of the host matrix thickness was not feasible.

(ii) Spin coating at room temperature for the fabrication of thin films of host matrix on the specimen surface. Applied for all 2 wt% PMMA / acetonitrile formulations according to Tab. 3.4 and for the

---

[1] The unit [cm^{-3}] represents [at/cm^3] and [ions/cm^3], respectively.

[2] The quantity of 30 ppm per weight Na^+ has been measured in 2 wt% PMMA in acetonitrile by means of flame atom absorption spectroscopy (F-AAS). A confirmation of this is given in section 5.1.3.

positive photoresist. In the following the important settings and aspects of the spin coating process are described.

60 μl of the host matrix formulations as given in Tab. 3.4 were spin coated onto the specimen, assigned to investigations. The settings and post-treatments for the respective host matrix formulations were

- 2 wt% PMMA in acetonitrile formulations:
  Ramp: 5 s to 3000 rpm; dwell: 28 sec
- Positive photoresist:
  Ramp: 5 s to 600 rpm; dwell: 18 sec ⇒ Ramp: 5 s to 900 rpm; dwell: 5 sec ⇒ pre-bake: 60 °C, 3 min ⇒ bake-out 100 °C, 30 min

The amount of PMMA in acetonitrile of course governed the layer thickness, due to increasing viscosity of the host matrix solution with increasing PMMA content. Fig. 3.3 shows this dependency as measured by means of ellipsometry[1]. Higher PMMA contents than 4 wt% were not applicable by spin coating at RT. For the positive photoresist, a layer thickness of ∼10 μm was estimated by shifting the focal plane during light microscopy (Olympus BX 60 using an objective with 100x magnification).

Subsequent to spin coating, a 40 nm Au layer (0.8×0.8 cm^2) was deposited onto the sample in a centered fashion, using a sputter mask. This was done by means of Ar induced plasma deposition using a BAL-TEC MED 020 system. The settings were: sputter current 60 mA, sputter time 64 s (For the 80 nm Au layer the sputter time was increased to 128 s).

As a final preparation step before application of B-T stress, excess host matrix material was removed from the vicinity of the specimen edges. The purpose was to avoid conducting paths and thus leakage currents between the deposited Au electrode and the n-doped Si substrate during B-T stress. For 2 wt% PMMA in acetonitrile formulations the 1 mm strip between Au electrode and specimen edge was cleaned via acetone treatment. For samples with positive photoresist as the host matrix, thin adhesive strips (0.5 μm width) were attached on two opposed specimen edges prior to spin coating (Note that the adhesive strip had to be stable up to 100 °C). Subsequently, the strip was removed providing access to the specimen surface as necessary for conductive surfaces (see section 3.2).

3.2. Bias-temperature stress

The application of a DC bias voltage V_{bias} at a constant temperature (bias-temperature (B-T) stress) was the basic approach to transfer mobile ions from the host matrix to the underlying material layer, i.e.

---

[1] Instrument: Plasmos SD 2300

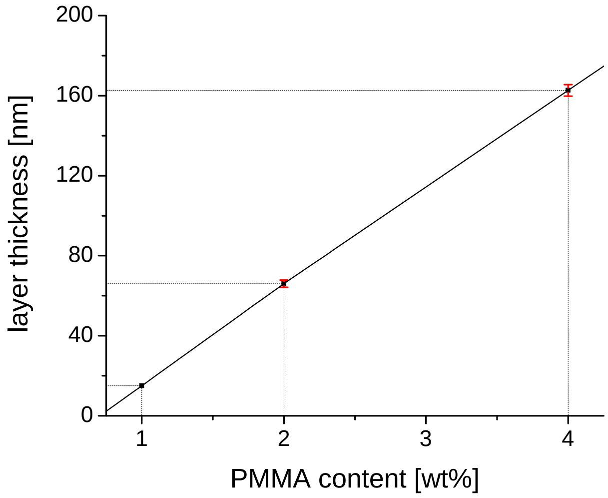

Figure 3.3.: Dependency of the spin coated host layer thickness on the PMMA content of the host matrix solution. The data are average values of 4 - 5 ellipsometry measurements. Deviations from these data are commented in the respective sections.

the mobile ion incorporation step. In the following the B-T stress approach will be described for Na^+ incorporation:

The sample was placed in a thermo-chuck (Eurotherm 3200) enabling temperature control via a power supply unit (Voltcraft® DPS-4005 PFC) combined with a thermocouple integrated in the thermo-chuck. Since the thermo-chuck was aligned for the use in a temperature range $>$ 400 °C, the temperature on the supply unit display had to be corrected for temperatures $\leq$ 200°C. This was done by placing a thermocouple directly onto the sample surface. In general 30 ± 5 °C were subtracted from the given temperature on the display, in order to receive the actual surface temperature on the sample. Application of a bias voltage was feasible using a source meter unit (SMU; Keithley 2611A) for the simultaneous DC application and current measurement. The sample was connected to the SMU via tungsten (W) electrode needles (bent, in order to reduce the pressure on the deposited Au layer) attached on micro-manipulators (manufacturer: Karl Süss, Germany). Dependent on the character of the sample top layer (insulating or conductive), contacting was carried out as shown in Fig. 3.4, in order to achieve a plate capacitor-like sample setup.

- Insulating top layer:

  The sample was placed onto a thin copper (Cu) disk (∅ 1.5 mm) in a centered fashion, with a direct electric contact between Cu and Si backside metalization. One electrode could thus be attached onto the Cu disk, just next to the specimen. The second electrode was attached to the Au layer. This configuration enabled the generation of an internal electric field acting in the host matrix and the insulating top layer. Thus, the voltage dissipated within these two layers. Due to the highly n-doped character of the Si substrate, its resistivity was taken as negligible.

- Conductive top layer

  One electrode was attached to the bare surface of the sample. The second electrode was again attached to the Au layer. Thus the V_{bias} dissipated within the host matrix, and an electric field was generated therein.

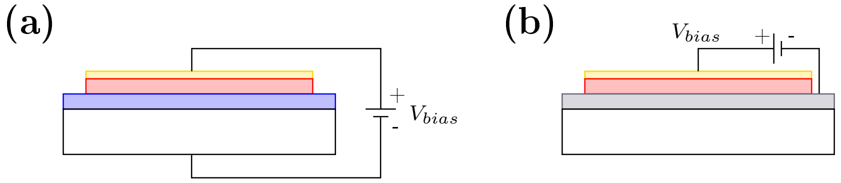

Figure 3.4.: (a) Setup for B-T stress on samples with an insulating top layer (respresented by the blue rectangle). (b) Setup for B-T stress on samples with a conductive top layer (represented by the gray rectangle). The host matrix and the Au electrode are marked by a red and golden rectangle, respectively.

B-T stress was controlled via Java Lab Software, version 0.991, DC Pot/Gal (©Uwe Traub, MPI Solid State Research, Stuttgart, Germany). A SMU background signal of 0.1 pA for the measurement setup was taken into account. Fig. 3.5 shows a typical current characteristic obtained by potentiostatic B-T stress application for samples with an insulating top layer. Note that for this sample type an initial electric current I due to capacitor charging has to be considered, due to the character of the sample setup, resembling plate capacitor:

$$I = \frac{V_{bias}}{R} \cdot \exp(-\frac{t}{R \cdot C}) \tag{3.4}$$

with R and C as the resistivity and capacity of the sample setup as given in Fig. 3.4(a). t is the application time of B-T stress. The capacitor charge up characteristic was acquired by a sample setup without host matrix, i.e. the 0.8×0.8 cm^2 Au layer was directly deposited onto the insulating top layer.

Subsequent to B-T stress, samples had to be prepared for physical analysis of the top layer by means of ToF-SIMS. Using a lift-off step (stripping), the host matrix had to be removed by ultrasonication in acetone for 30 s. If necessary, the samples were eventually rinsed with distilled H_2O (MilliQ 18.2 Ω/cm). A purge with N_2 finalized the lift-off step. For samples with an insulating top layer, the surface was

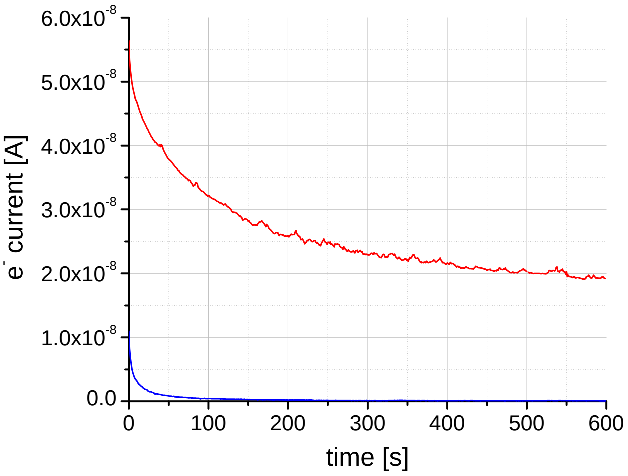

Figure 3.5.: Typical current characteristic during potentiostatic application of B-T stress (shown by the red curve). The blue curve shows the electric capacitor charging of the same sample, with an approximately one magnitude lower current response.

fully covered with a 40 nm thick Au layer (again by Ar-induced plasma deposition) to enable ToF-SIMS analysis (discussed in section 3.3.4).

3.3. Time of flight - Secondary ion mass spectrometry

Physical analysis was necessary, in order to determine the distribution of mobile ions, that were transported during B-T stress of the fabricated samples. Thus, the analytical approach had to fulfill several tasks:

- Unambiguous physical identification of elements and molecules
- Capability to map elements and molecules in lateral distribution
- Possibility to acquire in-depth information
- Quantification of identified elements and molecules of interest
- Low detection limit in order to resolve traces of mobile ions within the investigated material layer
- Possibility to analyze both insulating and conducting materials

Summarizing these points, time of flight - secondary ion mass spectrometry (ToF-SIMS) was chosen as the analysis technique for B-T stressed samples. Since this technique exhibits outstanding importance for this thesis, this section will give an insight into ToF-SIMS.

3.3.1. Principle

Many surface sensitive analysis techniques use a primary physical reagent (electrons, x-rays, ions, ...) interacting with the sample surface, thus causing different type of reactions from different depths of origin (backscattered ions, x-rays, electrons, secondary ions, ...). This can be utilized to get qualitative and quantitative information from the sample surface, with the surface sensitivity as an important parameter for the various techniques. From a phenomenological point of view, SIMS is the analysis of secondary ions arising due to bombardment of the sample surface with primary particles (ions or neutrals). In the following this procedure will be briefly discussed up to the detection of secondary ions and the information that can be gained from them. A complete overview of all aspects of (ToF-)SIMS is given in Ref. [54] and [55].

Accelerated by a voltage in the keV regime, primary ions impinge on the sample surface and cause collision cascades in the near surface region[1] (Fig. 3.6(a)). During this cascade, the energy of the impacting particle is transferred to particles in the target by conservation of momentum end energy as e.g. given for one target particle:

$$\begin{gathered} m_1 \cdot v_1 = m_1 \cdot v_1^{'} + m_2 \cdot v_2^{'} \\ \frac{1}{2} \cdot m_1 \cdot v_1^{2} = \frac{1}{2} \cdot m_1 \cdot v_1^{'2} + \frac{1}{2} \cdot m_2 \cdot v_2^{'2} \end{gathered} \tag{3.5}$$

with m_1 and m_2 being the mass of the primary and secondary ion, respectively. v_1 is the velocity of the impinging primary ion. $v_1^{'}$ and $v_2^{'}$ are the velocity of the primary projectile and the target particle after collision. Neglecting other factors in a first approximation, mass and energy of the primary ions determine the penetration depth of the collision cascade, also known as the altered layer or atomic mixing zone. The spatial extent of collisions in the sample has been computed by different approaches (e.g. [56, 57]): For projectiles used in SIMS the extent of region is typical in the nm regime. As a result of the collision cascade a portion of particles, in particular at the sample surface, take up enough energy to overcome the surface binding energy with adjacent particles within the sample matrix and thus escape from the sample surface. The number of particles of any constituent sputtered from the surface per incident primary ion is known as the total sputter yield Y_{tot} (For the sputter yield of a certain constituent A in the sample surface one has to consider its concentration by $Y_{tot} \cdot c_A$) [55]. Most of these secondary particles are of neutral character (Not taking into account secondary electrons). However, a small portion of these recoils leave the surface in the form of secondary ions, both of positive and negative polarity, given by the ionization probability $\alpha^{\pm}(A)$. Depending on the element or compound, this is typically in the magnitude

---

[1] It is not intended to go in detail with the collision theory. Details are given in Ref. [55] and Ref. [54].

of some per mill of the total amount of sputtered secondary particles of constituent A. The depth of their origin is largely the topmost monolayer (i.e. some Å), with an exponential decay for the amount of secondary ions from deeper layers [54, 58].

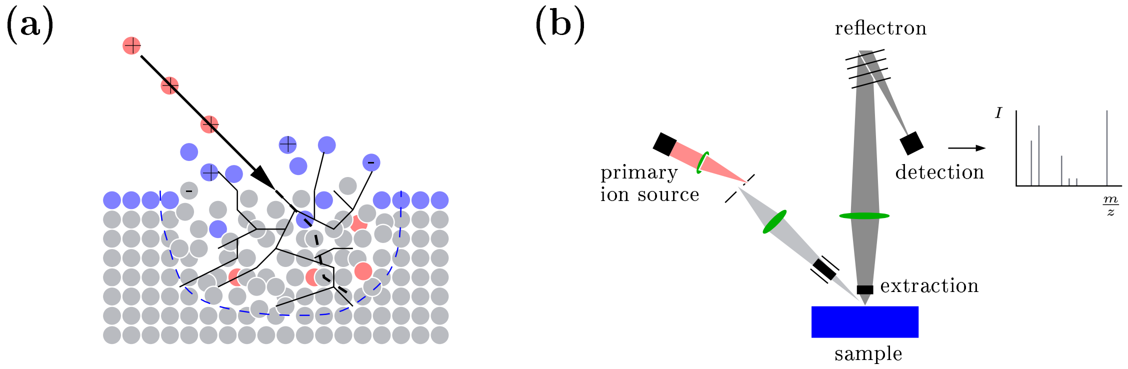

Figure 3.6.: (a) Collision cascade in the near surface region, as a result of primary ion bombardment (Marked by black lines). Secondary recoils are produced, with a small portion of them present as secondary ions. Particles from the topmost layer are marked by blue color. The spatial dimension of the collision cascade is marked by a dashed line. (b) Schematics of ToF-SIMS analysis, from the generation of primary ions to the acquisition of secondary ion mass spectra. Both schemes are adapted from ION-TOF GmbH application notes and from [54], respectively.

The principle of ToF-SIMS relies on the use of very low ion current densities (in the nA regime and below) impacting on the surface, by using a pulsing of the primary ion current with pulse widths of some tens of ns in the time frame of e.g. 100 μs. The damage on the sample surface per incident ion is given by the damage cross section σ, corresponding to the mean area where no further secondary ion can be generated after impact [59]. σ is a function of the sample surface properties and the primary ion properties. Assuming a low primary ion dose density (PIDD) bombarding the analyzed area (e.g 100 × 100 μm), each impact is hence statistically on a virgin surface spot. According to definition this is the case for $PIDD \leq 1$ % of the bombarded surface area (normalized to 1 cm^2 this equals to $PIDD = 10^{13}$ ions/cm^2). This threshold is known as the static limit, hence the maximum $PIDD$ to ensure static SIMS analysis. Above this threshold, sample erosion statistically starts to occur; this regime is used for dynamic SIMS analysis. ToF-SIMS typically is known as a static SIMS technique [54]. Consequently, the amount of produced secondary ions is comparable low and the analyzer has to be very efficient. A ToF analyzer fulfills this requirement.

By applied an extraction voltage, the secondary ions subsequently get collected by the analyzer as shown in Fig. 3.6(b). Considering an angular distribution of the secondary ion trajectories after their escape from the sample, this voltage has to be sufficiently high, in order to collect most of the secondaries of a certain polarity. The extracted ions, now accelerated to a defined kinetic energy E_{kin} get mass separated in the following electric field free drift path according to

$$E_{kin} = \frac{m \cdot v^2}{2} = z \cdot e \cdot U_a \tag{3.6}$$

with m being the mass of the respective secondary ion, v its velocity and U_a denoting the extraction voltage. Note that there is also an energy distribution of sputtered particles and hence secondary ions after the collision cascade [60]. Most of the secondary ions are singly charged, however, depending on the element there may also occur a small portion of multiply charged ones. Accordingly, t the time for a secondary ion to travel through the given flight path L_d is given by [54]

$$t = \frac{L_d}{v} = L_d \cdot \sqrt{\frac{m}{2 \cdot z \cdot e \cdot U_a}} \tag{3.7}$$

In modern ToF-SIMS instruments a reflectron type ToF analyzer with a 2 m flight path is used [61] (see section 3.3.2). The advantages of a ToF analyzer in comparison to other analyzer types are a high transmission and detection efficiency, a high mass resolution and the simultaneous detection of all secondary ions of a certain polarity. Additionally, a dynamic range of up to seven magnitudes can be handled. A single ion counting by means of a channel plate makes the detection of low secondary ion currents feasible with high sensitivity, while maintaining an appropriate signal to noise ratio [54]. The number of detected secondary ion yield of constituent A, divided by the number of sputtered particles of constituent A at the surface, defines $Y_u(A)$, the useful secondary ion yield of A. This quantity is governed on the one hand by $\alpha^{\pm}(A)$ and on the other hand by $f^{\pm}(A)$, the transmission efficiency of the ToF analyzer and the detector for constituent A (as given in eq. (3.8)). Typically, for a ToF-analyzer $f^{\pm}$ is close to unity. Restricted by the so called cycle time, the time between two primary ion pulses (e.g. 100 μs), the analyzer is able to separate and detect ions up to a maximum mass (given by L_d, corresponding to the respective cycle time). As the next primary ion pulse hits the sample surface and generates new secondary ions, the analyzer needs to blank out the remaining ions with longer flight times and to restart the ion detection with the lowest mass (thus with hydrogen(H)). The detected ions get converted into electrons, which get amplified and eventually enter a scintillator, in order to convert the signal into light. A time-to-digital converter digitalizes the obtained information, that is visualized on a computer in the form of ion flight time vs. ion intensity plots. An internal calibration enables the transition into the common mass-to-charge ratio [u] vs. intensity [cts] plots (sometimes just given by mass vs. intensity). The intensity of a secondary ion signal is the sum of all detected ions of a certain mass. This quantity is proportional to the abundance of the respective element or compound in the analyzed sample (i.e. on its surface). Basically, this relation can be expressed by the fundamental SIMS equation [55]:

$$I^{\pm}(A) = z \cdot I_p \cdot Y_{tot} \cdot c_A \cdot Y_u = z \cdot I_p \cdot Y_{tot} \cdot c_A \cdot \alpha^{\pm}(A) \cdot f^{\pm}(A) \tag{3.8}$$

with $I^{\pm}(A)$ the detected (positive or negative) secondary ion current of constituent A and I_p the primary ion current. For singly charged secondary ions: $z = \pm 1$. I_A, the detected intensity of constituent A in a mass spectrum is thus the number of detected particles in a certain analysis time frame, i.e. $I^{\pm}(A)$ integrated over time. Note that single ion count detectors encounter a problem concerning the detection of multievents: If one assumes the recovery of a channel on the channel plate after detection of an ion (i.e the dead time after an event) in the magnitude of some ns, there is no possibility to detect further events within this time frame. Thus, the detected $I^{\pm}(A)$ is reduced for high secondary ion currents. This problem has been solved by the so-called Poisson correction, i.e. mathematical postprocessing on statistical laws [62]. However, the maximum intensity of a peak in a spectrum is reached, when each channel on the channel plate has detected an event (i.e. the impact of a secondary ion). Therefore, constituents within the sample appearing in comparably high concentrations will cause saturation of the detector. As obvious from eq. (3.8), the saturation level is dependent on various parameters concerning the respective constituent, with $\alpha^{\pm}(A)$ as the most important. Regarding constituents exhibiting high ionization efficiency (e.g. alkali metals) the upper threshold is typically in the one digit %-range. For elements occuring in high concentrations, the detection of low abundand isotopes is therefore a solution to avoid detector saturation. Determined by the single ion counting system, the detection limit goes down to the 0.1 ppm range (Again dependent on the respective constituent). The range between detection limit and saturation is the dynamic range of the detector.

3.3.2. Historical and technical facts

A short look on the history of SIMS

Based on the discovery of secondary ions in 1910 [63], the fundamentals of SIMS go back until 1949 when Herzog and Viehböck built the first instrument [64]. Basically driven by the need for a microanalytical technique to obtain spatial element information from H to U and the isotopic composition of extraterrestrial material (In the beginning "space age"), Liebl and Herzog released the first commercially available SIMS [65]. Thereupon, based on the design of the ion optics and the used mass spectrometers, variations of further developments became broader [66] [55]. Historically, SIMS instrumentation can be separated into different concepts:

(i) Ion probe mass analyzers:

This concept was initially developed for trace analysis and depth profiling with a rather poor lateral resolution from ~10 μm up to 3 mm and thus without imaging capabilities. Designed with bright primary ion sources, i.e. using high primary ion currents (typically in the μA regime), these dynamic SIMS systems were aimed to applications in the semiconductor industry, caused by the increasing demand of a technique to acquire in-depth information of implantations, e.g. B into Si [67]. These systems used single or double focusing magnetic deflection mass analyzers, but also quadrupole analyzers came into play. The latter brought the advantage of compact and comparably cheap SIMS instruments for daily routine analysis to semiconductor industry [55]. Parallel to these developments, a system using low primary ion currents and a quadrupole analyzer was constructed; a surface sensitive technique was the consequence: The first static SIMS instrument [68]. Caused by the generation of only a low current of secondary ions, a crucial feature hereby was the change from the amplifying detector system, commonly in use for instruments with high current primary ion sources, to a single ion counter.

Basically, ion probe mass analyzers are nowadays of minor importance and have only historical relevance.

(ii) Ion microscopes

These instruments enabled direct stigmatic magnified imaging of the analyzed area by means of secondary ions on the detector system (e.g. a fluorescent screen), using a double focusing (by means of an electric and a magnetic field) magnetic deflection analyzer. A high lateral resolution could be achieved and it was thus possible to generate sample images in terms of lateral elemental distribution by the capability of selecting a desired mass. Images of different selected masses could be acquired in a consecutive manner and combined subsequently. Slodzian and collaborators were the pioneers in this field [69].

(iii) Ion microprobes using a primary ion beam, that rasters across the sample surface [70]. As for ion microscopes, secondary ions were analyzed via a double focusing magnetic deflection analyzer.

With the rising commercial interest in SIMS instruments, many features of the mentioned systems have been combined. Since quadrupole mass analyzers suffer from poor mass resolution ($M/\Delta M\ leq$ 1000) as well as from low transmission, static SIMS systems were equipped with other analyzer types. Since the late 70's, the use of ToF mass analyzers have gained increasing importance, for the raising interest on SIMS analysis of organic substances [71], commonly deposited on a solid substrate (e.g. Si) [72, 73]. This is due to the important features of ToF-SIMS instruments: An theoretically unlimited mass range, a quasi-simultaneous detection of secondary ions up to a defined mass as well as a high transmission of the analyzer. These benefits have been attractive, as fragmentation of organic molecules occurs during SIMS analysis of these substances. In the mid 80's, the use of reflectron type ToF analyzers was a further important step forward in terms of mass resolution ($M/\Delta M$ up to 10,000) [61] and towards the commercialization of ToF-SIMS. Due to the high transmission of ToF analyzers, imaging capabilities by scanning the primary ion beam across the sample surface area have been introduced for static SIMS instrument: A full mass spectrum is acquired for every pixel of the selected raster ($\equiv$ scan) and, by selection of the signal peaks of interest, a lateral mapping of these elements or compounds has become feasible.

Primary ion projectiles

At this point a brief overview of primary ions for SIMS will be given. Tab. 3.6 lists projectiles that have been used for SIMS instruments, with the emphasize on those of major importance for static SIMS and thus ToF-SIMS instruments[1]. Until the late 70's noble gas sources were the standard equipment, because they undergo no reaction with the target surface, hence leaving the sample undisturbed [55]. Concurrent to collision cascade theory [74] the sputter yield of the incident projectile increases with mass and energy, with the yield decreasing again for high primary ion energies, since implantation effects begin to dominate. Throughout the history of SIMS, argon (in the from of Ar^+) has been the most prominent candidate for noble gas sources. Primary ion generation was feasible for instance via electron impact or, resulting in high primary ion currents, a duoplasmatron (commonly used for dynamic SIMS instruments). However, Ar^+ was successively supplemented by projectiles that have been found to act in an enhancing manner for the secondary ion yield: As theoretically described by the bond-breaking model [75], a chemical reaction of electronegative primary ions as oxygen (${O_2}^+$) or nitrogen(${N_2}^+$) with the sample surface causes severe enhancement of positive secondary ion yields to several orders of magnitude compared to noble gas bombardment. Signal enhancements are basically reflected by an increase of $\alpha^{\pm}(A)$. The use of electron impact sources or duoplasmatron producing ${O_2}^+$ or O^- for the generation of thin oxide layers at the sample surface has become a routine approach for SIMS instrumentation. Alternatively, it is possible to provide O_2 to the target by a separate stream. The use of cesium ions (Cs^+) on the other hand has been shown to act in an enhancing manner with respect to the negative secondary ions yield, as described by the electron tunneling model [76]. In terms of Cs^+ generation, surface ionization sources have been applied with the advantage of obtaining a smaller spot size (down to $\sim 1\mu$m) than achievable by means of electron impact sources. A further advantage is the emission of secondary ion from the surface in the form of cesides (including sputtered neutrals; $M + Cs^+ \rightarrow MCs^+$),

---

[1] For details on primary ion sources it is referred to Ref. [55] and Ref. [54].

as theoretically described by the recombination model [77]. Thus quantification has become simplified due to a decrease of matrix effects [78].

Table 3.6.: Important primary ion sources and a survey of potential projectiles used for static SIMS and ToF-SIMS. The commercially relevant projectiles are marked in bold letters. The duoplasmatron is mentioned separately due to its importance for dynamic SIMS instruments.

Primary ion source	Projectiles (primary ions)
Electron impact source	$\mathbf{Ar}^+$, Ne^+, Xe^+, Kr^+, $\mathbf{O_2}^+$, N_2^+, $\mathbf{SF_5}^+$
Surface (thermal) ionization source	$\mathbf{Cs}^+$, I^-, $\mathbf{C_{60}}^{+(+)}$
Liquid metal ion gun (LMIG)	$\mathbf{Ga}^+$, $\mathbf{Au_{1\text{-}3}}^+$, $\mathbf{Bi_{1\text{-}7}}^{+(+)}$
Duoplasmatron	$\mathbf{Ar}^+$, Ne^+, Xe^+, Kr^+, $\mathbf{O_2}^+$, N_2^+, $\mathbf{Cs}^+$, $\mathbf{O}^-$, I^-

Regarding high resolution imaging capabilities of ToF-SIMS using a primary ion beam that scans over the surface in a defined field of view, the trend in the last two decades has been driven by the gradually increasing demand for smaller spot sizes of the primary ion beam. This was important since e.g feature size in the semiconductor industry became smaller and smaller and static SIMS applications in the field of biology and bioengineering have gained increasing significance. Operating as a low current source for static SIMS applications, liquid metal ion guns (LMIG; in literature the term LMIS for liquid metal ion source can be found frequently) enabled primary ion spot sizes below 0.1 μm. Due to its low melting point (29.8 °C), the favorable flow properties in liquid state and the outstanding beam stability, gallium (Ga) emitter have been become a standard for ToF-SIMS analysis, dominating the market for a long time [79, 54]. In the 90's the use of gold (Au) emitters (Using a Au/Ge alloy for decreasing the melting point of Au to $\sim$ 400 °C) have been shown to yield a certain amount of polyatomic cluster ions (Au_2 and Au_3) in the LMIG emission spectrum [80, 81]. This improves the ion yield of molecules compared to Ga^+ projectiles, since the single Au particles in a Au cluster contains only a portion of the total cluster energy (divided by the number of particles in the cluster) and thus the resulting impact energy per Au particle causes a more gentle ionization mechanism. With respect to ToF-SIMS analysis of biomolecules or polymers this has the consequence of lower molecule fragmentation and thus less complex mass spectra. The properties of bismuth (Bi) have been found found to be superior in contrast to Au, since the possibility to generate Bi clusters up to a cluster size of 7 and the additional possibility to condense doubly charged clusters out of the primary ion current [82, 83]. Spot sizes down to $\sim$ 0.1 μm have become feasible under certain conditions. Based on the need to further simplify mass spectra of organic molecules, the current state-of-the-art in LMIG emitters is a combined Bi-Mn source [84] for the application of the G-SIMS algorithm [85].

Parallel to the LMIG as primary ion source, other polyatomic cluster sources have been developed. In the late 80's, the use of sulfur hexafluoride (SF_6) for producing primary ions e.g. by electron impact revealed for the first time that polyatomic projectiles have a benefit in terms of lower fragmentation of large organic molecules [86, 59]. The use of buckminsterfullerenes (C_{60}) have been shown to give further crucial improvements [87, 88]. With respect to the used ion sources (Tab. 3.6), high primary ion currents of these projectiles may be applied as primary ion source and for sample erosion. As the latest development the use of Ar clusters with a cluster size up to Ar_{1000} has been proposed in literature [89]. Resulting in an effective impact energy on the sample surface of only some eV per Ar particle in the cluster, almost no fragmentation has been reported with the additional capability to non-destructive sample erosion [90, 91].

Dual beam depth profiling

15 - 20 years ago, ToF-SIMS was expanded by depth profiling capabilities, similar to dynamic SIMS. Since the task of the primary ion source has always been the generation of secondary ions in the static SIMS regime, a second ion gun have been attached to the instrument; the so-called sputter gun. Completely separated from SIMS analysis, the aim of the second ion source is solely sample erosion using the so-called dual beam technique [92, 93]. Sputter ions, accelerated to kinetic energies of 0.25 - 2 keV and bombarding the surface by a continuous beam, are utilized for eroding a crater of dimensions slightly larger than that of the SIMS analysis. Ionized by electron impact or surface ionization, typical sputter projectiles are e.g. ${O_2}^+$, Cs^+ or ${SF_5}^+$, thus signal enhancing effects for SIMS analysis must be taken into account. The low energy sputter process enables a very gentle sample erosion, resulting in a depth resolution in the single-digit nm regime, depending on the sample type and the surface roughness. For conductive samples, an interlaced SIMS analysis $\leftrightarrow$ crater erosion approach has been developed for assuring a short acquisition time for depth profiles [54]. Thereby, the sputter gun is operating between two primary ion pulses as shown in Fig. 3.7. However, since insulating samples are prone to surface charging (discussed in section 3.3.4), these samples cannot be depth profiled in the same fashion. A strict separation of the primary ion gun and sputter gun duty cycles is necessary, creating an alternating SIMS analysis $\leftrightarrow$ crater erosion sequence, in order to acquire depth profiles. This of course increases the acquisition time consequently. Note that in SIMS analysis using dual beam depth profiling, $Y_u(A)$ (the useful secondary ion yield of constituent A in the sample) is reduced, since the amount of sputtered material is drastically increased due to the sputter cycle and the effective transmission is reduced accordingly (the secondary recoils do not get analyzed during sputtering). This is considered by $Y_{eff}(A)$, the effective useful ion yield of a constituent A (Eq. (3.8)).

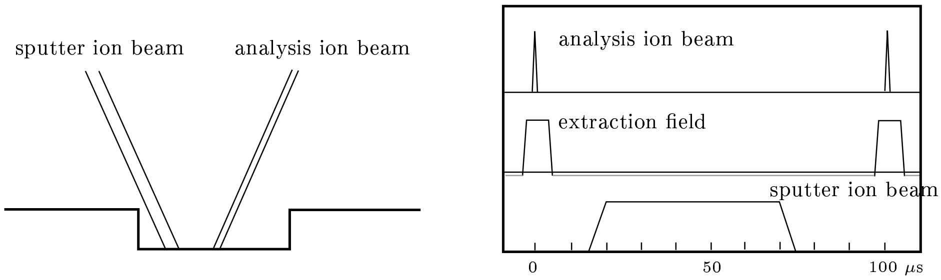

Figure 3.7.: (a) Principle of dual beam depth profiling in interlaced fashion as illustrated in Ref. [92]. SIMS analysis and sample erosion is decoupled by using two separate ion beams. As shown in the timing diagram, the sputter beam is off during primary ion bombardment, using a pulsed primary ion beam. Subsequently the primary ion beam and the secondary ion extraction are turned off, the sputter beam is eroding the surface and the next SIMS analysis is carried out at the crater bottom. A depth profile is thus acquired by repeating this sequence numerous times. Note that during sputtering, mass separation of secondary ions occurs in the ToF analyzer; SIMS analysis and sputtering is interlaced in one duty cycle (here 100 μm). Contrary to this methodology, insulating samples needs a strict separation of primary ion gun and sputter gun duty cycles.

The dual beam approach enables, by selection of the signals of interest, the reconstruction of the respective depth distribution by means of depth profiles [92]. Furthermore, a full mass spectrum and thus, in combination with the imaging capabilities of ToF-SIMS, lateral element and compound distribution in any depth with respect to the total sputter depth are accessible. By the combination of these possibilities 3D reconstruction and signal visualization is possible[1].

The data output of ToF-SIMS depth profiling is given in intensity vs. sputter time. In order to receive depth information, i.e. to convert the x-axis of the profile from time into depth, calibration is required. This can be done by using one of the following quantities: (i) Sputter yield Y_{sp}[2], reflecting the number of sputtered particles per incident sputter ion. (ii) Erosion rate $V(M)$ (the notation is derived from the German expression "Vorschub") of the sample matrix as given by

$$V(M) = \frac{I_{sp} \cdot M_w(M) \cdot Y_{sp}}{e \cdot \rho(M) \cdot N_A \cdot A \cdot n(M)} \tag{3.9}$$

$V(M)$ typically has the unit [nm/s], i.e. the sputtered depth per second of sputtering. I_{sp} is the sputter current, $M_w(M)$ the molecular mass of the sample matrix material, $\rho(M)$ its density and N_A Avogardo's constant. A denotes the sputter area, i.e. giving the edge length of the squared sputter crater and $n(M)$ the number of atoms in a compound (for monoatomic substrates $n(M) = 1$). It is obvious that E_{sp}, the energy of the sputter projectile, does not appear in eq. (3.9), however, this value is indirectly present via I_{sp} (The sputter current rises with increasing E_{sp}). Values for Y_{sp} are listed in section 3.4.1 (Tab. 3.10).

---

[1] Details on the different modes of a modern ToF-SIMS instrument are given in ION-TOF GmbH application notes

[2] Note that here Y_{sp} is caused by the sputter gun during the sputter cycle, thus sample material that is not used for analysis. Y_{tot} as given in eq. (3.8) on the other hand refers to the SIMS analysis cycle.

3.3.3. Used instrument

A TOF.SIMS^5 instrument, manufactured by ION-TOF GmbH (Münster, Germany) was used for experiments. The relevant features are listed in Tab. 3.7. The repetition rate of the primary ion source determines the cycle time between two pulsed primary ion shots and thus the acquisition time of the analyzer, which in turn determines the maximal detected m/z ratio (e.g 100 μs → 880 u).

Table 3.7.: Relevant features of the TOF.SIMS^5 instrument The angle of incidence with respect to the surface normal is 45° both for primary ions and sputter ions.

Component	Comment	Typical operation conditions
Primary ion gun		
Ion species	$\mathrm{Bi}_{1\text{-}7}{}^{+(+)}$, mass filtered	$\mathrm{Bi}_1{}^+$, $\mathrm{Bi}_3{}^+$
Repetition rate	10 - 50 kHz (→ 20 - 100 μ s)	10 kHz, 20 kHz
Acceleration voltage	25 kV	
Emission current		1 μA
Sputter gun		
Sputter ions	$\mathrm{O}_2{}^+$, Cs^+	
Acceleration voltage	up to 2 keV	0.25, 0.5, 1 or 2 keV
Other features		
Analyzer	Reflectron type ToF-analyzer; mass resolution up to m/Δm = 10,000	
Extraction voltage	up to 2 kV	2 kV
Reflection voltage	Adjustable range: -200 - 200 kV	-20 kV, 20 kV
Detector post acceleration	8.5 kV	
Detector dynamic range	10^0 - 10^7 counts (≡ cts)	
e^- Flood gun	e^- acceleration: up to 20 V; e^- current: up to 10 muA;	20 V
Gas valve	auxiliary gases can be supplied to the surface (e.g. $\mathrm{O}_2{}^+$)	not in use
Main chamber pressure	Dependent on sample type: 10^{-10} - 10^{-8} mbar	
Sample temperature variation	-130 - 500 °C	

For the primary ion gun, generally two modes were used for experiments [94]:

(i) In high current bunched mode (HCBU), two cross-overs of the beam along the primary ion optical path enables the conservation of maximum beam intensity (DC: ~15 nA, pulsed: up to ~1 pA, dependent on chosen Bi-cluster size). A bunching voltage compresses the primary ion pulse to a pulse width of max. 1 ns. This explains the advantage of HCBU: The high achievable mass resolution of the ToF analyzer and high Y_{tot}, thus high secondary ion signal intensities. But this includes also some limitations: The pulse compression induces an energy dispersion of primary ions, causing the ion beam focus on the sample surface to appear not in a sharp point, but in a certain region along the primary ion beam axis.

Due to this fact and additional distinctive coulomb repulsion by means of high primary ion density in the bunched ion pulse, a comparable poor lateral resolution of generated secondary ion images is achievable from the sample surface (~1 μm at its best).

(ii) In burst alignment mode (BA), one beam cross-over is generated in the primary ion optical path and the pulse with of the chopped primary ion package is not compressed. The advantage of BA lies in the obtainable lateral resolution (~0.2 μm at its best), however with the drawback of a poor mass resolution.

A sputter gun, operating with DC (up to ~600 nA, depending on the sputter ion species and acceleration.) was attached for dual beam depth profiling. Note that, since all presented ToF-SIMS depth profiles contain signals of positive secondary ions, $O_2{}^+$ was generally used for sputtering. Additionally, the instrument was equipped with a secondary electron detector, in order to enable the acquisition of secondary electron images, corresponding to the chosen field of view for primary ion bombardment. A low energy electron flood gun could be utilized for charge compensation for the analysis of insulating samples.

3.3.4. ToF-SIMS analysis of insulating samples

A major obstacle, commonly encountered in surface analysis by an ion beam or electron beam, is sample charging. ToF-SIMS analysis of insulating samples thus suffer from this problem as well. Considering a connected current circuit including a primary ion gun, a electron gun (discussed later) and a target sample, the incident currents arising from the primary ion beam (I_p) and the electron beam (I_e) on the one hand and I, the current through the insulating target, on the other hand have to fulfill Kirchhoff's first law according to [95]

$$I = I_p \cdot (z + \delta^T) - I_e \cdot (1 - \gamma^T) \tag{3.10}$$

assuming $I_p = I_p^+$ for single charged ions ($z = 1$). δ^T and γ^T are effective secondary ion yields arising from primary or sputter ion and electron bombardment, respectively. The sum of all incoming and outgoing currents in eq. (3.10) with their respective polarity has to be 0. Secondary ion currents have been neglected in this comparison,due to their low quantity. Contemplating an insulating sample as electrically represented by a resistivity and a capacity in parallel (RC circuit), I causes a capacitor charge up with the maximum achievable charge on the sample surface. Thus the arising voltage V in the insulator governed by the resistivity in by means of Ohm's law (eq. (2.22)) [95]. Sample charging can be of positive or negative polarity, dependent on whether I_p or I_e is dominating in eq. (3.10) and on the magnitudes of δ^T and γ^T. The latter is important, since a secondary electron leaving the sample surface produces a positive charge in the insulator, that contributes eventually to the charge induced by the primary ions. In ToF-SIMS analysis, where secondary ions are produced with a primary ion beam of positive charges, γ^T due to electron bombardment can be omitted in eq. (3.10). Analog, δ^T can be omitted for SIMS related techniques using electron beams for signal generation at the sample surface (e.g. Auger electron spectroscopy AES, scanning electron microscopy SEM, electron impact desorption ESD . . .).

In an exemplary static SIMS study of poly(tetrafluoro ethylen) surfaces [96], a surface potential of 10^4 - 10^5 V was theoretically achievable. However, due to surface discharge, this value was practically never reached, potentially resulting in fluctuations in the magnitude of sample charging. This inherently causes severe limitations and artifacts in the obtained measurement data. Adapted from [97], Tab. 3.8 gives a survey of typical implications of sample charging during ToF-SIMS analysis:

Table 3.8.: Commonly encountered effects of sample charging of insulators on ToF-SIMS analysis. Not included are effects due to the properties of surface charges as a potential barrier at the sample surface, possibly reducing the secondary ion yield $Y_u(A)$.

Effect	Explanation
Peak shift	Alteration of the effective extractor potential. E_{kin} of secondary ions after extraction changes (Eq. 3.6) causing a different ion flight time in the ToF analyzer (Eq. 3.7)
Reduced lateral image resolution, peak broadening	Disturbance of emitted particle trajectories (beam defocusing)
Signal reduction up to complete loss of signal	Caused by alteration of the effective extractor potential,. E_{kin} of secondary ions varies and may be out of the ToF analyzer reflectron acceptance. Partial sample charging of heterogeneous samples may also lead to such effects [96]
Change of the original depth distribution	Mobile ion migration: Sample charging causes mobile ions within the insulator to migrate away from (or towards) the sample surface, depending on the polarity of sample charging

Ref. [97] summarizes counteraction for sample charging. In the following, the common approaches to handle the mentioned effects during ToF-SIMS analysis using positively charged primary ions and sputter currents are discussed. In such cases sample charges typically have positive polarity and appear in a heterogeneous fashion. A successful combat or handling of surface charging is reflected in low fluctuations in the total detected secondary ion current, and thus in stable signals within the obtained mass spectrum.

Low energy electron flooding

Taking into account eq. 3.10, positive sample charging is encountered both when a positively charged primary ion beam or sputter beam irradiates the surface and when secondary electrons are produced (indicated by δ^T and γ^T). Due to the pulsed character of the primary ion beam, its contribution to sample charging is negligible in comparison to the DC sputter beam. An auxiliary electron gun with I_e is utilized to compensate appearing charges prior to static SIMS analysis. According to eq. 3.10, γ^T has to be < 1, in order to effectively provide negative charges to the sample surface and hence to enable the compensation effect. In order to guarantee this, the electron energy preferably has to be very low. This has the additional advantage of a negligible damaging effect on the sample surface. A detailed description as well as the timing of this so-called electron flood-gun is given in Ref. [96]. Operation is carried out in pulsed mode while the extraction voltage of the ToF analyzer is off, in order to avoid extraction of electrons when negative secondary ions are analyzed and acceleration of electrons to higher energies when positive secondary ions get extracted.

Deposition of thin conductive layers onto the insulating surface

In dynamic SIMS analysis, approaches have been applied that use a diaphragm or a conductive grid placed on the sample surface, which acts as a primary ion bombardment induced electron source or electron sink. For instance the use of a tantalum (Ta) diaphragm has been reported to compensate positive charges on insulating surfaces [95]. However, the disadvantage of such approaches in static SIMS analysis is the uncontrolled induced surface contamination.

For the use in ToF-SIMS depth profiling, this contamination issue would solely affect the first scan. After the first sputter cycle the acquired mass spectra are free of contamination. Deposition of a conductive layer hence does not inherently alter the resulting depth profile; the respective signal of this layer vanishes when the actual sample surface is reached. Furthermore a conductive layer electrically connects the sample holder, set to ground potential, with the vicinity of the eroded crater, accelerating charge compensation. Furthermore as for diaphragms or grids on the sample surface, the conductive layer serves as an additional electron source. The use of conductive layers for the analysis of insulating surfaces is also known for other SIMS related techniques (e.g. Au or C layer for SEM).

Considering the sample set-up for the experiments in this thesis (Fig. 3.4), a Au layer has been deposited by default, serving as contact electrode for the application of B-T stress. This Au layer was utilized as conductive layer for counteracting sample charging during ToF-SIMS depth profiling. Fig. 3.8 shows the difference of signal stability due to surface charges on a SiO_2 surface without and with coverage with 40 nm Au. The signal in the spot vicinity immediately recovered its full intensity in the 100×100 cm^2 field of view. Without Au layer, it takes approx. 5 min until the signal returns to the intensity present before a ~0.5 s sputter ion pulse was shot onto the surface.

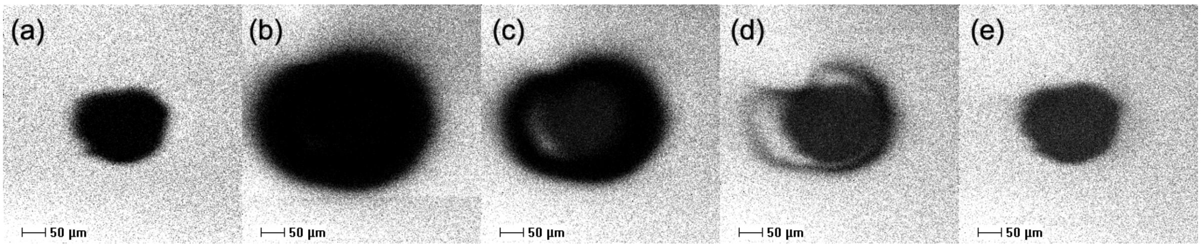

Figure 3.8.: Effect of Au coverage on an insulating SiO_2 surface on signal recovery after 0.5 s sputter ion bombardment (beam spot size on surface ~50-70 μm), as indicated by secondary ion (SI) images (total secondary ion intensity): (a) 40 nm Au layer on SiO_2. Image immediately taken after sputter ion bombardment. SI images taken without Au layer on SiO_2 after (b) 1 min (c) 2 min (d) 3 min (e) 5 min.

Adjustment of the reflecton voltage

After extraction, E_{kin} of secondary ions for each mass-to-charge ratio after extraction (given in eq. (3.6)) exhibit a certain distribution. Separating secondary ions solely by an electric field free drift path would result in signal peak broadening in the mass spectrum and thus in a poor mass resolution. A reflectron type ToF analyzer enables the compensation of energy dispersion within the analyzer flight path by using a two-stage ion mirror [61]. After an electric field free drift path and a retarding path, an ion mirror, adjusted at a defined potential (reflection voltage), reflects the secondary ion beam by almost 180° towards the detector; energy focusing is the result. The drift length into the ion mirror is governed by E_{kin}, causing a slightly prolonged drift length for ions with higher E_{kin} than given by L_d, the nominal length of the flight path. After a second electric field free drift path toward the detector, all secondary ions of a certain mass-to-charge number ratio get detected simultaneously, irrespective of their E_{kin}. The reflectron voltage (typically 20 V or -20 V, dependent on the polarity of the secondary ions) hence determines the ToF analyzers acceptance of additional E_{kin}, thus working like a low-pass filter. Ions with too high E_{kin} get canceled by the ion mirror and cannot contribute to the detected signal intensity. Sample charging would result in a drastic increase of the extraction voltage U_a and thus an inherent offset of E_{kin} is given. The reflectron voltage of the ToF-SIMS instrument can be regulated between -200 and 200 V. An increased energy acceptance may compensate fluctuations in E_{kin}. However, although signal intensity can be maintained in the presence of sample charges, very high mass resolution cannot be achieved.

3.3.5. The ToF-SIMS quantification issue

Based on the detected raw-data, the directly plotted output results of ToF-SIMS measurements are:

- Mass spectra → intensity vs. mass-to-charge ratio
- Depth profiles → intensity vs. sputter time
- Secondary ion images: Intensity maps, detected intensity digitalized by 8-bit color depth → color (or grey) scale in 256 increments.

Thus, ToF-SIMS cannot provide direct quantitative information on element or compound concentrations present within the sample (surface). Eq. (3.8) gives the correlation between intensity and concentration of a certain component, with some typically unknown quantities (e.g. $\alpha^{\pm}(A)$). A survey of quantification algorithms based on physical models or phenomenological aspects is given in [55]. In this thesis the quantitative interpretation of ToF-SIMS depth profiles is of high importance. Thus, this section will concentrate solely on this aspect.

A linear relation between concentration and $I^{\pm}(A)$ can be assumed for elements (and the respective isotopes) or compounds of low abundance within the probed surface area (≤ 1 %). This range is typically met by the dynamic range of secondary ion intensities I_A in ToF-SIMS instruments. Thus, eq. (3.8) simplifies to (for the example of singly charged secondary ions)

$$\begin{aligned} I^{\pm}(A) &= I_p \cdot S_p \cdot c_A \\ I_A &= PIDD \cdot S_p \cdot c_A \cdot A \end{aligned} \tag{3.11}$$

by considering $S_p(A)$, the instruments absolute sensitivity for element A (containing all instrument-related parameters) [55]

$$S_p(A) = \alpha^{\pm}(A) \cdot f_{pm}(A) \cdot Y_{tot} \tag{3.12}$$

Both expressions in eq. (3.11) are identical to the formalism in the fundamental SIMS equation (eq. (3.8)). I_A, i.e. $I^{\pm}(A)$ integrated over a certain analysis time, is proportional to $PIDD$, the cumulated I_p in this analysis time for a defined analysis area A.

A comparably simple phenomenological approach relates the absolute sensitivity of an element or constituent A to the absolute sensitivity of a reference (usually matrix) element or constituent M of known concentration c_M within the sample. One can then calculate the relative sensitivity of element A to element M

$$\frac{S_p(A)}{S_p(M)} = \frac{I^{\pm}(A) \cdot c_M}{I^{\pm}(R) \cdot c_A} = S_{r,A} \tag{3.13}$$

Using the relative sensitivity $S_{r,A}$ does not require the knowledge of I_p and thus simply relates detected secondary ion currents. If c_M is known, e.g. by taking into account a homogeneous matrix element within the sample, c_A the concentration of element A (e.g. contamination traces) can be calculated by considering M as internal standard. For depth profiles, however, the common methodology uses external standards as reference (Either implantations of given dose ($\equiv$ fluence) ϕ_A or homogeneous standards with known c_A) [98, 99, 54]. Using implanted standards the relative sensitivity factor $RSF_{A,M}$[1] can be given by

$$RSF_{A,M} = \frac{\phi_A}{d} \cdot \frac{\int I_M \cdot \mathrm{d}x}{\int I_A \cdot \mathrm{d}x - \int I_{BG} \cdot \mathrm{d}x} \cdot \frac{1}{f} \tag{3.14}$$

with d a length quantity from the depth profile (e.g. sputter crater depth or thickness of a thin film (see section 3.4.1), I_A the signal intensity of the chosen element to be quantified, I_M the signal intensity of the reference element within the sample matrix and I_{BG} the background of element A in the sample not originating from implantation (but from e.g. surface contaminations). Commonly, the reference signal is represented by the material of the implanted sample. However, it is usually advantageous to choose a low abundant isotope (e.g. ^{30}Si representing SiO_2), in order to avoid errors due to excessive Poisson correction or even detector saturation effects (see section 3.3.1). f considers the abundance of the respective isotopic within the matrix material. The intensities in the depth profiles get integrated over a certain sputter depth (for sputter time to sputter depth conversion in ToF-SIMS depth profiles see section 3.4.2), covering the implantation profile of element A. Thus, the integration limits in eq. (3.14) have to be chosen accordingly. For thin films, the layer thickness can be used as integration limits. Since the matrix and the measurement conditions of the external standard and the sample to be quantified are the same, c_M is not considered in eq. (3.14). Using $RSF_{A,M}$, and considering the linear relation between c_A and I_A (see above), the intensity scale in ToF-SIMS depth profiles can thus be converted into a concentration scale. Among numerous publication concerning SIMS quantification issues Wilson et al. published $RSF_{A,M}$ values for all major elements of significant importance in various matrix materials measured with both positive and negative polarity [100, 101, 102, 103][2]. However, due to differences in

---

[1] Note that $S_{r,A}$ and $RSF_{A,M}$ are related in a reciprocal fashion, due to the respective definition as given in [55] and [98]. For ToF-SIMS depth profiles, $RSF_{A,M}$ values are commonly is use for quantification.

[2] The values published by Wilson et al. are determined using a CAMECA IMS-3f SIMS instrument using a magnetic sector analyzer

instrument specifications, tabulated $RSF_{A,M}$ values cannot be used for every type of SIMS instrument [104].

Table 3.9.: $RSF_{A,M}$ according to eq. (3.14) for Na in different matrix materials as obtained by ToF-SIMS depth profiling using implantation standards. The value for Na in the SiO_2 matrix has been obtained by averaging over 3 implantations into SiO_2 with d = 100 nm, 200 nm and 400 nm, respectively. A comparison to literature values from [100, 102] is given

Matrix material	Reference signal M	ϕ_A [cm^{-2}]	$RSF_{Na,M}$ [cm^{-3}] (this thesis)	$RSF_{Na,M}$ [cm^{-3}] (literature)
Si	^{30}Si	$1 \cdot 10^{14}$	$8.19 \cdot 10^{20}$	$3.60 \cdot 10^{20}$
SiO_2	^{30}Si	$1 \cdot 10^{14}$	$2.99 \cdot 10^{21} \pm 0.25 \cdot 10^{21}$	$4.00 \cdot 10^{21}$
Si_3N_4	^{30}Si	$1 \cdot 10^{14}$	$2.67 \cdot 10^{21}$	$1.00 \cdot 10^{21}$
AlSiCu	^{27}Al	$8.75 \cdot 10^{15}$	$1.09 \cdot 10^{22}$	N/A

$RSF_{Na,M}$ values for quantification of ToF-SIMS depth profiles in this thesis have been obtained using external standards (here implantation profiles). The error in terms of reproducibility of depth profiling on a standard accounts for a deviation of leq 5%, however, the error in terms of reproducibility between several standards is leq 10%. $RSF_{Na,M}$ from ToF-SIMS measurements deviate from the given literature values by approx. factor 2 - 3.

3.4. Supporting techniques

3.4.1. Digital holographic microscopy

In order to gain informations on the sample topography during sample processing as indicated in Fig. 3.1, digital holographic microscopy (DHM) was employed (instrument: DHM R1000, Lynceé tec$^{\mathrm{DHM}}$, Lausanne, Switzerland). It is not intended to go into the details of this technique, which is given in the related literature (e.g. [105, 106]). Generally, complex holographic data arising from interference of an optical beam wave, reflected from the object, with a reference wave are recorded by a CCD camera. By means of numerical processing both real phase and real amplitude information can be extracted from of these data, enabling the visualization of phase-contrast and intensity images from the sample surface (an additional feature includes 3D reconstruction). The advantage of DHM lies in its excellent resolution depth of theoretically below 1 nm. However, transparent samples or transparent layers on reflecting surfaces may cause artifacts. This drawback has been faced recently by the development of appropriate algorithms for numerical processing by implication of the involved materials refractive indices [107]. DHM surface phase-contrast and intensity images can be investigated on various parameters of interest. Two of them are of particular relevance:

- Determination of the surface roughness as expressed by R_a, the averaged roughness in a certain field of view (here 500 × 500 μm).
- Crater depth measurement subsequent to ToF-SIMS depth profiling for determining Y_{sp} (acc. to eq. (3.9)).

DHM revealed $R_a = 15 \pm 5$ nm after sample preparation, i.e. before B-T stress (see Fig. 3.1), depending on factors as spin coating conditions of the used formulation (Tab. 3.5; e.g. due to variations in the viscosity). Fig. 3.9 shows the sample surface appearance after sample preparation (by DHM and light microscopy) with the typical features causing the measured sample surface roughness.

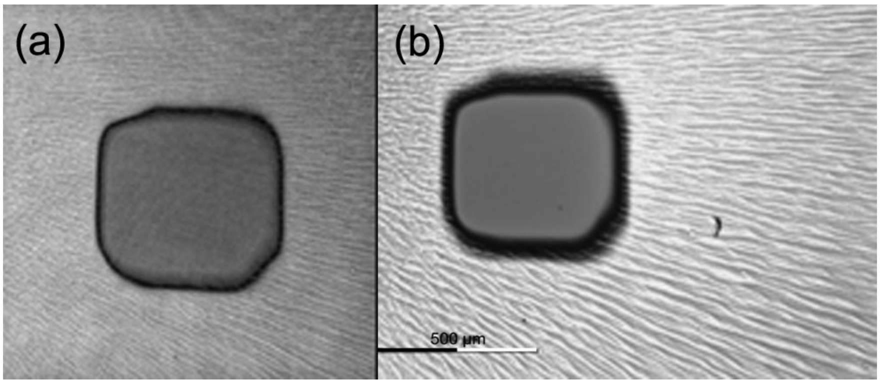

Figure 3.9.: Images of the vicinity of a ToF-SIMS sputter crater, showing the typical texture of the sample surfaces due to spin coating. (a) DHM intensity image (field of view ~ 870 × 870 μm). (b) Optical light microscopy image. The scale at the lower left hand corner accounts for 500 μm.

DHM crater depth determination was important concerning the Si-substrate. The thickness of thin material films, deposited onto Si was known a priori from the fabrication process at Infineon Technologies Austria AG in Villach. Thus, considering the sputter time in the respective material during ToF-SIMS depth profiling, $V(M)$ could be obtained[1] and thus Y_{sp} via eq. (3.9). Tab. 3.10 lists values of Y_{sp}, ordered by respective sputter gun settings using $O_2{}^+$ as the sputter species, due to the relevance in terms of positive secondary ion yield enhancement for mobile ion detection (see section 3.3.2). Obtained Y_{sp} values have been compared to theoretical ones, gained from Monte Carlo simulations using the TRIM (SRIM) code [57][2] and the code according to Yamamura et al. [108, 109]. Y_{sp} for SiO_xN_y and BPSG can not be given, since the stoichiometry of these materials was not exactly known due to industrial constrains. For these materials $V(M)$ was directly used for x-axis conversion in depth profiles.

---

[1] For instance assuming $I_{sp} = 254$ nA (for $E_{sp} = 1000$ eV) and $A = 300 \times 300$ μm gives $V(M) = 0.45$ nm/s for $O_2{}^+$ sputtering in Si.

[2] TRIM (Transport of ions in matter) is part of the SRIM (The stopping range of ions in matter) software; available at https://www.SRIM.org

Table 3.10.: Y_{sp} values, obtained at room temperature and averaged over 3 - 5 determinations, used for time to depth conversion in ToF-SIMS depth profiles concerning different sample matrix materials. The listed values according to E_{sp} for $O_2{}^+$ bombardment at 45° angle of incidence, were chosen due to their use in terms of ToF-SIMS depth profiles. SRIM simulation was carried out using $E_{sp}/2$ for choosing O as the sputter projectile instead of O_2. SiO_2 is assumed as dry oxide

Matrix material	E_{sp} [eV]	Y_{sp} measured	Y_{sp} SRIM	Y_{sp} Yamamura
Si	500	0.53 ± 0.05	0.75	0.65
	1000	1.38 ± 0.08	1.14	1.07
SiO_2	500	1.01 ± 0.09	1.32	N/A
	1000	2.32 ± 0.04	2.14	N/A
	2000	3.47 ± 0.10	2.79	N/A
Si_3N_4	1000	2.34 ± 0.10	2.42	N/A
AlSiCu	2000	1.04 ± 0.07	N/A	N/A

3.4.2. Impedance spectroscopy

This technique was employed for the following purposes:

- Determination of the sample capacity. Impedance spectroscopy could separate capacities from different insulating layers within the sample stack.
- Auxiliary studies on transport processes within samples. Different processes, possibly contributing to ion transport processes, could be separated. Insulating materials could be assigned according to their contribution to the total sample resistivity.

Basically, electrochemical impedance spectroscopy measures the impedance of a sample by means of probing it with an AC signal screened over a defined frequency range ($f = 1 \cdot 10^6$ Hz - $1 \cdot 10^{-1}$ Hz). It is not intended on this point to discuss details of this technique (e.g. given in [110, 111]); only facts regarding data interpretation are of relevance in the course of this thesis. The complex impedance Z reads

$$Z = Z' + j \cdot Z'' \tag{3.15}$$

with Z' being the real part of the impedance and Z'' its complex part. Commonly the notation for Z includes the suffix (ω) to account for the frequency dependence by $\omega = 2 \cdot \pi \cdot f$, with ω the circle frequency. Here the impedance of parallel RC-circuits was of interest, since sequential material layers can be represented by RC-circuits in series [112]. Z for a parallel RC-circuit is given by

$$Z(\omega) = \frac{1}{\frac{1}{R} + j \cdot \omega \cdot C} = \frac{R}{(\omega \cdot R \cdot C)^2 + 1} - j \cdot \frac{\omega \cdot R^2 \cdot C}{(\omega \cdot R \cdot C)^2 + 1} \tag{3.16}$$

Using a Novocontrol Alpha-A high performance impedance analyzer the AC input signal response got recorded as a function of frequency. Expanded by a Novocontrol high voltage boost unit, AC amplitudes of up to 200 V could be coupled into the sample. Impedance spectra were plotted by means of complex impedance planes (Nyquist plots), i.e. -$Z''(\omega)$ vs. $Z'(\omega)$ as recorded for the defined frequency range. Z' and Z'' can be related by

$$\tan\theta = \frac{Z'(\omega)}{Z''(\omega)} = \frac{\epsilon''(\omega)}{\epsilon'(\omega)} \tag{3.17}$$

$\tan\theta$ is the so called dielectric loss factor, relating the heat dissipated energy (given by $\epsilon''(\omega)$, the complex part of the permittivity) with the saved energy (given by $\epsilon'(\omega)$, the real part of the permittivity) within the RC circuit. In Nyquist plots parallel RC circuits are characterized by a semicircle (Fig. 3.10), with two important attributes as observable in eq. (3.16): (i) At low frequencies $Z \rightarrow Z' = R$: the intercept of the curves with the x-axis represent resistivities R. (ii) $\omega = \omega_{max}$ at maximum -$Z''(\omega)$ indicate capacities C by

$$\omega_{max} = \frac{1}{R \cdot C} \tag{3.18}$$

For impedance spectroscopy the same experimental setup was used than for B-T stress (section 3.2), with the signal source the impedance analyzer instead of a SMU.

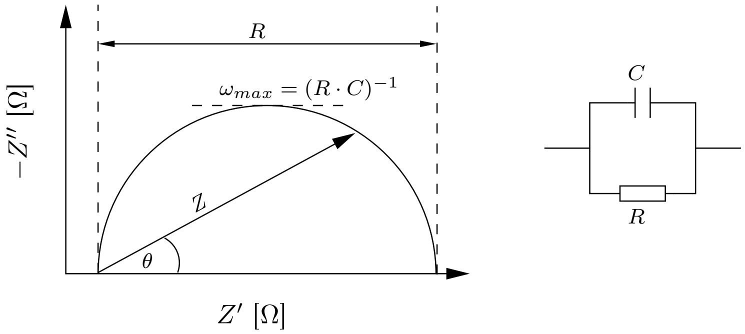

Figure 3.10.: Scheme of a Nyquist-plot for a parallel RC-circuit (Adapted from [110]). The respective RC equivalent circuit is shown separately.

Chapter 4

Investigation of mobile ion migration during ToF-SIMS depth profiling

Among various measurement artifacts, that may appear during ToF-SIMS depth profiling (Tab. 3.8 lists the most common ones), mobile ion migration is of utmost significance for this thesis. Therefore, this chapter is devoted to go into detail with this effect. Mobile ion migration is inherently connected with the bombardment of an insulating surface with a primary projectile. Obtained Mobile ion distributions in ToF-SIMS depth profiles are typically distorted and does not display the real distributions as actually present in the insulating sample. If the investigated sample contains a thin insulating film, mobile ion migration is even more pronounced. A discussion of a model proposed in literature gives an insight into involved processes which are considered to release mobile ion migration in insulators.

Investigations on the temperature dependence of the mobile ion migration and its consequence for artifacts in ToF-SIMS depth profiles is a substantial part of this chapter. Thin films of different insulating materials were investigated and assessed on appearing artifacts. In general, two scenarios were assigned to experiments:

(i) Samples prepared for B-T stress application as illustrated in Fig. 3.1, with a host matrix formulation containing $c_{MeOTf} = 300$ ppm spin coated on the insulating film to be invesitgated. The only difference was the deposition of the conductive gold (Au) layer: While for B-T stress application an area of 0.8×0.8 cm^2 was covered with Au, here a full coverage of the host matrix was carried out, in order to achieve proper electrical contact to the silicon (Si)-back side metalization. This procedure is carried out prior to ToF-SIMS depth profiling of thin insulating films by default.

(ii) Sodium (Na), implanted into silicon oxide (SiO$_2$) of different film thickness with a dose of $\phi_{Na} = 1{\cdot}10^{14}$ cm^{-2} (energy: 25 keV, angle of incidence: 7°). Thus a well defined Gaussian shaped implantation profile was given and mobile ion migration, here on the example of Na^+, could be examined systematically. Based on experimental data from this scenario, a mathematical model for data treatment is proposed that enables the reconstruction of an artifact free Na distribution in SiO_2.

4.1. Reasons for mobile ion migration

As discussed in section 3.3.4, insulating samples suffer from sample surface charges, prevalent of positive polarity, arising from ion bombardment. In ToF-SIMS depth profiling, ion sputtering is the predominant reason for this, since carried out using DC (I_{sp} in the magnitude of 10^2 nA), contrary to primary ion bombardment (pulsed I_p in the magnitude of 10^{-1} pA). These charges may interact with positive charged mobile ions within the sample, leading to migration effects. In literature, especially Na migration and the connected artifacts have been reported (e.g. [113])

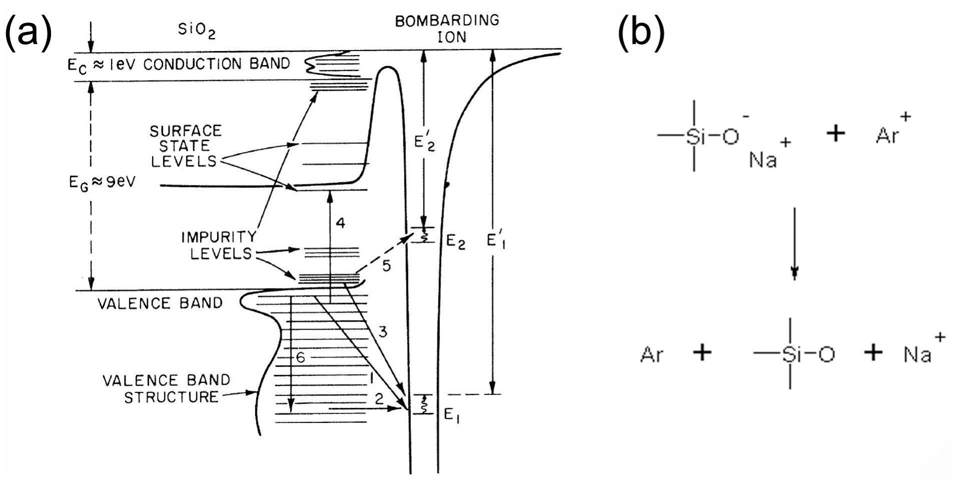

Figure 4.1.: (a) Band scheme of SiO_2 surface during ion bombardment as taken out of [114]. Each single process and situation is explained in the text. (b) Release of Na^+ from interaction with SiO_2 by neutralization of Ar^+ as sputter ion projectile.

In the 70's the impact of positively charged ions on insulators and the effect on mobile ion migration was investigated by several groups. McCaughan and collaborators proposed a mechanism, that involved neutralization processes of the impacting ion at the insulator surface [114, 115]. Fig. 4.1 shows the band scheme of an insulator containing impurities during ion bombardment. Two different situations may occur when bombarding the surface with ions, having a high ionization potential E_1 (e.g. Ag^+, N^+ or $N_2{}^+$) or ions having a low ionization potential (e.g. B^+, Si^+ P^+):

(i) For ions with ionization potentials E_1, this potential at impact changes to $E_1^{'}$. This changed value is a function of the distance to the surface ($E_1^{'} = E_1^{'}(x)$), due to interaction with image charge effects induced by polarization of the sample surface by means of the approaching ion. The ions of this class exhibit

$$E_1^{'} > E_G + E_C \tag{4.1}$$

with E_G being the energy band gap between valence and conduction band and E_C the energy width of the conduction band. According to eq. (4.1) several processes get energetically favorable. Transitions 1 and 3, as given in Fig. 4.1(a) are Auger transitions, including a "down" electron coming from a bulk (1) or impurity (3) level, respectively. This requires excitation of a second electron (transition 4) into a surface state level. If $E_1^{'}$ is large enough, this second electron can be entirely excited into vacuum level. Transition 2 arises from resonance processes without involving an electron excitation. The consequence of these transitions is the neutralization of the impacting ion by electron transfer at the surface. After this event, the ion travels further as a neutral particle. However, due to these transitions either holes are generated at the surface of the bulk material or positive charged impurities arise as illustrated in Fig. 4.1(b). In SiO_2, Na get released in the form of Na^+, since there are no free electrons available to provide another binding electron [114]. The positive surface charges, i.e the generated holes at the SiO_2 raise the electric potential of the surface. With respect to a counter ground potential, an electric field evolves. As shown in Fig. 3.1 the samples for B-T stress experiments in this thesis exhibited thin films of material at a conductive Si-substrate. Thus when an insulator is present as a thin film (with the thickness up to 400 nm), already minor potential shifts at the surface induce huge electric fields, since the voltage drops within a very small distance. These arising electric fields are the major driving force for inevitable mobile ion migration from the surface towards the counter electrode, as represented by the ground potential, where mobile ions finally accumulate. Na^+, frequently appearing in high abundance, is very prone to migration, since exhibiting high mobility in SiO_2 [116, 40, 117]. When the bombarding ion exceeds a certain energy, the time spent in the surface near region is supposed to be very short due to the high ion velocity [114], neutralization by Auger or resonance processes do not take place anymore and migration does not occur. However these energies are rather high (e.g. 20 keV for Ar^+).

(ii) Ions with values of E_2 exhibit low ionization potentials and thus

$$E_2^{'} < E_G + E_C \tag{4.2}$$

This implies that transition as present for E_1 class ions , cannot occur using E_2 class ions, since transitions as 5 are energetically forbidden. The consequence is that no neutralization will occur at the sample surface and thus the ion travels into the insulator in charged state and no impurities (i.e. mobile ions) get mobilized.

Sputter processes during ToF-SIMS depth profiling using both O_2^+ and Cs^+ have been shown to belong to ion bombardment with E_1 class ions. Thus, from these assumptions neutralization of the sputter projectile and mobilization of mobile ions were expected. In literature, mobile ion migration have also been reported for other surface analytical techniques using ion beams for analysis or sputter processes as for instance X-ray photon spectroscopy (XPS) or AES (e.g. [118, 119]). In Ref. [120] the increase of the non-bridging oxygen has been reported to be increased due to Ar^+ bombardment, resulting from hole generation as illustrated in Fig. 4.1(b). The big problem is that, according to the mechanism of McCaughan and collaborators, neutralization processes occur directly during ion bombardment. Thus all measures to handle with surface charges or to neutralize them as listed in Tab. 3.8 are not effective in terms of mobile ion migration.

In Fig. 4.2 the effect of mobile ion migration is illustrated by means of a ToF-SIMS depth profile of a Na implantation in a 100 nm SiO_2 film on Si-substrate (the sample is shown in the second last step of Fig. 3.1). This effect is well known in literature [121]. For reasons of comparison, the simulated Na implantation profile is included (obtained by using SRIM [57]). The depth profile illustrate properly the migration artifact as discussed above: Initially distributed in an Gaussian shape as given by the simulated data, Na is localized entirely at the SiO_2 / Si interface, due to Na migration during sputtering both by using O_2^+ and Cs^+ as the sputter species. This fact classifies both ions to the group of E_1 projectiles [122].

Using the same sample, but without Na implantation, the magnitude of the surface potential was estimated as generated by sputtering. The aim was to deliberately cause peak shifting due to the appearance of positive surface charges originated from sputtering. The Au layer was removed by sputtering, in order to uncover the SiO_2 surface. Subsequently, the surface was exposed to electron flooding for a few seconds (acceleration 20 V). In order to visualize the peak shift effect on the example of the ^{28}Si signal, the following sequence was applied: Acquisition of a static SIMS mass spectrum with $PIDD = 1{\cdot}10^{11}$ cm^{-2} → Deactivation of the electron flood gun → 2 s O_2^+ sputtering → Acquisition of a static SIMS mass spectrum with $PIDD = 1{\cdot}10^{11}$ cm^{-2} (repeated 2 times in order to increase the signal intensity). The result is illustrated in Fig. 4.3, with the spectrum calibrated in accordance to the first scan with activated electron flood gun.

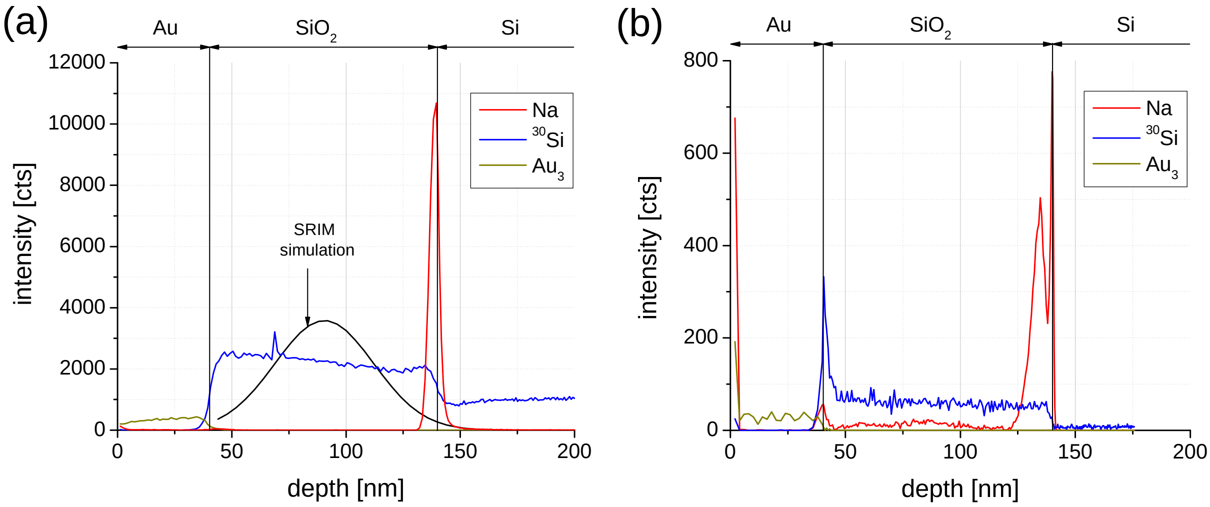

Figure 4.2.: ToF-SIMS depth profile of a Na implant ($\phi_{Na} = 1{\cdot}10^{14}$ cm^{-2}) in 100 nm SiO$_2$ using (a) 1 keV O$_2^+$ or (b) 1 keV Cs$^+$ for sputtering. The signals Au$_3$ and ^{30}Si were added, in order to localize material interfaces. The signal enhancing effect of O$_2^+$ is clearly pronounced.

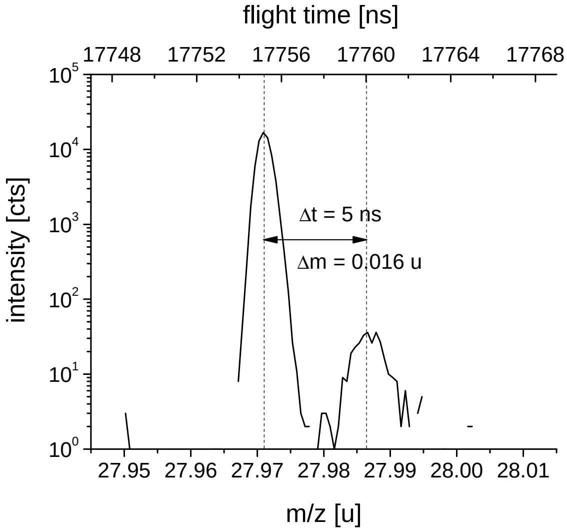

Figure 4.3.: ToF-SIMS mass spectrum acquired in static SIMS mode according to the sequence as described in the text. The larger peak is the ^{28}Si signal at the expected mass. When sample charging occurred, a second smaller signal arose adjacent to the first one, due to the appearance of positive charges at the sample surface caused by the sputter process.

It was found that the ^{28}Si signal shifted towards higher values, when no electron flooding was carried out after sputtering, assignable to the sample charging effect. Although generated with the 3 times higher $PIDD$ the shifted peak appeared magnitudes lower, corresponding to effects as listed in Tab. 3.8. Considering for the larger ^{28}Si peak $m = 27.971$ u and $t = 17755.2$ ns and using eq. (3.7) one can calculate a flight distance of the secondary $^{28}\mathrm{Si}^{+}$ within the ToF analyzer of $L_d = 2.086$ m. Expanding and rearrangement of eq. (3.7) leads to

$$\Delta U_a = \frac{m}{\left(\dfrac{t+\Delta t}{L_d}\right)^2 \cdot 2 \cdot e} - \frac{m}{\left(\dfrac{t}{L_d}\right)^2 \cdot 2 \cdot e} \tag{4.3}$$

with the second term being the defined extraction potential (here $U_a = 2$ kV). Thus, Δt as readable from Fig. 4.3 leads to an alteration of U_a to 1998,87 V. This would mean a decrease of the extraction potential, leading to a deceleration of the secondary ions. The characteristics of the peak shift towards higher masses is in accordance with this, corresponding to an increase in flight time, which in turn corresponds to an lower U_a. However, positive surface charges accounts to an increase in U_a in terms of the extraction of positive secondary ions. The explanation for this is most probably an inherent offset, due to interactions on the charged surface with the incident primary bismuth (Bi) ions, which get retarded and distorted in the surface near region. The starting point of single ion counting in the detector is synchronized with the primary ion pulses. If a retardation occurs, this offset may occur, leading to an apparent increase of the secondary ion flight time. Despite this and due to the superior mass resolution in HCBU mode, one would distinguish between magnitudes of sample charging. This experiment indicated sample charging of some volts during the sputter cycle for ToF-SIMS depth profiling.

In literature, several approaches have been proposed in order to counteract mobile ion migration, with the focus on Na migration:

- Magee et al. described a high energy electron beam irradiating the insulator surface in coincidence with an Ar^{+} analysis beam (using a dynamic SIMS instrument). It has been shown that a 2 keV electron beam is necessary to produce an artifact free SIMS depth profile of a Na implantation in a 500 nm $\mathrm{SiO_2}$ layer on Si substrate [123], with a substantial contribution for charge compensation assumed from secondary electrons, produced by the Ar^{+} beam. Lower electron beam energies did not effectively counteract Na migration. The penetration depth of electrons within $\mathrm{SiO_2}$ has to match the $\mathrm{SiO_2}$ film thickness, in order to avoid Na migration, and no conductive coating was necessary on the insulator [124]. The aim of this approach is to render the $\mathrm{SiO_2}$ conductive via the electron beam. However, slight shifts in the Na implantation profile can not be excluded.

- Distortion free Na depth profiles have been reported for dynamic SIMS, when a 5 keV Cs^+ primary beam was used (beam current: 50 nA) to analyze SiO_2 films on Si [125]. A thin conductive Cs^+ film, as detected via XPS, was thought to be responsible for effective charge neutralization at the SiO_2 surface. However, since ${O_2}^+$ acts superior for signal enhancement of positive secondary ions (see section 3.3.2), the use of this species for sputtering in ToF-SIMS depth profiling is preferred.

4.2. Temperature dependence of mobile ion migration

None of the approaches mentioned in the previous section are practicable with the instrument used in this work. Therefore an alternative approach has been considered, on the one hand in order to clarify whether an artifact caused by mobile ion migration is present in the ToF-SIMS depth profile, and on the other hand to suppress mobile ion migration as much as possible. Temperature controlled depth profiling has been proposed in literature to reduce Na migration [121, 126, 113]. In the following this issue will be discussed in detail, basically driven by two questions:

- Both mobility and diffusivity of ions within a solid substrate have an exponential dependency on temperature (e.g. [40]; eq. (2.17)). Does a reduction of the sample temperature during ToF-SIMS depth profiling cause a sufficient reduction of these transport processes, in order to acquire artifact free depth profiles?
- What type of mechanism is connected with mobile ion migration? Does mobile ions migrate under the influence of an generated electric field immediately throughout the insulating layer to the next interface with a conductive layer or does mobile ion migration occur continuously with the proceeding sputter front?

4.2.1. Mobile ion incorporation into a thin SiO_2 film

Mobile ion migration was encountered when samples, prepared for B-T stress experiments, were depth profiled. Host matrix formulations according to Tab. 3.5 containing 300 ppm MeOTf were attached on thin SiO_2. ToF-SIMS depth profiling at room temperature (RT) using ${O_2}^+$ as the sputter species showed different characteristics for various ions. Corresponding to the increasing ionic radius (Tab. 2.1), the distinctive tailing of the alkali signals towards the SiO_2 bulk decreased gradually ($Li^+ \rightarrow Na^+ \rightarrow K^+$) (Fig. 4.4). Since, the insulating film was initially free of any mobile ions, the tailing for alkali ions is unambiguously caused by mobile ion migration during ToF-SIMS depth profiling. Thus mobile ion incorporation from PMMA into SiO_2 occurred during analysis. For Li^+ and Na^+ distinctive exponential tailing was observed, with major peaks at the adjacent SiO_2 / Si interface. For K^+ comparably small amounts of ions were incorporated, with just a minor peak observable at the next interface. For comparison, Mg^{2+} did not show any significant tailing within SiO_2[1] and no Mg peak at the adjacent interface to to Si substrate. Changing the sputter ion energy did not alter the observed incorporation characteristics as shown in 4.5 for Na. The use of Cs^+ as the sputter species would not avoid mobile ion migration. (Fig. 4.2(b)).

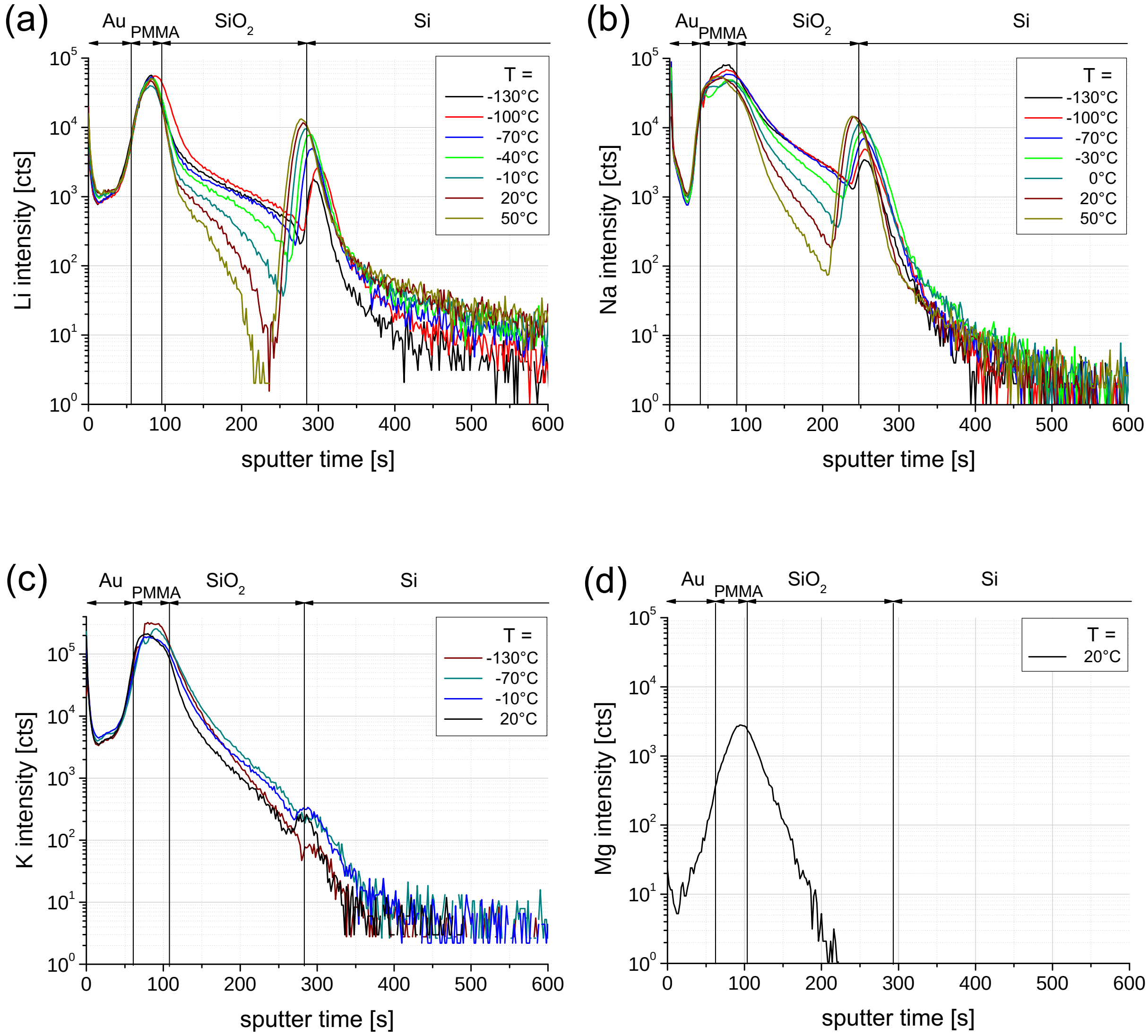

Figure 4.4.: ToF-SIMS depth profiles of samples before B-T stress using different host matrix formulations containing various mobile ions, obtained for a range of sample temperatures from 50 °C down to -130 °C: (a) lithium Li^+ (b) sodium Na^+ (c) potassium K^+ (d) magnesium Mg^{++}. All profiles were normalized on the same, arbitrarily chosen ^{30}Si signal.

---

[1] An additional host matrix formulation containing 300 ppm magnesium triflate ($Mg(OTf)_2$) in acetonitrile was prepared, however exhibiting almost no solubility. This formulation is not included in Tab. 3.5

There are some important features to be considered for RT depth profiles in Fig. 4.4:

(i) The depth resolution is comparably poor, as indicated by the rather shallow incline of the upward and downward slope of the peaks. This is especially true for sputtering in PMMA, which is considered as a soft material in comparison to SiO_2 and Si. This effect is obvious in Fig. 4.4(d), where the whole Mg^{++} dose is located at the PMMA / SiO_2 interface (caused by the poor solubility of $Mg(OTf)_2$ in acetonitrile and the thus arising precipitates in the host matrix formulation. Secondary ion signals, assignable to PMMA (i.e. hydrocarbons) exhibited the same characteristics in terms of depth resolution. The initial part of tailing until the slope of the exponential tailing changes in the log plots of Fig. 4.4(a-c) is therefore also assigned to caused by the depth resolution (Properly observable for Li^+).

(ii) Laterally, a homogeneous intensity was detected for each ion. This confirms a homogeneous distribution of mobile ions within PMMA, at least as long the precursor compound is soluble in the used solvent.

(iii) A distinctive fading of Li and Na was observed in the Si substrate. This is due to the sputtering procedure, where the first few nanometers of Si were converted into SiO_x by means of ${O_2}^+$ bombardment [127, 128]. This means in terms of mobile ion migration the same situation was present as for SiO_2, and the Li^+ and Na^+, were transported towards the Si bulk, resulting in a shallow decay of the signal. Using Cs^+ as the sputter species would avoid his effect as clearly visible in Fig. 4.2(b) due to the absence of the exponential tailing in comparison to the ${O_2}^+$ sputtered profile in Fig. 4.2(a).

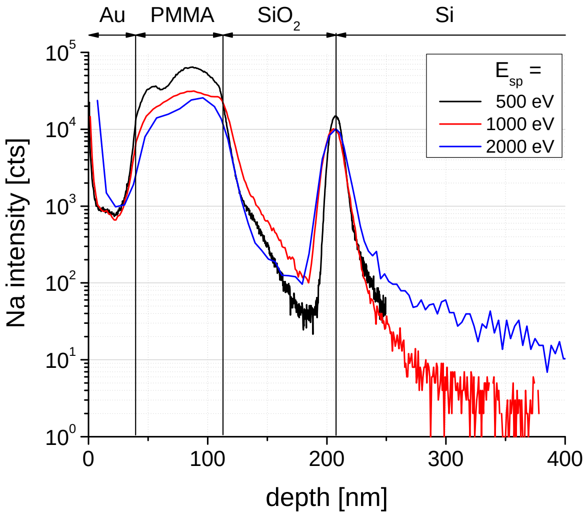

Figure 4.5.: Na migration effect during ToF-SIMS depth profiling using different E_{sp} values for ${O_2}^+$. For reasons of normalization, the x-axis was converted into a depth scale. The positioning of the PMMA / SiO_2 interface was difficult, due to the already mentioned poor depth resolution at this position.

For mobile ions with small ionic radii (Li^+ and Na^+) the amount of ions accumulating at the SiO_2 / Si interface could be remarkably lowered by successively decreasing the sample temperature, although migration was still present. The reason is the reduced diffusivity of the mobile species within SiO_2 according to eq. (2.17). Obviously, due to the larger ionic radius this effect is of minor relevance for K^+ [129], where the characteristics of depth profiles acquired at RT and -130 °C are roughly the same, as illustrated in Fig. 4.4. The proof that mobile ions incorporated during ToF-SIMS depth profiling was done in the following way: After acquiring depth profiles at various sample temperatures, the host matrix was removed from the sample and subsequently Au deposited again. Depth profiling of this altered layer sequence showed no mobile ion signals at all (Fig. 4.6). In summary, the answer for the initial question of whether sample temperature reduction avoids mobile ion migration is: No, total avoidance of mobile ion migration is not possible, barely a reduction of this effect by temperature reduction is feasible.

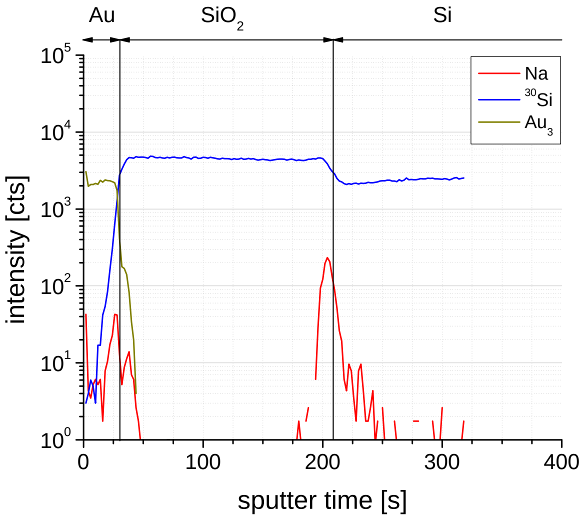

Figure 4.6.: Mobile ion intensity when PMMA was removed from the sample (Here Na was chosen as the illustrated signal, due to the highest abundance among mobile ions). No incorporation was observed, hence the migration effect was proven to arise from sputter ion bombardment during ToF-SIMS depth profiling.

On this point the second crucial question regarding the transport mechanism during mobile ion migration arose. 35 years ago McCaughan et al. [115] suggested an immediate drift of Na^+ to the SiO_2 / Si interface by bombarding the surface with ions of the E_1 class. However, there is also the possibility, that mobile ions drift with the proceeding sputter front. SRIM simulations gave a hint on the projected range of impacting projectiles during the sputter process (Tab. 4.1). The double of these projected ranges coincides with the in-depth range of the altered layer of disturbed sample surface composition as shown in Fig 3.6(a). The topmost monolayer of a SiO_2 film, where the secondary ions during SIMS analysis mainly come from [58], has a thickness of 0.20 - 0.27 nm [130], hence the altered layer due to sputtering has a much larger in-depth expansion for any value of E_{sp}. In order to keep the altered layer due to primary ion impact as shallow as possible, Bi_3^+ was generally used for the experiments, presented in this chapter.

Table 4.1.: Projected range R_p for O_2+ and Cs^+, during bombardment of SiO_2. For reasons of comparison R_p within Si_3N_4 for $E_{sp} = 1$ keV has been added.

Target	E_{sp} [eV]	R_p (O_2^+) [nm]	R_p (Cs^+) [nm]
SiO_2			
	250	1.0 ± 0.6	2.3 ± 0.6
	500	1.4 ± 0.8	2.9 ± 0.7
	1000	2.2 ± 1.3	3.6 ± 0.9
	2000	3.3 ± 2.0	4.6 ± 1.3
Si_3N_4			
	1000	1.4 ± 0.8	2.7 ± 0.7

In order to detect the present mechanism of migration, depth profiling of the same sample as in Fig.4.4(b) was started at RT and then stopped within the insulating layer. After reduction of the temperature to -130 °C, depth profiling was resumed. In Fig. 4.7(a), this measurement is displayed and compared to depth profiles, carried out at constant temperatures. As the temperature dropped, the obtained profile switched from the trend of the RT reference profile to that of the -130 °C reference profile. Hence, this gives evidence for Na migration with the progressive sputter front. Performing this experiment vice versa confirmed this statement (Fig. 4.7(b)).

From these cognitions one can conclude as following: Since the SiO_2 bulk beneath the altered layer remains unaffected by O_2^+ impact, an interface is generated between the altered layer due to sputtering and the SiO_2 bulk. This interface progresses dynamically in accordance to the moving sputter front. As discussed in section 4.1, the O_2^+ sputter process both releases Na^+ from its respective binding partner and generates positive charges. This occurs at the sample surface. As a result during sputtering, Na^+ migrates continuously towards the mentioned dynamic interface. This interface thus is then continuously enriched with Na^+. This statement is in good agreement with studies of Na migration in Si during O_2^+ bombardment, where the sub-surface region of the substrate in the range of a few nm (approx. twice the projected range of impinging O_2^+ ions) was converted into SiO_x by O_2^+ impact [128]. Thus a dynamic SiO_x / Si interface was created during depth profiling. As already mentioned, this effect explains the tailing of the Na peak at the SiO_2 / Si interface towards the Si substrate as observable in Fig. 4.4(a,b).

As it will be presented later in section 5.1.1, the incorporation of Na^+ from a NaOTf doped PMMA host matrix into unaltered SiO_2 is energetically unlikely at RT despite an external voltage of $V_{bias} = 20$ V was

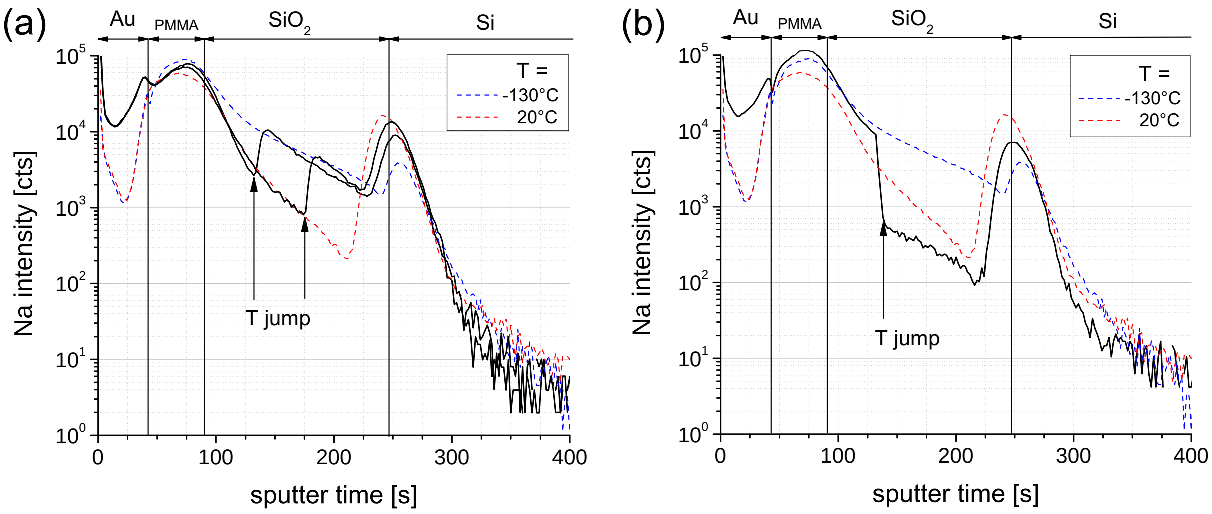

Figure 4.7.: Temperature change during depth profiling of a 100 nm SiO_2 attached by a PMMA host matrix containing 300 ppm NaOTf. (a) Start temperature: 20 °C → temperature jump to -130 °C. The characteristics were checked by performing the temperature change at two different sputter depths. (b) Start temperature: -130 °C → temperature jump to 20 °C.

applied (corresponding to $E = 2$ MV/cm within a 100 nm SiO_2). Accordingly, transition of Na^+ from the altered into the unaltered SiO_2 layer and Na^+ transport therein would not be expected for sample temperatures up to RT as applied in this work.

This mechanism and the reduced diffusivity of mobile ions at low temperatures explains the gradually reduced sloping in Fig. 4.4(a,b). Generally, a mobile ion can only be detected when present in the first monolayer. However when migration occurs this does not happen. The probability of a mobile ion to remain in the first monolayer is higher when drift and diffusivity are decelerated, i.e. at low temperatures. Therefore, a higher mobile ion intensity is expected for lower temperatures during migration through the SiO_2 layer. In agreement to Tab. 2.1, the difference in sloping between various temperatures in 4.4(a-c) is the more pronounced, the smaller the ionic radius of the mobile ion. An exponential tendency is obvious, with minor differences below -70 °C. For K^+ no significant difference in sloping can be recognized anymore.

4.2.2. Mobile ion incorporation into a thin films of SiO_xN_y and Si_3N_4

The cognitions from SiO_2 were compared to thin films of materials containing nitride compounds, in order to investigate the influence of nitrogen (N) on mobile ion incorporation effects during ToF-SIMS depth profiling. According to common standard procedures at Infineon Technologies Austria AG, the films were produced with 400 nm thickness. The host matrix contained 300 ppm NaOTf and 40 nm Au was deposited as usual. The obtained ToF-SIMS depth profiles are compared in Fig. 4.8. It get obvious immediately that an increasing nitride content within the insulator shows lower resistance against Na migration. Compared to the permeable SiO_2 film, the silicon oxynitride (SiO_xN_y) exhibited a remarkable lower penetrating depth of Na^+ within the insulator. Silicon nitride (Si_3N_4) showed a negligible amount of Na^+, penetrated into the insulating film, with barely some counts in intensity fading out with progression of the sputter front. Resembling observations for SiO_xN_y have been reported in literature [131]. For both nitride containing films, negligible accumulation is observed at the insulator / Si interface, assignable to a change of the sample matrix at this position and its consequences to an altered matrix effect. This led to a slightly higher signal intensity compared to respective bulks of the adjacent layers.

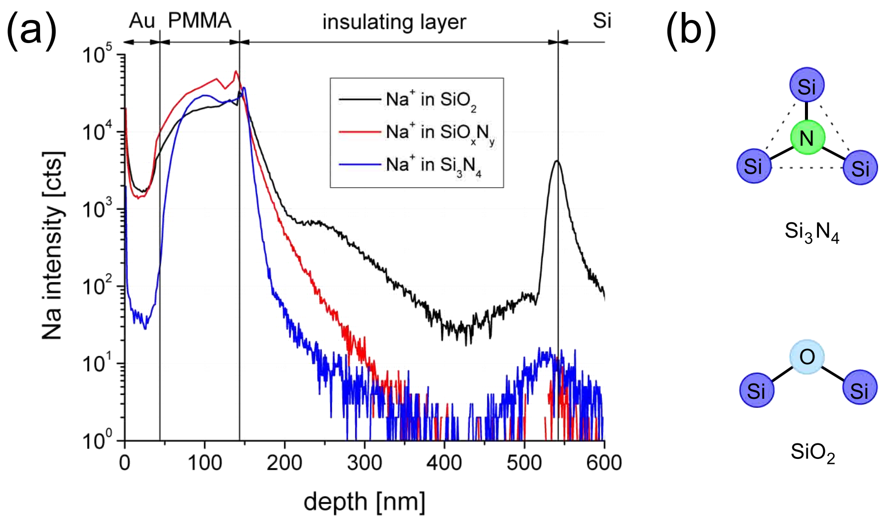

Figure 4.8.: (a) ToF-SIMS depth profiles of samples, prepared for B-T stress containing thin films (400 nm) of either SiO_2, SiO_xN_y or Si_3N_4 (Sputtering with 1 keV $O_+{}^2$). With increasing N content, the susceptibility to Na migration and incorporation is reduced dramatically. Due to normalization, the x-axis has been converted into a depth scale. The profiles were acquired at RT. (b) Molecular structures of Si_3N_4 and SiO_2.

The explanation of the positive effect on Na migration is the increased stiffness, when nitride bondings are introduced into SiO_2 successively. O in the SiO_2 molecule exhibits two covalent bondings to adjacent Si atoms (Fig. 4.8(b), by means of two sp hybrid orbitals) whereas two non-binding orbitals (p_y, p_z) remain, yielding a rather flexible molecule with a Si-O bonding length of 1.61 Å, with degrees of freedom in rotation and vibration for the O atom. The Si_3N_4 molecule in contrast is a rigid stiff assembly of atoms with 3 sp^2 hybrid orbitals making covalent bonds with adjacent Si atoms Fig. 4.8(b), leaving just one non-bridging orbital (p_z). This disables rotation within the molecule and vibration is hindered severely. The Si-N bonding length has been reported with 1.71 Å [132, 133]. The observed effects in Fig. 4.8(a) can be concluded out of the molecular structures. Mobile ions get transported via an interstitial mechanism, thus within SiO_2 vibration frequently opens pathways for these interstitials between the single molecules, making the SiO_2 structure a very permeable one for mobile ion transport. Reduction of the sample temperature, decelerates particle motions within SiO_2 thus reducing the ability for drift and diffusion for mobile ions, with this effect dependent on the ionic radius (Tab. 2.1). This results in a lower migration during ToF-SIMS depth profiling as already shown in Fig. 4.4. In nitride containing materials, this permeability is not the case. The stiff character of the Si_3N_4 molecule impedes interstitial transfer. The associated profiles in Fig. 4.4 did not show a change on temperature variation, which confirms this statement. Besides having outstanding mechanical properties (e.g. stiffness, hardness, young's modulus) [134], its structural properties make Si_3N_4 a very prominent barrier layer for semiconductor devices. On the other hand the resistance against crack propagation is worse than for SiO_2. SiO_xN_y has an improved protection ability against Na migration, however with a better crack resistance than Si_3N_4 [135].

Further investigations on these layers using B-T stress and ToF-SIMS depth profiling are presented and discussed in section 5.3.

4.2.3. Mobile ion incorporation into a thin films of BPSG

A further material, that was examined for Na migration during ToF-SIMS depth profiling is boron phosphosilicate glass (BPSG). For many decades, the use of phosphorus-doped SiO_2 have been known to exhibit a getter effect against contaminations as mobile ions, in order to protect MOSFET devices against V_{th} shifts [136, 137]. Hence, the use of phosphosilicate glass (PSG) has been widely used in device fabrication. There are different ways to produce a PSG layer, resulting in variations of properties as mobile ion getter ability or film integrity [138]. Addition of B to PSG has advantages in terms of flow properties for a proper planarization of the deposited getter layer.

Fig. 4.9 shows the temperature dependence of ToF-SIMS depth profiling of a sample comprising a BPSG layer, attached by a PMMA host matrix (c_{NaOTf} = 300 ppm). The specimen consisted of the sequence: 910 nm BPSG / 400 nm SiO_xN_y / Si substrate. Hence, Na transition at the BPSG / SiO_xN_y interface could be examined. A distinctive variation in the Na migration behavior on temperature was detected for the BPSG layer.

Up to -100 °C hardly any difference can be seen in the profiles. However, according to ToF-SIMS depth profiles, the Na budget as provided in PMMA, was found after ~30 nm sputtering in BPSG roughly in the form of a Gaussian peak. Different to Na migration in SiO_2 using 2 keV O_2^+ for sputtering (Fig. 4.5), a comparable low intensity of Na^+ was detected in PMMA. Since in Fig. 4.9 an additional upwards slope can be observed in PMMA, it is conceivable that the provided Na^+ was transferred by means of

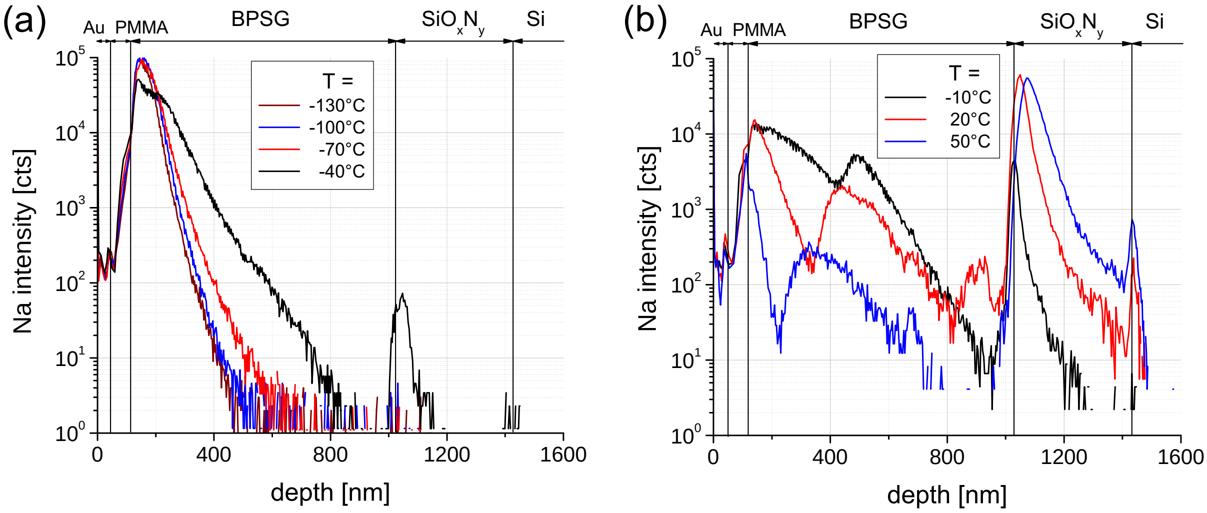

Figure 4.9.: Na migration into BPSG during ToF-SIMS depth profiling. In order to avoid confusion by too many profiles in one plot, there are two depth profiles including the temperature ranges (a) -130 °C - -40 °C and (b) -10 °C - 50 °C. 2 keV O_2^+ was used as sputter species, in order to achieve a reasonable erosion rate for the present sample. The intensities in the profiles were normalized with respect to an arbitrarily chosen ^{30}Si signal.

Na migration into the underlying BPSG in a larger amount than for SiO_2. Within BPSG the getter effect seems to avoid further Na transport towards the BPSG bulk. With the onset at approx. -70 °C, an explicit Na migration effect can be observed in Fig. 4.9. With increasing sample temperature Na^+ gradually accumulated at the BPSG / SiO_xN_y interface.

In Fig. 4.8, a ToF-SIMS depth profile is included, that indicated a minor effect Na migration at RT in SiO_xN_y. This characteristic can also be observed in Fig. 4.9, with Na transition from BPSG into SiO_xN_y. Note that the depth resolution in the two mentioned figures is different. This is caused on the one hand due to the difference in E_{sp} during sputtering (1 keV vs. 2 keV). However, one has to consider a decrease in depth resolution due to sample roughening after a long period of sputtering until the SiO_xN_y layer is reached in a depth of > 1 μm. At temperatures ≥ 20 °C, a second accumulation of Na^+ at the SiO_xN_y / Si interface can be seen, where finally the Na migration stopped and no further transition was possible.

Regrading the bulk of the BPSG layer, regions of gettered Na^+ are visible in Fig. 4.9(b). Considering the logarithmic scale of the y-axis, these Na^+ accumulations were however of low magnitude in comparison to the accumulation at the interface to SiO_xN_y. Additionally, the position of the gettered Na^+ shifted when the sample temperature varied. Obviously, BPSG is capable to getter some Na^+ when migrating with the sputter front during ToF-SIMS depth profiling. A reason for the appearance of Na^+ gettered at these certain positions in the BPSG bulk can not be concluded based on these measurements.

It can be assumed that the deposited BPSG layer has a poor getter ability for Na^+ provided in a quantity of $c_{NaOTf} = 300$ ppm. Further experiments with this sample type using B-T stress the assessment of the examined BPSG and a respective discussion can be found in section 5.4.

4.2.4. Migration effects in Na implanted SiO_2

Apart from incorporation mobile ion from the host matrix, the migration effect during ToF-SIMS depth profiling has consequences on implantation profiles as well. In order to investigate this, Na implanted SiO_2 films, deposited on Si and covered with 40 nm Au, were assigned to temperature varied ToF-SIMS depth profiling. The implantation conditions were: $\phi_{Na} = 1{\cdot}10^{14}$ cm^{-2}[1], energy: 25 keV, angle of incidence: 7°. Fig. 4.10 shows the typically obtained characteristics for Na implantations in 100, 200 and 400 nm SiO_2. The artifact, obtained at room temperature has already been illustrated in Fig. 4.2, with the entire implanted Na found at the SiO_2 / Si interface due to migration. This effect is independent of the insulating film thickness.

As temperature decreased (temperature steps: 30 °C), Na could be successively detected also within the SiO_2 layer. Note that the chronology of profile acquisition was arbitrary without influencing the result. During depth profiling of Na implantations in 200 and 400 nm SiO_2 two significant peaks arose:

(i) The maximum of the first peak with $R_{p,1}$ (R_p stands for projected range) corresponded to the simulated implantation depth. For the present implantation conditions SRIM simulation gave the following R_p (thus the maximum of Na concentration according to the implantation conditions) for dry and wet SiO_2 with subsequent addition of the 40 nm Au layer: dry SiO_2: $R_p \pm \Delta R_p = 90.33 \pm 21.15$ nm, wet SiO_2: $R_p \pm \Delta R_p = 93.35 \pm 21.97$ nm. Note that ΔR_p gives the standard deviation of a Gaussian shaped distribution.

(ii) The second peak with projected range $R_{p,2}$ however shifted with increasing temperature towards the SiO_2 / Si interface. No further shift could be observed when $R_{p,2} \approx 2.1 \times R_{p,1}$ was reached. The pronounced tailing and the low intensity for the $R_{p,2}$ peak made an accurate determination of $R_{p,2}$ at higher temperatures difficult. The resulting characteristics in the ToF-SIMS depth profiles resemble those reported in literature [126] (obtained by quadrupole SIMS).

For 100 nm SiO_2 the layer thickness approximately coincided with $R_{p,2}$, thus $R_{p,1}$ and $R_{p,2}$ characteristics could not be observed. Here the majority of Na was detected at the SiO_2 / Si interface even at low temperatures (Fig. 4.10(a)). Thus, for the implantation conditions chosen in this work the thickness of the insulating layer had to be at least 200 nm in order to exhibit a proper $R_{p,1}$ and $R_{p,2}$ characteristic.

---

[1] The unit for mobile ion dose is given in [cm^{-2}] representing [at/cm^2] and [$ions/^2$], respectively.

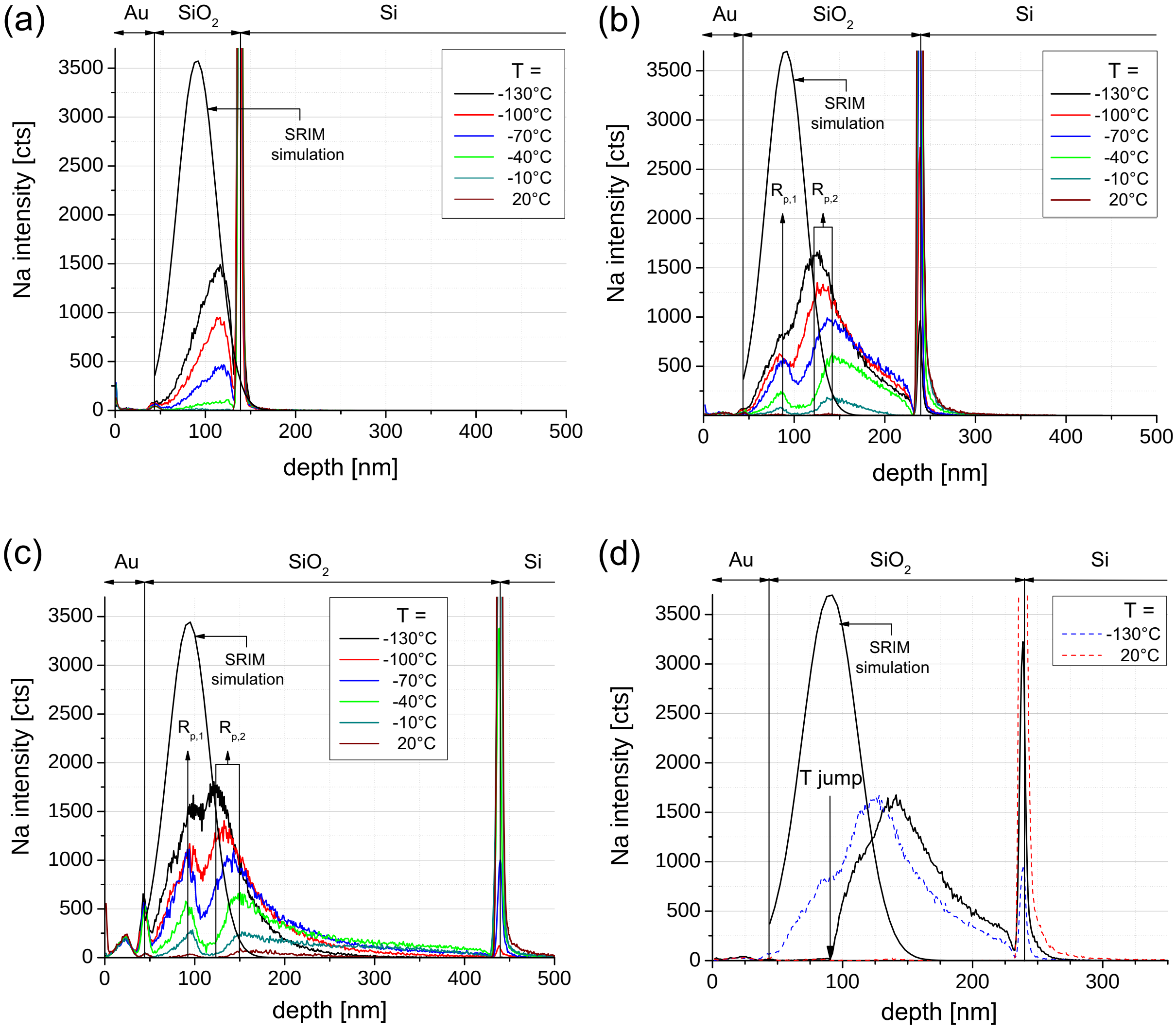

Figure 4.10.: Depth profiles of Na implantations in (a) 100 nm (b) 200 nm and (c) 300 nm SiO_2, deposited on Si. Corresponding to Fig. 4.4(b), the migration effect during ToF-SIMS depth profiling is clearly suppressed at reduced temperatures, revealing $R_{p,1}$, $R_{p,2}$ characteristics. In order to compare to an artifact free Gaussian shaped Na implantation, the SRIM simulated data (according to the implantation conditions) were included. (d) Temperature change during depth profiling of a 200 nm SiO_2 layer, confirmed the proposed migration mechanism with the proceeding sputter front.

In order to discuss the observed profiles, some thoughts on defect formation during implantation in SiO_2 should be considered. Especially for electropositive implants (elecronegativity < 2.5) depletion of oxygen by the implanted species has been found with the consequence of leaving Si-Si bonds [139]. The stoichiometry locally changed from SiO_2 to $SiO_{x<2}$. These silicon clusters have been reported beyond the projected range of the implanted species $R_p \pm \Delta R_p$ as well, accompanied by the occurrence of negative bulk charges [140]. At the SiO_2 / Si there is the same situation, with instantaneous oxygen depletion and silicon enrichment within a few nanometers. The getter ability of this interface is unambiguously demonstrated by the migration artifact (Fig. 4.2). In other materials a relative maximum of the implanted species beyond R_p has been reported by means of SIMS depth profiling, which could be explained by the so-called $transR_p$ effect [141, 142].

The appearance of $R_{p,2}$in the depth profiles of Fig. 4.10(b,c) may be attributed to the above discussed effects. During implantation of Na in SiO_2, clustering of Si as well as the appearance of negative bulk charges may form getter centers in SiO_2 beyond $R_{p,1}$. The driving force for Na transport in the form of migration is the electrical field within SiO_2, which arises during depth profiling as by sputter ion bombardment (see section 4.1). The appearance of $R_{p,2}$ can now be explained by taking into account the additional getter centers. Consequently, temperature influences the position of $R_{p,2}$ and hence its shift with respect to $R_{p,1}$. However, obviously corresponding to the range of Si clustering beyond $R_{p,1}$ there is a maximum possible spatial shift length (until a depth of 140 ± 2 nm; see Fig. 4.10(b,c)). Note also in this graph the difference in the tailing characteristic of $R_{p,2}$, which is less pronounced at low temperatures. This again is in agreement with the decelerated Na migration at reduced temperatures as mentioned in section 4.2.1 concerning mobile ion incorporation during ToF-SIMS depth profiling. In this context it is evident, by comparing $R_{p,1}$ with the simulated Na distribution, that the $R_{p,1}$ peak is the remainder of the respective undistorted, hence artifact free, Gaussian Na distribution with projected range R_p. Estimating the integrated intensity, i.e. the area of the $R_{p,1}$ peak in Fig. 4.10(b,c), a higher percentage of Na remaining at $R_{p,1}$ can be observed at low temperatures. This can be attributed to the suppressed Na migration.

Fig. 4.10(d) shows the depth profile of a Na implantation in 200 nm SiO_2 with the initial temperature at RT and a subsequent decrease to -130 °C at the position of the simulated R_p. After the temperature jump the Na distribution approached the trend for the profile detected at constant -130 °C, which is in agreement to the profiles in Fig. 4.7. This supports the mentioned mechanism of Na migration throughout SiO_2, i.e. along with the sputter front. However, as for depth profiles at higher temperature, the above mentioned maximum shift length of $R_{p,2}$ could be observed in this profile. That means the $R_{p,2}$ shift is more pronounced than in a profile acquired at constant -130 °C, which is obviously caused by the initial RT sputter process.

4.3. Approach for the artifact free reconstruction of Na profiles

The findings and cognitions in the previous section initialized contemplations on a removal of the migration artifact by means of mathematical post-treatment of the obtained data. Thorough examination of the profiles in Fig. 4.10(b,c) led to the fact, that no distortion of the Gaussian shaped Na implantation profile, as simulated using the SRIM software, should occur, when the sample temperature would be at 0 K, i.e the absolute zero point for temperature. According to definition, the entropy of a system is zero at 0 K and thus all particle involved in a system (here SiO_2 as the sample matrix and Na^+ as the migrating species) exhibits minimal motion. Vibration and rotation within SiO_2 does not occur in an extent, necessary to open path for Na^+ to get transported in an interstitial mechanism. Additionally, translation of Na^+ in any direction is minimal. At 0 K the processes drift and diffusivity are therefore not possible.

Fitting the $R_{p,2}$ peak by a Gaussian distribution and extrapolation towards $T = 0$ K

As it is of course not possible to decrease the sample temperature during ToF-SIMS depth profiling to 0 K, the profiles, obtained for different temperatures, were assessed on their affinity to a Gaussian shaped distribution (compare to the simulated profiles in Fig. 4.10(b,c)):

$$y = y_0 + \frac{Q}{\sqrt{2 \cdot \pi \cdot \sigma^2}} \cdot \exp(-\frac{(x-\mu)^2}{2 \cdot \sigma^2}) \tag{4.4}$$

with y_0 the baseline offset of the Gaussian distribution (taken as 0) and Q the area under the curve. μ denotes the mean of the distribution and σ the standard deviation with respect to μ.

Taking into account the $R_{p,2}$ peak from the depth profiles in Fig. 4.10(b,c), the relation to a Gaussian shape is obvious, when one keeps in mind that the slope towards the SiO_2 / Si interface is affected by the Na migration artifact. The $R_{p,2}$ peak approaches the $R_{p,1}$ peak by decreasing temperature with $R_{p,1}$ remaining at the same position for any sample temperature. Corresponding to the initial contemplation, at 0 K, where no Na migration occurs anymore, both peaks finally merge to a Gaussian distribution at the position $R_{p,1}$. Considering the approach of $R_{p,2}$ towards $R_{p,1}$, the parameters describing the Gaussian shape of the $R_{p,2}$ peak extrapolated to 0 K should lead to an artifact free Na implantation profile with the maximum at position $R_{p,1}$. To achieve this the following procedure was applied:

The front slope of the $R_{p,2}$ peak towards the PMMA / SiO_2 interface did not exhibit an artifact due to Na migration until $R_{p,2}$ is reached. Thus a Gaussian profile could be iteratively fitted into this peak using a data analysis software package (OriginPro 7.5G SR6, OriginLab Corporation, USA). The fitted distributions for each temperature are shown in Fig. 4.11 at the example of the Na implantation in 200 nm SiO_2.

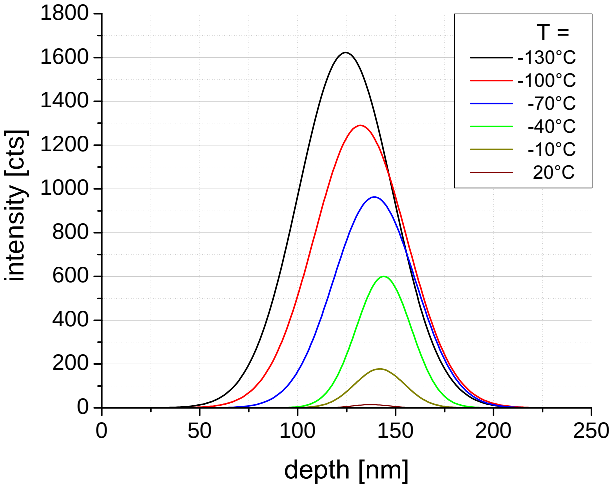

Figure 4.11.: $R_{p,2}$, iteratively fitted by a Gaussian distribution by taking $R_{p,2} = \mu$ and considering the slope towards the PMMA / SiO_2 interface as not affected by any artifacts from ToF-SIMS depth profiling.

Out of the fitted data the quantities describing the Gaussian shape could be extracted: (i) $R_{p,2}$, the maximum of the Gaussian fit (ii) $Q_{R_{p,2}}$, the area of the fitted $R_{p,2}$ peak. (iii) σ was accessible from the fitted data. However, especially at higher temperatures, the accuracy of σ was very poor due to the low intensity of the fitted peak. The maximum peak height y_c represented a more precise value, that is directly related to σ via

$$\sigma = \frac{Q_{R_{p,2}}}{(y_c - y_0) \cdot \sqrt{2 \cdot \pi}} \tag{4.5}$$

y_c is given by the maximum intensity of the Gaussian fit at position $R_{p,2}$ in Fig. 4.11.

Obtained from depth profiles, acquired at different temperatures, these quantities were plotted versus temperature and extrapolated to 0 K (Fig. 4.12). The extrapolated values were inserted as the necessary parameters in eq. (4.4): $R_{p,2} \rightarrow \mu$; $\sigma(y_c) \rightarrow \sigma$; $Q_{R_{p,2}} \rightarrow Q$.

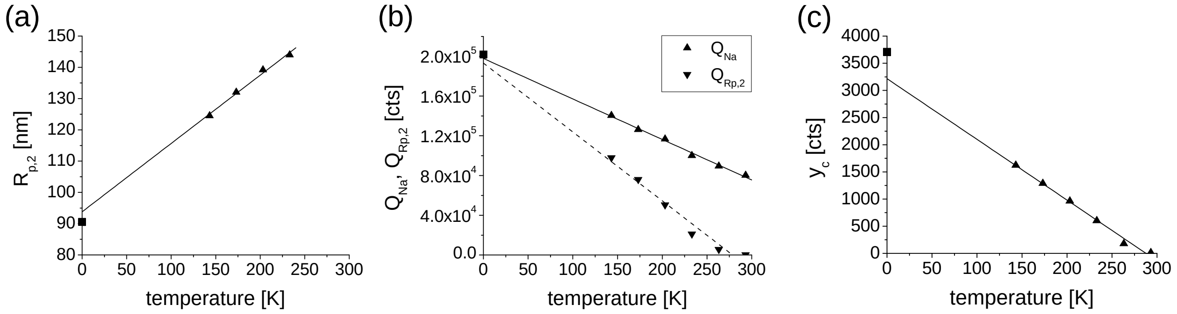

Figure 4.12.: Extrapolation of parameters for the description of a Gaussian distribution. The data were obtained from temperature varied ToF-SIMS depth profiling (Fig. 4.10(b,c)), showing the temperature dependence of (a) $R_{p,2}$; (b) $Q_{R_{p,2}}$, Q_{Na}; (c) y_c. For reasons of comparison, SRIM simulated data has been added. Note that the SRIM data was converted from concentration into intensity using the appropriate $RSF_{Na,M}$, extrapolated to 0 K.

Temperature dependence of $RSF_{Na,M}$

A subject to be discussed in the course of this section is the temperature dependence of the RSF value of Na in SiO_2. Due to the different degree of the migration effect dependent on temperature, there there is a different amount of Na migrated to and accumulated at the SiO_2 / Si interface (Fig. 4.10(b,c)), where the matrix gradually changes to a Si lattice. Thus a different matrix effect occurs at this position in comparison to the SiO_2 bulk, and the detected intensity decreased with increasing amount of Na at the interface, thus at higher sample temperatures. As discussed in section 3.3.5, $RSF_{Na,M}$ relates the detected Na intensity (here termed by Q_{Na}) to the detected ^{30}Si intensity, both integrated over the SiO_2 layer. If there is a change in Q_{Na} due to matrix effects, it is justified that the resulting $RSF_{Na,M}$ according to eq. (3.14) changes with temperature. This relation is plotted in Fig. 4.13.

By comparison with Fig. 4.10(b,c), the exponential fit is justified by a gradual decrease of Na accumulated at the interface with reduced temperature, until at very low temperatures, the change in RSF becomes negligible. Extrapolation to 0 K results in (incl. standard error of the fitting procedure and the coefficient of determination R^2 from the exponential fits as measure of their accuracy): For Na implantation in 200 nm SiO_2: $RSF_{Na,M} = 1.21 \cdot 10^{21} \pm 0.33 \cdot 10^{21}$ cm^{-3} ($R^2 = 0.9958$). For Na implantation in 200 nm SiO_2: $RSF_{Na,M} = 1.25 \cdot 10^{21} \pm 0.18 \cdot 10^{21}$ cm^{-3} ($R^2 = 0.9871$). Using these values, the y-axis of SRIM simulated profiles could be converted from concentration into intensity.

ToF-SIMS depth profile at $T = 0$ K

Apart from using $Q_{R_{p,2}}$, there is an alternative value for representing Q in eq. (4.4): Observable in Fig. 4.2 there is no transition of Na^+ from SiO_2 into Si. Hence, the implanted Na dose ϕ_{Na} has to be constant within the SiO_2 layer, in which the respective cumulated Na intensity Q_{Na} has to be detected. The

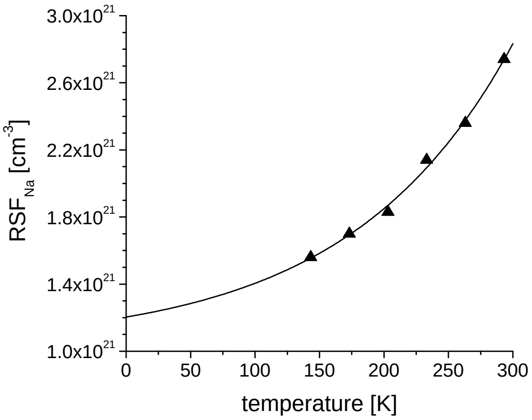

Figure 4.13.: RSF factor for Na in SiO_2 as a function of temperature calculated using the ^{30}Si signal as reference matrix signal. The data was acquired using a Na implantation in 200 nm SiO_2. The dataset was fit by an exponential function of the form $y = T_1 \cdot exp(-x/T) + y_0$. Therein, T_1 denotes a pre-exponential factor and y_0 the general offset of the fitted function to the x-axis. $RSF_{Na,M}$ at 0 K is obtained by $T_1 + y_0$.

variation of the matrix effect at the SiO_2 / Si interface is mentioned above. Due to this effect and the increased Na migration at higher temperatures Q_{Na} varies with temperature and could be extrapolated towards 0 K, in order to cancel out the changed matrix effect at the interface. The extrapolation is shown in Fig. 4.12(b) in order to compare the result to the extrapolation of $Q_{R_{p,2}}$. The lower the temperature, the lower the effect of Na migration, thus the more Na could be detected in the $R_{p,2}$ peak until $Q_{R_{p,2}}$ would match Q_{Na} at 0 K. At higher temperatures ($T >$ -10 °C), however, a drawback is the pronounced tailing by the Na migration effect, which made the fitting procedure less accessible. This is avoided by using Q_{Na}, describing a constant value for ϕ_{Na} for each temperature. Thus the extrapolated Q_{Na} was preferred for representing Q in eq. (4.4).

Tab. 4.2 summarizes all derived parameter describing the Gaussian distribution at 0 K, in order to provide a comparison between the extrapolated data to the simulated data, data, showing the good agreement of both distributions by means of a percental deviation both data sets (referred on simulated data). As theoretically expected, without any contribution of Na migration the peak height in Fig. 4.11 would reach its maximum value at R_p, corresponding to the simulated y_c. Fig. 4.14 compares the extrapolated Gaussian distribution of a hypothetical ToF-SIMS depth profile, obtained at 0 K, with the simulated distribution. The y-scale of the extrapolated data has been converted from an intensity scale into a concentration scale using the respective $RSF_{Na,M}$ value, extrapolated to 0 K. Note that the deviations in this comparison originated not only from the here described approach of data treatment. SRIM simulations contain deviations as well, since this Monte Carlo based approach does not include electrical effects between particles in the collision cascade. For Na implantation in 100 nmSiO_2 film the here presented approach could not be properly applied. The reason is that, as already mentioned in this section, the respective depth profile did not exhibit a similar $R_{p,1}$, $R_{p,2}$ characteristics for the chosen implantation conditions.

Table 4.2.: Summary of parameters, describing the Gaussian distribution of implanted Na in SiO_2. Experimental values, extrapolated to 0 K by linear regression, are compared to respective SRIM simulated values. The extrapolated values are given with the respective standard errors from linear regression. The deviation of extrapolation from simulation is quantified by the difference in %. As a measure of accuracy of the extrapolation, R^2 values are inluded in parenthesis.

SiO_2 thickness	Parameter	Extrapolated value	Simulated value	Difference [%]
200 nm	$R_{p,2}$	93.82 ± 2.88 (0.9905)	90.49	3.68
	Q_{Na}	197873 ± 3707 (0.9935)	201289	1.70
	$Q_{R_{p,2}}$	193216 ± 14636 (0.9657)	201289	4.01
	y_c	3217 ± 111 (0.9921)	3705	13.17
400 nm	$R_{p,2}$	85.08 ± 3.18 (0.9924)	93.47	8.98
	Q_{Na}	233378 ± 12326 (0.9636)	200219	16.56
	$Q_{R_{p,2}}$	198271 ± 15467 (0.9632)	200219	0.97
	y_c	3260 ± 116 (0.9915)	3450	5.51

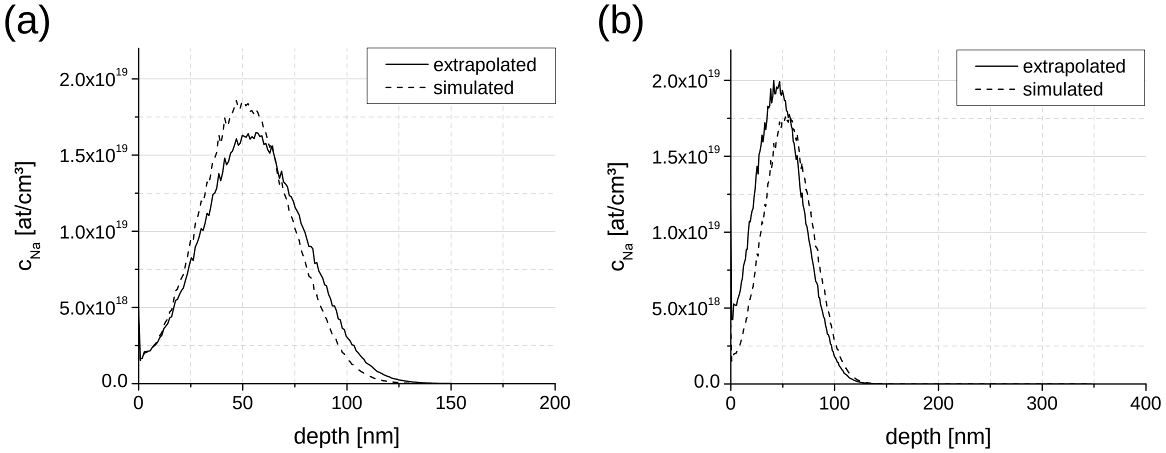

Figure 4.14.: Comparison between the hypothetical Na distribution at 0K sample temperature, as obtained by extrapolation, and the distribution as received from SRIM simulation. The 40nm Au layer, necessary for ToF-SIMS depth profiling, has been subtracted in this graph. The extrapolated data intensity has been converted into concentration values. (a) 200 nm SiO_2 and (b) 400 nm SiO_2.

Chapter 5

Mobile ion incorporation and transport in insulating materials

The behavior of mobile ions in a sample setup as presented at the beginning of chapter 3 (Fig. 3.1) under the influence of B-T stress is the subject of this chapter. This includes the investigation of response signals during B-T stress as well as the subsequent physical analysis using ToF-SIMS. The methodology is presented and discussed in chapter 3. Basically, PMMA was used as the host matrix for MeOTf, added in a defined amount (Tab. 3.5). Experiments were carried out using samples comprising insulating films on conductive Si-substrates, with the emphasis on thin SiO_2 films. The dependence of incorporation and transport behavior on parameters as bias voltage V_{bias}, Temperature T and the mobile ion dose ϕ_{Na} (for Na^+) provided in the host matrix were investigated for Na^+ as the mobile ion. However, results for other insulating materials, relevant for the semiconductor industry with respect to mobile ion transport, are also presented and related to barrier properties prohibiting mobile ion transport. Based on the properties of SiO_2 during B-T stress, a qualitative assessment of the potentiostatic data provided parameters describing mobile ion transport in the chosen sample setup, based on physico-chemical models.

Since conductive paths or possible leakage currents on the sample edges would prevent the application of V_{bias} or severely disturb the measurement, each sample was checked on resistivity. The samples that did not pass this test were discarded. Prior to any B-T stress experiments, the capacitance of the insulating material was measured by means of impedance spectroscopy, in order to proof the properties of the sample setup as a plate capacitor structure. Tab. 5.1 lists capacitances C for samples passing the resistivity check, with the defined parameters. The permittivity ϵ_r of the material was calculated according to

$$\epsilon_r = \frac{d \cdot C}{\epsilon_0 \cdot A} \tag{5.1}$$

A is the area of the Au electrode as illustrated in Fig. 3.1 (0.8×0.8 cm^2) and d the material film thickness deposited on Si. ϵ_0 is the vacuum permittivity. If available, a comparison to literature values is listed in Tab. 5.1.

Table 5.1.: Capacitances of insulating material films, obtained by impedance spectroscopy.

Material	Layer thickness [nm]	Measured capacity [nF]	Permittivity (Calculated)	Permittivity (Ref. [143])
	100	22.56	3.98	3.9
SiO_2	200	18.84	4.16	3.9
	400	5.54	3.91	3.9
Si_3N_4	400	10.32	7.24	7.5
SiO_xN_y	400	7.55	5.30	5.1
BPSG	910	3.27	5.25	N/A

5.1. Investigations of thin SiO_2 films

A typical SMU response signal on B-T stress applied on a thin SiO_2 films has already been illustrated in Fig. 3.5 with a considerably higher response current than expected for sole electrical capacitor charging. In the first period (~3000 s) the time dependence of this response signal described an exponential decay resembling to capacitor charge-up characteristics (Fig. 5.1). Subsequently a more linear decrease was detected. Already the first 600 s of the SMU response signal contains all information relevant for the processes appearing during B-T stress. Therefore, B-T stress was basically restricted to 600 s application time.

Note that large deviations between identical samples produced at different times have occurred (up to a factor of 5). This can have several reasons

- Differences in the exact viscosity of the host matrix formulation could have effects on the host matrix thickness and surface roughness.
- The spin coating process was not a completely reproducible during sample production. The exact moment for attachment of the host matrix formulation with respect to the start point of sample spinning could not be controlled exactly. It took 5 seconds acceleration time until the spinning velocity achieved its maximal value of 3000 rps. During this time the host matrix formulation was attached and variations of 1 - 2 s could have an influence of the condition of the PMMA film. Additionally, variations in the host matrix thickness may have occurred. For formulations containing 2 wt% PMMA (Tab. 3.5), a range of ~65 - 115 nm was measured by means of ellipsometry.

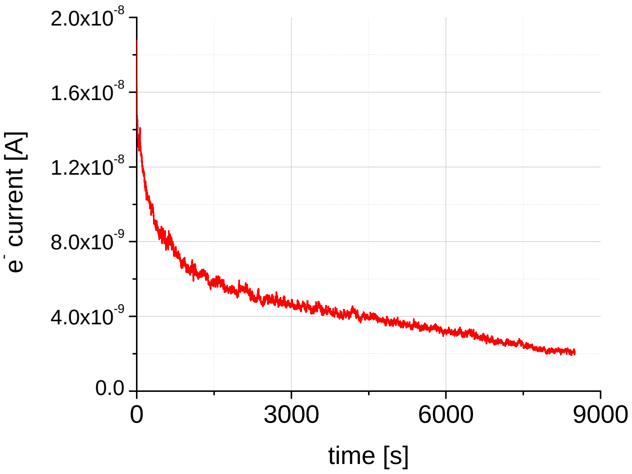

Figure 5.1.: SMU response current for a sample with a thin PMMA host matrix layer, containing a 300 ppm NaOTf, on a 100 nm SiO_2 film, stressed with V_{bias} = 20 V at T = 150 °C.

As indicated in Fig. 3.5, only a minor part of the response current arises from capacitor charging, i.e. a second contributor is superimposed. ToF-SIMS analysis allowed unambiguous identification of the species, possibly incorporated from the host matrix into the underlying SiO_2 film. Analysis of a B-T stressed sample is given in Fig. 5.2. The investigated sample had the following features, taken as standard sample for investigations as further presented: ~70 - 100 nm PMMA (containing 300 ppm NaOTf) attached on a 100 nm SiO_2 film, which was thermally grown on Si. B-T stressing was carried out again using V_{bias} = 20 V (resulting in an electric field of E = 2 MV/cm, i.e. below the breakdown voltage value of a SiO_2 film of in this thickness range) and T = 150 °C.

The ToF-SIMS depth profiles clearly indicated Na^+ accumulation at the SiO_2 / Si interface, with the accumulated amount dependent on the chosen B-T stress application time. In order to analyze the depth profiles on Na migration, profiles were acquired both at RT and at -130 °C. Subtracting the amount of Na^+, that migrated into SiO_2 from the interface with Au (originating from Na^+ traces due to Au deposition), no difference can be seen between Fig. 3.5(a) and (b). This confirms the fact, that Na^+ was really transported to the SiO_2 / Si interface due to B-T stress and the profiles were not affected by Na migration due to the sputter process during ToF-SIMS depth profiling with $O_2{}^+$.

These evaluation allow the following conclusions:

(i) Na^+, provided by the compound NaOTf in the PMMA host matrix, was unambiguously incorporated into SiO_2 by B-T stress and accumulated at the interface to Si. The driving force for this process is the electrochemical potential $\tilde{\mu}$ as discussed in section 2.4 (eq. (2.18)). The chemical potential gradient is governed by the difference in the Na concentration in PMMA and SiO_2. Since the amount of Na in SiO_2

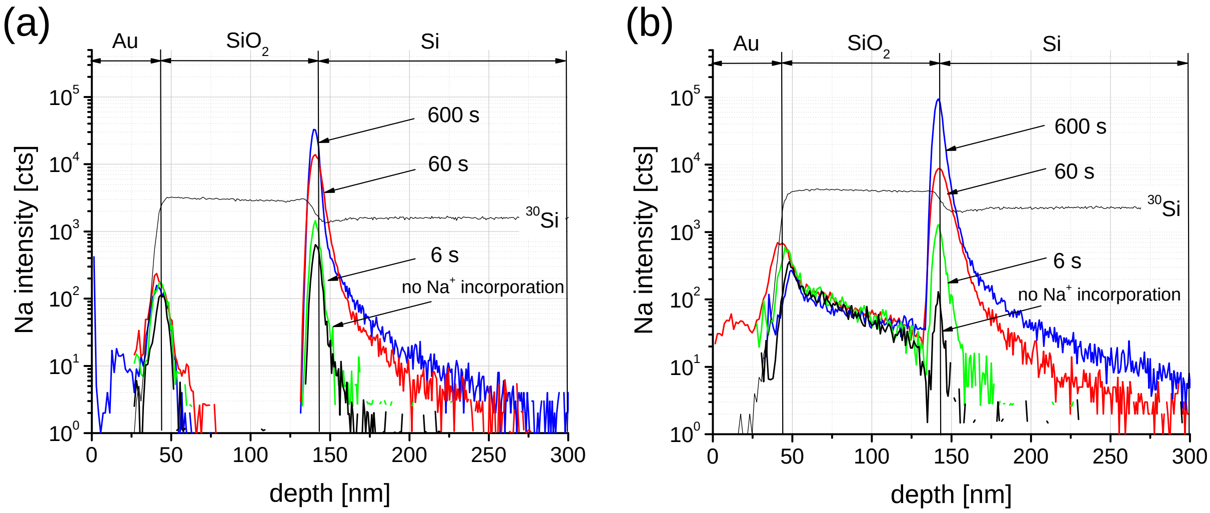

Figure 5.2.: ToF-SIMS depth profiles (sputtering with 1 keV $O_2{}^+$) of a B-T stressed sample clearly indicate Na^+ incorporation during the stressing procedure. B-T stress duration was varied: 6 s, 60 s, 600 s. Comparison to a sample without B-T stress is shown within the depth profiles. (a) Depth profiles obtained at RT. (b) Depth profiles obtained at -130 °C.

is negligible the approximation $\Delta c = c_{Na^+,calc}$ (Tab. 3.5) is valid and the electrical potential gradient is governed by the applied V_{bias} (i.e. $\equiv \phi$ from eq. (2.18)). The quantitative accumulation in Fig. 5.2 indicates, that the electrical term (i.e. drift) dominates the electrochemical potential. Therefore, sample resistivity can be approximated by Ohm's law (eq. (2.22)). The incorporation of Na^+ at the PMMA / SiO_2 interface is in general a Na^+ exchange flux at this position with a negligible back transition into PMMA.

(ii) Within the insulator charge accumulation is not possible, as the system would consequently charge up. An anionic counterpart has to be present for Na^+, in order to fulfill charge neutrality. This means that at each position x, according to the depth scale in Fig. 5.2, mass continuity for Na^+ is assumed; when one Na^+ arrives at x one Na^+ gets transported further into the sample with respect to $\nabla\widetilde{\mu}$.

(iii) The claim for charge neutrality within SiO_2 is also valid for the SiO_2 / Si interface. As given in Fig. 5.2 no incorporation of Na^+ is possible into Si. The tailing of the accumulated peak is due to Na migration during $O_2{}^+$ sputtering (see section 4.2.1). Since it is unlikely that electrons transit the SiO_2 / Si for neutralization, the appearance of a charge double layer is assumed with one Na^+ having one electron as mirror charge at the interface. Therefore, the amount of Na^+ arriving at the interface in a stoichiometric relation to electrons accumulating at the Si-faced side of the interface. The SMU detects an electronic current I, which thus represents the ionic Na^+ current through the interface. In graphs the y-scale is therefore consequently labeled with I with units [A]. Integration of the response signal during B-T stress over time results thus in the cumulated Na^+ charge arriving and accumulating at the interface (giving transient charge-time (Q-t) plots, Fig. 5.3(a)). Consideration of the elemental charge (for Na^+ $z = 1$) and normalization to 1 cm^2 by

$$\phi_{Na^+,DC} = \frac{\int I \cdot \mathrm{d}t}{z \cdot e \cdot A} \tag{5.2}$$

gives the Na^+ dose, incorporated by means of potentiostatic B-T stress and accumulated at the interface at time t. The detected electronic current hence directly relates to Na^+ (Fig. 5.3(b)). Since Na^+ was provided as NaOTf, the anionic charge in PMMA is carried by the triflate anion, which in turn have to be neutralized by positive mirror charges. This is assumed to appear at the Au / PMMA interface.

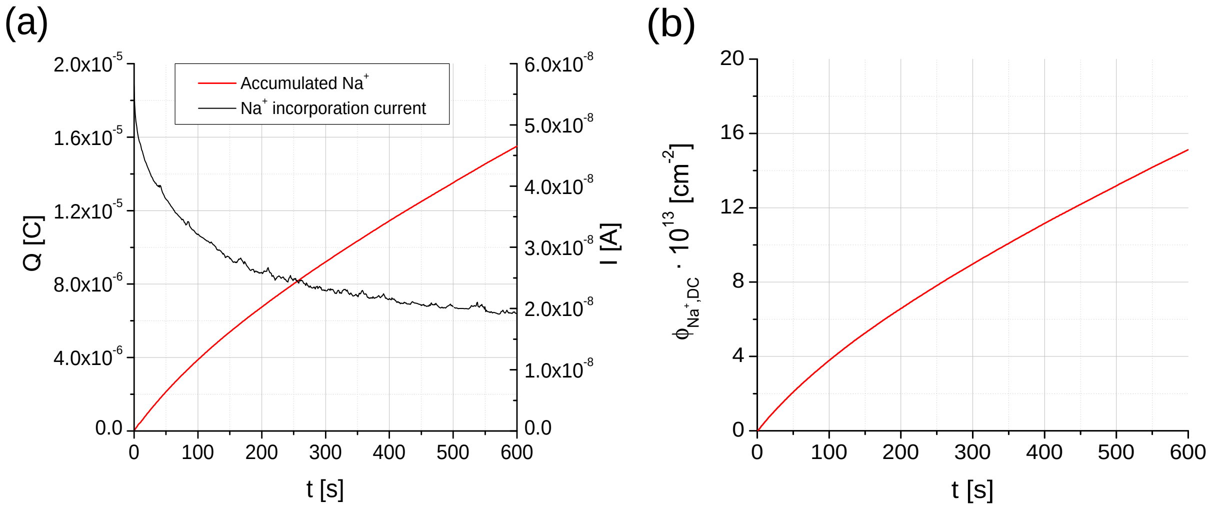

Figure 5.3.: (a) The detected electronic current equals the Na^+ incorporation current. Integration over time gives the charge accumulated at the SiO_2 / Si interface. (b) By eq. (2.18), the Na^+ incorporation current can be converted into $\phi_{Na^+,DC}$, the Na^+ dose accumulated at the interface.

Variation of the SiO_2 thickness resulted in the same exponential response current, when the electric field E, corresponding to the applied V_{bias}, was kept constant. However, $\phi_{Na^+,DC}$ decreased with increasing SiO_2 thickness as shown in Fig. 5.4. According to the fact, that the SMU response current corresponds to the detected Na^+ incorporation current, this variation is assumed to be a function of the SiO_2 film thickness, thus on the increasing resistivity, although E was kept constant at 2 MV/cm. In Fig. 5.4; $\phi_{Na^+,DC}$ in 100 nm SiO_2 was obtained from a different sample than for the graph in Fig. 5.3(b), showing a slight deviation. Possible reasons for this have been itemized above.

The following investigations based on the cognitions from the results presented in this section. Thorough studies were carried out by varying a certain parameter while keeping the others constant. By means of the

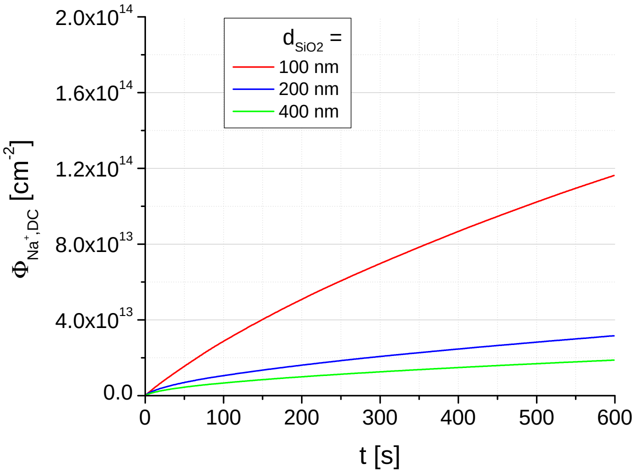

Figure 5.4.: Variation of SiO_2 Na^+ incorporation by means of in B-T stress. Conditions Temperature: 150 °C, V_{bias} was adjusted to obtain $E = 2$ MV/cm for each SiO_2 film.

semiquantitative capabilities of ToF-SIMS, the obtained Na^+ accumulation in ToF-SIMS depth profiles after B-T stress could be quantified using RSF values, taking into account only Na^+. Potentiostatic data as given in Fig. 5.3(b) on the other hand, are measured by means of electronic currents.

5.1.1. Temperature variation

The role of sample temperature was investigated, with constant V_{bias} of 20 V for samples containing a 100 nm SiO_2 layer. The temperature was varied in four steps from RT to 150 °C for B-T stress applications (Fig. 5.5(a)). In order to enable proper illustration of each potentiostatic B-T stress characteristic, the y-axis is given in logarithmic scale. Up to a temperature of at least 70 °C no distinctive increase of the response signal could be detected (note the logarithmic scale in Fig. 5.5), corresponding to the background noise of the used SMU. As also found in Fig. 5.5(b), Na^+ incorporation current could be detected when the temperature exceeded ~100 °C. However, further increase to ~130 °C led to a response signal, ~1.5 orders of magnitude larger than at 100 °C. Note that for reasons mentioned above concerning sample preparation, a comparison between quantities in Fig. 5.5(a) and (b) was not feasible. However, it could be shown, that for $V_{bias} = 20$ V, the temperature must exceed at least 100 °C in order to obtain a response signal, assignable to Na^+ incorporation into 100 nm SiO_2 and clearly distinguishable from the SMU background level. Proper signals during B-T stressing could be achieved at 150 °C sample temperature.

In order to examine the role of thermal diffusion of Na^+ in SiO_2, decoupled from electrical drift, the following experiment was carried out: A B-T stressed sample, with the incorporated Na^+ accumulated at

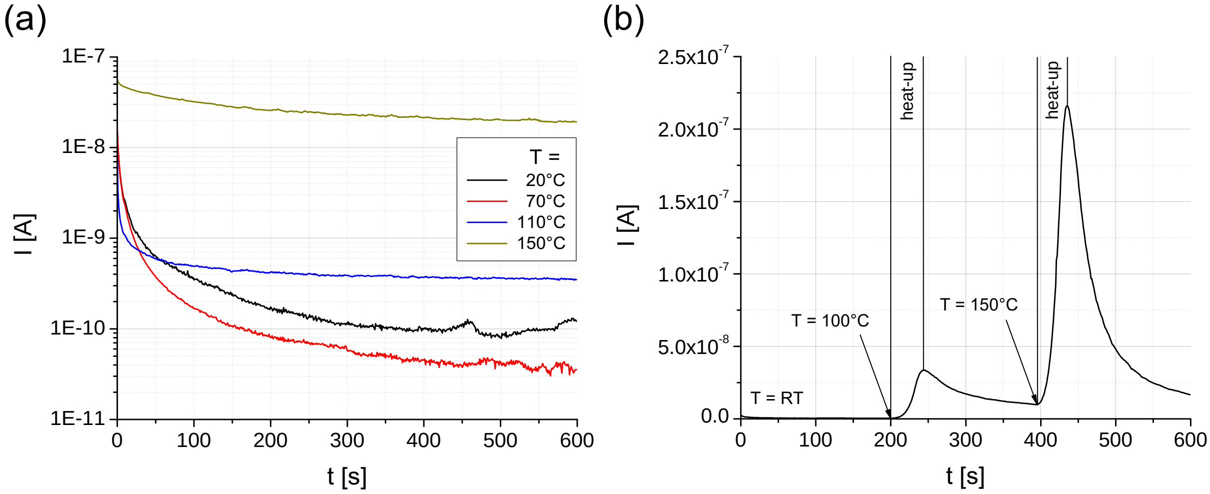

Figure 5.5.: (a) Na^+ incorporation current as a function of temperature at $V_{bias} = 20$ V. (b) Temperature increase during Na^+ incorporation gave response peaks with subsequent exponential decay.

the interface (Fig. 5.3(b)), was prepared for ToF-SIMS depth profiling as usual. The initial acquisition resulted in a profile characteristic shown in Fig. 5.2. Thereupon, the sample was heated several times in-situ using the heating/cooling capabilities of the ToF-SIMS instrument. After each heating cycle, the sample was cooled down to -130 °C, for the acquisition of a ToF-SIMS depth profile. Thus, several "read-outs" were obtained, showing the effect of each heating cycle on the profile characteristics. The measurement sequence was as follows. A heating cycle had the duration of 30 min with the first cycle at 100 °C and $\Delta T = +\,50$ °C for each ensuing heating cycle until 400 °C were reached (maximum temperature for longer in-situ heating cycles in the used ToF-SIMS instrument), i.e. seven read outs were achieved. Three of them are presented in Fig. 5.6.

Na^+ accumulation at the SiO_2 / Si interface disappeared with increasing in-situ heating. Simultaneously a peak appeared at the adjacent Au / SiO_2 interface until, at temperatures ≥ 300 °C, the profile characteristics resembled those of Fig. 4.4(b). As discussed in section 4.2.1, the profile shapes were affected by an artifact due to Na incorporation caused by migration during ToF-SIMS depth profiling. It is obvious that Na^+, as detected at the Au / SiO_2 interface in the read-outs of Fig. 5.6, migrated into the bulk during depth profiling[1]. This implies that on thermal impact, Na^+ changes its location with respect to the adjacent interface. As assumed from the B-T characteristics (Fig. 5.3), no Na^+ was present within the SiO_2 independent on the conditions (temperature, V_{bias}) predominant in the sample. Hence, thermal back-diffusion, according to Fick's law (eq. (2.12)) was not possible for Na^+ in SiO_2. Arguably, the reason is the absence of an anionic binding partner, which would be necessary for ambipolar diffusion

---

[1] The small peak at the Au / SiO_2 interface in the initial profile origins as already mentioned from Na traces due to Au deposition in the course of sample preparation

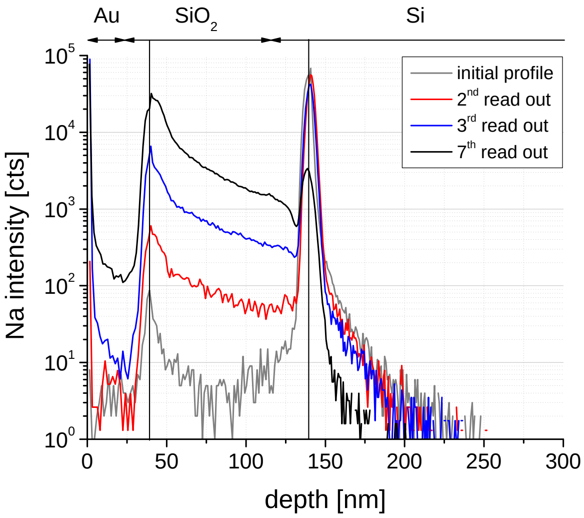

Figure 5.6.: ToF-SIMS in-situ heating of a B-T stressed sample. The 2^{nd} read out is doneafter keeping the sample at 150 °C for 30 min. 3^{rd} read out: 200 °C / 30 min. 7^{th} read out: 400 °C / 30 min.

in SiO_2. It is therefore indispensable that Na^+ is present at any interface, either with Si or with Au. The Au faced interface is energetically favored, so that Na^+ get transported across the SiO_2 film during thermal stress. An induced voltage within SiO_2 can be excluded, since the experiment shown in Fig. 5.6 was carried out with an electrical conductive path between Au and Si as well as with an isolated Au electrode (0.8×0.8 cm^2). Both variations gave the same result.

In order to check, whether Na^+ left the SiO_2 film during in-situ heating, the obtained data from the read outs were quantified according to eq. (3.14) and thus checked on the conservation of ϕ_{Na} (Tab. 5.2). The data indicate that no amount of Na^+ was lost during in-situ heating. Deviations in $\phi_{Na^+,SIMS}$ (denoting the Na^+ dose, as detected by quantification of ToF-SIMS depth profiles) were recognized at a read-out number > 7. Since, these depth profiles showed a large amount of Na^+present at the Au / SiO_2 interface, the changed matrix effect is assumed to be the reason for this deviations.

5.1.2. Bias variation

This section deals with effects, arising upon sample bias V_{bias} variation while keeping the temperature constant at 150 °C. Fig. 5.7 shows the results of this variation as $\phi_{Na^+,DC}$ vs. time plots. Higher values than $V_{bias} = 40$ V were not feasible, since dielectric breakdown of the SiO_2 film occurred at slightly higher values. Applying 40 V caused a drop-out rate for samples of~50% by short-circuits due to SiO_2 breakdown. Some effects were obvious immediately:

Table 5.2.: Quantified read-outs after in-situ heating in the ToF-SIMS instrument and subsequent depth profiling.

Read-out	Heating cycle parameter	$\phi_{Na^+,SIMS}$ [cm^{-2}]
initial profile		5.12·^{14}
1	100 °C / 30 min	5.82·^{14}
2	150 °C / 30 min	5.43·^{14}
3	200 °C / 30 min	5.18·^{14}
4	250 °C / 30 min	4.08·^{14}
5	300 °C / 30 min	6.29·^{14}
6	350 °C / 30 min	5.89·^{14}
7	400 °C / 30 min	7.30·^{14}

(i) The initial slope increased drastically at higher bias voltage. This implies a higher Na^+ transfer rate at the PMMA / SiO_2 interface. The exponential decay of the SMU response signal (Fig. 5.3) was more rapid at higher V_{bias}, finally approaching a steady state corresponding to the SMU background level. The process observed in Fig. 5.1 was accelerated at V_{bias} = 30 V or 40 V.

(ii) The initial slopes did not follow a linear function. However, for a steady incorporation of Na^+ at the PMMA / SiO_2 interface a linear behavior would be expected. Taken into account the electric drift predominant in the electrochemical potential (eq. (2.18)), a possible depletion of Na^+ in PMMA would not explain this curved characteristic of $\phi_{Na^+,DC}$.

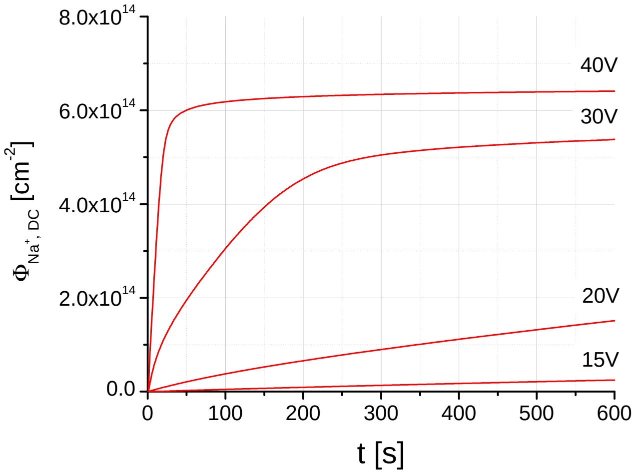

Figure 5.7.: V_{bias} variation during B-T stress application on a sample comprising a 100 nm SiO_2 layer. Thus E = 1, 1.5, 3 and 4 MV/cm took effect in SiO_2 for Na^+ drift towards the interface to Si.

Considering accumulation of Na^+ at the SiO_2 / Si interface after incorporation, it seems plausible that the electrical potential at this position got increased with increasing $\phi_{Na^+,DC}$ at the interface. Hence, the externally applied potential difference (thus V_{bias}), with the Si-substrate set at ground potential, would be diminished, leading to a gradual decrease of $\nabla\widetilde{\mu}$ as given in eq. (2.19). In other words, an internal electrical counter-field would decrease the effective driving force responsible for the transport of Na^+. The diminished effective V_{bias} is reflected in the mentioned curved characteristic in Fig. 5.7. The resembling appearance of the Na^+ incorporation current to capacitor charge-up characteristics, interpretable as the charging of an internal chemical capacitor, supports this assumption. Fig. 5.8 illustrates the scheme of this process.

(iii) For higher values of V_{bias}, $\phi_{Na^+,DC}$ reaches a steady state after a certain incorporation time. Deviations between upper thresholds in $\phi_{Na^+,DC}$ for V_{bias} = 30 V and 40 V are assignable to sample preparation as mentioned in section 5.1. Two possibilities are conceivable for the appearance of a steady state: The first one assumes the internal counter-field diminishing the external applied bias to the whole extent, thus completely canceling the effective electric field within SiO_2. In this situation the driving force would be $\nabla\widetilde{\mu} = 0$ and no further Na^+ incorporation and transport would be possible. The other possibility emanates from the fact, that the provided Na^+ dose within the host matrix was consumed quantitatively. Investigations on this question will be presented in the course of the next section.

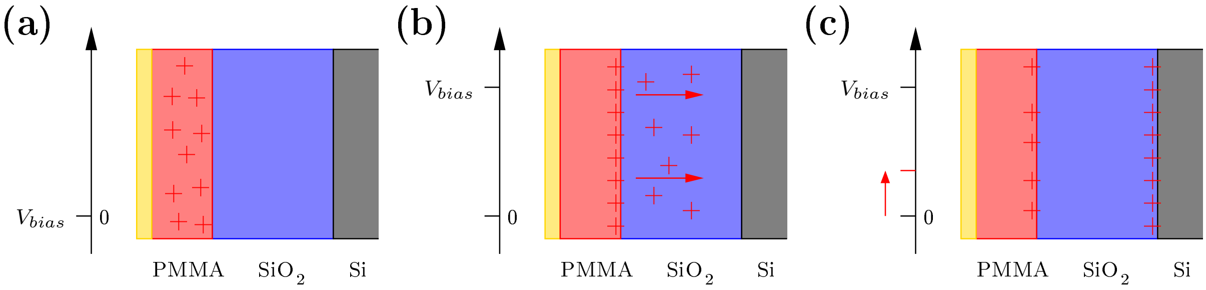

Figure 5.8.: Process scheme of Na^+ incorporation and transport from PMMA into SiO_2, resembling the charging of a chemical capacitor. (a) Situation before B-T stress. (b) Incorporation of Na^+ into SiO_2 and transport towards the SiO_2 / Si interface. (c) Accumulation of Na^+ at the SiO_2 / Si interface. The assumed increase of the potential at the SiO_2 / Si interface as mentioned in the text is marked by a red line, resulting in a decrease of the effective V_{bias}.

Quantitative aspects

Na^+ intensities in the ToF-SIMS depth profiles, obtained after B-T stress using a certain V_{bias}, were quantified and compared to potentiostatic data. This gives an idea on the amount of secondary currents detected during B-T stress and superposing the Na^+ incorporation current. Tab. 5.3 lists this comparison for various bias voltages. Additionally, a time dependent quantification is included corresponding to Fig. 5.2. ToF-SIMS quantification was hereby carried out using $RSF_{Na,M}$ values, obtained at RT. The reason is the resemblance of the depth profiles after Na^+ incorporation with that from the implanted sample at RT (Fig. 4.2), that is severely affected by Na migration. The quantification error is therefore assumed to be minimal. Quantification using $RSF_{Na,M}$ values, obtained at -130 °C led to $\phi_{Na^+,SIMS}$ values, which were up to 30% lower than quantification using $RSF_{Na,M}$ values, obtained at RT.

Table 5.3.: Comparison of the number of Na^+, incorporated into SiO_2,obtained by potentiostatic data $\phi_{Na^+,DC}$ and spectrometric data $\phi_{Na^+,SIMS}$, respectively.

V_{bias} [V]	Incorporation time t [s]	Detected Na^+ dose [cm^{-2}]	
		$\phi_{Na^+,DC}$	$\phi_{Na^+,SIMS}$
15	600	$2.49{\cdot}10^{12}$	$3.34{\cdot}10^{12}$
20	600	$3.99{\cdot}10^{14}$	$3.11{\cdot}10^{14}$
30	600	$3.99{\cdot}10^{14}$	$3.11{\cdot}10^{14}$
40	600	$6.41{\cdot}10^{14}$	$7.20{\cdot}10^{14}$
20	6	$8.79{\cdot}10^{12}$	$4.35{\cdot}10^{12}$
20	6	$7.78{\cdot}10^{13}$	$9.11{\cdot}10^{13}$

A good agreement between $\phi_{Na^+,DC}$ and $\phi_{Na^+,SIMS}$ was observed in the data of Tab. 5.3 with a deviation of up to factor 1.5 - 2. The deviation could arise from both types of quantification:

- Potentiostatic data contains secondary contributions as electrical capacitor charging, electrical leakage currents or contributions by other mobile ions (e.g. Li^+, K^+, H^+, ...) comprised in $\phi_{Na^+,DC}$. These superimposed components could not be separated from Na^+ currents. An exception is electrical capacitor charging, that could be subtracted from the total SMU response signal (compare Fig. 3.5).

  The response signal and thus the total detected charge Q is therefore assumed to be slightly higher than the signal barely assignable to Na^+ incorporation currents.

- ToF-SIMS quantification by means of *RSF* factors may cause certain deviations. As given in eq. (3.14), there are some quantities included, all possible sources of error (e.g. integrated Na^+ and matrix signal intensities, $\cdots$). Additionally, as mentioned in section 3.3.1 high intensities at the single ion detector may cause statistical errors (e.g. observable in the ratio of natural abundances of Si isotopes) even if the data was Poisson corrected.

5.1.3. Variation of the Na^+ dose in the host matrix

In order to address the question on the reason for the appearance of a steady state during Na^+ incorporation in SiO_2 at higher values of V_{bias} (Fig. 5.7), host matrix formulations with a varying c_{NaOTf} were used (see Tab. 3.5). Doing this some deviations were expected, due to the slightly different viscosity and final host matrix condition. Since, a maximal amount of Na^+, should be incorporated from PMMA into SiO_2, $V_{bias} = 40$ V was used for a 100 nm SiO_2 film (i.e. $E = 4$ MV/cm). The temperature was kept constant at 150 °C. Fig. 5.9(a) shows the results of B-T stress application in terms of $\phi_{Na^+,DC}$ vs. time plots. Subsequent ToF-SIMS depth profiling revealed a Na^+ free PMMA layer (Fig. 5.9(b)). Only a background signal could be detected (note the logarithmic scale); comparison to Fig. 4.4(b), the respective ToF-SIMS depth profile before B-T stress, confirmed the complete depletion of Na^+ in PMMA.

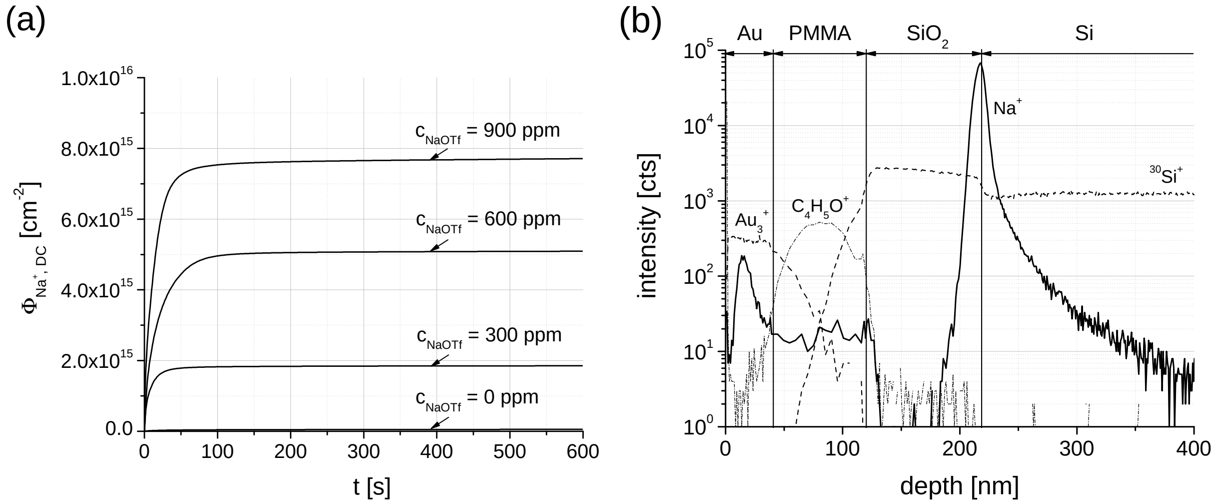

Figure 5.9.: (a) Variation of c_{NaOTf} in PMMA and its effect of the detected $\phi_{Na^+,DC}$. (b) ToF-SIMS depth profile representing the state of the Na^+ distribution within B-T stressed samples ($V_{bias} = 40$ V). In order to check the PMMA layer on remaining Na, host matrix lift-off as given in the process flow scheme in Fig. 3.1 was skipped. The $C_4H_5O^+$ signal represents the PMMA layer. The profile corresponds to $c_{NaOTf} = 300$ ppm in PMMA. All other host matrix formulations resulted in the same profile characteristics after B-T stress.

From Fig. 5.9 it can be concluded that the stopping condition of Na^+ incorporation is the depletion of the Na precursor within PMMA. However, as mentioned above, the curved initial sloping is assigned to a diminished effective V_{bias}, due to internal charge-up of a chemical capacitor.

An interesting side effect was the appearance of electrostatic discharges at the sample surface, leading to damages at the surface (Fig. 5.10). These phenomena could cause dielectric breakdown of the SiO_2 film, as for $V_{bias} > 40$ V (for 100 nm SiO_2) due to a short-circuit between Au and Si. Basically, each discharge could potentially lead to SiO_2 breakdown, with the probability for this being higher at increased c_{NaOTf}. The appearance of these electrostatic discharges was however only observed in the first 1 - 2 seconds of B-T stress application. Due to the relation the frequency of occurrence with c_{NaOTf}, it is obvious that Na^+ was involved in these discharges. Because of this limitation, the upper threshold for feasible B-T stress application at $V_{bias} = 40$ V for 600 s was $c_{NaOTf} = 900$ ppm.

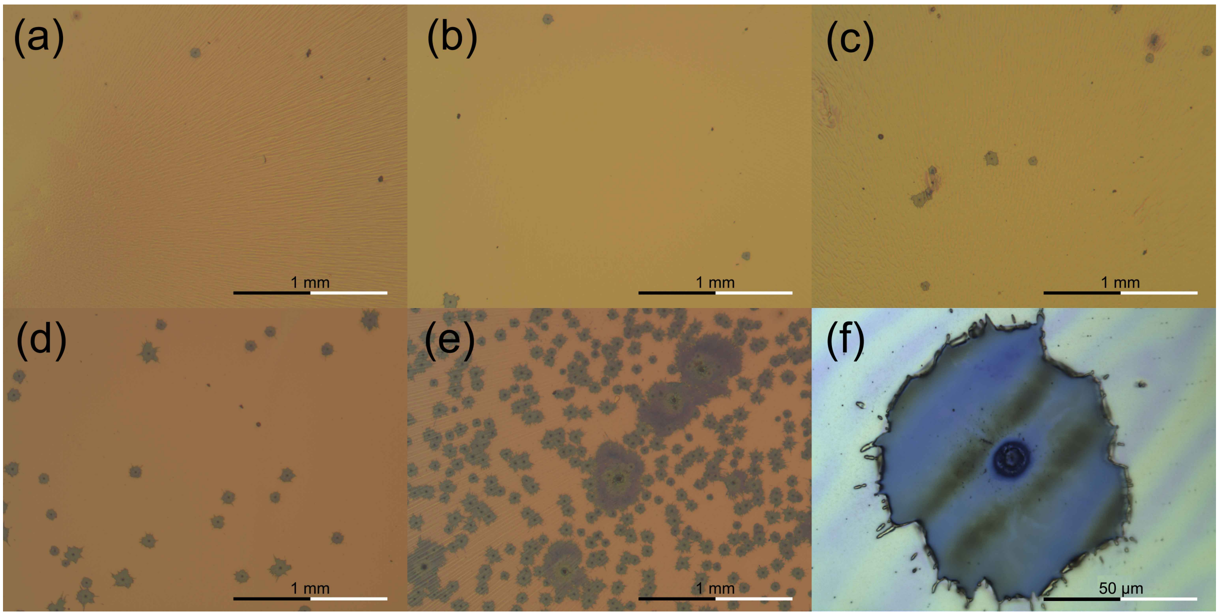

Figure 5.10.: Light microscopy images of the sample surface after B-T stress using $V_{bias} = 40$ V. (a) $c_{NaOTf} = 0$ ppm (b) $c_{NaOTf} = 300$ ppm (c) $c_{NaOTf} = 600$ ppm (d) $c_{NaOTf} = 900$ ppm (e) $c_{NaOTf} = 1200$ ppm. (f) displays a 20× close up of a damage at the sample surface as visible in the other images.

Quantitative aspects

Based on the fact that the total provided amount of Na was incorporated into SiO_2 when applying $V_{bias} = 40$ V, a quantitative comparison between calculated, potentiostatic and spectrometric data was carried out. An overview on this comparison is given in Tab. 5.4. d_{PMMA}, the thickness of the PMMA host matrix was determined via ellipsometry. Note that for $\phi_{Na^+,calc}$ an offset was considered, accounting for the intrinsic Na^+ concentration in PMMA (30 ppm, see 3.1.1). $\phi_{Na^+,calc}$ for $c_{NaOTf} = 0$ ppm reflects this quantity.

Table 5.4.: Comparison of detected Na^+ doses with calculated values from c_{NaOTf} as obtained by ToF-SIMS and from potentiostatic B-T stress response data sample processing.

c_{NaOTf} [ppm]	d_{PMMA} [nm]	$\phi_{Na^+,calc}$ [cm^{-2}]	$\phi_{Na^+,SIMS}$ [cm^{-2}]	$\phi_{Na^+,DC}$ [cm^{-2}]	ϕ-ratio DC/SIMS [%]
0	67.1	$6.33{\cdot}10^{13}$	$6.29{\cdot}10^{13}$	$5.54{\cdot}10^{13}$	88
300	77.6	$5.91{\cdot}10^{14}$	$9.83{\cdot}10^{14}$	$1.85{\cdot}10^{15}$	188
600	116.9	$1.67{\cdot}10^{15}$	$1.79{\cdot}10^{15}$	$5.09{\cdot}10^{15}$	284
900	63.1	$1.36{\cdot}10^{15}$	$1.83{\cdot}10^{15}$	$7.71{\cdot}10^{15}$	421

The values for $\phi_{Na^+,SIMS}$ are in the same order of magnitude as $\phi_{Na^+,calc}$, which is a good agreement for this low quantities. The excess of ~60% can be assigned to sytematic errors in $\phi_{Na^+,calc}$ due to the preparation processes of the host matrix formulations, and due to uncertainties from ToF-SIMS quantification, which is considered as the way larger error source. The comparison of $\phi_{Na^+,SIMS}$ with $\phi_{Na^+,DC}$ showed a different behavior than in Tab. 5.3, though. Up to $c_{NaOTf} = 300$ ppm a consistensy between the data of Tab. 5.3 and 5.4 is given, however at higher values of c_{NaOTf} the ϕ-ratio of potentiostatic and spectrometric data increased dramatically. Due to reasons of illustration, this relation is plotted in Fig. 5.11 as a bar chart. The reason for this increase is assumed to lie in the appearance of electrostatic discharges at the sample surface during B-T stress (mentioned above; Fig. 5.10). Such processes are consuming energy, provided by means of an electric current. This additional current superimposed to the Na^+ incorporation current and could not be seperated.

The data in Tab. 5.4 emphasize an important advantage of the used approach for experiments as presented in this thesis: Spectrometric data out of quantified ToF-SIMS depth profiles solely contain informations on Na^+ incorporation, without any contribution to secondary sources, whereas quantification of the SMU response signal, also contains a lot of secondary currents.

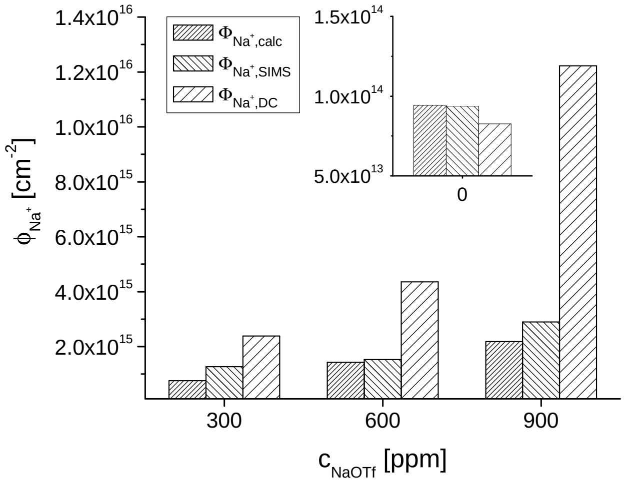

Figure 5.11.: Bar diagram showing the data of Tab. 5.4. The good agreement between calculated and ToF-SIMS quantification and the increasing ϕ-ratio DC/SIMS with increasing c_{NaOTf} are shown.

5.1.4. Variation of the mobile ion

The influence of the ionic radius of mobile ions on the response signal during B-T stress and the subsequent ToF-SIMS depth profiling analysis is presented in this section, with the results set in comparison to the findings of Na^+ incorporation experiments. Fig. 4.4 gives an idea of the respective ion mobility of Li^+, Na^+ and K^+ in terms of mobile ion migration during ToF-SIMS depth profiling. A similar relation was expected during B-T stress. In the previous sections it became clear, that potentiostatic data could solely give informations on mobile ion incorporation into SiO_2, when transported all the way through the SiO_2 film and thus set in relation with a stoichiometric number of electrons at the SiO_2 / Si interface.

Li^+ incorporation and transport

A 400 nm SiO_2 film was chosen as the material to be examined, with the attached host matrix containing $c_{LiOTf} = 300$ ppm, in order to achieve a proper comparison to Na^+ incorporation as shown in Fig. 5.4, V_{bias} was set to 80 V ($E = 2$ MV/cm) with the sample temperature at 150 °C . Converted into $\phi_{Me^+,DC}$, Fig. 5.12(a) compares SMU response signals, assignable to Li^+ and Na^+ incorporation. As expected, Li^+ incorporation also yielded curved characteristics, assignable to charging of the internal chemical capacitor (as already described for Na^+ incorporation). The deviation between the achieved values of $\phi_{Me^+,DC}$ are assumed due to differences in the host matrix condition (see section 4.1). Fig. 5.12(b) compares the respective ToF-SIMS depth profiles after B-T stress application, confirming the resembling behavior of Li^+ and Na^+ during incorporation: Both mobile ions accumulate at the SiO_2 / Si interface and no distinct difference could be determined with the used conditions.

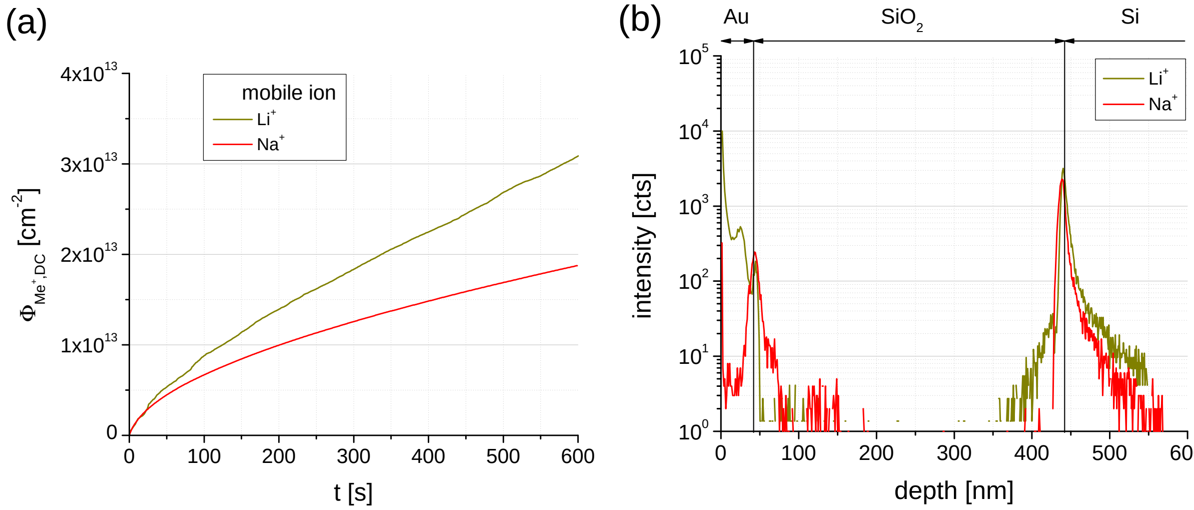

Figure 5.12.: (a) Comparison of the $\phi_{Me^+,DC}$ arising from Li^+ and IonNa+, respectively, during B-T stress application of a 400 nm SiO_2 film with $V_{bias} = 80$ V. (b) Comparison of the ToF-SIMS depth profiles (acquired at RT), obtained after B-T stress.

K^+ incorporation and transport

Fig. 4.4(c) gave the hint, that K^+ was supposed to get incorporated in a lower quantity than Na^+ at similar conditions (V_{bias}, temperature, SiO_2 thickness). Negligible K^+ accumulated at the SiO_2 / Si interface by means of K migration, which indeed has shown to be a process of minor relevance compared to mobile ions with a smaller ionic radius. Thus, in order to obtain any signal, distinguishable from the SMU background noise, harsher B-T stress conditions were chosen with $E = 4$ MV/cm within the SiO_2 film. Fig. 5.13(a) illustrates the obtained response signal on B-T stress. Despite the rigorous B-T conditions, the detected signal (converted into $\phi_{K+,DC}$) was half a magnitude lower than for even more moderate conditions in terms of Li^+ and Na^+ incorporation. Corresponding to Fig. 4.4(c) and taking into account the larger ionic radius of K^+ in contrast to Na^+, K^+ accumulation at the interface in ToF-SIMS depth profiles is negligible as expected (Fig. 5.13(b)). The potentiostatic signal as converted into $\phi_{K+,DC}$ arose in major parts from secondary effects as for instance leakage currents. In ToF-SIMS depth profiles, K^+ was unambiguously detected within the SiO_2 layer. The profile was checked on K migration by obtaining profiles at different sample temperatures (RT; -70 °C; -130 °C). Accordingly K^+, initially hosted in the PMMA layer, was pumped into SiO_2, but did not get transported through, in order to accumulate at the interface and thus did not give a potentiostatic signal assignable to K^+ transport through SiO_2 during B-T stress. Still considering K migration even at -130 °C sample temperature, the incorporated K^+ front proceeded ∼100 - 110 nm into SiO_2 in 10 min under B-T stress. Note the electrical field of $E = 4$ MV/cm, chosen for B-T conditions, is slightly below the breakdown voltage of the insulating film. At more moderate conditions no significant amount of K^+ could be found.

Since, K^+ was transfered into SiO_2, but did not proceed to the interface with Si, positive charges were introduced into the insulator and the question on conservation of the charge neutrality arose. ToF-SIMS depth profiling with detection of negative secondary ions did not unambiguously reveal a possible anionic binding partner of K^+ within the first ∼100 nm in SiO_2. A minor detected signal in this region could be assigned to CF^-, that possible could be fragmented from the triflate anion of the K^+ precursor KOTf.

5.2. Kinetic aspects of mobile ion transport in SiO_2

The findings of section 4.1 enables a closer look on a quantitative description of the incorporation behavior of mobile ions into SiO_2 in terms of kinetic parameters. In section 5.1.2 it has been demonstrated, that for moderate bias conditions ($E \leq 2$ MV/cm), the detected response current during B-T stressing could be set in direct relation to Na^+ transition at the PMMA / SiO_2 interface. It has been shown in Fig. 5.3(a) that the SMU response current resembled the charge up of a capacitor. This includes a non-steady mobile ion incorporation behavior at the PMMA / SiO_2 interface with time. Considering only the first second of the response signal, shorter intervals were not feasible by the used control software, the influence of the involved secondary effects was assumed to be minimal.

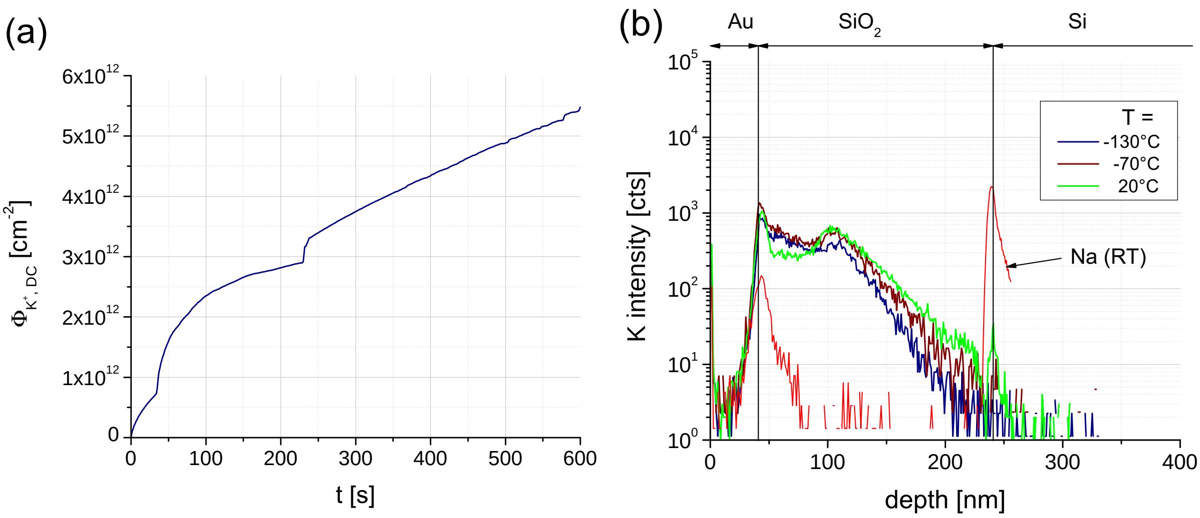

Figure 5.13.: (a) Detected $\phi_{K+,DC}$ as response on rigorous B-T stress (V_{bias} = 80 V, temperature = -130 °C, c_{KOTf} = 300 ppm in the host matrix). (b) ToF-SIMS depth profiles of the B-T stressed sample, obtained at different sample temperatures. For reasons of comparison the depth profile according to Na^+ incorporation using V_{bias} = 80 V and -130 °C for a host matrix comprising c_{NaOTf} = 300 ppm is given.

5.2.1. I-V characteristics

Limiting the bias voltage by a maximum value corresponding to $E = 2$ MV/cm, current - voltage (I-V) characteristics were acquired, by ramping V_{bias} in 20 steps up to the maximum, with a dwell time of 1 s. This procedure was examined in temperature steps of $\Delta T = 10$ °C, thus simultaneously investigating current - temperature characteristics. Electric capacitor charging, as illustrated in Fig. 3.5, had to be subtracted from the response signal, since having a severe influence on the initially detected signal. Therefore, "blank" samples were ramped with the same parameters as the samples to be investigated. For the blank samples the Au electrode was directly attached on the SiO_2 layer, i.e. without an attached host matrix in between, in order to solely account for electric currents charging the MOS structure.

Fig. 5.14 exemplarily shows I-V and I-T plots for Na^+ incorporation into 100 nm SiO_2. Further I-V and I-T plots for varying SiO_2 film thickness and other mobile ions are given in Appendix A. It is unambiguously illustrated that a threshold for B-T stress for triggering mobile ion incorporation into SiO_2 existed, for obtaining a response current, which was significantly higher than the SMU noise level. In Fig. 5.14 the parameters $V_{bias} \approx 8$ V ($\equiv E \approx 0.8$ MV/cm) and ≈ 130 °C[1] could be identified as the minimum B-T stress, necessary to obtain a response signal, significantly distinguishable from the SMU background noise. A proof was given by ramping V_{bias} and the temperature in reverse direction, i.e. starting at $V_{bias} = 20$ V. Once one of these parameters fell below the mentioned threshold values, the

---

[1] For Li^+, thus a mobile ion with smaller ionic radius than Na^+, a lower threshold temperature was detected (≈ 100 °C; see Fig. A.3 in Appendix A).

significant response current stopped. Note that for the data presented in Fig. 5.14, blank values from capacitor charging were subtracted.

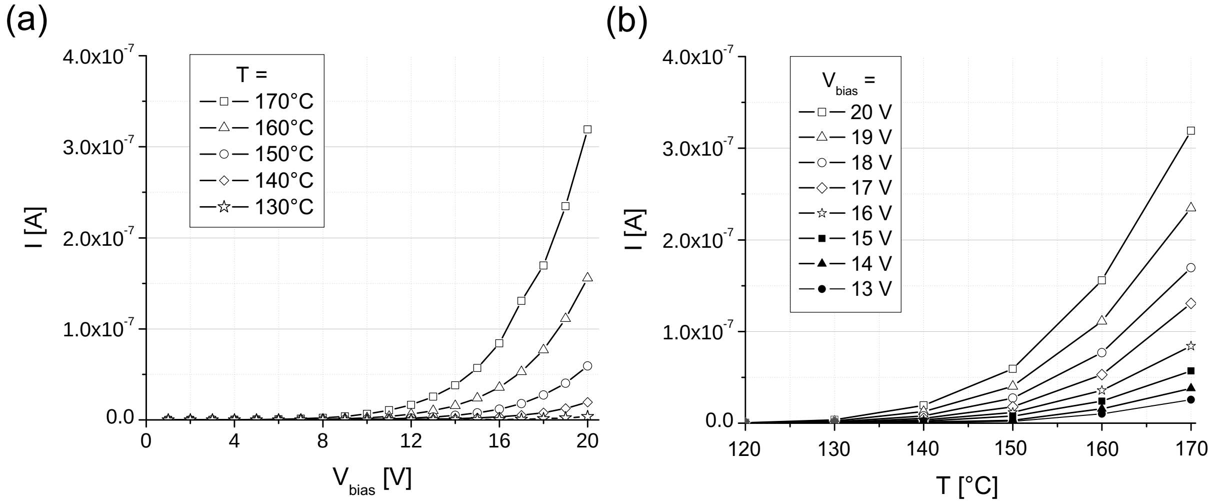

Figure 5.14.: (a) I-V plots obtained by ramping V_{bias}, recording Na^+ incorporation into 100 nm SiO_2 (c_{NaOTf} = 300 ppm). For each data point a dwell time at the respective V_{bias} was chosen. (b) I-T plots obtained by temperature ramping, carried out for temperatures in a range between RT and 170 °C.

As verifying technique impedance spectroscopy was applied. Fig. 5.15 shows typical Nyquist plots recorded with increasing amplitude, representing V_{bias} applied as AC signal, at a sample temperature of 150 °C. In the low frequency region (f = $1{\cdot}10^{-1}$-$1{\cdot}10^{1}$ Hz), a process could be recorded at higher amplitudes ($>$ 8 V $\equiv$ threshold of V_{bias} in Fig. 5.14(a)), that could be assigned to a RC circuit, which did not get captured in its whole extent by the chosen frequency range. Comparison of Nyquist plots in mid frequency region (Fig. 5.14(b); f = $1{\cdot}10^{1}$-$1{\cdot}10^{3}$ Hz) indicated the onset of this process at $Z' \approx 1{\cdot}10^{4}$ Ω. No further significant differences between the various curve characteristics could be observed at higher frequencies (towards the origin of the axes.), as implied in Fig. 5.14(b).

At low V_{bias}, impedance spectroscopy suggests bare capacitive behavior. This is in agreement with Fig. 5.14(a), where no response current was detected in this region of bias voltage regime. The decreasing resistivity of the RC circuit, that was recorded at higher amplitudes, could be assigned to an increased conductivity within SiO_2 as caused by incipient Na^+ incorporation at the mentioned threshold B-T conditions. Temperature variation showed a resembling behavior as observable in the high frequency range of Fig. 5.16. An inconsistency was detected in the temperature range of 90 °C - 130 °C. This might be connected with the glass transition of PMMA, occurring at ~125 °C (see section 3.1.1). Further two Nyquist plots, obtained at RT are shown for reproducibility reasons.

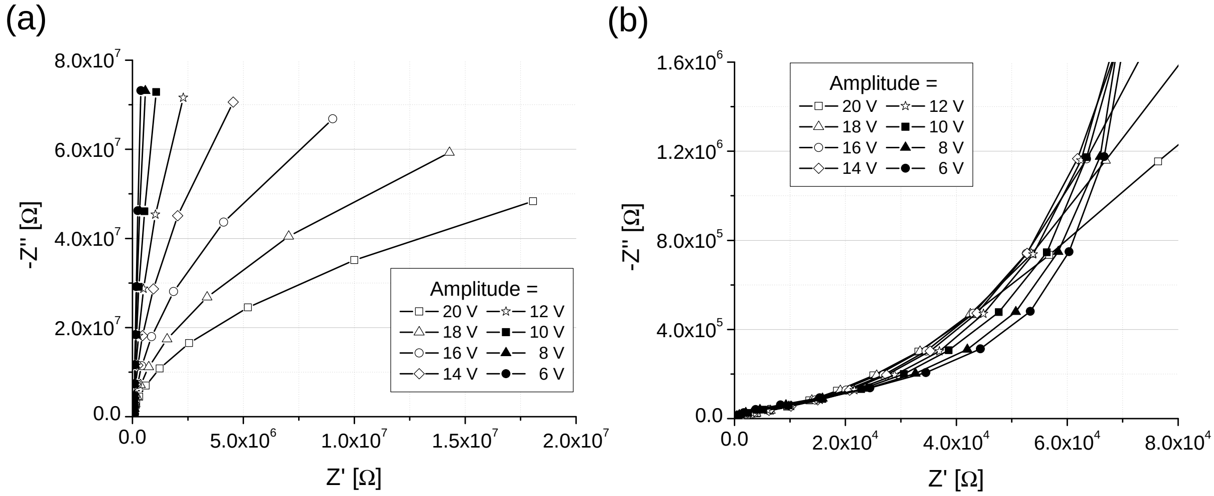

Figure 5.15.: Impedance spectroscopy plot showing Na^+ incorporation into 100 nm SiO_2 with varying amplitude at a constant temperature of 150 °C. (a) low frequency range $f = 1{\cdot}10^{-1}$-$1{\cdot}10^{1}$ Hz. (b) mid frequency range $f = 1{\cdot}10^{1}$-$1{\cdot}10^{3}$ Hz.

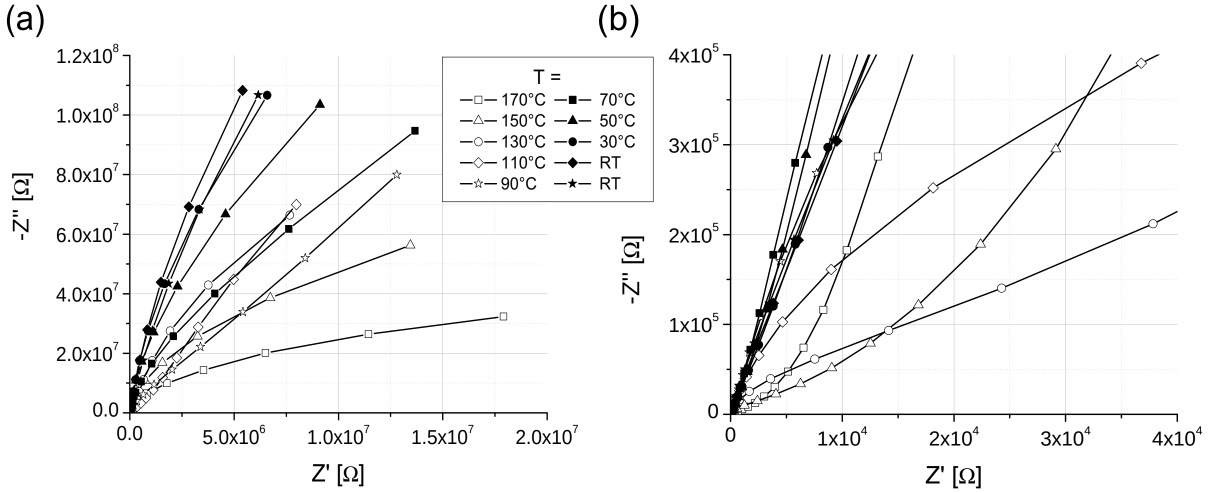

Figure 5.16.: Impedance spectroscopy plot showing Na^+ incorporation into 100 nm SiO_2 with varying the temperature at an amplitude of 20 V. (a) low frequency range $f = 1{\cdot}10^{1}$-$1{\cdot}10^{-1}$ Hz. (b) Mid frequency range $f = 1{\cdot}10^{3}$-$1{\cdot}10^{1}$ Hz.

Summarizing, impedance spectroscopy indicated a process in the low frequency region by variation of V_{bias} and temperature. This process exhibited a rather high resistivity in the magnitude of $1{\cdot}10^{10}$ Ω (low V_{bias}, low temperature) down to $1{\cdot}10^{8}$ Ω (high V_{bias}, high temperature). Only the SiO_2 layer could be connected with such a high resistivity (with resistivity R_{SiO_2}). Applying V_{bias} and temperatures above the detected threshold values, caused an increased conductivity, indicating Na^+ incorporation into SiO_2 and transport therein. The driving force of this process is the gradient of the electrochemical potential $\nabla\widetilde{\mu}$ (eq. (2.19)) within the sample. Since the electric drift was the dominating contributor in transport processes, R_{SiO_2} could be obtained from mobile ion conductivities by Ohm's law (eq. (2.22)). Tab. 5.5 lists values for R_{SiO_2} as given by the detected process in Fig. 5.15(a). Taken into account 100 nm for the thickness of the insulator, the obtained values are in good agreement with the resistivity of SiO_2 from literature [144]. Further values for R_{SiO_2} for different samples (varying SiO_2 thickness and mobile ion) are given in Appendix A. The PMMA / SiO_2 interface should exhibit an additional resistivity R_{if}. It was not possible to unambiguously fit the results from impedance spectroscopy by means of a reasonable equivalent circuit, and thus no second resistivity, assignable to R_{if} could be extracted. Though, since the interface is a very thin region in comparison to the SiO_2 film, R_{if} was supposed to be by magnitudes lower than R_{SiO_2}. The impedance spectra for thicker SiO_2 films (200 and 400 nm) give similar results to those than presented. During the next section a short estimation will proof this cognitions.

Note that quantitative calculations, based on Fig. 5.14 were only feasible for the case that the insulating film exhibited full permeability for mobile ions, as observed for Li^+ and Na^+ in SiO_2. As indicated by means of ToF-SIMS depth profiling (Fig. 5.13), this was not the case for K^+ transport.

Table 5.5.: Values for R_{SiO_2} and the respective capacities of a 100 nm SiO_2 layer as indicated by impedance spectroscopy (Fig 5.15(a)).

Amplitude [V]	R_{SiO_2} [Ω]	Capacity [nF]	Amplitude [V]	R_{SiO_2} [Ω]	Capacity [nF]
3	$1.81{\cdot}10^{10}$	21.72	12	$2.24{\cdot}10^{9}$	22.22
4	$1.67{\cdot}10^{10}$	21.75	13	$1.61{\cdot}10^{9}$	22.32
5	$1.61{\cdot}10^{10}$	21.75	14	$1.10{\cdot}10^{9}$	22.45
6	$1.40{\cdot}10^{10}$	21.75	15	$7.29{\cdot}10^{8}$	22.86
7	$1.10{\cdot}10^{10}$	21.78	16	$5.04{\cdot}10^{8}$	23.38
8	$9.16{\cdot}10^{9}$	21.76	17	$3.73{\cdot}10^{8}$	24.08
9	$6.87{\cdot}10^{9}$	21.80	18	$2.61{\cdot}10^{8}$	25.36
10	$4.96{\cdot}10^{9}$	21.84	19	$1.91{\cdot}10^{8}$	27.06
11	$3.16{\cdot}10^{9}$	22.14	20	$1.48{\cdot}10^{8}$	28.90

5.2.2. Physico-chemical description of mobile ion transport

The characteristics of Fig. 5.14, enabled the application of physico-chemical models, in order to describe the incorporation of mobile ion into SiO_2 kinetically. This lead to calculation of the activation energy E_a, necessary for mobile ion transport within SiO_2 as well as to insights into the quantity of the transfer rate at the PMMA / SiO_2 interface and with the knowledge of these values to calculations of the respective diffusion constants D.

Butler-Volmer kinetics based approach

The concept of Butler-Volmer kinetics is commonly applied to describe charge transfer currents and electrode kinetics of electrochemical cells [145, 146]. Thermally, the mobile ion transfer current density ($\equiv$ mobile ion transfer flux) j_{th} is determined by E_a (For equations in this section singly charged mobile ions are discussed with $z = 1$. z is therefore not include in the equations):

$$j_{th} = j_0 = \frac{I}{A} = F \cdot c_{Me^+} \cdot k \tag{5.3}$$

with I being the incorporation current as measured for instance in Fig. 5.5 or 5.14, A the area of the Au electrode (0.8×0.8 cm^2) and F denoting Faraday's constant. c_{Me^+} is the mobile ion concentration difference between different sites, separated by E_a, for the present sample setup being equivalent to the provided mobile ion concentration in PMMA, which can related to $c_{Me^+,calc}$ as given in Tab. 3.5 for each c_{MeOTf}. Considering transfer of mobile ions from the host matrix into SiO_2 this is because the SiO_2 layers of the investigated samples contained no significant amounts of mobile ions. k represents the incorporation rate at the interface given in [cm/s]. Fig. 5.17(a) illustrates the transfer flux at the PMMA / SiO_2 interface. In electrochemical cells, the thermal net flux at an interface is considered as j_0 being the difference between forward and backward flux. Thus the difference in the chemical potential $\nabla\mu$ is the driving force for the ion flux, represented by thermal diffusion as discussed in section 2.4. No mobile ions in SiO_2 justifies a zero backward flux. j_{th} in eq. (5.3) can thus also be given as a thermal net flux j_0 from the host matrix into the SiO_2 layer.

As expected, j_0 has a dependency on temperature, which is governed by a temperature dependency of k

$$k = k_0 \cdot \exp(-\frac{E_a}{R \cdot T}) \tag{5.4}$$

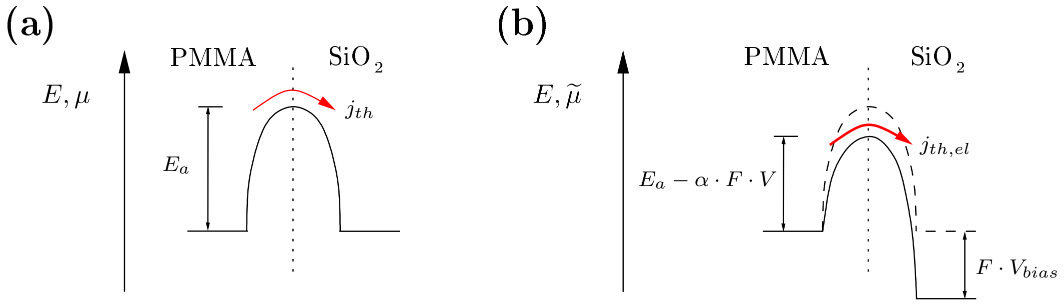

Figure 5.17.: (a) j_{th} at the PMMA / SiO_2 interface, determined by E_a. (b) $j_{th,el}$ (with the negative pol at the SiO_2 faced side), with a reduced activation energy under the influence of the applied external field V_{bias}.

comparably to D in eq. (2.17). Phenomenologically, k_0 can be considerede as the attempt frequency of mobile ions to overcome th energy barrier with height E_a as shown in Fig. 5.17(a). One can immediately get k as the fraction of successful attempts to overcome E_a.

The application of an external voltage V_{bias} acts accelerates mobile ion transitions from PMMA into SiO_2 as observable in Fig. 5.17(b). The electrochemical potential difference $\nabla\widetilde{\mu}$ governs hereby the mobile ion flux[1]. V_{bias} is responsible for a reduced activation energy, given by a modified version of eq. (5.3):

$$j_{th,el} = \frac{I}{A} = F \cdot c_{Me^+} \cdot k_0 \cdot \exp(-\frac{E_a - \alpha \cdot F \cdot V_{bias}}{R \cdot T}) \tag{5.5}$$

α denotes a symmetry factor considering the position of the energy barrier maximum. Usually, $\alpha = 1/2$. Since singly charged mobile ions are the species of interest, $j_{th,el}$ will be termed as j_{Me^+}. It is obvious that the accelerating effect of V_{bias} results in an increase of the appearing mobile ion incorporation current I by means of an increase in k by

$$k = k_0 \cdot \exp(-\frac{E_a}{R \cdot T}) \cdot \exp(\frac{\alpha \cdot F \cdot \Delta\phi}{R \cdot T}) \tag{5.6}$$

V_{bias} is therein replaced by the electrical potential difference $\Delta\phi$. As mentioned above, any backward transition from SiO_2 into PMMA is neglected in eq. (5.5). This equation is known as Butler-Volmer equation, usually applied for the calculation of kinetic parameters of the electrode / electrolyte interface in electrochemical cells.

---

[1] It is referred to the discussions of drift and field-assisted diffusion in section 2.4

Combining the Butler-Volmer approach with hopping dynamics

For the response current on B-T stress, eq. (5.5) could not be directly applied, since V_{bias} did not instantaneously drop at the PMMA / SiO_2 interface. In case of mobile ion incorporation into SiO_2, the electric potential decreases across the SiO_2 film of certain thickness. Thus, only a fraction of V_{bias} acted in a reducing manner on E_a at the interface.

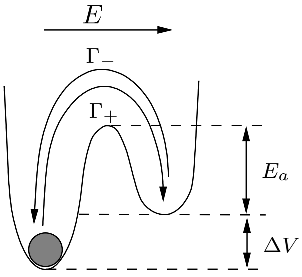

Figure 5.18.: Scheme of an asymmetric double well potential under the influence of an electric field, adapted from [145].

On this point, the concept of hopping dynamics came into play. For solid materials, the mechanism of mobile ion transport by means of hopping dynamics has been described in detail on a microscopic level [145, 147, 148]. According to this theory, one can phenomenologically consider the solid material as potential landscape with ions preferably located in potential wells of minimum relative energy, separated by energy barriers (Fig. 5.18). In the one-dimensional case, one can introduce an average hopping distance a between these sites of minimal relative energy. Under the influence of an electric field E, the jump rate of ions Γ_+ from one well of minimum energy into the adjacent one is described by (for a singly charged ion)

$$\Gamma_+ = \Gamma_0 + \cdot \exp(\frac{e \cdot a \cdot E}{2 \cdot k_B \cdot T}) \tag{5.7}$$

with Γ_0+ the ion jump rate without assistance of E. Again, backward transition is not of interest and thus Γ_- (the jump rate against E as given in Fig. 5.18), is neglected. Note that in amorphous materials, a is not a constant physical parameter, which can be found, e.g. in the lattice [145]. Under certain circumstances, mobile ions are able to jump into adjacent potential wells, resulting in a jump cascade throughout the solid material. The application of V_{bias} results thus in a distortion of the potential landscape with the result of a lowered energy barrier towards the cathode. Macroscopically, an ion current results parallel to the electric field. Comparing eq. (5.7) with eq. (5.5) suggests a correlation of Γ_+ with k and by insertion one receives

$$j_{Me^+} = \frac{I}{A} = F \cdot c_{Me^+} \cdot k_0 \cdot \exp(-\frac{E_a}{R \cdot T}) \cdot \exp(\frac{F \cdot a \cdot E}{2 \cdot R \cdot T}) \tag{5.8}$$

Eq. (5.8) is a Butler-Volmer based equation, modified for the investigation of mobile ion transport as plotted in Fig. 5.15. Other than indicated in Fig. 5.17(b), where the V_{bias} drops during one transition step, the modified Butler-Volmer approach considers V_{bias} to drop successively within the SiO_2 film. This is illustrated in Fig. 5.19.

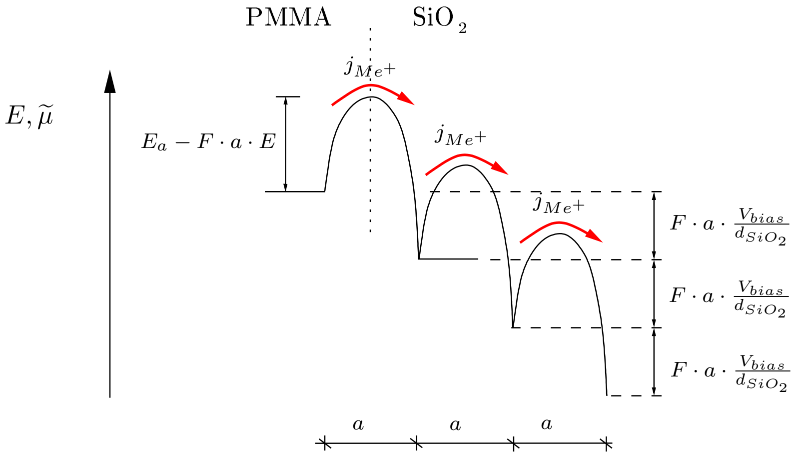

Figure 5.19.: Illustration of eq. (5.8) by means of the first three jumps of mobile ions from PMMA into the bulk of SiO_2, resulting in a mobile ion current I and the respective density j_{Me^+}.

Phenomenologically, mobile ions, initially located in PMMA, incorporate SiO_2 and are hopping throughout the insulating film of thickness d_{SiO_2} until finally reaching the interface to Si and accumulating there as detected via ToF-SIMS depth profiling. Thus each jump, between two sites of minimal relative energy is favored in forward direction in terms of lowering E_a by an amount governed by the jump distance a, the applied V_{bias} and d_{SiO_2} (as indicated in Fig. 5.19).

There are two simplifications, that were made for applying eq. (5.8) on measured data:

(i) The electric field acts solely parallel to the interfaces with potential wells within SiO_2 separated by a constant value for E_a. In literature, a within SiO_2 has been reported to be 20 - 25 Å [145, 149]. We thus consider $a = 25$ Å and the same distance for the first jump, i.e., the transition from PMMA into SiO_2.

(ii) Two different activation energies were taken into account for mobile ion transport from PMMA to the SiO_2 / Si interface: $E_{a,1}$ assignable to the PMMA / SiO_2 interface (with resistivity R_{if}) and $E_{a,2}$ for n successive jumps within SiO_2 (R_{SiO_2}) to the interface to Si. It is assumed, that $E_{a,1}$ could be larger than $E_{a,2}$ (Fig. 5.21). Impedance spectroscopy was not able to distinguish between these values. With $a = 25$ Å, a 100 nm SiO_2 layer comprises 25 jumps of an activation energy $E_{a,2}$ within SiO_2. In contrast, there is only one jump at the PMMA / SiO$_2$ interface with $E_{a,1}$. Taking into account two arbitrary activation energies with $E_{a,1} > E_{a,2}$ one can estimate

$$\frac{R_{if}}{R_{SiO_2}} = \frac{\exp(\frac{1.8}{k_B \cdot T})}{\exp(\frac{1.3}{k_B \cdot T} \cdot 25)} \approx 10^4 \tag{5.9}$$

Under this assumption R_{if} would be way larger than R_{SiO_2}. This was obviously not the case according to the values in Tab. 5.5. The rate determining step for mobile ion transport towards the SiO$_2$ / Si interface is therefore assumed to be the mobile ion jump cascade within SiO$_2$ with activation energy $E_{a,2}$ and not the mobile ion incorporation from PMMA with activation energy $E_{a,1}$. Therefore one can claim $E_{a,1} < E_{a,2}$. Data analysis according to the modified Butler-Volmer approach, are considered to provide quantitative values for $E_{a,2}$, which in the following will be termed E_a for the rate determining step in B-T stress experiments.

Calculations based on the modified Butler-Volmer approach

Putting the data of Fig. 5.14 in an Arrhenius plot, (i.e. ln(I) vs. 1/T) gives a relation as displayed in Fig. 5.20 [1]. Between 140 °C and 170 °C, thus in the temperature range where a significant SMU response signal was detectable (as obvious in Fig. 5.14), a linear relation is observable.

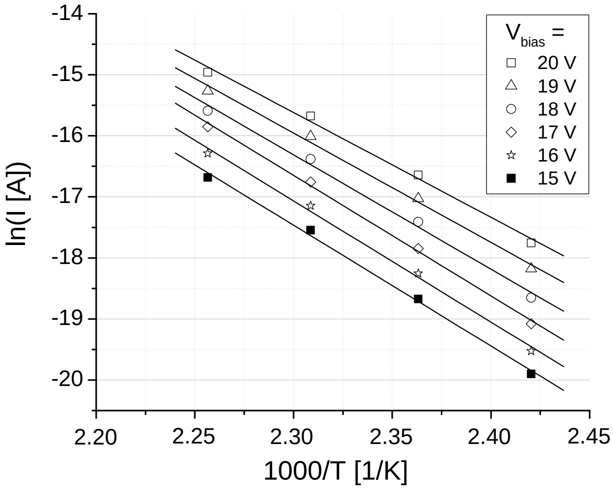

Figure 5.20.: Arrhenius plot of the data in Fig. 5.14 (Na$^+$ transport in 100 nm SiO$_2$, c_{NaOTf} = 300 ppm) according to the modified Butler-Volmer approach for the temperature range 140 °C - 170 °C.

---

[1] Further Arrhenius plots for Na$^+$ transport in 200 and 400 nm SiO$_2$ as well as Li$^+$ transport in 100 nm SiO$_2$ are given Appendix A

The data in Fig. 5.20 could be fitted by a linear regression, whereas the slope of the function and the intercept points with the y-axis correspond to eq. (5.8), rearranged in the Arrhenius-type form

$$\ln(I) = \frac{-E_a + F \cdot a \cdot E}{2 \cdot R \cdot T} + \ln(A \cdot F \cdot c_{Me^+} \cdot k_0) \tag{5.10}$$

with c_{Me^+} in [mol/cm^3] as derived from $\phi_{Na^+,calc}$ in Tab. 5.4 by considering the host matrix layer thickness. Eq. (5.10) represents the mathematical expression of linear regressions in Fig. 5.20. The activation energy E_a for mobile ion transport within SiO$_2$ is thus obtainable from the slopes and the attempt frequency k_0 for transitions between sites of minimal relative energy within SiO$_2$ can be read from the intercept points (compare to Fig. 5.19). Based on the data plotted in Fig. 5.14, Tab. 5.6 - 5.9 give the according analysis for obtaining E_a and k_0 for Na$^+$ transport in 100, 200 and 400 nm SiO$_2$ as well as for Li$^+$ transport in 100 nm SiO$_2$. As mentioned in the previous section, a reliable analysis for K$^+$ transport in SiO$_2$ was not feasible.

Table 5.6.: Quantities from Arrhenius plot (as displayed in Fig. 5.20) from Na$^+$ transport in 100 nm SiO$_2$ (c_{NaOTf} = 300 ppm). Calculations are according to eq. (5.10).

V_{bias} [V]	R^2	Slope	Incident point	$E_a - \alpha \cdot F \cdot a \cdot E$ [eV]	E_a [eV]	k_0 [cm/s]
15	0.99676	-19771	28.01	1.71	1.88	$1.88 \cdot 10^{11}$
16	0.99564	-19839	28.56	1.71	1.90	$3.27 \cdot 10^{11}$
17	0.99780	-19734	28.74	1.70	1.90	$3.89 \cdot 10^{11}$
18	0.99407	-18734	26.78	1.62	1.82	$5.47 \cdot 10^{10}$
19	0.99469	-17901	25.22	1.54	1.76	$1.15 \cdot 10^{10}$
20	0.99441	-17161	23.85	1.48	1.71	$2.94 \cdot 10^{9}$
				Average E_a	1.83 ± 0.08	

Table 5.7.: Quantities from Arrhenius plot of data obtained from Na$^+$ transport in 200 nm SiO$_2$ (c_{NaOTf} = 300 ppm). Calculations are according to eq. (5.10).

V_{bias} [V]	R^2	Slope	Incident point	$E_a - \alpha \cdot F \cdot a \cdot E$ [eV]	E_a [eV]	k_0 [cm/s]
30	0.97233	-16017	19.09	1.38	1.55	$2.52 \cdot 10^{7}$
32	0.98180	-16103	19.53	1.39	1.57	$3.90 \cdot 10^{7}$
34	0.98758	-16072	19.69	1.39	1.58	$4.56 \cdot 10^{7}$
36	0.98941	-15421	18.45	1.33	1.54	$1.32 \cdot 10^{6}$
38	0.99702	-15270	18.31	1.32	1.54	$1.15 \cdot 10^{6}$
40	0.99886	-14674	17.14	1.27	1.50	$3.55 \cdot 10^{6}$
				Average E_a	1.55 ± 0.03	

Table 5.8.: Quantities from Arrhenius plot of data obtained from Na^+ transport in 400 nm SiO_2 ($c_{NaOTf} = 300$ ppm). Calculations are according to eq. (5.10).

V_{bias} [V]	R^2	Slope	Incident point	$E_a - \alpha \cdot F \cdot a \cdot E$ [eV]	E_a [eV]	k_0 [cm/s]
64	0.98349	-22340	33.44	1.93	2.11	$4.28 \cdot 10^{13}$
68	0.98450	-21868	32.73	1.89	2.08	$2.11 \cdot 10^{13}$
72	0.98022	-21772	32.80	1.88	2.09	$2.25 \cdot 10^{13}$
76	0.98200	-20681	30.63	1.78	2.00	$2.57 \cdot 10^{12}$
80	0.98178	-19333	27.75	1.67	1.90	$1.44 \cdot 10^{11}$
				Average E_a	2.04 ± 0.09	

Table 5.9.: Quantities from Arrhenius plot of data obtained from Li^+ transport in 100 nm SiO_2 ($c_{LiOTf} = 300$ ppm). Calculations are according to eq. (5.10).

V_{bias} [V]	R^2	Slope	Incident point	$E_a - \alpha \cdot F \cdot a \cdot E$ [eV]	E_a [eV]	k_0 [cm/s]
60	0.99630	-10958	7.48	0.95	1.12	227
64	0.99860	-11029	7.87	0.95	1.14	335
68	0.99948	-11039	8.09	0.95	1.15	418
72	0.99962	-10902	7.95	0.94	1.15	366
76	0.99956	-10808	7.90	0.93	1.15	346
80	0.99956	-10715	7.84	0.92	1.16	327
				Average E_a	1.14 ± 0.01	

An average over values of E_a, obtained by different V_{bias} is added at the end of each table. The results from the calculations as listed in Tab. 5.6 - 5.9 can be commented in the following:

- Values for E_a are in a reasonable range, with E_a for Na^+ transport being higher than for Li^+, as it has been expected, due to the difference in the ionic radius. Comparison with literature is not easy, since comparable values of E_a may vary dependent on the technique of determination. Tab. 5.10 refers to different sources in literature. E_a as obtained by Neuhaus et al. showed the best agreement with the presented data [150]. The sample setups are comparable, whereas Neuhaus used Na^+ doped polyimide as host matrix. One can easily claim, that the value from [150] and from this thesis, accounts for E_a of Na^+ incorporation at the PMMA / SiO_2 interface. Though, as mentioned in section 5.2.1, the measured sample resistivity clearly indicated SiO_2 itself as the rate determining step for Na^+ transfer.
- Variations of E_a between different SiO_2 film thicknesses may have various reasons. Apart from simply caused by errors due to the data fit by means of a linear regression, the blank sample could have contributed in a too high or too low manner. Additionally a difference in the Na^+ transport

behavior in dry oxide (100 nm, 200 nm) and wet oxide (400 nm), as given in the material description in Tab. 3.1, may have an effect on E_a.

- The obtained values for k_0 did not allow any physical conclusions, as the different samples vary within orders of magnitudes. Even within a set of analyzed data according to eq. (5.10) there is an unacceptable deviation of approximately one magnitude. The apparent reason for this deviation was the linear regression as illustrated in Fig. 5.20. Extrapolation to the incident point with the y-axis led to large errors, which disabled any reasonable data interpretation.

Table 5.10.: Comparison of E_a for mobile ion transport in SiO_2 with literature values.

Reference	E_a [eV]	Temperature range [°C]	Approach
Na^+ transport in SiO_2			
This thesis	1.55 - 2.04	130 - 190	Butler-Volmer
This thesis	0.87 - 1.45	130 - 170	Nernst-Einstein
[16]	1.38	70 - 200	C-V plot
[13]	0.75 - 1.10	250 - 300	positive B-T stress; radiochemical analysis
[150]	1.90	200 - 300	Transient charge-time plot
[117]	0.44	100 - 300	Isothermal transient ion current
[47]	1.30	N/A	N/A
Li^+ transport in SiO_2			
This thesis	1.14	130 - 190	Butler-Volmer
This thesis	0.99	130 - 170	Nernst-Einstein
[117]	0.47	100 - 300	Isothermal transient ion current

5.2.3. Diffusion of mobile ions in SiO_2

Nernst-Einstein equation

As discussed in section 2.4 drift and diffusion are coupled phenomena. Considering Nernst-Einstein relation (eq. (2.23)) with c taken from $\phi_{Na^+,calc}$, the conductivity of the SiO_2 during B-T stress experiments gave the diffusion coefficient D_α, a quantity which however does not relate directly to thermal diffusion according to Fick's law. Specific conductivities could be obtained from B-T stress data by reciprocal resistivities. According to eq. (2.17), the temperature dependence of D_α can be plotted in an Arrhenius plot, thus in an analog manner that it has been done in Fig. 5.20. Rearrangement of eq. (2.17) to a linear function gives

$$\ln(D_\alpha) = \frac{-E_a}{R \cdot T} + \ln(D_{\alpha,0}) \tag{5.11}$$

For representative purposes, Fig. 5.21 shows an Arrhenius plot including linear regression of the data for Na^+ transport in SiO_2, using the data from the I-V and I-T ramps in Fig. 5.14. Further Arrhenius plots of examined samples are given in the Appendix A. Again, from the slope of linear regressions E_a could be obtained and $D_{\alpha,0}$ from the intercept points with the y-axis. Tab. 5.11 lists the acquired values of E_a and $D_{\alpha,0}$ for different types of samples. Additionally, for reasons of comparison with values obtained from the modified Butler-Volmer approach and with literature values, the obtained E_a is included in Tab. 5.10.

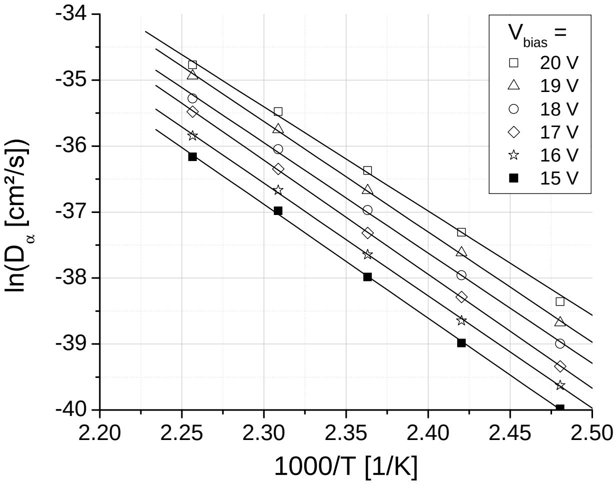

Figure 5.21.: Arrhenius plot of the data in Fig. 5.14 (Na^+ transport in 100 nm SiO_2, c_{NaOTf} = 300 ppm) according to Nernst-Einstein equation for the temperature range 130 °C - 170 °C.

Table 5.11.: E_a and $D_{\alpha,0}$ for mobile ion transport in SiO_2 out of data analysis according to Nernst-Einstein equation for different samples. Each data entry is an average over 6 linear regressions as given in Fig. 5.21.

d_{SiO_2} [nm]	E_a [eV]	$D_{\alpha,0}$ [cm^2/s]
Na^+ transport in SiO_2		
100	1.45 ± 0.05	15.6 ± 9.76
200	0.87 ± 0.02	$1.01 \cdot 10^{-6} \pm 0.70 \cdot 10^{-6}$
400	0.95 ± 0.01	$4.22 \cdot 10^{-6} \pm 2.58 \cdot 10^{-6}$
Li^+ transport in SiO_2		
400	0.99 ± 0.03	$7.47 \cdot 10^{-6} \pm 4.66 \cdot 10^{-6}$

$D_{\alpha,0}$ values for Na^+ transport in 100 nm SiO_2 gave a $D_{\alpha,0}$, 7 magnitudes higher than for the other samples. This arises from a slightly different R_{SiO_2} characteristics between the single temperatures for the SiO_2 100 nm layer.

Butler-Volmer vs. Nernst-Einstein

As given in Tab. 5.10 calculations by means of Nernst-Einstein, resulted in slightly lower values for E_a than obtained via the modified Butler-Volmer approach. In order to examine the calculated E_a values on their reliability, some comparisons were carried out.

In the following the results from section 5.2.2 (modified Butler-Volmer approach) and the from Nernst-Einstein equation based calculations are compared with regard to diffusivities. On atomic scale k in eq. (5.4) is connected to the Diffusion coefficient D, according to Fick's law (eq. (2.12) by

$$D = a \cdot k \tag{5.12}$$

with a assumed to be 25 Å as mentioned in the previous section. k can be calculated by the Boltzmann relation in eq. (5.4) using the data from Tab. 5.6 - 5.9 with k_0 taken as average over 6 values. As already mentioned, k_0 is not a reliable physical quantity, due to the large error of the obtained values. However, since that error arose mainly from extrapolation, k-values in the temperature range of $\sim$ 100 °C - 200 °C did not exhibit that large deviation. A qualitative comparison of D derived from Butler-Volmer data with data from Nernst-Einstein equation seems therefore reasonable. Fig. 5.22 shows Arrhenius plots of diffusion constants for Li^+ and Na^+ in SiO_2, with additionally attached plots from literature values. Note that values acquired by Nernst-Einstein equation actually account for D_α.

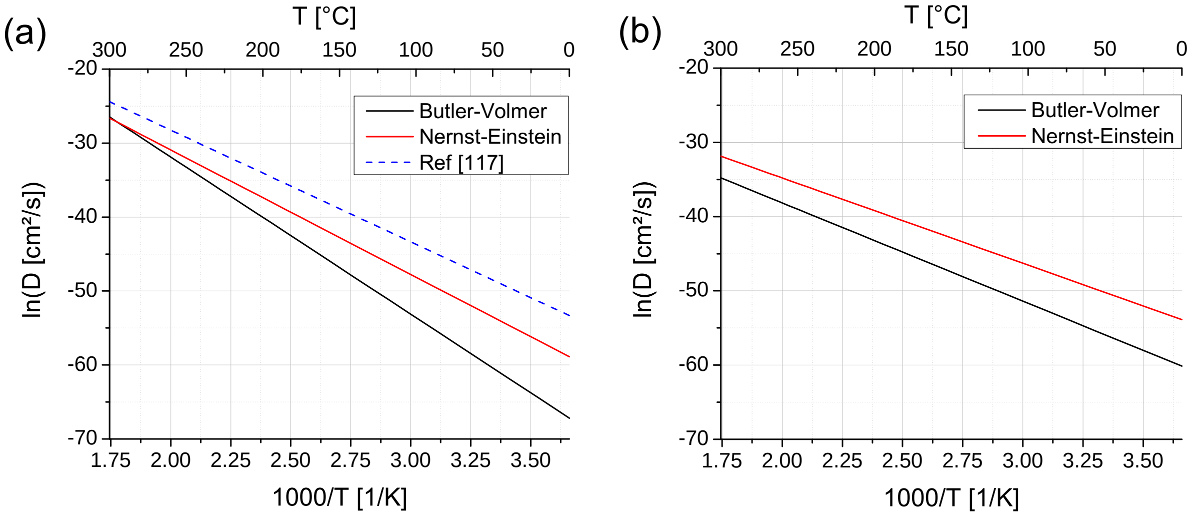

Figure 5.22.: Comparison of diffusivities, obtained from modified Butler-Volmer approach and Nernst-Einstein equation. (a) Na^+ diffusion in SiO_2 (plotted from values obtained from sample comprising 100 nm SiO_2). (b) Li^+ diffusion in SiO_2. A plot from literature values [47] is included.

The agreement of the two applied approaches was quite good for Na^+ (Note the logarithmic scale in Fig. 5.22(a)). However, the diffusivity from Ref. [47] was way faster. Li^+ diffusivities from the two approaches differed more than for Na^+. This was mainly due to significant differences in D_0 while E_a had a fairly good agreement. A possible reason for this deviation of the two plots of Li^+ diffusivities is the difference of D to D_α, which is not considered in Fig. 5.22. A better comparison could be possible by knowledge of the respective Haven ratios (e.g. [44]).

In order to check, D and E_a values on their reliability, a calculation according to the appropriate solution of Fick's second law (eq. (2.16)) was done. Thus, a situation with the diffusing species of dose $\phi_{Na+,calc}$ deposited onto the surface of SiO_2 and spreading into one half-space was assumed [44]. Therefore, mobile ion incorporation for an external source into SiO_2 and pure thermal diffusion could be illustrated as diffusion profiles. The respective D values are extracted from Fig. 5.22(a). Basically parameters as obtained from data analysis with the modified Butler-Volmer approach for Na^+ transport in 100 nm SiO_2 were used. Three different diffusion times were chosen, with the diffusion length $2 \cdot \sqrt{D \cdot t}$ as the important parameter indicating the progression of mobile ion incorporation and thermal in-diffusion: 1 week, 1 year and 10 years. Fig. 5.23(a-c) show the different comparisons from plots of eq. (2.16):

(i) In Fig. 5.23(a), the diffusion time was varied at a constant temperature of 150 °C.

(ii) The temperature impact of diffusion profiles is shown in Fig. 5.23(b) for a constant diffusion time of 1 week.

(iii) In Fig. 5.23(c), a comparison of diffusion profiles with D, obtained by the modified Butler-Volmer approach, Nernst-Einstein equation and D according to literature, is given. The temperature was set to 150 °C for a diffusion time of 1 week. Tab. 5.12 lists the obtained diffusion lengths. A comparison with quantification of a ToF-SIMS depth profile is given, after keeping at a constant temperature of 150 °C for 1 week (Fig. 5.23(d)).

Calculated diffusion profiles show a significant in-diffusion at temperatures $> 100\,^\circ$C with a diffusion length of > 5 nm. Comparison of calculated diffusion profiles with the ToF-SIMS profile of a real sample kept at constant temperature gave some hints on the reliability of parameters, describing thermal diffusion by two different approaches. In this comparison, the literature value as well as the diffusion length according to the Nernst-Einstein related profile, seems to give too large values (Tab. 5.12). The calculated diffusion lengths were larger as the SiO_2 layer thickness and could therefore not be reliable values for the present system. On the other hand, the diffusion length according to Butler-Volmer (39 nm) was more reasonable. The ToF-SIMS depth profile showed however no Na^+ incorporation at all. If there would be incorporated Na^+ present within SiO_2, a significant peak at the SiO_2 / Si interface would be detectable. The peak visible in Fig. 5.23(d) solely occurs by Na^+ traces due to Au sputter process and accounts for a Na^+ free sample[1]. Two reasons for this behavior are considered:

(i) Note that, due to the formalism of eq. (2.16) on each time, the totally provided $\phi_{Na+,calc}$ could be detected within SiO_2. This solution of Fick's second law assumes the external Na^+ source as infinitesimal thin sheet deposited on SiO_2. Thus integration of the diffusion profiles would always result in $\phi_{Na+,calc}$. Real samples contained a host matrix of a certain thickness, though. Therefore M within eq. (2.16) is certainly larger than the actually Na^+ dose present at the PMMA / SiO_2 interface in real samples.

(ii) For practical purposes it was necessary to remove the host matrix of the sample kept at 150 °C for 1 week. This lift-off procedure possibly leached Na^+ out of the first few nanometers of SiO_2. For deeper layers this was certainly not the case, which confirms that parameters derived from Nernst-Einstein equation and taken from literature considered a too fast diffusion of Na^+ in SiO_2 for the present sample setup.

Table 5.12.: Diffusion lengths out of Fig. 5.23(c) and (d).

Profile	$2 \cdot \sqrt{D \cdot t}$ [nm]
Diffusion profile acc. to Butler-Volmer	39
Diffusion profile acc. to Nernst-Einstein	141
Diffusion profile acc. to Ref [47]	734

5.3. Investigations of thin nitride containing films: SiO_xN_y, Si_3N_4

Different to SiO_2 films, nitride-containing Si-based materials are well known to be a barrier against mobile ion transport [26]. But how do these materials react on such rigorous B-T stress conditions with respect to mobile ion transport as presented for SiO_2 in section 5.1.3? For Na^+ incorporation and transport two materials were investigated and set in comparison with pure SiO_2 films: SiO_xN_y and Si_3N_4. The nitrogen content increased according to $SiO_2 < SiO_xN_y < Si_3N_4$. All layers had a constant thickness of 400 nm, covered with a ~100 nm PMMA host matrix ($c_{NaOTf} = 300$ ppm), and were B-T stressed using $V_{bias} = 160$ V ($E = 4$ MV/cm) at 50 °C. Samples with nitride-containing material films on Si showed no dielectric breakdown even when $V_{bias} = 160$ V was applied during B-T stressing. In contrast to that, for SiO_2 films a 50% drop out was observed as given in section 5.1.3.

---

[1] This topic has been discussed in detail in section 4.2.1; compare to Fig. 4.6.

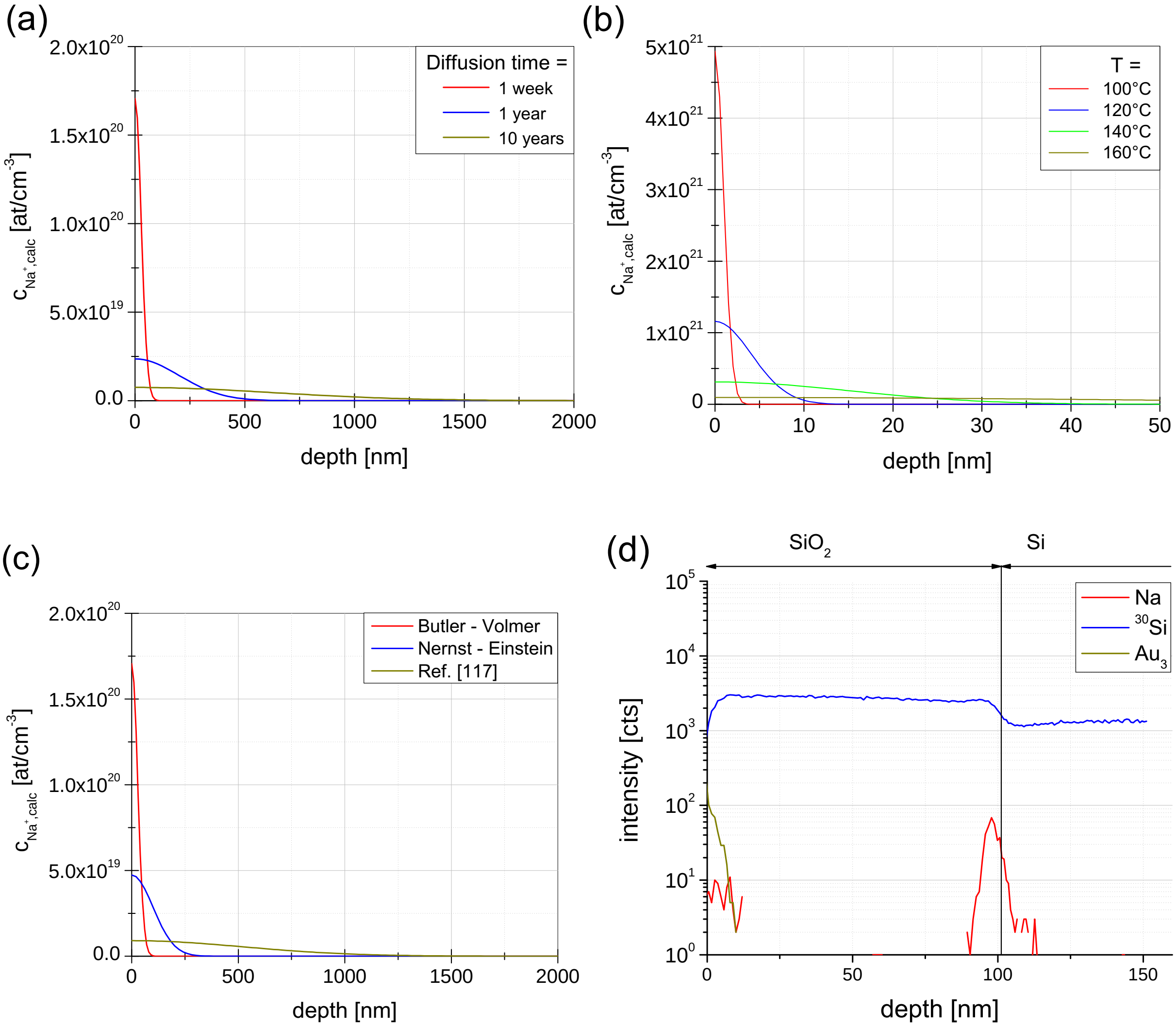

Figure 5.23.: Diffusion profiles calculated by eq. (2.16) using data from Fig. 5.22(a). The different comparisons are given: (a) diffusion time variation, (b) temperature variation and (c) different approaches to calculate D using data from Tab. 5.10 and Tab. 5.11. (d) shows the ToF-SIMS depth profile after keeping a sample with a host matrix comprising $c_{NaOTf} = 300$ ppm 1 week at 150 °C. The top Au layer was not considered in the presentation of the depth profile for reasons of comparison with diffusion profiles.

Fig. 5.24 shows ToF-SIMS depth profiles of the B-T stressed samples and comparison to a 400 nm SiO_2 film. Due to the enormous bias voltage for the 400 nm SiO_2 film, it was not feasible to apply $V_{bias} = 160$ V during B-T stress application. For that reason, the 400 nm SiO_2 film was BT stressed with $V_{bias} = 120$ V ($E = 3$ MV/cm), qualitatively resulting in the same profile characteristics. These more gentle conditions prevented dielectric breakdown, and a proper comparison could be given.

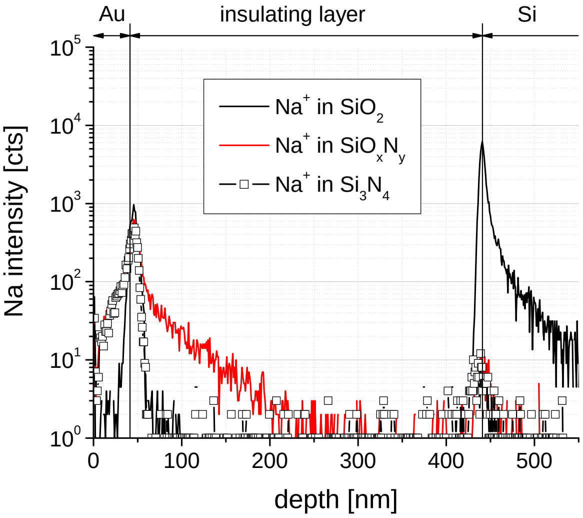

Figure 5.24.: ToF-SIMS depth profile of insulating films (SiO_2, SiO_xN_y and Si_3N_4; 400 nm film thickness) after BT stress using E = 4 MV/cm. The Na^+ permeability of the insulating layer was suppressed with increasing nitride content.

In general, the results of B-T stress application showed the same tendency as already observed for Na migration during ToF-SIMS depth profiling (Fig. 4.8). In section 4.2.2 the structural properties of SiO_2, SiO_xN_y and Si_3N_4 have been discussed. Due to structural reasons, Na^+ diffusivity and thus permeability through the nitride containing insulating layer is severely hindered. From Fig. 5.24 it is obvious that in contrast to SiO_2, Si_3N_4 did not exhibit any permeability to Na^+ ions during B-T stressing. Thus, no incorporation took place in Si_3N_4, even at such rigorous bias voltage conditions. This property makes the Si_3N_4 a material with superior attributes for the use as mobile ion barrier layer in semiconductor devices in crucial regions of a device.

The SiO_xN_y film however showed a slight tailing towards the insulators bulk. In contrast to SiO_2, the detected magnitude of Na in SiO_xN_y was very low, and no Na^+ reached the SiO_xN_y / Si interface in the chosen time interval, although rigorous BT conditions were applied. A lower V_{bias} or a lower sample temperature decreased the depth in SiO_xN_y where Na^+ could still be detected (In Fig. 5.24 ~200 nm) until for $V_{bias} = 80$ V no difference to a blank signal could be observed anymore (not shown in Fig. 5.24).

5.4. Investigations of thin BPSG films

Following up Na migration experiments, as presented for BPSG in section 4.2.3, this material was also assigned to B-T stress. The examined sample consisted of a PMMA host matrix (thickness = 77 nm; c_{NaOTf} = 300 ppm), attached on a specimen with the sequence 910 nm BPSG / 400 nm SiO_xN_y / Si-substrate. As usual, a 40 nm Au layer served as anode for B-T stress application. V_{bias} = 182 V [1] was applied for 10 min. This resulted in an electric field of E = 1.39 MV/cm. In Fig. 5.25 the detected SMU response signal as a function of time is plotted in its integrated form. A resembling behavior has been shown in Fig. 5.13(a), for K^+ incorporation transport experiments in SiO_2 using similar B-T stress conditions (resulting in E = 4 MV/cm). Therefore, the detected $\phi_{Na^+,DC}$ is assumed to be attributed to sole secondary effects as leakage currents.

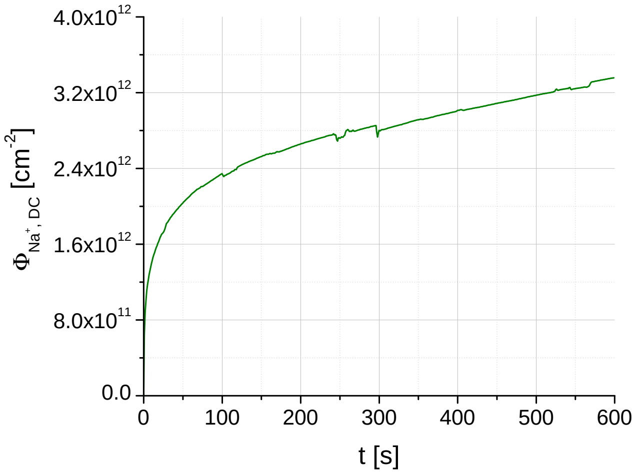

Figure 5.25.: Detected SMU response current during B-T stress, integrated over time and converted into $\phi_{Na^+,DC}$, from a sample comprising 910 nm BPSG (on 400 nm SiON). V_{bias} = 182 V.

In section 4.2.3 it was found that Na migration during depth profiling had a strong temperature dependency. Therefore, the profiles after B-T stress were acquired at two different sample temperatures as given in Fig. 5.26. The incorporated Na^+ is located in BPSG, close to the interface to Au. As for the potentiostatic SMU response this resembles the depth profile of SiO_2, after K^+ incorporation (Fig. 5.13(b)). Na^+ did not get pumped into BPSG by an enormous electric field. In fact, an effective gettering of Na^+ in BPSG is considered to be the reason of the profile characteristics in Fig. 5.26. Keeping the sample temperature at RT, an artifact concealed the information in the depth profile. Although even at -130°C Na migration could not be avoided completely, a much more realistic scenario is considered in the

---

[1] Note that the used voltage source was could provide a maximal V_{bias} of 200 V. E = 2 MV/cm could not be achieved due to this reason.

obtained depth profile of Fig. 5.26(a). The maximum of the Na^+ peak in BPSG at ~60 nm should not be severely shifted due to Na migration. However, the tailing towards the BPSG / SiO_xN_y interface is considered to be affected by Na migration.

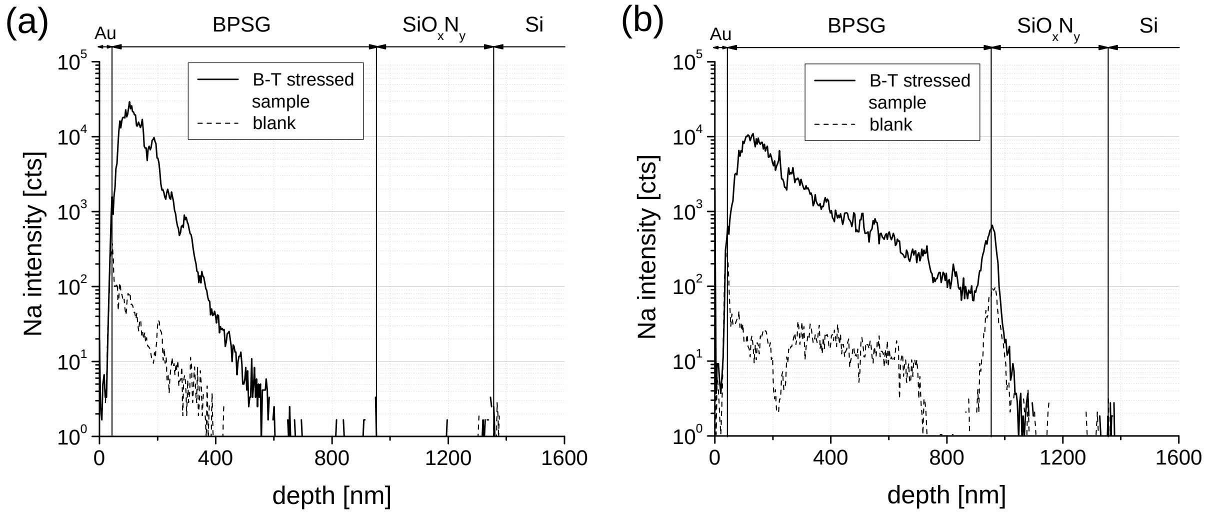

Figure 5.26.: ToF-SIMS depth profiles of the BPSG film containing sample obtained at (a) -130°C and (b) RT. For reasons of comparison, depth profiles from a blank sample (i.e. without attached host matrix) are included by means of a dashed line. 2 keV O_2^+ was used for sputtering.

In Fig. 5.26(b) Na migration caused a transport of Na^+ all the way to the BPSG / SiO_xN_y interface. However, no significant transfer into SiO_xN_y was detected[1].

The following conclusion can be drawn from these experiments:

(i) BPSG gettered Na^+ effectively within the first ~100 nm. BPSG had thus not the property as a barrier layer during B-T stress experiments as shown for Si_3N_4 and, in a lower efficiency, for SiO_xN_y in the previous section.

(ii) Comparison of ToF-SIMS depth profiles of B-T stressed samples in Fig. 5.26, with profiles of sample before B-T stress (thus with the host matrix still attached on the specimen during analysis as given in Fig. 4.9) reveals that a larger amount of Na^+ was incorporated into BPSG by Na migration than by B-T stress. This implies that during sputtering with O_2^+ a higher voltage was induced on the insulating layers that applied via V_{bias}. The induced voltage on the insulator surface is hence assumed to be higher than a few volts as given by the estimation in section 4.1. At least, the occurred charge-up was sufficient to cause effective Na^+ incorporation into BPSG solely by means of Na migration.

---

[1] Note the logarithmic scale in Fig. 5.26. Much more Na^+ accumulation at the BPSG / SiO_xN_y interface is necessary to cause a detectable Na^+ transfer into SiO_xN_y (as given in Fig. 4.9).

(iii) Considering a host matrix containing $\phi_{Na^+,calc} = 5.86 \cdot 10^{14}$ cm^{-2}, the 910 nm BPSG film was capable to getter the entire provided amount of Na$^+$. However, the getter efficiency is considered to be reduced when $\phi_{Na^+,calc}$ would be significantly higher, hence when the effective getter centers are saturated. In literature a 12.5 nm PSG layer has been shown to be an effective barrier against 10^{12} Na$^+$/cm^{-2} [137].

Chapter 6

Mobile ion incorporation and transport in conductive materials

In this chapter, a aluminum-silicon-copper alloy (AlSiCu), a material of major importance for device fabrication, is investigated in terms of incorporation by sodium (Na) from an externally attached host matrix. AlSiCu is a prominent candidate for metalization to achieve electrical contact between different components in a device. As given in Fig. 3.4(b), the sample setup was slightly different from those for samples comprising an insulating top layer. Thin films of PMMA (up to ∼130 nm), attached via spin coating of a host matrix formulation were not appropriate for experiments on samples with a conductive top layer. As illustrated in Fig. 3.4(b), the host matrix had to endure the complete voltage drop, governed by V_{bias}. At an application temperature of 150 °C a thin PMMA layer would be rendered to very low resistivity. Performing the sample preparation step by step according to Fig. 3.1, the sample check at 150 °C by means of an ohmmeter would indicate a short circuit between gold (Au) and the conductive AlSiCu layer by dielectric breakdown. Thus, conductive paths were present in the thin PMMA film.

There were two possibilities to counteract this problem: (i) Application of an alternative host matrix, which could handle huge electric fields for a long time (i.e. hours) without exhibiting short circuits. As discussed in section 3.1.1, a positive photoresist was used for this purpose. (ii) The PMMA layer thickness had to be increased, in order to keep the host matrix resistive, even at high temperatures. Acetonitrile as solvent in host matrix formulations could only dissolve up to 4 wt% PMMA, with the formulation remaining at an appropriate viscosity for the application for spin coating (see section. Therefore anisole was used as PMMA solvent, enabling higher concentrations of the polymer in the host matrix formulation. In order to keep the PMMA layer thickness as large as possible, the host matrix formulation was not attached onto the specimen by spin coating, but by putting one drop of the formulation on the specimen surface and performing a bake-out procedure for solvent vaporization[1]. However, one big disadvantage of both possibilities is that neither enabled the calculation of an exact $\phi_{Me^+,calc}$ as done for the spin coated PMMA host matrix in the previous chapter.

The used AlSiCu is a polycrystalline material. In semiconductor devices, barrier layers are commonly used to avoid interdiffusion between the metalization layers and adjacent materials. E.g. titanium nitride (TiN) prohibits for instance interdiffusion between Al and Si. Usually a thin Ti layer is applied as adhesion promotor for TiN. For the experiments of this chapter two specimen were manufactured in order to evaluate possible differences in mobile ion transport due to different materials as present at the surface prior to AlSiCu deposition:

- Without barrier layer: 1 μm AlSiCu / 200 nm SiO_2 / Si-substrate.
- With barrier layer: 1 μm AlSiCu / 200 nm TiN / 20 nm Ti / SiO_2 / Si-substrate.

Fig. 6.1 shows images of the specimen surface prior to host matrix attachment as obtained by scanning electron microscopy (SEM)[2].

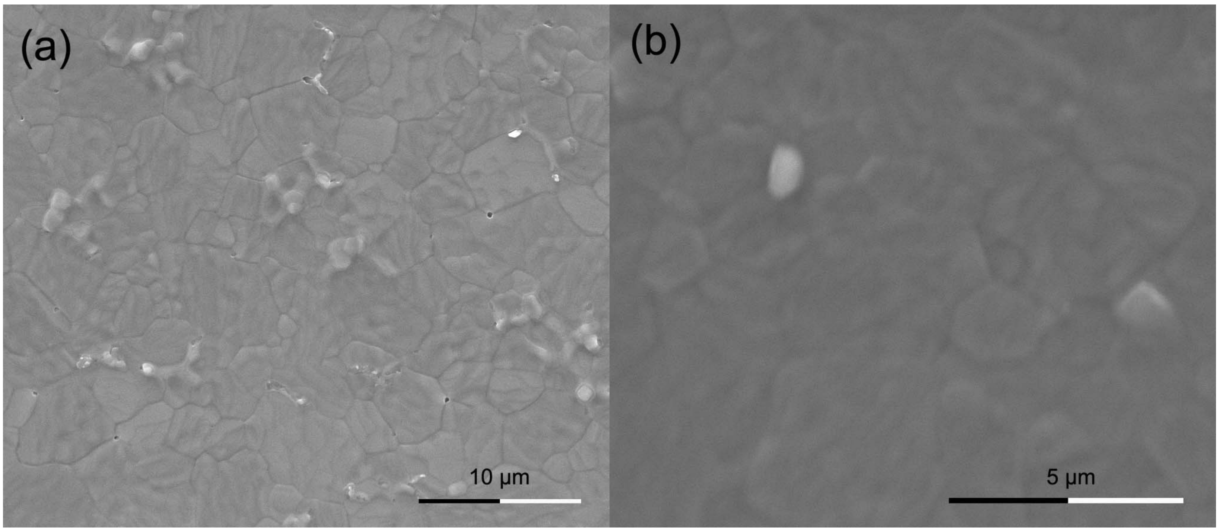

Figure 6.1.: SEM images of the AlSiCu surface. (a) specimen: AlSiCu / SiO_2 / TiN-Ti / Si-substrate. (b) specimen: AlSiCu / SiO_2 / Si-substrate.

For Fig. 6.1(a), the polycrystalline appearance of the AlSiCu surface can be properly observed, showing a distinctive grain boundary structure with a grain size in the one-digit μm region. However, a second important feature are protrusions on the specimen surface, identified as hillock formations. Hillocks arise due to relief of thermally-induced compressive stress on thin metal films [151]. Both mentioned specimen

---

[1] For details on host matrix deposition see section 3.1.2

[2] Instrument: FEI Quanta 200.

comprising AlSiCu layers exhibited these features. A distinctive roughness had thus to be considered for AlSiCu surfaces. The diameter of hillocks are in the range of 1 - 3 μm. Fig. 6.2 shows a sketch of a cross-section through the sample setup, in order to give an idea on its structure. Due to the grain size $>$ 3 μm, the grain boundaries were considered to be grown through the entire AlSiCu layer.

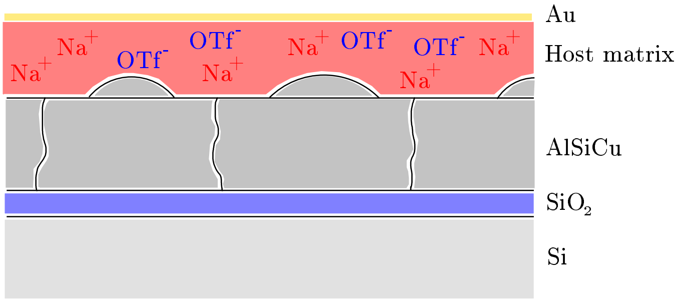

Figure 6.2.: Cross-section schematically sketched without consideration of real scales. Note the hillock formations on the AlSiCu surface and the indication of the grain boundaries between single AlSiCu grains.

In the following two sections, B-T stress experiments on the mentioned samples are presented. The way of sample contacting has already been illustrated in section 3.2 (Fig. 3.4). Note that in a conductive layer no electrical potential difference exists. Thus the driving force for mobile ion transport according to eq. (2.18) is the gradient in the chemical potential μ, i.e. pure thermal diffusion. The relevant parameter for this process is the sample temperature. Since, the aim of the studies was to examine, whether AlSiCu is permeable for mobile ions a host matrix formulations containing a large amount of Na^+, c_{NaOTf} = 900 ppm was applied. Experiments were solely carried out using Na^+ as the mobile ion, due to its immense relevance for reliability issues in semiconductor devices. For PMMA, applied as one drop of the host matrix formulation at AlSiCu and post-processed via bake-out in order to vaporize the solvent, a layer thickness evaluation did not make sense due to the convex appearance of the attached host matrix. The generated electric field, which quantity is an unknown value, was therefore inhomogeneously distributed. Only locally, in the magnitude of some microns an approximation by means of a plate capacitor was reliable.

As usual, a lift off procedure was used, in order to remove the host matrix prior to analysis by means of ToF-SIMS depth profiling. Basically depth profiling for the B-T stressed samples in this chapter was carried out using 2 keV ${O_2}^+$ for sputtering. Different to measurements in chapter 5, the BA mode was used for ToF-SIMS analysis (for the different ion optical modes concerning the primary ion gun see section 3.3.1). This mode is beneficial for measurements on AlSiCu, in order to achieve a proper lateral resolution of grain boundaries and hillocks on the surface.

6.1. Positive photoresist for the use as host matrix

As given in the experimental part in section 3.1, a positive photoresist was considered to be an appropriate host matrix for B-T stress application. Gentle spin coating conditions enabled the deposition of a ∼10 μm thick photoresist layer. Protection of a 0.5 mm broad strip at two opposing sample edges by means of adhesive strips left small blank regions. This was necessary, in order to achieve an electric contact to the AlSiCu layer. Note that, as mentioned in section 3.2, the use of positive photoresist restricted the temperature during B-T stress to 100 °C. Theoretically also 130 °C could be applied, however with the drawback of rendering the host matrix too brittle. Cracks, both in the host matrix and thus in the deposited Au layer, would be the consequence, with the result in short circuiting between Au and AlSiCu. $V_{bias} = 200$ V were applied by default, in order to achieve the highest achievable Na^+ incorporation rate. This was the highest possible voltage for the used voltage source.

Fig. 6.3 depicts a typical SMU response signal in terms of the detected current and its integrated version (Q [C]). This characteristic was obtained for samples with both above mentioned setups, i.e. with or without TiN-Ti layer. This is evident, since the voltage was applied between Au and AlSiCu without affecting the layers below.

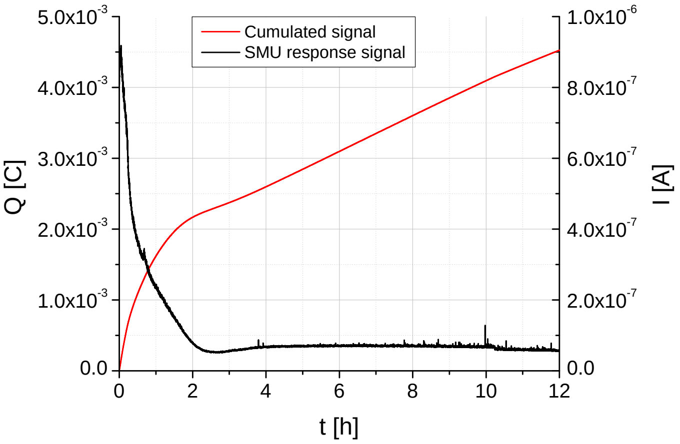

Figure 6.3.: Typical SMU response current and the respective integrated form for B-T application on a sample comprising an AlSiCu layer beneath the host matrix consisting of ∼10 μm positive photoresist. Conditions: $V_{bias} = 200$ V; 100 °C sample temperature.

Similarly to the data out of B-T stress experiments of insulating samples, the reason for the response current in Fig. 6.3 is of crucial interest:

(i) For samples comprising an insulating layer deposited onto n-doped Si, the SMU response current is considered to be equal to the mobile ion incorporation current at the host matrix / insulator surface.

Analog for the situation of the insulating host matrix attached on conductive AlSiCu a resembling scenario is expected. Considering a low electronic leakage current through the host matrix, there is again the requirement for charge neutrality at the host matrix / AlSiCu interface. If thus Na^+ from the host matrix bulk approached the vicinity of the interface, the same number of electrons must be delivered from the AlSiCu facing side. This electronic current in turn would be detectable by the SMU amperemeter.

(ii) Similarly to experiments with insulating films no conclusion whether Na^+ incorporated into AlSiCu could be drawn solely from potentiostatic data.

6.1.1. Localization of Na^+ after bias-temperature stress

In Fig. 6.4 the corresponding ToF-SIMS depth profile after 12 h B-T stress at $V_{bias} = 200$ V is presented. The profile was quantified, using $RSF_{Na,M} = 8.75{\cdot}10^{15}$ (see Tab. 3.9) and is hence presented in concentration vs. depth. Profile reconstruction from raw data therein was carried out without the first two scans, i.e. starting after some seconds of pre-sputtering. This was done in order to avoid the addition of Na traces at the AlSiCu surface. An exponential decay towards the AlSiCu bulk is observable. This could indicate the incorporation of Na^+ from the host matrix into the underlying conductive layer and thermal diffusion therein. All other signals remained at a constant level during sputtering in AlSiCu (after a short period, i.e. 1 - 2 scans, of signal equilibration). In order to clarify the assumption of Na^+ incorporation, Fig. 6.4 was examined by secondary ion (SI) images reconstructed from obtained raw data.

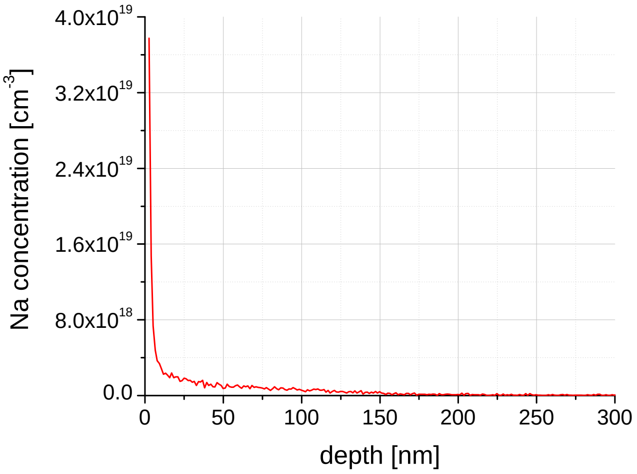

Figure 6.4.: ToF-SIMS depth profile after B-T stress application of a sample consisting of the sequence: 1 μm AlSiCu / 200 nm SiO_2 / Si-substrate.

Fig. 6.5(a) shows the Na SI image, corresponding to the depth profile in Fig. 6.4 (the illustrated image and thus the displayed Na intensity is the sum of all scans acquired during ToF-SIMS depth profiling). No laterally homogeneous distributed Na signal could be observed. The signal arose from single spots, randomly distributed in the 100×100 μm^2 field of view. A corresponding secondary electron (SE) image (Fig. 6.5(b)) was acquired prior to ToF-SIMS depth profiling. The SE image shows the same features as observed in Fig. 6.2, with the AlSiCu grains appearing in distinguishable gray scales and hillocks properly observable at the sample surface. A feature of the SE image, is shadowing as observable on the right hand side edge of each hillock. This is caused due to the 45° incident angle of impacting primary ions during image acquisition, which leaves a non bombarded region next to the hillock , where no SE signal can be generated. This problem regarding to sample topography is of course encountered also for secondary ion generation during ToF-SIMS analysis [152].

An overlay of SI and SE images, revealed that the detected Na signal arose from the hillock positions (Fig. 6.5(c)). Some additional minor traces were detected from other positions as well. This is attributed to remnants from surface contaminations at this position, which did not get removed during the first two scans of pre-sputtering. In Fig. 6.5(d) a cross section in xz direction through the analyzed volume is shown. Note that the proportions in the cross-section are distorted. The z-size of the image, accounting for 200 nm, is given by the maximum sputter depth of the profile in Fig. 6.4. The x-size of the image is the same as for SI and SE images.

Fig. 6.6 shows a 5× close up of a large elevation, arguably a hillock, at the AlSiCu surface by means of a Na SI image and the SE image corresponding to the field of view, showing a high intensity Na secondary ion signal arising from the potential hillock. The SE image emphasizes the mentioned shadowing effect during primary ion bombardment due to surface topography.

From the information out of Fig. 6.5, the following cognitions can be concluded:

- During application of B-T stress, Na^+ got transported to the host matrix / AlSiCu interface. According to ToF-SIMS depth profile analysis, the preferred locations for Na^+ attachment at the AlSiCu surface were identified as hillocks.
- Both the depth profile in Fig. 6.4 and the xz cross section in Fig. 6.5(d) are afflicted by an artifact: In the illustration of ToF-SIMS data, the sample surface was assumed to be totally flat per default with sputtering beginning at $z = 0$. I.e. no topography was taken into account. However, the hillocks caused a certain topography. Assuming the AlSiCu layer at $z = 0$, the hillocks exhibited

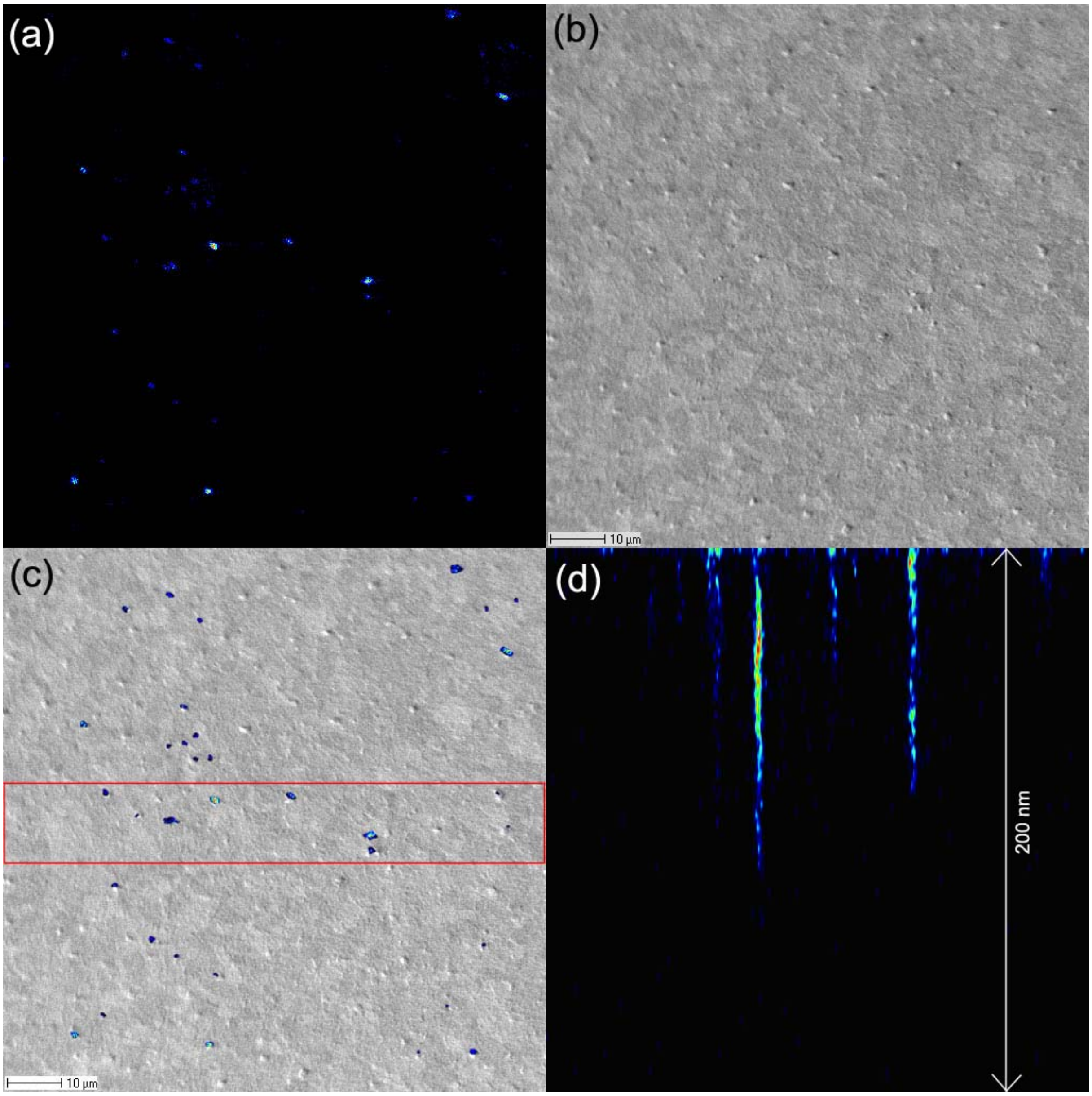

Figure 6.5.: (a) SI image, mapping the origin of Na signals at the chosen field of view. (b) Corresponding SE image. (c) The Na spots of the SI image were copied from the SI image, in order to obtain an overlay with the SE image. A 512 × 512 raster was chosen for primary ion bombardment, giving the pixel resolution of the acquired SI and SE images. (d) xz cross section through the first part of the sample, acquired by post processing of the raw data from ToF-SIMS depth profiling. A red rectangle in the SI/SE overlay, gives the projected position of the integrated data for the xz cross section.

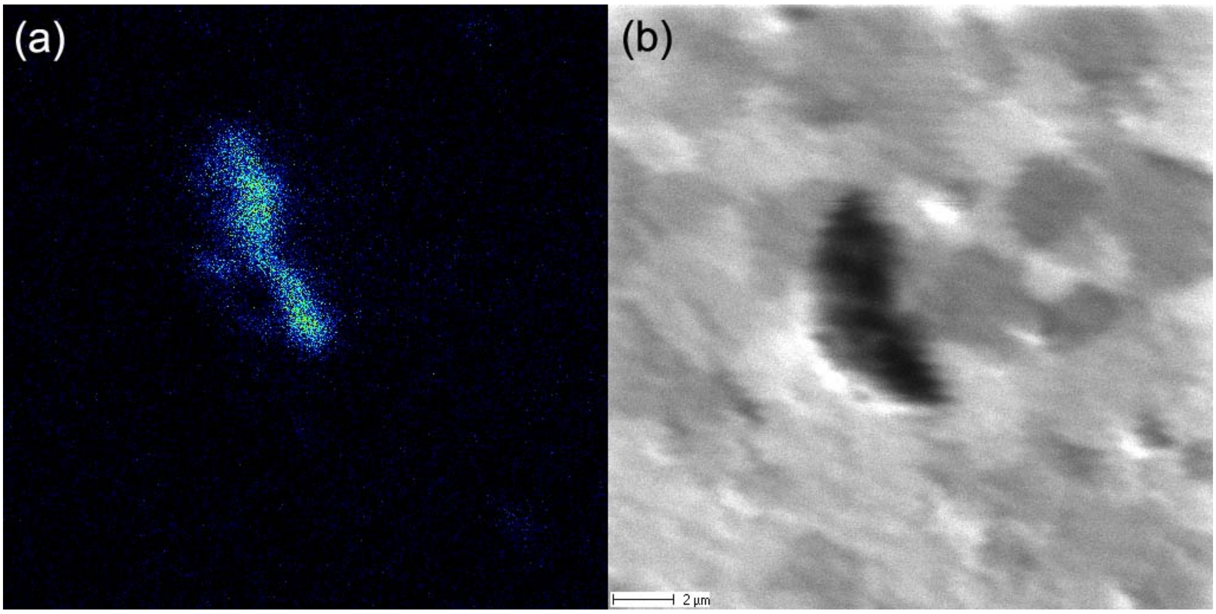

Figure 6.6.: Close up of an elevation at the AlSiCu surface, emphasizing Na^+ accumulation at this position. The field of view is 20 × 20 μm^2 (a pixel resolution of 512 × 512 was chosen for SI image acquisition). (a) Na SI image (b) SE image. Note the displacement of the two images in y-direction. In particular noticeable for very small raster sizes for the field of view, this was due to a slight lateral misalignment between SI and SE detectors in the used ToF-SIMS instrument.

thus negative z positions. A certain number of sputter cycles were thus necessary to achieve $z = 0$ at the hillock positions (Fig. 6.7). Due to this fact, an exponential decay is shown in the depth profile and Na spikes towards the AlSiCu bulk are observable in the cross section, but the detected Na was actually present on the surface of hillocks in the quantity as given from the depth profile in Fig. 6.4.

Considering this, the height of hillocks can be estimated from the xz cross section in the range of up to ~100 nm.

- No significant amount of Na^+ was detected in the grain boundaries. Based on the knowledge of the topography artifact in ToF-SIMS depth profiles, it has been shown that no Na^+ was incorporated into the AlSiCu bulk either. Thus, one can conclude that generally no Na^+ transited the host matrix / AlSiCu interface even at such rigorous B-T stress conditions with $V_{bias} = 200$ V. The applied voltage had barely the purpose of a driving force towards the interface, where an accumulation of Na^+ appeared (Na precipitations). The lift-off of the host matrix prior to ToF-SIMS depth profiling, carried out solely with acetone, left these Na precipitates at the AlSiCu surface. Two scans of pre-sputtering removed Na traces from the solvent.
- In ToF-SIMS depth profiles no significant amount of Na, assignable to Na^+ incorporation, was detected at the AlSiCu / SiO_2 interface.

- The detected potentiostatic SMU response signal in Fig. 6.3 cannot be assigned to a Na^+ transport current within the host matrix, with a stoichiometric number of electrons detected by the amperemeter in terms of charge neutrality at the interface to AlSiCu. The response signal is therefore assumed to be affected by a large amount of electric current, that arose by secondary effects as e.g. leakage currents through the photoresist. The steep linear increase of Q with the onset at ~2 h, corresponding to a steady SMU response signal, emphasizes this.
- The preferred attachment of Na^+ at the hillocks is assumed to have topographical reasons. From a thermodynamic point of view, it is obviously favorable to attach Na^+ at hillocks rather than at a flat AlSiCu surface or in grain boundaries.

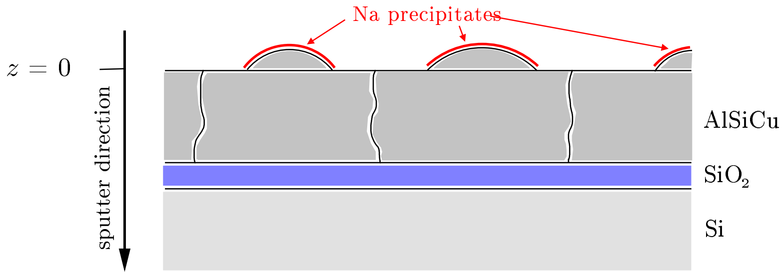

Figure 6.7.: Sketch of a cross section through the layer sequence of a specimen after B-T stress application. As a result of B-T stress Na precipitates are present on hillocks located at the AlSiCu surface.

B-T stress and subsequent ToF-SIMS depth profiling using a sample with a TiN-Ti layer between AlSiCu and SiO_2 gave the same results as the sample without TiN-Ti layer. Thus the barrier layer had no influence on the property of the AlSiCu surface topography in terms of transport and incorporation behavior of Na^+ under B-T stress.

6.1.2. Examination of process steps and parameters during sample processing

The aim of the experiments presented in this section was to evaluate the influence of each process step in the course of sample preparation as well as alterations due to differences in the B-T conditions. A set of samples was prepared and stopped in the process flow (compare to Fig. 3.1) at the respective step. This procedure was solely carried out for the specimen with the layer sequence 1 μm AlSiCu / 200 nm SiO_2 / Si-substrate.

ToF-SIMS depth profiling was carried out at different stages of sample processing:

1. Specimen: 1 μm AlSiCu / 200 nm SiO_2 / Si-substrate, as-received.
2. After spin coating of the host matrix formulation + bake-out; no B-T stress was carried out.

3. After keeping the sample for 12 h at a constant temperature of 100 °C. Host matrix lift-off solely with acetone.
4. After 4.5 h B-T stress (V_{bias} = 200 V; 100 °C). Host matrix lift-off solely with acetone.
5. After 12 h B-T stress (V_{bias} = 200 V; 100 °C). Host matrix lift-off solely with acetone.
6. After 12 h B-T stress (V_{bias} = 200 V; 100 °C). Host matrix lift-off with acetone and distilled H_2O (MilliQ 18.2 Ω/cm).

For each process step quantification of ToF-SIMS depth profiles (similar to that in Fig. 6.4) was carried out (Again with a field of view of 100 × 100 μm^2). As mentioned in the previous section, the quantified data represents the actual detected amount of Na at the sample surface, although the topography artifact had to be taken into account. Hence, it was possible to calculate the Na dose $\phi_{Na^+,SIMS}$, present at the AlSuCu surface. This was done by integration the quantified depth profiles, referred to respective integrated ^{27}Al signals. In order to be consistent, the integration boundaries were chosen from $z = 0$ nm to $z = 200$ nm. In this frame the entire signal was captured by the integration. Fig. 6.8 gives a bar diagram, comparing $\phi_{Na^+,SIMS}$ of each process step as given in the enumeration.

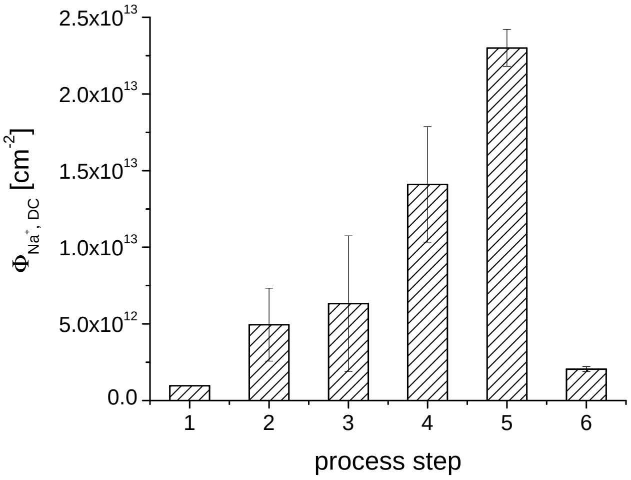

Figure 6.8.: $\phi_{Na^+,SIMS}$ from the AlSiCu surface, obtained by quantification of ToF-SIMS depth profiles, compared for different process steps as given in the enumeration in the text. Except from the "as-received" sample (process step 1), the data are averages from 3 - 4 measurements, with the standard deviation indicated by the error bar.

A negligible coverage with Na^+ was detected for the "as received" sample (step 1). The signal in the 10^{11} cm^{-2} magnitude arose from contaminations on the AlSiCu surface. For sole spin coating of the host matrix (process step 2) as well as for additional performed temperature treatment of the sample (process step 2), $\phi_{Na^+,SIMS}$ had the same magnitude. Large deviations in the data made a precise comparison impossible. The deviation occurred due to differences in the integral amount of detected Na^+ during depth profiling for different analysis areas. As soon as $V_{bias} = 200$ V was applied, an increase in the detected $\phi_{Na^{+},SIMS}$ could be observed (process steps 4 and 5), with larger detected amounts for longer B-T stress application time. This confirms the assumption from the previous section, that the generated electric field is the driving force for Na^{+} transport to the host matrix / AlSiCu surface. This is in agreement with other investigations on mobile ion transport, with basically $\nabla\widetilde{\mu}$ the driving force (see section 5.2.2). Rinsing the sample subsequently with distilled H_2O caused the removal of Na precipitates from the surface. As expected due to the hydrophobic nature of the solvent, sole lift-off with acetone only removed the host matrix without dissolving the Na precipitates.

The cognitions of Fig. 6.8 confirm two observations: First, Na^{+} was actually attached on hillocks as observable in Fig. 6.5(c) and second Na^{+} was unambiguously present solely at the AlSiCu surface, only removable by H_2O.

6.2. PMMA for the use as host matrix

In order to enable higher temperatures during B-T stress than 100 °C, a host matrix formulation containing 9 wt% PMMA in anisole ($c_{NaOTf} = 900$ ppm) was applied by attaching one drop at the AlSiCu surface (for the experimental procedure see section 3.1.2). The Au electrode had a dimension of 3×3 mm^2. The specimen for experiments consisted of the following layers: 1 μm AlSiCu / 200 nm SiO_2 / Si-substrate. B-T stress for 12 h was applied with $V_{bias} = 40$ V at a temperature of 190 °C. This conditions were chosen due to industrial relevance. In the previous section it has been shown, that V_{bias} was responsible for Na^{+} transport to the host matrix / AlSiCu interface. The value for the applied V_{bias} was thus assumed to be of minor relevance, if a certain threshold was exceeded. 40 V was considered to ensure Na^{+} transport in PMMA (compare to section 5.1.2). The relevant issue of this section is the use of a sample temperature of 190 °C, in order to examine its effect on possible Na^{+} transport by means of thermal diffusion in AlSiCu.

Fig. 6.9 shows the detected SMU response current (I [A]) and the respective cumulated signal (Q [A]). The characteristic resemble those obtained for Na^{+} incorporation into SiO_2 (section 5.1.2), with V_{bias} adjusted to obtain electric field of $E = 1.5$ -2 MV/cm. However, here a large amount of secondary effect superimpose to Na^{+} transport in PMMA and thus disabled a direct relation to the number of Na^{+} arriving at the interface host matrix / AlSiCu. As mentioned in the previous section, the conductive nature of AlSiCu would imply a stoichiometric number of electrons arriving at the interface from the AlSiCu facing side. Due to the secondary currents this could not directly be detected by the used ampere-meter.

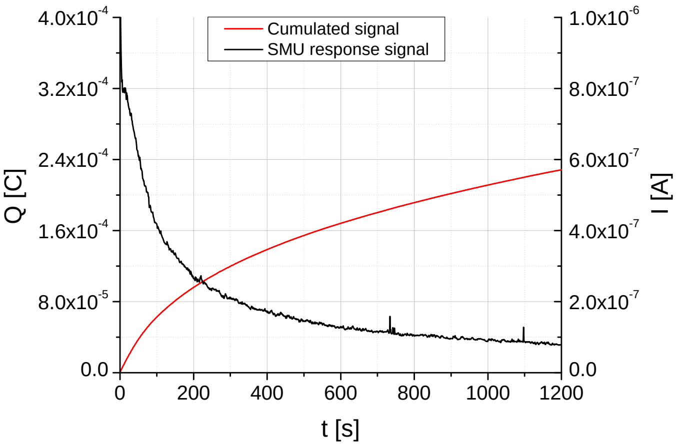

Figure 6.9.: Typical SMU response current and the respective integrated form for B-T application on a sample comprising an AlSiCu layer beneath the PMMA host matrix. Conditions: $V_{bias} = 40$ V; Temperature: 190 °C.

ToF-SIMS imaging

After B-T stressing, the host matrix was removed by acetone lift-off and analyzed via ToF-SIMS depth profiling. Fig. 6.10(a) shows the SI image of the Na signal, acquired during ToF-SIMS depth profiling. The corresponding SE image of the chosen field of view is presented in Fig. 6.10(b). The results were similar to those from Fig. 6.5, with Na precipitates attached on hillocks, that were located at the AlSiCu surface. Thus even for temperatures of 190 °C, no Na^+ incorporation into and transport within AlSiCu could be detected, neither in the AlSiCu bulk nor along the grain boundaries. Again, rising the AlSiCu surface with distilled H_2O removed Na precipitates as visible in Fig. 6.10(a).

Examination of the influence of topography on the deposition of Na^+ on a AlSiCu surface was done in the following manner: After attaching a drop of the host matrix formulation, a grid of scratches was generated at the AlSiCu surface using a pair of tweezers (carefully cleaned before use, in order to remove contaminants). Subsequently, the host matrix formulation drop was treated by the bake-out procedure. Apart from generating a distinctive topography at the AlSiCu surface, this procedure had a second advantage: Native Al_2O_2 was removed from the specimen surface, without the possibility of instantaneous regrowth, since the specimen surface was protected by the host matrix formulation. Thus the influence of the native Al_2O_2 on Na^+ incorporation into AlSiCu could be evaluated.

Fig. 6.10(a) and (b) shows the corresponding Na SI image and the SE image, respectively. The topography of the scratch, deliberately cut in the AlSiCu surface, is properly visible in the SE image. Corresponding to the material protuberances along the scratch, a significant signal is visible in the Na SI image. This

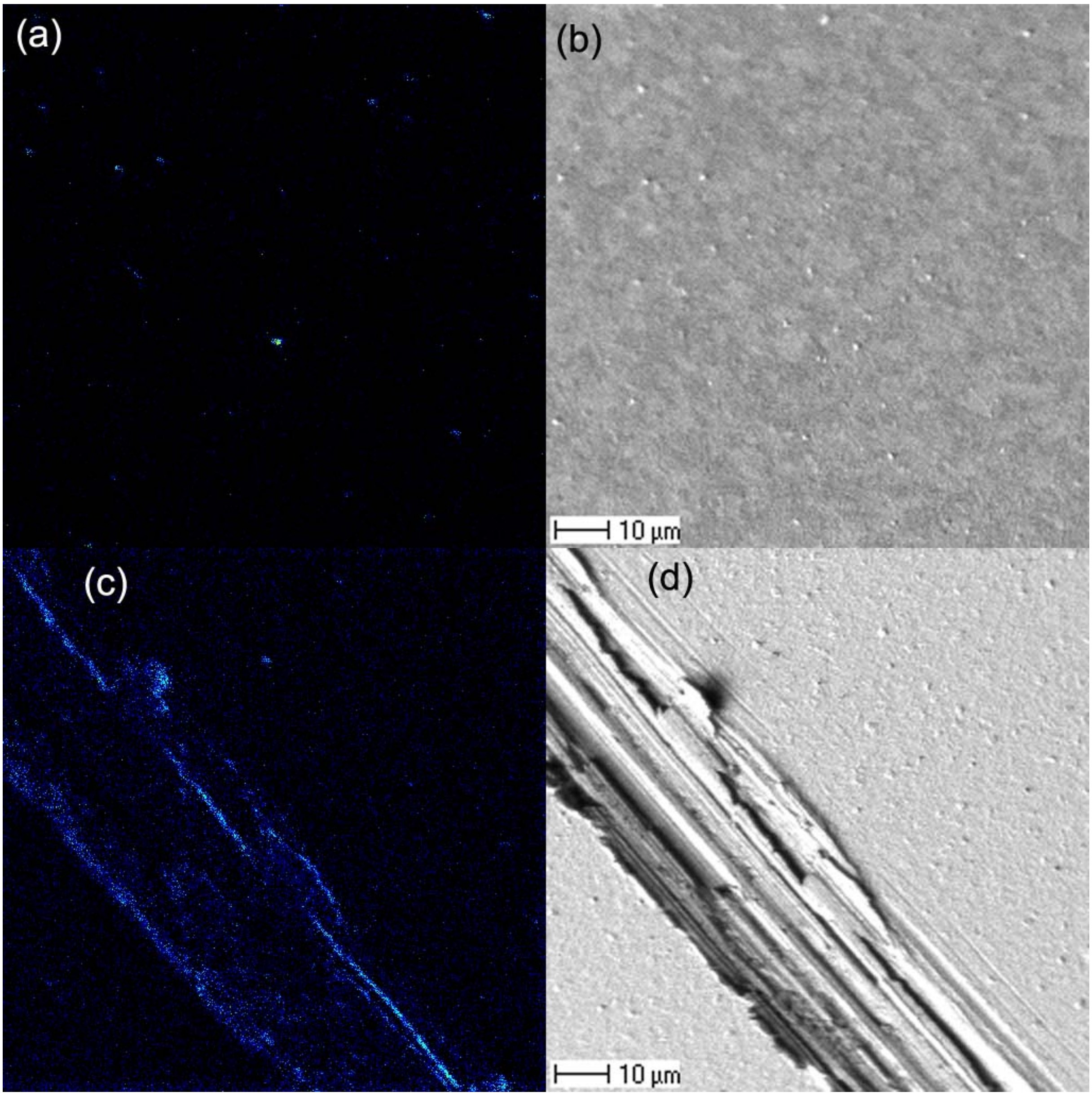

Figure 6.10.: (a) Na SI image of the AlSiCu surface after B-T stress of a sample with PMMA, containing c_{NaOTf} = 900 ppm, attached on AlSiCu. (b) Corresponding SE image. (c) Na SI Image of the same sample setup including a scratch, deliberately cut in the AlSiCu surface. (d) Corresponding SE image, indicating the topography of the scratch.

supports the findings of section 6.1, with regions of significant topography exhibiting favorable locations for Na precipitates. The absence of the Al_2O_2 layer did not play a role in this behavior.

OBIRCH measurements

Since this analytical method is barely a complementary technique used for B-T stress experiments at AlSiCu, there is no basic introduction in the methodology of optical beam induced resistance change (OBIRCH) in section 3.4. For measurement presented here, a $\lambda = 1300$ nm infrared laser was used with a scan duration of 300 s for one scan. A detailed description on this technique can be found in the respective literature (e.g. [153])

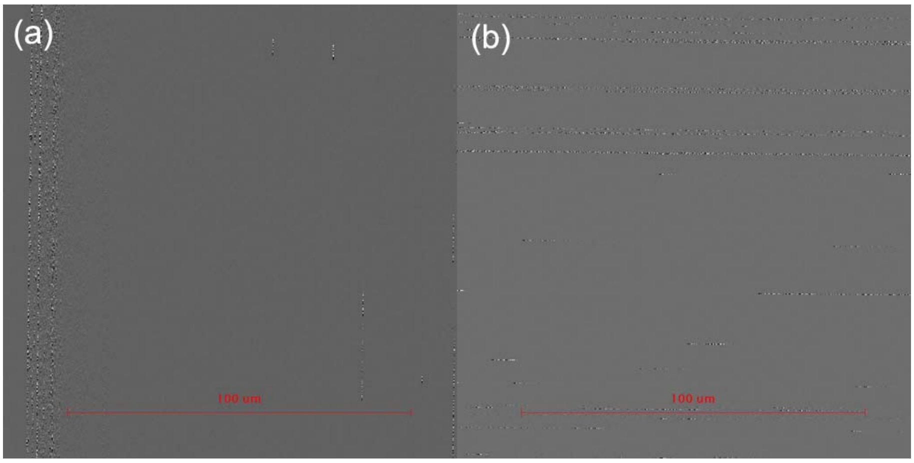

Figure 6.11.: OBIRCH measurements using the same sample type as for B-T stress experiments in this section. An objective 100× magnification was used (a) horizontal scan direction (b) vertical scan direction.

In order to confirm the favorable precipitation of Na at positions of the AlSiCu surface where hillocks are located, OBIRCH was employed as a reference technique. Thus, from an projected view in z direction, spots of attenuated resistance in the host matrix could be detected. These spots were assignable to Na^+ transport within PMMA towards the host matrix. Fig. 6.11 shows the result of OBIRCH measurements, acquired on the one hand in horizontal scan direction and on the other hand perpendicular to the first scan. Dashed lines in a black and white fashion, indicate that somewhere in the lateral position of these features, a change in the resistance was detected. By combining thus both scans, the cross-over of dashed lines in perpendicular directions localizes a spot of different resistance in the chosen field of view. A comparison with Fig. 6.5 and Fig. 6.10 indicate a resembling distribution of these spots with Na precipitates found at hillock positions in ToF-SIMS images. Thus a change in the resistivity in OBIRCH measurements gave a hint on Na^+ transport within PMMA, at lateral positions where hillocks are assumed to be located.

Chapter 7

Summary and conclusion

Knowledge on mobile ion transport in thin films of materials in use for device fabrication is of major interest for the semiconductor industry. A manufacturer has to guarantee a defined product lifetime. Contamination by mobile ions, however, may cause severe damage and performance limitation in terms of device stability and reliability. For MOSFET devices, especially for those of n-channel type, this is due to a gradual shift of the threshold voltage as a function of mobile ions present at the gate oxide / semiconductor interface. The threshold voltage defines the minimum gate voltage to be applied for switching the transistor from *off* in *on*-state. It is obvious that instabilities of this parameter may have fatal consequences.

The content of this thesis is the development and presentation of an approach, in order to investigate thin film of materials used for MOSFET devices, both of insulating and conductive character, on their properties for mobile ion transport, triggered by electrical and thermal driving forces (Drift and diffusion). Under the influence of these driving forces, mobile ions have the property of being fast diffusors in a broad variety of materials. Typical candidates are alkali ions: Lithium, sodium and potassium. Due to the relevance as a device contaminant or impurity, because appearing in comparable high abundance, sodium is the mobile ion with major importance for experiments in this thesis. The basic concept is the following: Thin material films are deposited on a n-doped silicon-substrate using clean room facilities at Infineon Technologies Austria AG, in order to ensure a negligible intrinsic contamination with mobile ions. A polymer host matrix is attached on the produced specimen by means of spin coating or in the form of a drop. This is possible by using host matrix formulations, i.e. solutions, that contained a certain polymer concentration as well as a mobile ion precursor (various alkali triflate compounds). Consequently, the host matrix exhibits a defined concentration and, by the knowledge of the host matrix thickness, defined dose of mobile ions. PMMA and a positive photoresist are hereby used as polymer materials. After the final deposition of an thin gold electrode, bias-temperature (B-T) stress can be applied on the produced sample. B-T stress comprised an external applied voltage while keeping the sample at a defined temperature. This causes transport processes of mobile ions within the host matrix towards the interface to the underlying material film. Depended on the type of material, incorporation and further transport of mobile ions is triggered. Subsequent to B-T stress application, the stressed samples are analyzed by means of time of flight - secondary ion mass spectrometry (ToF-SIMS) depth profiling, enabling unambiguous detection of the spatial location of mobile ions within the sample layer stack. Qualitative and quantitative data assessment of the spectrometric data is able to assess the permeability of the analyzed material films against mobile ions. As a further consequence, qualitative and quantitative examination of the potentiostatic data from B-T stress application is possible. When insulating films are the subject of interest for investigations, a crucial feature of the mentioned approach is to acquire ToF-SIMS depth profiles at different sample temperatures. An evaluation of the obtained results from spectrometric sample analysis is thus possible, indicating whether artifacts are present or not.

The results and achievements of this thesis can be split into two major subjects:

(i) The first issue concerns the analytical approach. ToF-SIMS depth profiling of insulating samples is often connected with the appearance of artifacts. This is especially true when mobile ions are the signals of interest. The occurrence of surface charges by the sputter process causes mobile ion migration away from the surface and a severe distortion of the resulting depth profile is the result. This effect is especially pronounced for thin insulating films deposited an conductive substrates, as represented by the layer setup of the investigated samples. Here, an accumulation of mobile ions at the interface of insulating film and conductive surface can be observed, independent of the initial mobile ion distribution within the insulator. In chapter 4 a detailed discussion on this effect is given. The used ToF-SIMS instrument employed oxygen (O_2^+) and cesium (Cs^+) as sputter projectiles, with the further preferably used as sputter projectiles ToF-SIMS instrument, due to its enhancing effect in terms of the formation of positive secondary ions as e.g. the mentioned candidates for mobile ions. Both projectiles have shown to cause a migration artifact.

Mobile ion migration was investigated for different mobile ions (lithium, sodium, potassium) in silicon dioxide. For further insulating films (silicon oxynitride, silicon nitride, boron-phosphosilicat glass) solely sodium migration was of interest. Two scenarios were chosen for experiments: First, depending on the type of the insulating film, samples prepared for B-T stress application showed distinctive mobile ion incorporation from the host matrix into the insulator during ToF-SIMS depth profiling. Different materials could hence be examined on the appearance of a migration artifact and additionally assessed on permeability against mobile ions. Second, a Gaussian shaped distribution of sodium in silicon dioxide was accessible via implantation. This well defined sodium distribution could be systematically investigated on sodium migration during ToF-SIMS depth profiling.

Variation of the sample temperature had a strong effect on mobile ion migration. This was mainly due to adjustment of diffusivities, which exhibit a exponential dependency on temperature. The observed effect varied with ionic radius of the mobile ion, where, as expected, lithium exhibited the most obvious migration effect. The experiments in chapter 4 go in detail with this issue. Magnesium, in contrast to mobile ions, showed no migration effect at all, confirming mobile ion incorporation for alkali ions during ToF-SIMS depth profiling. By means of sample temperature variation it has been shown that the migration process occurs with the proceeding sputter front. ToF-SIMS depth profiles of samples containing sodium implantations showed a systematic pattern of the initially Gaussian shaped sodium distribution upon sample temperature variation. Based on features of this pattern, a methodology of data treatment for depth profiles has been presented, enabling the reconstruction of the Gaussian shaped distribution out of depth profiles, which were affected by sodium migration. The principle of this approach is to extrapolate parameters describing a Gaussian distribution to a temperature of 0 K. These can be extracted from real depth profiles obtained at different sample temperatures. At 0 K minimal motion of all involved constituents, i.e. sodium and the sample matrix, prohibits sodium migration. The comparison of hypothetical ToF-SIMS depth profiles at 0 K with simulated data showed excellent agreement.

(ii) The second issue concerns investigations of transport processes in different material films, insulating and conductive ones, upon B-T stress application. In chapter 5 insulating films were probed by the above mentioned approach. Variation of sample temperature, sample bias, mobile ion concentration in the host matrix and the type of alkali compound in the host matrix enabled thorough examination of the involved processes. It could be shown that certain conditions are necessary, in order to enable mobile ion incorporation. E.g. for sodium a sample temperature of 130 °C and a electric field of 0.8 MV/cm (resulting from the applied bias voltage) had to be exceeded in order to enable significant incorporation and transport processes in silicon dioxide. Varying the ionic radius of the mobile ion resulted in different threshold values. Mobile ions could be localized in the insulating film using ToF-SIMS depth profiling. Acquisition of profiles at different sample temperatures (room temperature and -130 °C) gave a hint whether the results were affected by artifacts due to mobile ion migration. It have been shown that silicon dioxide is fully permeable for the transport of lithium and sodium when B-T conditions exceeded the threshold values. Silicon oxynitride and silicon nitride prohibit mobile ion transport by the presence of nitride bindings, due to missing degrees of freedom in terms of vibration and rotation.

Quantitative analysis of potentiostatic data was possible, requiring a full permeability of the insulating film for mobile ions. This was enabled by the assumption of a stoichiometric number of electrons present at the interface of insulator and n-doped silicon, in order to assure charge neutrality when mobile ions are accumulating at this position. Comparison of potentiostatic data from B-T stress application and quantified spectrometric data were in well agreement as long as secondary effects as sample surface discharge phenomena could be kept on a minimal level. For sodium the dose of incorporated ions as detected by ToF-SIMS depth profiling has been shown to be in well agreement with the calculated dose, initially provided in the host matrix. This is independent of the quantity of provided sodium precursor, which is an important advantage of spectrometric data in contrast to potentiostatic data: ToF-SIMS depth profiling gave solely information on the quantity of incorporated sodium; secondary effects as discharge phenomena or leakage currents did not superimpose. Appropriate physico-chemical models enabled the calculation of parameters describing lithium and sodium transport in silicon dioxide. A modified Butler-Volmer based approach and calculations by means of the Nernst-Einstein relation were applied for this purpose. Basically, a reduction of the activation energy for transport within silicon dioxide by the presence of the bias voltage have been found to enable mobile ion incorporation and transport.

An aluminum-silicon-copper (referred to as aluminum) alloy, commonly applied for metalization layers in semiconductor devices, was investigated for sodium incorporation and transport in a conductive material. Owing to the absence of an electric field, no significant incorporation of sodium in aluminum was detected, independent on B-T conditions. However, occurring topography at the aluminum surface (e.g. hillocks) have been shown to exhibit a preferred location for sodium precipitation.

Appendix A

Additional figures and tables

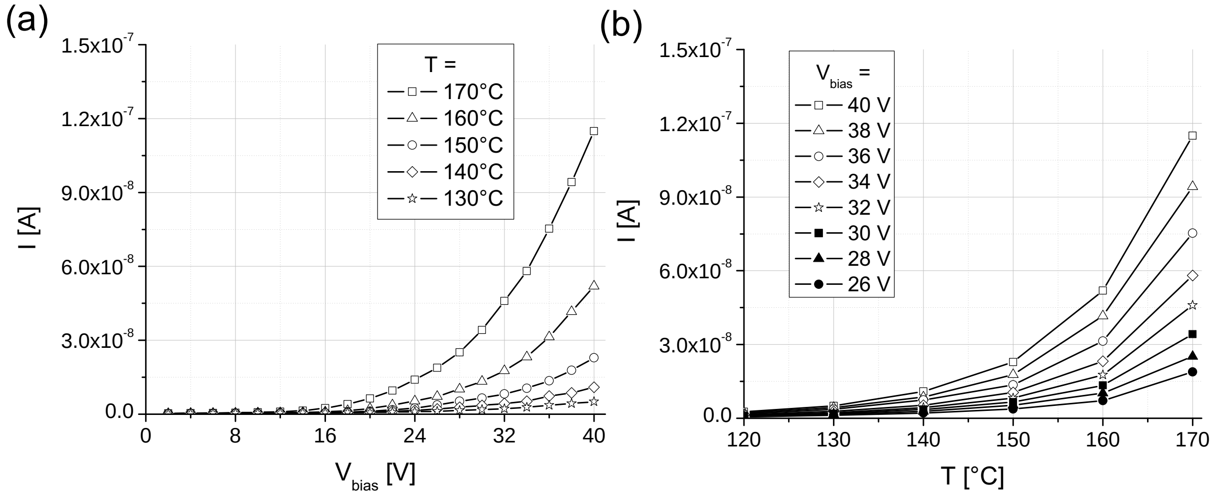

Figure A.1.: (a) I-V plots obtained by ramping V_{bias}, recording Na^+ incorporation into 200 nm SiO_2 ($c_{NaOTf} = 300$ ppm). For each data point a dwell time of 1 s at the respective V_{bias} was chosen. (b) I-T plots obtained by temperature ramping, carried out for temperatures in a range between RT and 170 °C.

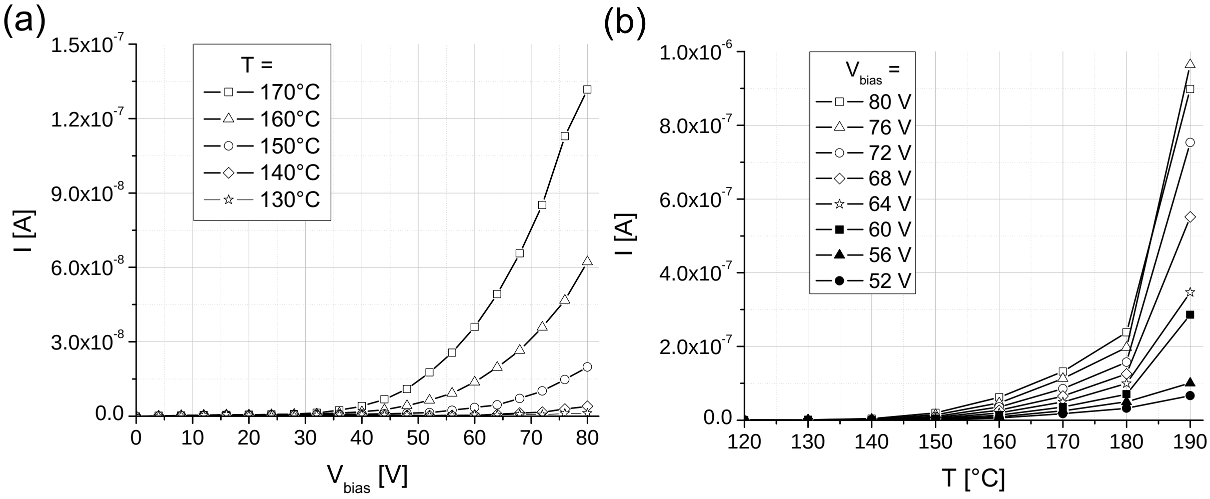

Figure A.2.: (a) I-V plots obtained by ramping V_{bias}, recording Na^+ incorporation into 400 nm SiO_2 (c_{NaOTf} = 300 ppm). For each data point a dwell time of 1 s at the respective V_{bias} was chosen. (b) I-T plots obtained by temperature ramping, carried out for temperatures in a range between RT and 190 °C.

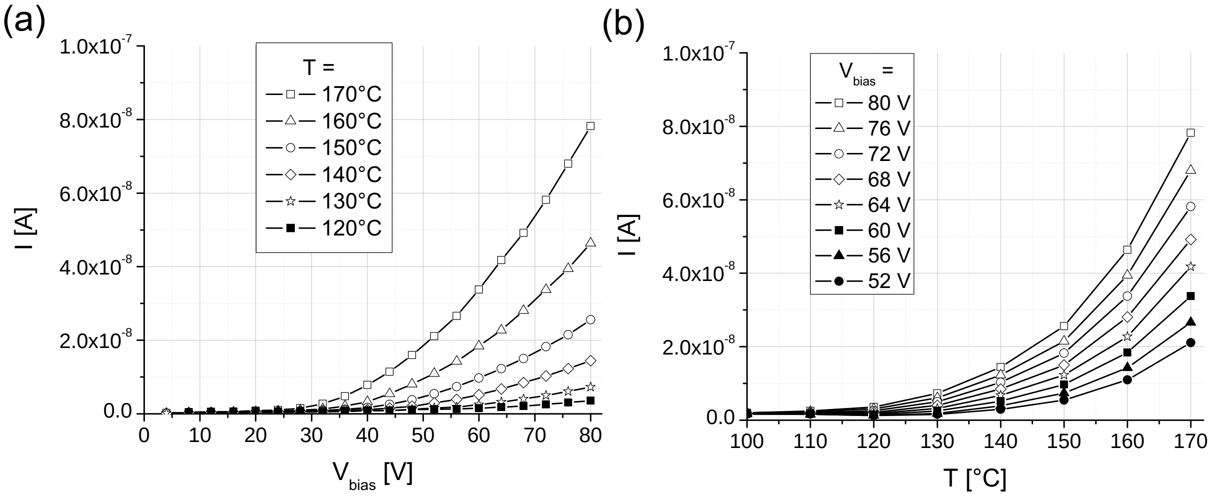

Figure A.3.: (a) I-V plots obtained by ramping V_{bias}, recording Na^+ incorporation into 100 nm SiO_2 (c_{LiOTf} = 300 ppm). For each data point a dwell time of 1 s at the respective V_{bias} was chosen. (b) I-T plots obtained by temperature ramping, carried out for temperatures in a range between RT and 170 °C.

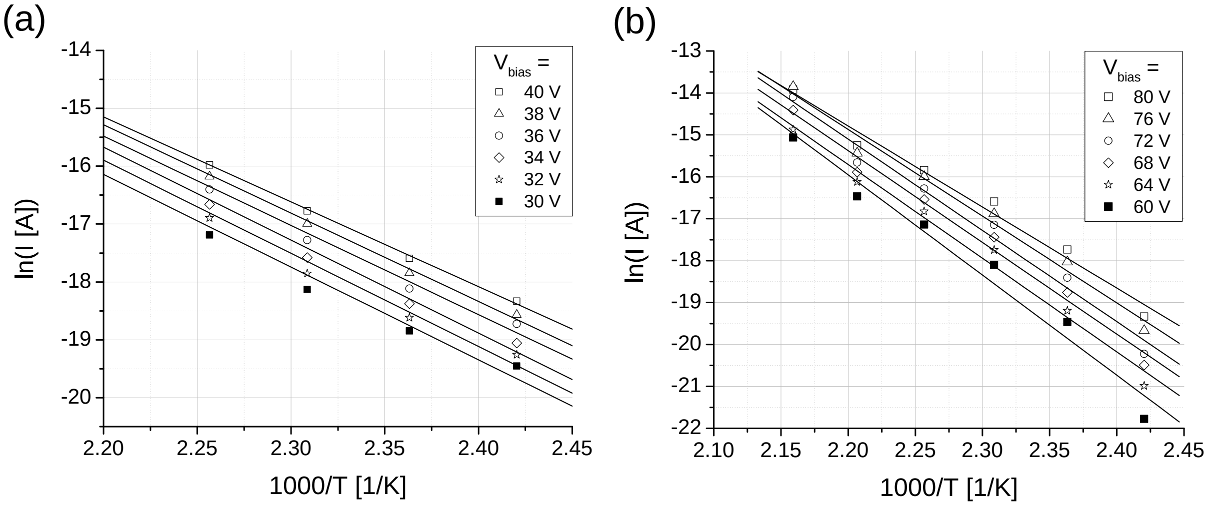

Figure A.4.: Arrhenius plots of the data in (a) Fig. A.1 (Na^+ transport in 200 nm SiO_2, $c_{NaOTf} = 300$ ppm, temperature range: 140 °C - 170 °C). (a) Fig. A.2 (Na^+ transport in 400 nm SiO_2, $c_{NaOTf} = 300$ ppm, temperature range: 140 °C - 190 °C).

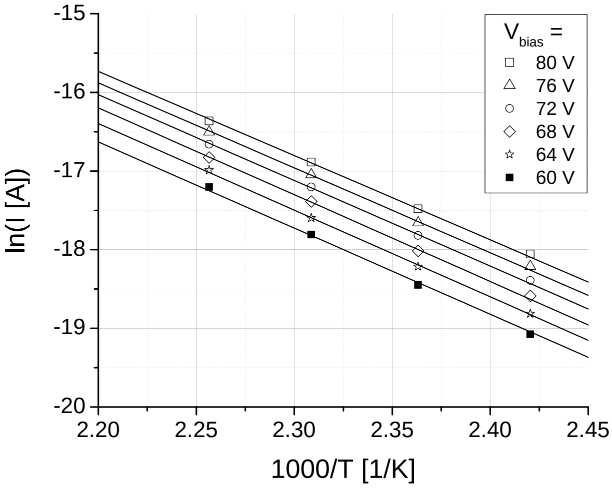

Figure A.5.: Arrhenius plot of the data in Fig. A.3 (Na^+ transport in 40 nm SiO_2, $c_{LiOTf} = 300$ ppm) according to the modified Butler-Volmer approach for the temperature range 140 °C - 170 °C.

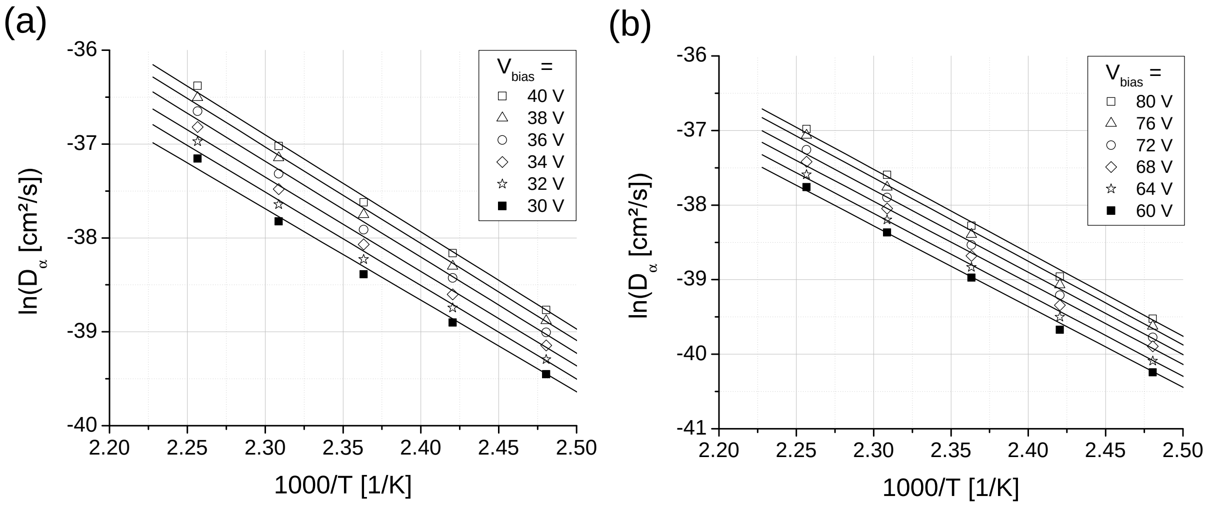

Figure A.6.: Arrhenius plots according to Nernst-Einstein equation for the temperature range 130 °C - 170 °C as obtained from (a) the data in Fig. A.1: Na^+ transport in 200 nm SiO_2, c_{NaOTf} = 300 ppm. (b) The data in Fig. A.2: Na^+ transport in 400 nm SiO_2, c_{NaOTf} = 300 ppm.

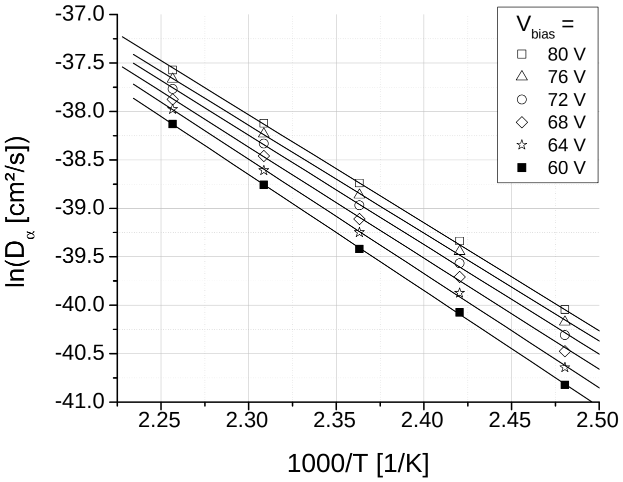

Figure A.7.: Arrhenius plot of the data in Fig. A.3 (Na^+ transport in 100 nm SiO_2, c_{LiOTf} = 300 ppm) according to Nernst-Einstein equation for the temperature range 130 °C - 170 °C.

Table A.1.: Values for R_{SiO_2} and the respective capacities of a 200 nm SiO_2 layer as indicated by impedance spectroscopy.

Amplitude [V]	R_{SiO_2} [Ω]	Capacity [nF]	Amplitude [V]	R_{SiO_2} [Ω]	Capacity [nF]
6	$7.26 \cdot 10^{9}$	19.9	24	$3.46 \cdot 10^{9}$	12.11
8	$7.19 \cdot 10^{9}$	12.00	26	$3.06 \cdot 10^{9}$	12.15
10	$6.65 \cdot 10^{9}$	12.00	28	$2.56 \cdot 10^{9}$	12.18
12	$6.34 \cdot 10^{9}$	12.00	30	$2.18 \cdot 10^{9}$	12.25
14	$5.79 \cdot 10^{9}$	12.01	32	$1.81 \cdot 10^{9}$	12.36
16	$5.36 \cdot 10^{9}$	12.02	34	$1.46 \cdot 10^{9}$	12.52
18	$5.06 \cdot 10^{9}$	12.03	36	$1.21 \cdot 10^{9}$	12.68
20	$4.63 \cdot 10^{9}$	12.04	38	$9.65 \cdot 10^{8}$	12.94
22	$4.18 \cdot 10^{9}$	12.06	40	$6.71 \cdot 10^{8}$	13.46

Table A.2.: Values for R_{SiO_2} and the respective capacities of a 400 nm SiO_2 layer as indicated by impedance spectroscopy.

Amplitude [V]	R_{SiO_2} [Ω]	Capacity [nF]	Amplitude [V]	R_{SiO_2} [Ω]	Capacity [nF]
12	$2.88 \cdot 10^{10}$	5.84	48	$9.76 \cdot 10^{9}$	5.91
16	$2.65 \cdot 10^{10}$	5.84	52	$7.85 \cdot 10^{9}$	5.93
20	$2.45 \cdot 10^{10}$	5.84	56	$6.40 \cdot 10^{9}$	5.94
24	$2.28 \cdot 10^{10}$	5.84	60	$5.17 \cdot 10^{9}$	6.02
28	$2.08 \cdot 10^{10}$	5.85	64	$4.03 \cdot 10^{9}$	6.09
32	$1.92 \cdot 10^{10}$	5.85	68	$3.31 \cdot 10^{9}$	6.17
36	$1.63 \cdot 10^{10}$	5.86	72	$2.39 \cdot 10^{9}$	6.25
40	$1.40 \cdot 10^{10}$	5.87	76	$2.35 \cdot 10^{9}$	6.32
44	$1.18 \cdot 10^{10}$	5.88	80	$1.81 \cdot 10^{9}$	6.50

Appendix B

Acronyms and symbols

In the following relevant acronyms are listed, that frequently appear in the course of the thesis. Chemical symbols and abbreviations are given in the chapters on their first appearance (an exception PMMA, due to its crucial relevance).

AC	Alternating current
BA	Burst alignment
BPSG	Boron-phosphosilicate glass
B-T	Bias - temperature
C-V	Capacitance - voltage
CVD	Chemical vapor deposition
DC	Direct current
DHM	Digital holographic microscopy
HCBU	High current bunched
LMIG	Liquid metal ion gun
SMU	Source meter unit; Signal measurement unit
MOS	Metal oxide semiconductor
MOSFET	Metal oxide semiconductor field effect transistor
OBIRCH	Optical beam induced resistance change
PMMA	Poly(methyl methacrylate)
PVD	Physical vapor deposition
N/A	Not available
RT	Room temperature
RSF	Relative sensitivity factor

SEM	Scanning electron microscopy
SE	Secondary electron
SI	Secondary ion
SIMS	Secondary ion mass spectroscopy
SRIM	The stopping range of ions in matter
ToF-SIMS	Time of flight - secondary ion mass spectroscopy
TRIM	Transport of ions in matter
TSIC	Thermally stimulated ionic current
TVS	Triangular voltage sweep

Symbols

a	Hopping distance (typically given in [Å])
A	Area [cm^2]
c	Concentration [mol/cm^3]
c_A	Concentration of e.g. constituent A in the sample matrix (typically given in [at/cm^3]
c_{MeOTf}	Concentration of MeOTf in the host matrix [ppm per weight]
$c_{Me^+,stock}$	Concentration of Me^+ in the stock solution [mol/cm^3]
$c_{Me^+,calc}, c_{Me^+}$	Calculated concentration of Me^+ in PMMA acc. to c_{MeOTf} [mol/cm^3]
C	Capacity [F]
C_{Ox}	Capacity of the gate oxide (e.g. SiO_2) [F]
d	Layer thickness (typically given in [nm])
D	Diffusion constant [cm^2/s]
D_0	Pre-exponential factor, frequency factor [cm^2/s]
D^*	Tracer diffusion constant [cm^2/s]
$\widetilde{D}$	Chemical diffusion constant [cm^2/s]
D_α	Diffusion constant according to Nernst-Einstein relation [cm^2/s]
e	Elemental charge ($1.602 \cdot 10^{-19}$ C)
E	Electric field [V/cm]
E_a	Activation energy [eV]
E_1	Ionization potential e.g. of ion 1 [eV]
E_G	Energy band gap between valence and conduction band [eV]
E_C	Energy width of the conduction band [eV]
E_{kin}	Kinetic energy [J]
E_{sp}	Sputter ion energy [eV]
f	Represents: Correlation factor [-] or frequency [Hz]
$f^{\pm}(A)$	Transmission efficiency of the ToF analyzer and the detector [-]
F	Faraday constant (96485 [C/mol])
I	Electric Current; Mobile ion current [A]
I_A	Secondary ion intensity e.g. of constituent A [cts]
I_D	Drain current [A]
$I^{\pm}(A)$	Detected secondary ion current of constituent A [A]
I_e	Auxiliary electron current [A]
I_p	Primary ion current [A]

I_sp	Sputter current [A]
J	Particle flux [at/cm^2 s], [ions/cm^2 s]
j	Electric current density [A/cm^2]
j_{th}, j_0	Thermally driven mobile ion transfer current density [A/cm^2]
$j_{th,el}, j_{Me^+}$	Thermally and electrically driven mobile ion transfer current density [A/cm^2]
k	Mobile ion incorporation rate at interfaces [cm/s]
k_0	Attempt frequency for mobile ion incorporation at interfaces [cm/s]
k_B	Boltzmann's constant (8.617·10^{-5} eV/K)
L_d	Flight lenght of secondary ions in the ToF analyzer [m]
m_{stock}	mass (e.g. of the stock solution) [g]
M_{MeOTf}	Molecular weight (e.g. of MeOTf) [g/mol]
n	Charge carrier density [cm^2]
n_t	Number of mobile ions at the SiO$_2$ / Si interface at time t
n_{MeOTf}	Number of MeOTf molecules in the host matrix [ppm per weight]
N_A	Avorgardo's constant (6.022·10^{23} at/mol or ions/mol)
$PIDD$	Primary ion dose density [ions/cm^2]
q	Charge of a mobile ion charge [C]
Q_m, Q_{Na^+}	Cumulated charge of mobile ions at the SiO$_2$ / Si interface [C]
Q_{SS}	Cumulated charge of intrinsic interface traps or fixed charges at the SiO$_2$ / Si interface [C]
$Q_{R_{p,2}}$	Cumulated Na signal from the fitted peak at position $R_{p,2}$ [cts]
Q_{Na}	Cumulated Na signal within SiO$_2$ [cts]
Q_s	Total charge generated in the semiconductor [C]
R	used for: Resistivity [Ω] or Gas constant (8.314 [J/mol K])
R_a	Averaged sample roughness [nm]
R_p	Projected range of Na due to implantation (typically give in [nm])
$R_{p,1}$, $R_{p,2}$	Projected ranges of significant peaks in ToF-SIMS depth profiles of Na implantations in SiO$_2$ [nm]
R_{if}	Interface resistivity [Ω])
R_{SiO_2}	Resistivity of SiO$_2$ [Ω])
$RSF_{A,M}$	Relative sensitivity factor of the constituent A with respect to a chosen matrix element M [cm^{-3}]
s	Preexponential factor
$S_p(A)$	Absolute sensitivity of the constituent A during ToF-SIMS analysis [-]
$S_{r,A}$	Relative sensitivity of the constituent A with respect to a chosen matrix element during ToF-SIMS analysis [-]
t	Time [s]
T	Temperature [°C]
U_a	Extraction voltage [V]
v	Velocity [m/s]
V_{GS}	Gate source voltage [C]
V_{th}	Threshold voltage [V]
V_{FB}	Flat-band voltage [V]
V_{SB}	Source bulk voltage [V]
V_{GB}	Gate bulk voltage [V]
V_{bias}	Applied bias voltage during B-T stress [V]
$V_{solvent}$	Solvent volume [cm^3]
$V(M)$	Erosion rate of the sample matrix M [nm/s]
x_{DL}	Depletion layer width [nm]
x_{Ox}	Gate oxide thickness [nm]
y_c	Maximum height of the fitted, Gaussian shaped peak at position $R_{p,2}$ [cts]
Y_{sp}	Sputter yield during sample erosion [-]
Y_{tot}	Total sputter yield due to primary ion bombardment[-]
$Y_u(A)$	Useful secondary ion yield [-]
z	Charge number [-]
$Z(\omega)$	Impedance [Ω]

$Z'(\omega)$	Real part of the impedance [Ω]
$Z''(\omega)$	Complex part of the impedance [Ω]
α	In section 2.3: Heating rate [$^\circ C^{-1}$]
	In section 5.2.2: Symmetry factor [-]
$\alpha^{\pm}(A)$	Ionization probability [-]
γ	Body factor [V]
γ^T	Effective secondary ion yield due to sputter ion bombardment [-]
Γ_+	Jump rate with assistance of an electric field [-]
$\Gamma_{0,+}$	Jump rate without assistance of an electric field [-]
δ^T	Effective secondary ion yield due to electron bombardment [-]
ΔV_{th}	Threshold voltage shift [V]
ΔR_p	Standard deviation of the Gaussian shaped profile resulting from Na implantation [nm]
$\Delta\phi$	Electrical potential difference ($\equiv V_{bias}$) [V]
$\epsilon_{r,ox}$	Dielectric constant or permittivity (e.g. of the gate oxide) [-]
ϵ_0	Vacuum permittivity ($8.854 \cdot 10^{-12}$ [F/m])
μ	Chemical potential [J/mol]
	In section 3.3.1: Mean of a Gaussian shaped distribution [nm]
$\widetilde{\mu}$	Electrochemical potential [J/mol]
$\rho(x)$	Mobile ion distribution mobile ion distribution within the gate oxide
$\rho_{solvent}$	Density (e.g. of a solvent) [g/cm^3]
σ	In section 3.3.1: Damage cross section (acc. to literature)
	In sections 2.4 and 5.2.3: Conductivity [S]
	In section 4.3: Standard deviation of the fitted, Gaussian shaped peak at position $R_{p,2}$ [nm]
ϕ	Electric potential [J/mol]
ϕ_A, ϕ_{Na}	Implantation dose of constituent A (e.g. Na) in a sample [cm^{-3}]
ϕ_F	Potential difference between the intrinsic Fermi level and the actual Fermi level [V]
ϕ_{Ox}	Voltage drop across the gate oxide [V]
ϕ_S	Voltage drop due to majority carrier accumulation in Si for a MOS transistor in inversion [V]
ϕ_{MS}	Work function difference between metal and semiconductor [V]
ϕ_{Me^+}	Me^+ dose at the SiO_2 / Si interface [cm^{-2}]
$\phi_{Me^+,calc}$	Me^+ dose in the host matrix calculated according to c_{MeOTf}
	and the host matrix thickness [cm^{-2}]
$\phi_{Me^+,DC}$	Me^+ dose incorporating the SiO_2 layer
	as measured potentiostatically [cm^{-2}]
$\phi_{Me^+,SIMS}$	Me^+ dose detected within the SiO_2
	by means of quantification of ToF-SIMS depth profiles [cm^{-2}]
ω	Circle frequency [Hz]

Appendix C

Presentations and published articles

Parts of the results presented in this thesis were contents for contributions at international conferences and publications in scientific journals:

Talks

S. Krivec, M. Buchmayr, T. Detzel, M. Nelhiebel, H. Hutter; *"Drift and diffusion behavior of sodium in thin silicon dioxide films"*; 13$^{\text{th}}$ European Conference on Applications of Surface and Interface Analysis (ECASIA'09), Antalya, Turkey, 18 - 23.10.2009

S. Krivec, T. Detzel, M. Buchmayr, H. Hutter; *"On the temperature dependence of Na migration in thin* SiO_2 *films during ToF-SIMS* O_2^+ *depth profiling"*; SIMS Europe 2010, Münster, Germany, 20 - 21.09.2010

S. Krivec, M. Buchmayr, T. Detzel, H. Hutter; *"Untersuchung von* Na^+ *Inkorporation in dünne nichtleitende Schichten mittels ToF-SIMS"*; 16. Arbeitstagung Angewandte Oberflächenanalytik, AOFA 16, Kaiserslautern, Germany, 27 - 29.09.2010

Publications

S. Krivec, M. Buchmayr, T. Detzel, M. Nelhiebel, H. Hutter; *"Voltage-assisted sodium ion incorporation and transport in thin silicon dioxide films"*, Surf. Interface Anal., **2010**, 42, 6-7, 886-890

S. Krivec, T. Detzel, M. Buchmayr, H. Hutter; *"On the temperature dependence of Na migration in thin* SiO_2 *films during ToF-SIMS* O_2^+ *depth profling"*, Appl. Surf. Sci., **2010**, 257, 1, 25-32

S. Krivec, M. Buchmayr, T. Detzel, T. Froemling, J. Fleig, H. Hutter; *"The effect of bias-temperature stress on Na+ incorporation into thin insulating film"*, Anal. Bioanal. Chem., **2010**, 400, 3, 649-657

References

[1] G. A. Klutke, P. C. Kiessler, and M. A. Wortman, "A critical look at the bathtub curve," *IEEE T. Reliab.* **52**, pp. 125 – 129, 2003.

[2] N. Wan and K. Manning, "Exceeding 60-year life expectancy from an electronic energy meter," in *Metering Asia Pacific Conference*, 2001.

[3] M. Ohring, *Reliability and Failure of Electronic Materials and Devices*, Academic Press, 1998.

[4] H. Eigler, *Die Zuverlässigkeit von Elektronik- und Mikrosystemen*, expert verlag, 2003.

[5] J. Y. Dai, S. K. Loh, S. F. Tee, C. L. Tay, S. Ansari, E. Er, and S. Redhar, "High resistance via induced by marginal barrier metal step coverage and f diffusion," in *Proceedings of 8^{th} IEEE Int. Conf. Phys. Failure Anal. Integr. Circuits*, pp. 183–186, 2001.

[6] G. Ghidini, C. Clementini, D. Drera, and F. Maugain, "The impact of F contamination induced by the process on the gate oxide reliability," *Microelectron. Reliab.* **38**, pp. 255–258, 1998.

[7] K. Saga and T. Hattori, "Identification and removal of trace organic contamination on silicon wafers stored in plastic boxes.," *J. Electrochem. Soc.* **143**, pp. 3279–3284, 1996.

[8] K. M. Kim, J. Y. Kim, H. B. Kang, B. Y. Lee, and S. M. Park, "Effects of organic contaminants during metal oxide semiconductor processes," *J. Electrochem. Soc.* **155**, pp. H426 – H431, 2008.

[9] K. Saga and T. Hattori, "Influence of silicon-wafer loading ambients in an oxidation furnace on the gate oxide degradation due to organic contamination.," *Appl. Phys. Lett.* **71**, pp. 3670–3672, 1997.

[10] S. R. Kasi, M. Liehr, P. A. Thiry, H. Dallaporta, and M. Offenberg, "Hydrocarbon reaction with HF-cleaned Si(100) and effects on metal-oxide-semiconductor device quality," *Appl. Phys. Lett.* **59**(1), pp. 108–110, 1991.

[11] K. Saga and T. Hattori, "Influence of surface organic contamination on the incubation time in low-pressure chemical vapor deposition.," *J. Electrochem. Soc.* **144**, pp. L253–L255, 1997.

[12] M. Khan, T. Tarter, and H. Fatemi, "Aluminum bond pad contamination by thermal outgassing of organic material from silver-filled epoxy adhesives," *IEEE T. Compon. Hybr.* **10**(4), pp. 586 – 592, 1987.

[13] S. R. Hofstein, "Proton and sodium transport in SiO_2 films," *IEEE T. Electron. Dev.* **14**, pp. 749 – 759, 1967.

[14] P. L. Hefley and J. W. McPherson, "The impact of an external sodium diffusion source on the reliability of MOS circuitry.," in *Proc. IEEE Int. Reliab. Phys. Symp.*, *IEEE Int. Reliab. Phys. Symp.* , pp. 167–172, 1988.

[15] K. Hoffmann, *System Integration - From Transistor Design to Large Scale Integrated Circuits*, John Wiley & Sons, Ltd, 2004.

[16] E. H. Snow, A. S. Grove, B. E. Deal, and C. T. Sah, "Ion transport phenomena in insulating films.," *J. Appl. Phys.* **36**, pp. 1664–73, 1965.

[17] K. O. Jeppson and C. M. Svensson, "Negative bias stress of MOS devices at high electric fields and degradation of MNOS devices.," *J. Appl. Phys.* **48**, pp. 2004–14, 1977.

[18] T. Grasser, B. Kaczer, and W. Gös, "An energy-level perspective of negative bias temperature instabilitiy," in *Proc. IEEE Int. Rel. Phys. Symp.*, pp. 28–38, 2008.

[19] P. Van Zant, *Microchip fabrication: A practical guide to semiconductor processing*, McGraw-Hill Companies, Inc., 5th edition ed., 2004.

[20] R. H. Koch and A. Hartstein, "Evidence for resonant tunneling of electrons via sodium ions in silicon dioxide," *Phys. Rev. Lett.* **54**(16), pp. 1848–1851, 1985.

[21] B. R. Tuttle, S. Dhar, S.-H. Ryu, X. Zhu, J. R. Williams, L. C. Feldman, and S. T. Pantelides, "High electron mobility due to sodium ions in the gate oxide of SiC-metal-oxide-semiconductor field-effect transistors," *J. Appl. Phys.* **109**, pp. 023702–1 – 023702–6, 2011.

[22] A. Dreizner, J. Nagel, and R. Scharfe, “A new wafer level reliability method for evaluation of ionic induced pmosfet drift effects,” *Microelectron. Reliab.* **36**(11-12), pp. 1855 – 1858, 1996.

[23] D. Constant, F. Tardiff, and J. Derrien, “Deposition and removal of sodium contamination on silicon wafers,” *Semicond. Sci. Technol.* **15**, pp. 61 – 66, 2000.

[24] J. Chinn, Y.-S. Ho, and M. Chang, “Built-in reliability through sodium elimination,” in *IEEE Int. Rel. Phys. Symp.*, 1994.

[25] T. E. Burgess, J. C. Baum, F. M. Fowkes, R. Holmstrom, and G. A. Shirn, “Thermal diffusion of sodium in silicon nitride-shielded silicon oxide films.,” *J. Electrochem. Soc.* **116**, pp. 1005–8, 1969.

[26] J. W. Osenbach and S. S. Voris, “Sodium diffusion in plasma-deposited amorphous oxygen-doped silicon nitride (a-SiON:H) films,” *J. Appl. Phys.* **63**(9), pp. 4494–4500, 1988.

[27] J. A. Shideler, M. Ivey, J. Finn, and M. Johnson, “Is BPSG an effective sodium barrier? a WLR success story.,” in *IEE Int. Integr. Rel. Workshop Final Report*, pp. 66–71, 1997.

[28] A. S. Grove, E. H. Snow, B. E. Deal, and C. T. Sah, “Simple physical model for the space-charge capacitance of metal-oxide-semiconductor structures.,” *J. Appl. Phys.* **35**, pp. 2458–60, 1964.

[29] A. Grove, B. E. Deal, and E. H. Snow, “Investigation of thermally oxidized silicon surfaces using metal-oxide-semiconductor structures,” *Solid State Electron.* **8**, pp. 145–163, 1965.

[30] B. E. Deal, “A scientist’s perspective on the early days of MOS technology,” *Interface* **3**, pp. 42 – 45, 2007.

[31] L. Anderson, S. Parikh, S. Nagalingam, and C. Haidinyak, “A case study in a 100 x reduction in sodium ions in a 0.8m BiCMOS process using triangular voltage sweep,” *IEEE Int. Rel. Workshop, Final Report* , pp. 45–48, 1995.

[32] M. Kuhn and D. J. Silversmith, “Ionic contamination and transport of mobile ions in MOS structures,” *J. Electrochem. Soc.* **118**, pp. 966–970, 1971.

[33] K. Schjoelberg-Henriksen, G. Jensen, A. Hanneborg, and H. Jakobsen, “Sodium contamination of SiO_2 caused by anodic bonding,” *J. Micromech. Microeng.* **13**, pp. 845–852, 2003.

[34] M. W. Hillen, G. Greeuw, and J. F. Verweij, “On the mobility of potassium ions in SiO_2,” *J. Appl. Phys.* **50**, pp. 4834 – 4837, 1979.

[35] M. A. Chonko, R. Khamankar, T. Tiwald, T. Allen, and B. Vasquez, “Measurement of mobile ion contamination in multilayer metalization by triangular voltage sweep.,” *J. Electrochem. Soc.* **141**, pp. 1862–1866, 1994.

[36] J. Quick and P. Schley, “Improved triangular voltage sweep (TVS) technique for measurements of ionic charge in (MOS) structures,” *Electron. Lett.* **29**, pp. 275–277, 1993.

[37] T. E. Hickmott, “Thermally stimulated ionic conductivity of sodium in thermal SiO_2,” *J. Appl. Phys.* **46**, pp. 2593–2598, 1975.

[38] M. R. Boudry and J. P. Stagg, “The kinetic behavior of mobile ions in the aluminum-silicon dioxide-silicon system.,” *J. Appl. Phys.* **50**, pp. 942–50, 1979.

[39] J. P. Stagg and M. R. Boudry, “Sodium passivation in ai-SiO_2-si structures containing chlorine,” *J. Appl. Phys.* **52**, pp. 886–899, 1981.

[40] J. P. Stagg, “Drift mobilities of sodium(+) and potassium(+) ions in silicon dioxide films.,” *Appl. Phys. Lett.* **31**, pp. 532–533, 1977.

[41] J. Maier, *Physical Chemistry of Ionic Materials*, John Wiley & Sons, Ltd, 2004.

[42] M. E. Glicksman, *Diffusion in Solids*, John Wiley & Sons, Ltd, 2000.

[43] J. Crank, *The Mathematics of Diffusion*, Clarendon Press, 2nd edition ed., 1975.

[44] H. Mehrer, *Diffusion in Solids: Fundamentals, Methods, Materials, Diffusion-Controlled Processes*, Springer, 2007.

[45] P. W. Atkins, *Physikalische Chemie*, VCH, 1996.

[46] R. A. McKee, “Thermodynamics and kinetics of interstitial diffusion in a two-component system,” *Phys. Rev. B* **22**, pp. 2649–2657, 1980.

[47] J. C. C. Tsai, *VLSI Technology*, ch. Chapter 5: Diffusion, pp. 169–218. McGraw-Hill Companies, Inc., 2nd edition ed., 1988.

[48] V. Milman, M. C. Payne, V. Heine, R. J. Needs, J. S. Lin, and M. H. Lee, “Free energy and entropy of diffusion by ab initio molecular dynamics: Alkali ions in silicon,” *Phys. Rev. Lett.* **70**(19), pp. 2928–2931, 1993.

[49] S. E. Ormrod and D. L. Kirk, “The relationship between sodium ion diffusion and conductivity in polycrystalline p"-alumina,” *J . Phys. D: Appl. Phys.* **10**, pp. 1497–1507, 1977.

[50] J. O. Isard, “The haven ratio in glasses,” *J. Non-Cryst. Solids* **246**(1-2), pp. 16 – 26, 1999.

[51] T. Hirata, T. Kashiwagi, and J. E. Brown, “Thermal and oxidative degradation of poly(methyl methacrylate): Weight loss,” *Macromolecules* **18**(7), pp. 1410–1418, 1985.

[52] J. Brandrup, E. H. Immergut, E. A. Grulke, A. Abe, and D. R. Bloch, eds., *Handbook of Polymers*, John Wiley & Sons, Ltd, 4th edition ed., 1999.

[53] C. G. Zoski, ed., *Handbook of Electrochemistry*, Elsevier, 2007.

[54] J. C. Vickerman and D. Briggs, eds., *ToF-SIMS: Surface analysis by mass spectrometry*, IM Publications, 2001.

[55] A. Benninghoven, F. G. Rüdenauer, and H. W. Werner, *Secondary ion mass spectrometry*, John Wiley & Sons, Ltd, 1987.

[56] Y. Yamamura and Y. Kitazoe, "Computer simulation of cascade developments in amorphous targets," *Radiat. Eff.* **39**, p. 251, 1978.

[57] J. F. Ziegler, J. P. Biersack, and M. D. Ziegler, *The Stopping and Range of Ions in Matter*, SRIM Co., 2008. SRIM software is available at: https://www.SRIM.org.

[58] L. Van Vaeck, A. Adriaens, and R. Gijbels, "Static secondary ion mass spectrometry (S-SIMS) part 1. methodology and structural interpretation," *Mass Spectrom. Rev.* **18**, pp. 1–47, 1999.

[59] F. Kötter and A. Benninghoven, "Secondary ion emission from polymer surfaces under Ar^+, Xe^+ and ${SF_5}^+$ ion bombardment," *Appl. Surf. Sci.* **133**, pp. 47–57, 1998.

[60] M. Urbassek, "The energy distribution of sputtered particles at low bombarding energies," *Nucl. Instrum. Meth. B* **4**, pp. 356–363, 1984.

[61] E. Niehuis, T. Heller, and A. Benninghoven, "Design and performance of a reflectron based time-of -flight secondary ion mass spectrometer with electrodynamic primary ion mass separation," *J. Vac. Sci. Technol. A* **A5**, p. 1243, 1987.

[62] T. Stepan, J. Zehnpfennig, and A. Benninghoven, "Correction of dead time effects in time-of-flight mass spectrometry," *J. Vac. Sci. Technol. A* **12**, pp. 405–410, 1994.

[63] J. J. Thomson, "Rays of positive electricity," *Phil. Mag.* **20**, pp. 752–767, 1910.

[64] R. F. K. Herzog and F. P. Viehböck, "Ion source for mass spectrography," *Phys. Rev.* **76**(6), pp. 855–856, 1949.

[65] H. J. Liebl and R. K. F. Herzog, "Sputtering ion source for solids," *J. Appl. Phys.* **34**, pp. 2893–2896, 1963.

[66] R. E. Honig, "The growth of secondary ion mass spectrometry (SIMS): A personal view of its development," in *Proc. SIMS V*, 1986.

[67] E. Zinner, "Sputter depth profiling of microelectronic structures," *J. Electrochem. Soc.* **130**, pp. 199C–222C, 1983.

[68] A. Benninghoven and E. Loebach, "Tandem mass spectrometer for secondary ion studies," *Rev. Sci. Instrum.* **42**, pp. 49–52, 1971.

[69] R. Castaing and G. Slodzian, "Analytical microscopy by secondary ion imaging techniques," *J. Phys. E: Sci. Instrum.* **14**, pp. 1119–1127, 1981.

[70] H. Liebl, "Ion microprobe mass analyzer," *J. Appl. Phys.* **38**, pp. 5277–5283, 1967.

[71] A. Benninghoven, D. Jaspers, and W. Sichtermann, "Secondary-ion emission of amino acids," *Appl. Phys.* **11**, pp. 35–39, 1976.

[72] B. T. Chait and K. G. Standing, "A time-of-flight mass spectrometer for measurement of secondary ion mass spectra," *Int. J. Mass Spectrom. Ion Phys.* **40**, pp. 185–193, 1981.

[73] A. Benninghoven, "Some aspects of secondary ion mass spectrometry of organic compounds," *Int. J. Mass Spectrom. Ion Phys.* **53**, pp. 85–99, 1983.

[74] P. Sigmund, "Theory of sputtering I. sputtering yield of amorphous and polycrystalline targets," *Phys. Rev.* **184**, p. 383, 1969.

[75] M. L. Yu and K. Mann, "Bond breaking and the ionisation of sputtered ions," *Phys. Rev. Lett.* **57**, pp. 1476–1479, 1986.

[76] M. L. Yu and N. D. Lang, "Direct evidence ofelectron tunneling in the ionisation of sputtered atoms," *Phys. Rev. Lett.* **50**, pp. 127–130, 1983.

[77] Y. Gao, "A new secondary ion mass spectrometry technique for III - V semiconductor compounds using the molecular ions CsM^+," *J. Appl. Phys.* **64**, pp. 3760–3762, 1988.

[78] C. W. Magee, W. L. Harrington, and E. M. Botnick, "On the use of CsX^+ cluster ions for major element depth profiling in secondary ion mass spectrometry," *Intern. J. Mass Spectrom. Ion Process* **103**(1), pp. 45–56, 1990.

[79] V. E. Krohn and R. G. R., "Ion source of hig brightness using liquid metal," *Appl. Phys. Lett.* **27**, pp. 479–481, 1975.

[80] M. Benguerba, A. Brunelle, J. Della-Negra, S.and Depauw, H. Joret, Y. Le Beyec, M. G. Blain, G. Schweikert, E. A. Ben Assayag, and P. Sudraudd, "Impact of slow gold clusters on various solids: nonlinear effects in secondary ion emission," *Nucl. Instrum. Meth. B* **62**, pp. 8–22, 1991.

[81] N. Davies, D. E. Weibel, P. Blenkinsopp, N. Lockyer, R. Hill, and J. C. Vickerman, "Develompent and experimental application of a gold liquid metal ion source," *Appl. Surf. Sci.* **203-204**, pp. 223–227, 2003.

[82] F. Kollmer, "Cluster primary ion bombardment of organic materials," *Appl. Surf. Sci.*. **231-232**, pp. 153–158, 2004.

[83] F. Kollmer and P. Hoerster, "Mass spectrometers and liquid-metal ion source for the mass spectrometers.," U.S. Patent No. 2006/0202130 A1, issued September 14, 2006.

[84] F. Kollmer, P. Hoerster, and A. Dütting, "The liquid metal ion source, secondary ion mass spectrometer, secondary ion mass spectrometric analyisis method and the use thereof," Int. Patent WO 2009/056236 A1, issued Mai 7, 2009.

[85] I. S. Gilmore and M. Seah, "Static SIMS: towards unfragmented mass spectra - the G-SIMS procedure," *Appl. Surf. Sci.* **161**, pp. 465–480, 2000.

[86] A. D. Appelhans and J. E. Delmore, "Comparison of polyatomic and atomic primary beams for secondary ion mass spectrometry of organics," *Anal. Chem.* **61**, pp. 1087–1093, 1989.

[87] D. Weibel, N. Wong, S. Lockyer, R. Blenkinsopp, P. Hill, and J. C. Vickerman, "A C_{60} primary ion beam system for time of flight secondary ion mass spectrometry: Its development and secondary ion yield characteristics," *Anal. Chem.* **75**, pp. 1754–1764, 2003.

[88] S. C. C. Wong, R. Hill, P. Blenkinsopp, N. P. Lockyer, D. E. Weibel, and J. C. Vickerman, "Development of a $C_{60}{}^{+}$ ion gun for static SIMS and chemical imaging," *Appl. Surf. Sci.* **203-204**, pp. 219–222, 2003.

[89] S. Ninomiya, Y. Nakata, K. Ichiki, T. Seki, T. Aoki, and J. Matsuo, "Measurements of secondary ions emitted from organic compounds bombarded with large gas cluster ions," *Nucl. Instrum. Methods Phys. Res., Sect. B* **256**, pp. 493–496, 2007.

[90] J. L. S. Lee, S. Ninomiya, J. Matsuo, I. S. Gilmore, M. P. Seah, and A. G. Shard, "Organic depth profiling of a nanostructured delta layer reference material using large argon cluster ions," *Anal. Chem.* **82**, pp. 98–105, 2010.

[91] S. Ninomiya, K. Ichiki, H. Yamada, Y. Nakata, T. Seki, T. Aoki, and J. Matsuo, "The effect of incident energy on molecular depth profiling of polymers with large Ar cluster ion beams," *Surf. Interface Anal.* **43**(1-2), pp. 221–224, 2011.

[92] K. Iltgen, C. Bendel, and A. Benninghoven, "Optimized time-of-flight secondary ion mass spectroscopy depth profiling with a dual beam technique," *J. Vac. Sci. Technol. A* **15**, pp. 460–464, 1997.

[93] H.-G. Cramer, U. Jürgens, E. Niehuis, M. Terhorst, Z. Zhang, and B. A., "Surface and depth analysis of wafer surfaces by TOF mass spectrometry of sputtered material," in *Proc. SIMS IX*, 1994.

[94] R. N. S. Sodhi, "Time-of-flight secondary ion mass spectrometry (TOF-SIMS) - versatility in chemical and imaging surface analysis," *Analyst* **129**, pp. 483–487, 2004.

[95] H. W. Werner and A. E. Morgan, "Charging of insulators by ion bombardment and its minimization for secondary ion mass spectrometry (SIMS) measurements," *J. Appl. Phys.* **47**, pp. 1232–1242, 1976.

[96] B. Hagenhoff, D. Van Leyen, E. Niehuis, and A. Benninghoven, "Time-of-flight secondary ion mass spectrometry of insulators with pulsed charge compensation by low-energy electrons.," *J. Vac. Sci. Technol., A* **7**, pp. 3056–64, 1989.

[97] H. W. Werner and N. Warmoltz, "Beam techniques for the analysis of poorly conducting materials," *J. Vac. Sci. Technol. A* **2**, pp. 726–731, 1984.

[98] R. G. Wilson, F. A. Stevie, and C. W. Magee, *Secondary ion mass spectrometry: A practical handbook for depth profiling and bulk impurity analysis*, John Wiley & Sons, Ltd, 1989.

[99] D. Phinney, "Quantitative analysis of microstructures by secondary ion mass spectrometry.," *Microsc. Microanal.* **12**, pp. 352–355, 2006.

[100] R. G. Wilson, "SIMS quantification in Si, GaAs, and diamond - an update.," *Int. J. Mass Spectrom. Ion Processes* **143**, pp. 43–9, 1995.

[101] F. A. Stevie, P. M. Kahora, S. Singh, and L. Kroko, "Atomic and molecular relative secondary ion yields of 46 elements in Si for $O_2{}^{+}$ and Cs^{+} bombardment," in *Proc. SIMS VI*, 1988.

[102] R. G. Wilson, C. L. Kirschbaum, G. E. Lux, S. P. Smith, and C. J. Hitzman, "SIMS depth profiling and relative sensitivity factors and systematics for more than 50 elements from H to U implanted in insulators (SiO_2, Si_3N_4, Al_2O_3, UO_2, ZnS, ZnSe, diamond)," in *Proc. SIMS VIII*, 1992.

[103] S. W. Novak and R. G. Wilson, "Systematics of positive secondary ion mass spectrometry relative sensitivity factors for silicon and silica measured using oxygen and argon ion bombardment.," *J. Appl. Phys.* **69**, pp. 463–5, 1991.

[104] D. S. Simons, P. H. Chi, P. M. Kahora, G. E. Lux, J. L. Moore, S. W. Novak, C. Schwartz, S. A. Schwarz, F. A. Stevie, and R. G. Wilson, "Are relative sensitivity factors transferable among SIMS instruments?," in *Proc. SIMS VII*, 1990.

[105] E. Cuche, F. Bevilacqua, and C. Depeursinge, "Digital holography for quantitative phase-contrast imaging," *Optics Letters* **24**, pp. 291–293, 1999.

[106] J. Kühn, J. Charrière, T. Colomb, E. Cuche, F. Montfort, P. Emery, Y. Marquet, and D. C, "Axial subnanometer accuracy in digital holographic microscopy," *Meas. Sci. Techn.* **19**, pp. 1–8, 2008.

[107] T. Colomb, S. Krivec, H. Hutter, A. Akatay, N. Pavillon, F. Montfort, E. Cuche, J. Kühn, C. Depeursinge, and Y. Emery, "Digital holographic reflectometry," *Optical Express* **18**, pp. 3719–3731, 2010.

[108] Y. Yamamura, Y. Itikawa, and N. Itoh, *Angular dependence of sputtering yields of monatomic solids*, Institute of Plasma Physics, Nagoya University, 1983.

[109] Y. Yamamura and T. H., "Energy dependence of ion-induced sputtering yields from monoatomic solids at normal incidence," *Atom. Data Nucl. Data* **62**, pp. 149–253, 1996.

[110] M. E. Orazem and B. Tribollet, *Electrochemical impedance spectroscopy*, John Wiley & Sons, Ltd, 2008.

[111] J. Ross MacDonald, *Impedance spectroscopy*, John Wiley & Sons, Ltd, 1987.

[112] J. T. S. Irvine, D. C. Sinclair, and A. R. West, "Electroceramics: characterization by impedance spectroscopy.," *Adv. Mat.* **2**, pp. 132–8, 1990.

[113] R. Saito, S. Hayashi, and M. Kudo, "Migration behaviour of sodium in silicon oxide during sims analysis at various sample temperatures," in *Proc. SIMS XII*, 2000.

[114] D. V. McCaughan, R. A. Kushner, and V. T. Murphy, "Ion neutralization processes at insulator surfaces and consequent impurity migration effects in silicon dioxide films.," *Phys. Rev. Lett.* **30**, pp. 614–17, 1973.

[115] R. A. Kushner, D. V. McCaughan, V. T. Murphy, and J. A. Heilig, "Mobilization of sodium in SiO_2 films by ion bombardment," *Phys. Rev. B* **10**, pp. 2632–2641, 1974.

[116] R. J. Kriegler and T. F. Devenyi, "Direct measurement of Na^+ ion mobility in SiO_2 films," *Thin Solid Films* **36**, pp. 435–439, 1976.

[117] G. Greeuw and J. F. Verwey, "The mobility of sodium(1+), lithium(1+) and potassium(1+) ions in thermally grown silicon dioxide films.," *J. Appl. Phys.* **56**, pp. 2218–24, 1984.

[118] D. L. Malm, M. J. Vasile, F. J. Padden, D. B. Dove, and C. G. Pantano Jr., "Depth profile of sodium and calcium in glasses: A comparison of secondary ion mass analysis and auger spectrometry," *J. Vac. Sci. Technol. A* **15**, pp. 35–38, 1978.

[119] C. G. Pantano Jr., D. B. Dove, and G. Y. Onoda Jr., "AES compositional profiles of mobile ions in the surface region of glass," *J. Vac. Sci. Technol. A* **13**, pp. 414–418, 1976.

[120] B. M. J. Smets and T. P. A. Lommen, "Ion beam effects on glass surfaces.," *J. Am. Ceram. Soc.* **65**, pp. C80–C81, 1982.

[121] J. J. Vajo, "Effects of sample cooling on depth profling of na in SiO_2 thin films," *Surf. Interface Anal.* **25**, pp. 295–298, 1997.

[122] H. L. Hughes, R. D. Baxter, and B. Phillips, "Dependence of mos device radiation-sensitivity on oxide impurities," *IEEE T. Nucl. Sci.* **19**(6), pp. 256 –263, 1972.

[123] C. W. Magee and W. L. Harrington, "Depth profiling of sodium in silicon dioxide films by secondary ion mass spectrometry.," *Appl. Phys. Lett.* **33**, pp. 193–6, 1978.

[124] J. M. McKinley, F. A. Stevie, C. N. Granger, and D. Renard, "Analysis of alkali elements in insulators using a CAMECA IMS-6f.," *J. Vac. Sci. Technol., A* **18**, pp. 273–277, 2000.

[125] Y. Yamamoto and N. Shimodaira, "SIMS depth profile analysis of sodium in silicon dioxide.," *Appl. Surf. Sci.* **255**, pp. 860–862, 2008.

[126] S. Hayashi and K. Matsumoto, "Sample cooling effect in SIMS depth profile analysis of Na and H in glasses," in *Proceeding of SIMS IX*, 1994.

[127] C. J. Vriezema, K. T. F. Janssen, and P. R. Boudewijn, "Field-induced segregation effectsduring secondary-ion mass spectrometry depth profiling of Cu and Na implanted in silicon," *Appl. Phys. Lett.* **54**, pp. 1981–1983, 1989.

[128] C. J. Vriezema and P. C. Zalm, "Impurity migration during SIMS depth profiling," *Surf. Interface Anal.* **17**, pp. 875–887, 1991.

[129] G. F. Derbenwick, "Mobile ions in SiO_2: Potassium," *J. Appl. Phys.* **48**, pp. 1127–1130, 1977.

[130] H. Brunner, T. Vallant, U. Mayer, and H. Hoffmann, "Stepwise growth of ultrathin SiO_x films on Si(100) surfaces through sequential adsorption/oxidation cycles of alkylsiloxane monolayers," *Langmuir* **12**, pp. 4614–4617, 1996.

[131] R. Saito, M. Nagatomo, N. Makino, S. Hayashi, and M. Kudo, "Characterization of ion-induced sodium migration in various kinds of silicon oxide films.," *Appl. Surf. Sci.* **203-204**, pp. 508–511, 2003.

[132] M. Yashima, Y. Ando, and Y. Tabira, "Crystal structure and electron density of α-silicon nitride: Experimental and theoretical evidence for the covalent bonding and charge transfer," *J. Phys. Chem. B* **111**, pp. 3609–3613, 2007.

[133] D. du Boulay, N. Ishizawa, T. Atake, V. Streltsov, K. Furuya, and F. Munakata, "Synchrotron x-ray and ab initio studies of β-Si_3N_4," *Acta Cryst.* **B60**, pp. 388–405, 2004.

[134] D. Galusek, F. L. Riley, and R. Riedel, "Nanoindentation of a polymer-derived amorphous silicon carbonitride ceramic," *J. Am. Ceram. Soc.* **84**, pp. 1164–1166, 2001.

[135] E. Ibok, S. Gang, and O. B., "Material, fractural and optical properties of PECVD silicon nitride and oxynitride films," in *Proc. 13th Int. Conf. Chem. Vap. Dep.*, 1996.

[136] D. R. Kerr, J. S. Logan, P. J. Burkhardt, and W. A. Pliskin, "Stabilization of SiO_2 passivation layers with P_2O_5," *IBM J. Res. Develop.* **8**, pp. 376–384, 1964.

[137] P. Balk and J. M. Eldridge, "Phosphosilicate glass stabilization of FET devices," *Proc. IEEE* **57**, pp. 1558–1563, 1969.

[138] T. H. Tom Wu, K. O'Brien, and D. G. Hemmes, "Comparison of passivation films: The effect of thermal cycles and comparison of phosphorous doped oxide films," *J. Vac. Sci. Technol. B* **11**, pp. 2090–2095, 1993.

[139] H. Hosono, "Chemical interaction in ion-implanted amorphous SiO_2 and application to formation and modification of nanosize colloid particles.," *J. Non-Cryst. Solids* **187**, pp. 457–72, 1995.

[140] A. P. Baraban and L. V. Malyavka, "Long-range effects in ion-implanted silicon–silicon-dioxide structures," *Tech. Phys. Lett.* **23**, pp. 786–787, 1997.

[141] Y. M. Gueorguiev, R. Kogler, A. Peeva, A. Mucklich, D. Panknin, R. A. Yankov, and W. Skorupa, "High-energy ion-implantation-induced gettering of copper in silicon beyond the projected ion range: the trans-projected-range effect.," *J. Appl. Phys.* **88**, pp. 5645–5652, 2000.

[142] R. Kögler, C. Debrois, J. W. Gerlach, H. Hutter, A. Mücklich, and W. Skorupa, "Trans-R_p gettering and out-diffusion of oxygen implanted into highly b-doped silicon," in *Proc. GADEST'09*, 2009.

[143] H. Kaeslin, *Digital Integrated Circuit Design*, Cambridge University Press, 2008.

[144] S. M. Sze, *Physics of Semiconductor Devices*, John Wiley & Sons, Ltd, 1981.

[145] B. Roling, "Hopping dynamics of ions and polarons in disordered materials: On the potential of nonlinear conductivity spectroscopy," *J. Chem. Phys.* **117**, pp. 1320–1327, 2002.

[146] E. D. Tsagarakis and W. Weppner, "Electrode kinetic phenomena of solid state ionic devices," *Ionics* **11**, pp. 240–247, 2005.

[147] A. Heuer, S. Murugavel, and B. Roling, "Nonlinear ionic conductivity of thin solid electrolyte samples: Comparison between theory and experiment.," *Phys. Rev. B: Condens. Matter Mater. Phys.* **72**, pp. 174304/1–174304/7, 2005.

[148] B. Roling, S. Murugavel, A. Heuer, L. Luehning, R. Friedrich, and S. Roethel, "Field-dependent ion transport in disordered solid electrolytes.," *Phys. Chem. Chem. Phys.* **10**, pp. 4211–4226, 2008.

[149] J. L. Barton, "Electric conduction of glasses at intermediate field strengths," *J. Non-Cryst. Solids* **203**, pp. 280–285, 1996.

[150] H. J. Neuhaus, D. R. Day, and S. D. Senturia, "Sodium transport in polyimide-silicon dioxide systems.," *J. Electron. Mater.* **14**, pp. 379–404, 1985.

[151] B. Cao Martin, C. J. Tracy, J. W. Mayer, and L. E. Hendrickson, "A comparative study of hillock formation in aluminum films," *Thin Solid Films* **271**(1-2), pp. 64–68, 1995.

[152] B. Hagenhoff, "High resolution surface analysis by TOF-SIMS," *Microchim. Acta* **132**, pp. 259–271, 2000.

[153] K. Nikawa, "Optical beam induced resistance change (OBIRCH): Overview and recent results," in *Proc. IEEE Lasers and Electro-Opt. Soc. 16th Annu. Meet.*, 2003.

Curriculum vitae

Dipl.-Ing. Stefan Krivec

Personal Information

Address	Birkenweg 23 A-9241 Wernberg
Place and date of birth	Villach, 12.06.1981
Marriage status	unmarried
Nationality	Austria
E-mail	stefan.krivec@gmx.at

Education

08/2008 - 06/2011	**KAI GmbH, Villach, Austria** PhD student in collaboration with the Vienna University of Technology and Infineon Technologies Austria AG in Villach in the framework of the project "Robust Metalization and Interconnects" dealing with the subject "Test Methods for Mobile Ions" Supervisor: Ao. Univ. Prof. Dr. Herbert Hutter
06/2008	Graduation in technical chemistry with highest distinction
10/2002 - 06/2008	**Vienna University of Technology, Austria** Study of Technical Chemistry; Focus on Macromolecular Chemistry Diploma thesis: "Porous hybrid materials as carrier for polymeric waveguides" Supervisor: Ao. Univ. Prof. Dr. Robert Liska Privatdoz. Dr. Helga Lichtenegger
01/2007 - 06/2007	**University of Bergen, Norway** Projectwork in Petroleum Chemistry: "Validating a new titration procedure for total acid number determination in crude oil" Supervisor: Prof. Dr. Tanja Barth
09/1995 - 06/2000	**Secondary Technical and Vocational College Villach, Austria** Subject of education: Constructional Engineering of Buildings

Internships and other activities

10/2008 - 06/2009	Participation at TUtheTOP, the TU Vienna high potential program
09/2006 - 10/2006	ARC Seibersdorf, Austria, Group for radiation safety
08/2006	Borealis AG, Linz, Austria, Research and Development
07/2005	ARC Seibersdorf, Austria, Group for radiation safety
08/2004 - 09/2004	Omya GmbH, Gummern, Austria, Quality Management
07/2004	ARC Seibersdorf, Austria, Group for radiation safety
07/2004	ARC Seibersdorf, Austria, Group for radiation safety
09-2000 - 05/2001	Military service, Rohrkaserne Villach, Austria

Personal skills

Languages	German - mother tounge English - fluent Norwegian - advanced
Computer skills	MS Office (Word, Excel, PowerPoint), OriginPro, AutoCAD, Adobe Photoshop. SciFinder Scholar, LateX
Technical	Time of flight - secondary ion mass spectrometry Digital holography microscopy Thermo gravimetric anaysis Differential scanning calorimetry

Vienna, May 2011